Energy Conversion through Photo-electrocatalysis and Electrocatalysis to Value-added Products from Simulated Seawater and Biomass Components

by

Inderjeet Chauhan

Registration Number: 10CC18A26057

A thesis submitted to the

Academy of Scientific & Innovative Research

for the award of the degree of

DOCTOR OF PHILOSOPHY

in

Science

Under the supervision of

Dr. Chinnakonda S. Gopinath

CSIR- National Chemical Laboratory, Pune

Academy of Scientific and Innovative Research,
AcSIR Headquarters, CSIR-HRDC campus,
Sector 19, Kamla Nehru Nagar,
Ghaziabad, U.P. – 201 002, India

July 2024

CERTIFICATE

This is to certify that the work incorporated in this Ph.D. thesis entitled **"Energy Conversion through Photo-electrocatalysis and Electrocatalysis to Value-added Products from Simulated Seawater and Biomass Components"** submitted by **Inderjeet Chauhan** to Academy of Scientific and Innovative Research (AcSIR) in fulfilment of the requirements for the award of the Degree of **Doctor of Philosophy in Science**, embodies original researchwork under my guidance. I further certify that this work has not been submitted to any other University or Institution in part or full for the award of any degree or diploma. Research materials obtained from other sources has been duly acknowledged in the thesis. Any text, illustration, table etc., used in the thesis from other sources, have been duly cited andacknowledged.

Inderjeet Chauhan
(Research Student)

Dr. Chinnakonda S. Gopinath
(Research Supervisor)

Date: 24/07/2024
Place: CSIR-NCL, Pune

STATEMENTS OF ACADEMIC INTEGRITY

I, **Inderjeet Chauhan**, a Ph.D. student of the Academy of Scientific and Innovative research (AcSIR) with Registration No.10CC18A26057 hereby undertake that the thesis entitled "**Energy Conversion through Photo-electrocatalysis and Electrocatalysis to Value-added Products from Simulated Seawater and Biomass Components"** has been prepared by me and that the document reports original work carried out by me and is free of any plagiarism in compliance with the UGC Regulations on *"Promotion of Academic Integrity and Prevention of Plagiarism in Higher Educational Institutions (2018)"* and the CSIR Guidelines for *"Ethics in Research and in Governance (2020)"*.

इन्जीत चौहान

Signature of the Student

Name: Inderjeet Chauhan

Date: 24/07/2024

Place: Pune

It is hereby certified that the work done by the student, under my/our supervision, is plagiarism free in accordance with the UGC Regulations on *"Promotion of Academic Integrity and Prevention of Plagiarism in Higher Educational Institutions (2018)"* and the CSIR Guidelines for "*Ethics in Research and in Governance (2020)*".

24/7/24

Signature of the Supervisor

Name: Dr. Chinnakonda S. Gopinath

Date:

Place: Pune

This thesis is dedicated to those who extend a helping hand, to the brave souls who sacrificed their lives for our nation, and to the selfless individuals whose acts of kindness embody the spirit of humanity.

ACKNOWLEDGEMENT

Embarking on the journey to complete a PhD has been one of the most challenging and rewarding experiences of my life. The road to this point has been marked by countless hours of hard work, moments of doubt, and profound realizations. As I reflect on this journey, I recognize that it would not have been possible without the support, encouragement, and guidance of many incredible individuals. It is with immense gratitude that I take this opportunity to acknowledge their contributions and express my heartfelt thanks.

First and foremost, I extend my deepest gratitude to my supervisor, ***Dr. Chinnakonda S. Gopinath (Gopi)****. Your unwavering support, insightful guidance, and patience have been instrumental in the successful completion of my research. From the earliest stages of formulating the research questions to the final stages of writing this thesis, you have been a constant source of inspiration and motivation. Your expertise and commitment to excellence have significantly shaped my academic journey, and for that, I am profoundly grateful. The numerous discussions we had, your prompt feedback, and your continuous encouragement helped me to stay focused and to strive for the highest standards. Your belief in my abilities, even during times when I doubted myself, has been a cornerstone of my success. Your lessons extended beyond academics, teaching us kindness, selflessness, and the value of serving others. I thank you for your impact on my life.*

I also want to extend my heartfelt thanks to the members of my supervisory committee, ***Dr. Ulhas K. Kharul, Dr. J. Nithyanandan,*** *and* ***Dr. Sakya S. Sen****. Your valuable feedback, constructive criticism, and encouragement have greatly contributed to the refinement and depth of my research. I extend my heartfelt thanks to* ***Dr. Sapna Ravindranathan*** *for her invaluable assistance in resolving complex problems****, Dr. Suwarna Datar*** *for K-PFM measurements and to* ***Dr. Kavita Joshi*** *for her collaborative work on DFT. Your diverse perspectives and scholarly insights have greatly enriched my research, pushing me to explore new dimensions in my study. I would also like to express my appreciation to* ***Dr. Avishek Saha*** *and* ***Dr. Jayashree*** *for their valuable help and support.*

I am sincerely thankful to ***Dr. Kshirodra Kumar Patra*** *and* ***Dr. Naresh Nalajala*** *for the rigorous academic discussions and intellectual challenges that have helped me grow as a researcher and develop a deeper understanding of my field. Additionally, I owe a special debt of gratitude to* ***Mr. Vijay PM*** *for his continuous support in all aspects of my work. His*

unwavering willingness to help and dedication has made him the best trainee I could have ever asked for.

I want to express my gratitude to Dr. Ashish Lele, the current director of the CSIR-NCL, and Prof. Ashwini Kumar Nangia, the previous director, for allowing me to work at this esteemed organization for providing the resources and infrastructure I needed. For their generous assistance throughout the course of my Ph.D., I am incredibly grateful to Dr. V. V. Bokade, Chairperson, Catalysis and Inorganic Chemistry Division, and Drs. Chinnakonda S. Gopinath and Shubhangi B. Umbarkar (former Chairpersons). Many thanks to the division staff members specially Mr. Dhutraj who assisted me with the many office tasks. I want to express my gratitude to the entire administrative and non-teaching personnel of CSIR-NCL for all of their help and support over the years.

I also want to express my gratitude to all the staff members at NCL's Center for Materials Characterization, who have helped me through their services over the years. I sincerely appreciate the prompt assistance provided by Mr. S. S. Deo, Mr. Niteen, Mr. R. S. Gholap, Chetan, Tushar, Medha, and Shurti for the XPS, TEM, HRTEM, FESEM, and SEM measurements. Special thanks to Medha, Tushar and Chetan for providing me with urgent slots on request. Many thanks to Dr. Tejas, Mr. Ratnesh Jha for providing me with the XRD and UV- Vis's spectroscopy and BET slots. I would like to express my gratitude to the SAAC and AcSIR office staff, including Mr. Purushottam, Mrs. Khole, Ms. Komal, Mrs. Vijaya, and Ms. Vaishali, for their invaluable support and assistance.

I extend my heartfelt thanks to the non-scientific departments for their invaluable support. Special thanks go to Dinesh, Santosh, Sandy, the C&P section, and the billing section for their assistance with my bills and fellowship SE/UC throughout my tenure. I am also grateful to the NCL canteen staff for their polite behavior and excellent service. Along with I thank NCL medical Centre all staff members and Dr. Jyotsana Chitalkar. The support provided by the library staff specially from Gati sir and DIRC offices has been invaluable in ensuring that I had access to the necessary resources and support throughout my studies.

I sincerely acknowledge for the ***DST-INSPIRE*** *and* ***HCP-44 project*** *Fellowship given to me during my PhD research work at NCL.*

A special mention goes to CSG (Catalysis and surface Science) group. The collaborative environment and the spirit of teamwork within our group have been truly inspiring. I am

thankful to each member, Dr. Pradnya Bharad, Dr. Manoj Kumar Ghosalya, Dr. Ruchi Jain, Dr. Kasala Prabhakar Reddy, Dr. P. Devaraji, Dr. Sadhu Kolekar, Dr. Abhaya Kumar Mishra, Dr. Himanshu Bajpai, Dr. Ravi Ranjan, Dr. Nitin Mhamane. They have shared experiences with me that I will never forget, and I intend to keep in touch with them. I would like to thank all my dear labmates, Nivedhitha (tendi) for constant support and friendship, Kranti, Subhashree, Arindam, Dr. Priyabrata, Shinto Tom K S, Elsa Dais, Nashwa V P, Sayana (sister), Sibo Chetry, Sarika, Avadhi Trivedi, Sreeya Raj, Omkar Borade, Rahul Mendhe, Hamid P. Kanattil, Jyoti, Nikita, Dr. Mahendra Pawar, Akhila, Athira S babu (sister), Dr. Pranjal Saikia, Nayanjyothi, Avani, Vasunthara Devi, Garima, Anjana, Chnimay, Akshay Murli, Athira PA, Athira trainee, Dr. Kishor, Dr. Jayasmita, Dr. Mukta, Nasrin, Jiffin, Jayalaxmi, Vishal, Shubhankar, Sudipto, Tejas, Prajakta, Karan for their help and fostering a friendly and conducive work environment in the lab. I cherish the unforgettable lab trips and gathering outside or sir's home, made possible by our wonderful labmates and our cool supervisor, Dr. Chinnakonda S. Gopinath.

I thank to all my divisional friends Shiva, Aakash (never said no for any kind of help), Gorab, Shweta Sharma, Samuruddhi, Pragati, Mayuri, Sheetal, Archana, Amin, Eeshwar, M. Prabhu, K. Prabhu, Nittan, Pavan, Ankit baba, Asma, Arunima, Dr. Govind, Anuradha, Pavan, Jyotsna, Betsy, Pooja, Twinkle, Sanket, Dr. Milan, Dr. Gargi. Dr. Rohit, Kritika, Vishal, Ajith, Kajal, Biplab, Kailash, Zinoy, Sonu, Manoj, Meera, Dr. Dhananjay, Dr. Shunotra, Dr. Priyanka, Dr. Seema, Akshay, Vipul bhaiya, Vasi, Rushi, Shubham, Simbha, Muthu, Visnumaya, Jyoti T, Deepali, Dr. Dheerendra, Dr. Yayti, Dr. Priya, Kalyani, Lavanya, Dr. Jyoti, Tufeil, Dr. Susmita, Shrijith for their help.

My Special thanks to Sonu Kumar and Sidharth Barik (malai boys) for all the fruitful and entertainment discussion late nights. Your love and encouragement were indispensable for the success of this and I am grateful for those experiences.

I'd want to thank all of my NCL Cricket's and Volleyball friends, including Pavan Dongapure, Mahendra Bhaiya, Manish, Rohit Sr., Rohit Jr., Akash, Dr. Arun, Dr. Ashish, Bharath, Ashish NCIM, Kundan, Dharmendra, Naru bhai, Pinka bhai, Nitin (polymer), Prashant (polymer), Priyam, Sandy Bhai, Soumya, Ravi Bagel, Umasharan, Yogesh, DJ(Bio), Bejosh, Rakesh, Nishad, Juned, Shabaz Bhai, S Pradeep, Ajay, Dr. Anupam, Arshad, Junaid, Viresh, Kiran chetta, Tanha, Sahil, Ankita, Rutuja, Pranali, Pratiksha, Jayram, Mayur. Your camaraderie and joyful environment during GJPL and daily matches have been deeply appreciated.

Beyond the realm of scientific work lies a life enriched with friends, the most beautiful gift of my life in Pune. I also want to thank Akash, Sangram, Sai, Ashwini, Bhagyshree, Geetu, Abdulla, Thanna, Kiran, Viksit, Swapnil, Manoj, Pawan (Utpal Das Sir), Archana, Darshana, Mayur, Pooja (BLV sir), Shubham, Subodh bhaiya, Supriya, Monika, Monika ma'am, Amrita, Dr. Amrish, Chandan, Rajni, Soumya, Smita, Aishwarya, Surya, and Neha, Dr. Dipesh, Chandni, Tubai, Debjani, Pragnya(sister), Jesna, Dr. Anirban, Nikhil, Tushar, Chandrodaya, Amit, Ravi, Mayank, Prem, Manoj, Prachi, Abha, Bhanu Bhai, Priyanka halder, Ashvini, Neha, Arindam (Arooprath sir), Tanuja, Ankita Bagde, Reshma Mohan, Aliha, Amrutha, Elizabeth, Upasana, Jayesh, Ashish sharma , Ruchi, Anoushka, Ayeesha, Ajmal, Yogesh, Poonam, Simmi, Shilpa k, ***Dr. Sapna Bhardwaj (FRI)****. Thanks, Sujeet and Chotu bhaiya, Vishal bhaiya, Subash, for giving me the best meals during my tenure.*

To my family, I owe my deepest gratitude. My parents, Kamal Singh Chauhan and Sama Devi, your unconditional love and unwavering belief in me have been my guiding light. Your sacrifices and encouragement have provided me with the strength to overcome the many obstacles I encountered along this journey. You have been my biggest cheerleaders, and your faith in my abilities has been a constant source of motivation. My siblings, Sumit and Ankit, your support and understanding have been a source of great comfort. Thank you for always being there for me and for providing a sense of normalcy and stability in my life.

To my extended family and friends, your encouragement and belief in my abilities have been immensely motivating. My sincere appreciation goes to my school, colleagues and friends at Goswami G D S V M I C Uttarkashi, RCU PG college Uttarkashi and SGRR PG college Dehradun, Uttarakhand. The camaraderie and intellectual exchange we shared have been invaluable. I am particularly grateful to Gaurav Bisht, Harish, Pooja, Manisha, Karamveer bhaiya, Ashish Rana and ***Dr. Kameshwar Prasad*** *for their support and encouragement during the tough times. A special thanks to K. Prasad, who took me to NCL for the interview, which was a pivotal moment in my journey.*

To my mentors and educators who have guided me along the way, your influence has been profound. From my early days in academia to the advanced stages of my doctoral studies, each one of you has played a pivotal role in shaping my intellectual and personal growth. I am particularly grateful to Mr. Sushil Kumar Sharma, Dr. Gulshan Kumar Dhingra and Dr. Shyamveer Singh for their early encouragement and for instilling in me a love for learning and

research. Your passion for your fields and your dedication to teaching have been truly inspiring.

In conclusion, this thesis is not just the culmination of my hard work and dedication, but also a testament to the collective support and encouragement of all the wonderful individuals mentioned above. I am profoundly grateful to each one of you for your contributions, and I dedicate this work to all of you. Thank you for being a part of my journey and for making this achievement possible. Your support has been the foundation upon which this work has been built, and I am forever indebted to you.

This acknowledgment is not just a formality but a heartfelt expression of my appreciation for each of you. The journey to complete this PhD has been a collective effort, and I am humbled and honored to have had the privilege of working with and knowing such extraordinary individuals. As I move forward in my academic and professional career, I carry with me the lessons learned, the relationships forged, and the memories created during this remarkable journey.

Thank you all from the bottom of my heart.

Thank You All

With Best Regards,

Inderjeet Chauhan

LIST OF ABBREVIATIONS

Acronym	Full form
GHG	Greenhouse gas
GMST	Global mean surface temperature
IPCC	Intergovernmental Panel on Climate Change
IEA	International Energy Agency
FCVs	fuel cell vehicles
NHEM	National Hydrogen Energy Mission
PEC	Photo-electrochemical
HER	Hydrogen evolution reaction
OER	Oxygen evolution reaction
CER	Chlorine evolution reaction
PEM	Proton exchange membrane
AEM	Anion exchange membrane
SO	Solid oxide
AOR	Anodic oxidation reaction
GLYOR	Glycerol oxidation reaction
GLUOR	Glucose oxidation reaction
MalOR	Maltose oxidation reaction
LacOR	Lactose oxidation reaction
UOR	Urea oxidation reaction
HzOR	Hydrazine oxidation reaction
GNA	Gluconic acid
GRA	Glucaric acid
HMF	5-hydroxymethylfurfural
2D	Two-dimensional
CV	Cyclic voltammetry or Cyclic Voltammogram
DI	Deionized
ECSA	Electrochemical surface area
EG	Ethylene glycol
EDS	Energy-dispersive X-ray spectroscopy
FESEM	Field emission scanning electron microscope

HRTEM	High resolution transmission electron microscope
JCPDS	Joint committee on powder diffraction standards
NMR	Nuclear magnetic resonance
LSV	Linear sweep voltammetry
NF	Nickel foam
PEC	Photoelectrochemical
C_{dl}	Double layer capacitance
SAED	Selected area electron diffraction pattern
h	Hour
min	Minute
CA	Chronoamperometry
CP	Chronopotentiometry
a. u.	Arbitrary unit
et al.	And others
PVP	Polyvinylpyrrolidone
RHE	Reversible hydrogen electrode
FE	Faradaic efficiency
SCE	Saturated calomel electrode
TEM	Transmission electron microscope
HPLC	High-performance liquid chromatography
UV	Ultraviolet
XRD	X-ray diffraction
XPS	X-ray photoelectron spectroscopy
XVB	X-ray valance band spectroscopy

Table of Contents

Chapter 2: Synthesis and Experimental Methods

Chapter 3: Nanostructured Co-doped $BiVO_4$ for Efficient and Sustainable Photo-electrochemical Chlorine Evolution from Simulated Sea-Water

Chapter 4: Electrocatalytic Glycerol Conversion: A Low-Voltage Pathway to Efficient Carbon-Negative Green Hydrogen and Value-Added Chemical Production

Chapter 1

Introduction

General Insights on water splitting, water electrolyzer and Strategies to replace the energy extensive water oxidation reaction

Image ref: Generated by Canva based on a prompt by Inderjeet Chauhan, 2024.

1.1 Challenge Description: Mitigating Fossil Fuel Dependency and Possibly Addressing Climate Imperatives

The late eighteenth century saw the beginning of the industrial revolution, which resulted in a dramatic increase in manufacturing capacity, facilitated with the use of new energy sources including internal combustion engines, coal, steam engines, and petroleum.[1-3] As the 19th century progressed, fossil fuels, notably coal and petroleum, emerged as the predominant energy sources, extensively utilized for electricity generation, transportation, and various industrial and domestic applications. But burning fossil fuels releases a variety of harmful particles and compounds, such as sulphur oxides, nitrogen oxides, and carbon dioxide, which have a detrimental impact on the environment and human health. These include acid rain, smog, poor air quality, and global warming, which is mostly caused by the greenhouse effect of CO_2 emissions.[4] Based on the study published by the Intergovernmental Panel on Climate Change (IPCC), the global mean surface temperature (GMST) has increased by 0.87 degrees Celsius between 2006 and 2015, indicating a noticeable departure from the pre-industrial condition of the climate.[5,6] This elevation in GMST has already instigated multiple observable climatic alterations, and unabated greenhouse gas (GHG) emissions stand to exacerbate the situation, potentially propelling GMST by an additional 4 degrees Celsius or more by the year 2100.[6] The high confidence estimate that any GMST increase above 1.5 °C may cause long-term and irreversible effects is highlighted in the most recent IPCC report.

Therefore, it is necessary to control the variables that lead to GMST overshoot. This calls for coordinated actions to reduce CO_2 and other GHG emissions by decreasing the use of fossil fuels and promoting the development of environmentally friendly alternative energy sources.[4] The need for the scientific community to create practical methods for the creation of sustainable energy conversion and storage devices is highlighted by the negative environmental effects, rising energy use, and depleting fossil fuel reserves. In this regard, utilising a variety of renewable energy sources, including solar, wind, hydro, geothermal, and biomass, has received a lot of interest.[7] Nonetheless, the intermittent and localized nature of these renewable energy reservoirs impels scrutiny of their ramifications on global energy security, warranting the development of energy storage technologies capable of accommodating such irregular energy influxes.

In light of these considerations, hydrogen emerges as a promising avenue, using the greatest gravimetric energy density of all known fuels while avoiding the drawbacks of traditional

energy storage technologies by taking use of the chemical simplicity of hydrogen produced from water.[1,2,7] As a result, hydrogen production offers a complete answer for supplying a sustainable energy source as well as storing intermittent renewable energy, especially when hydrogen is produced from plentiful water reservoirs. Intriguingly, hydrogen serves not only as a fuel but also as a versatile energy carrier, thereby heralding the prospect of a transition from the prevailing 'carbon-based economy' to a 'hydrogen economy'.[8] Nevertheless, questions concerning the quantum of water requisite for hydrogen generation, given the constrained supply of freshwater and the imperative for clean water in water splitting for enhanced energy efficiency, are pertinent. Turner's quantitative analysis sheds light on this issue, revealing that approximately 100 billion gallons of water annually suffice for generating hydrogen for some 230 million fuel cell vehicles, constituting nearly one-third of the water requirement for equivalent gasoline production.[8] Thus, the hydrogen economy emerges as a promising contender to supplant the prevailing carbon-based economy, underscoring its potential as a sustainable alternative.

1.2 Tracing the Evolution: Hydrogen Economy Through Time

The emergence of the hydrogen economy represents a pivotal moment in our quest for sustainable energy solutions, driven by mounting concerns over environmental degradation and fossil fuel dependency.[9] Historical records trace hydrogen's utility back to the 16th century, but it wasn't until the latter part of the 20th century that serious considerations regarding its potential as an energy carrier began to take root. In the 1970s, global oil crises and rising environmental consciousness propelled research and development efforts in hydrogen technologies, with investments exceeding $1 billion annually by the 1990s.[10] This surge in interest led to the establishment of dedicated research programs and institutions, including the U.S. Department of Energy's Hydrogen Program in 1978 and the European Union's Hydrogen and Fuel Cell Technology Platform in 2003.[11] As we stand on the brink of a hydrogen-powered future, understanding the historical context of the hydrogen economy is imperative for navigating the complexities of energy transition and shaping a cleaner, more sustainable world. Bockris identified additional challenges associated with transitioning to hydrogen economy, including (i) a reluctance to depart from traditional fossil fuels, (ii) insufficient education in the electrochemical domain, and (iii) public apprehension regarding hydrogen.[12] Therefore, to ensure the effective adoption of the hydrogen economy, it is imperative to tackle these aforementioned obstacles.

1.3 Assessing the Contemporary Landscape: The State of the Hydrogen Economy

As of the current status, the hydrogen economy is experiencing a notable surge in global interest and investment. According to the International Energy Agency (IEA), global investments in hydrogen-related projects reached approximately $320 billion upto 2030 in figure 1.1, with expectations of further growth in the coming years.[13] Countries such as Japan, Germany, and South Korea are leading the charge in hydrogen infrastructure development and deployment, with ambitious targets for hydrogen production and utilization.

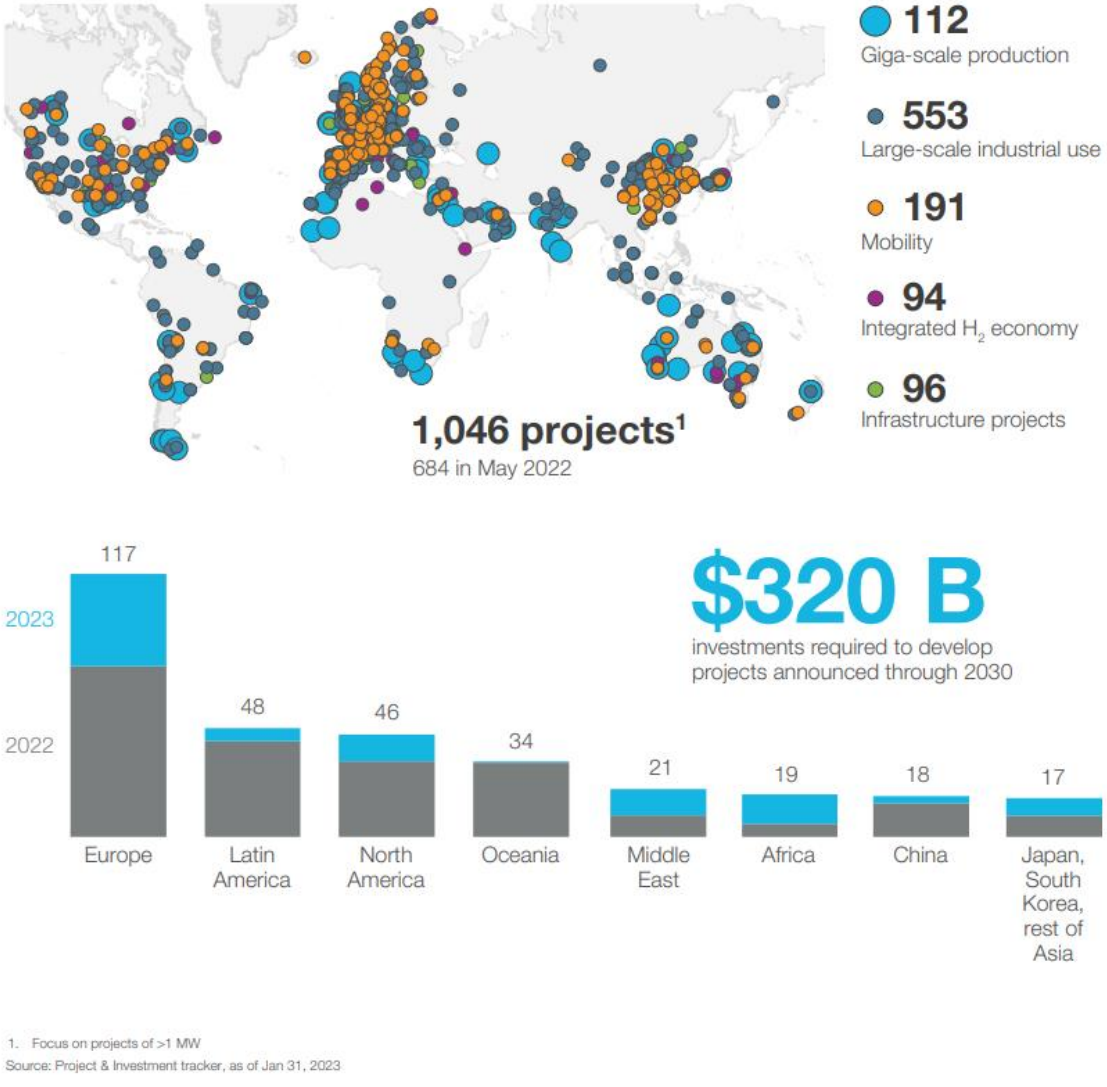

Figure 1.1 Global investments in hydrogen-related projects up to 2030. (Source: Hydrogen Insights 2023, Hydrogen Council, 2023.)

In terms of technology, significant advancements have been made in hydrogen production, storage, and utilization. Electrolysis, particularly using renewable energy sources such as wind and solar, has emerged as a key method for green hydrogen production. According to data from

the Hydrogen Council, the cost of green hydrogen production has fallen by approximately 50% over the past decade, making it increasingly competitive with other energy sources. [13] The transportation sector is also witnessing a shift towards hydrogen fuel cell vehicles (FCVs) and hydrogen-powered buses and trucks. Manufacturers such as Toyota, Hyundai, and Nikola Motors are ramping up production of hydrogen FCVs, with forecasts predicting a significant increase in the global hydrogen vehicle fleet in the coming years.[14]

Furthermore, governments around the world are implementing policies and incentives to support the growth of the hydrogen economy. The European Union's Hydrogen Strategy, for example, aims to establish a clean hydrogen market and infrastructure across the region, with a target of 40 gigawatts of electrolyzer capacity by 2030.[15] Despite these positive developments, many many challenges remain to be attended, including the need for further cost reductions, the expansion of hydrogen infrastructure, and addressing public perception and acceptance of hydrogen technologies. Nonetheless, with continued investment, technological innovation, and supportive policies, the hydrogen economy is poised for significant expansion and integration into the broader energy system in the years to come.

1.4 Hydrogen Production Landscape in India: Current State and Future Prospects

In India, research into hydrogen energy development commenced in 1976 and has since encompassed various aspects crucial to the advancement of hydrogen as an energy carrier.[16] This study covers the production of H_2 from water by electrochemical, photochemical, and biophotochemical water electrolysis; it also covers the storage of H_2 in the form of metal hydrides and liquid H_2; and finally, it covers the use of H_2 as heat and engine fuel. Significant progress was made by the AMM Murugappa Chettiar Research Centre (MCRC) in Chennai, which demonstrated the production of H_2 on a batch scale from distillery waste. This led to the development of a pilot plant that can produce up to 18,000 litres of H_2 per hour.[17] As per data from reputable sources such as the Ministry of New and Renewable Energy (MNRE) and the Central Electricity Authority (CEA), hydrogen production in India is witnessing a significant uptick, with diverse methods being employed to generate this versatile energy carrier. In India, electrolysis is one method of producing hydrogen, especially when using renewable energy sources like solar and wind power. Following the Prime Minister's declaration at COP26, the MNRE is actively striving to attain a non-Fossil electricity generation capacity of 500 GW by the year 2030.[18] This growth in renewable energy infrastructure has laid a strong foundation

for scaling up electrolysis-based hydrogen production, contributing to the nation's efforts towards decarbonization.

Chlor-alkali industries stand out as major contributors to hydrogen production in India. Present endeavours focus on both R&D advancements and scaling-up technologies for hydrogen generation, including efforts toward establishing hydrogen purification units, compression systems for cylinder filling, and on-board hydrogen applications in vehicles. Recent data underscores the growing momentum in hydrogen production, highlighting India's strides towards embracing hydrogen as a key component of its energy landscape. The CEA's data reveals that the chlor-alkali industry accounts for a substantial share of hydrogen production, reflecting the importance of industrial sectors in driving hydrogen production in the country. Additionally, research institutions and pilot projects are exploring innovative approaches to hydrogen production, including hydrogen generation from biomass and waste streams. Collaborative efforts between academia, industry, and government bodies are fostering innovation and driving advancements in sustainable hydrogen production technologies. Looking ahead, India's National Hydrogen Energy Mission (NHEM) aims to accelerate the adoption of hydrogen as a key enabler of the country's energy transition.[19]

The mission sets ambitious targets for hydrogen production, infrastructure development, and technology deployment, aligning with the nation's broader objectives of achieving energy security, reducing carbon emissions, and fostering economic growth. In summary, the scenario of hydrogen production in India is characterized by a diverse mix of sources and technologies, underpinned by concerted efforts to promote clean energy and sustainable development. With supportive policies, investment incentives (such as production linked incentives (PLI)), and collaborative initiatives, India is poised to emerge as a key player in the global hydrogen economy, driving innovation and shaping the future of clean energy.

1.5 Water Splitting: Mechanisms and Variants

To mitigate the cost of hydrogen derived from water, it is imperative to comprehend the underlying principles and diverse pathways involved in water splitting reactions. Consequently, the next sections will focus on clarifying the workings of different possible routes for producing hydrogen from water.

The process of water splitting is the dissolution of the H-O-H bond into its component parts, which is followed by the creation of molecules of oxygen and hydrogen (Figure 1.2). Due to

its thermodynamically unfavourable nature, water splitting invariably necessitates an external energy source.[20]

$$H_2O\ (l) \rightarrow H_2\ (g) + ½\ O_2\ (g) \qquad \Delta G°= +237\ kJ/mol \qquad \text{Eq. (1.1)}$$

Water splitting can be divided into several types, such as thermocatalytic, electrocatalytic, and photocatalytic, depending on the type of energy input. In the current thesis, we extensively address the process of photo-electrochemical and electrocatalytic water splitting.

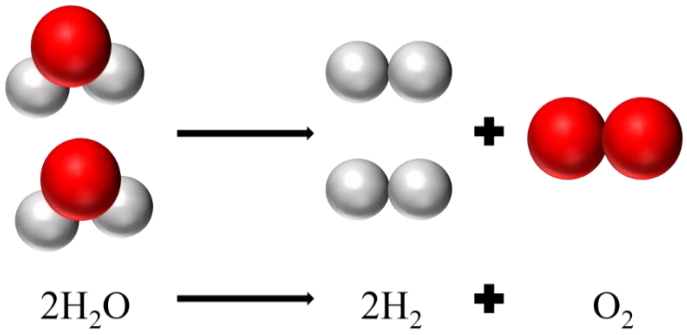

Figure 1.2 A schematic depiction elucidating the disintegration of a water molecule into its constituent elements.

1.5.1 Photo-electrochemical (PEC) water splitting: Water splitting in a PEC unit is dependent upon two separate half-reactions called the oxygen evolution reaction (OER) and the hydrogen evolution reaction (HER), each occurring on separate electrodes shown in figure 1.3. The photooxidation of water at the anode produces oxygen, requiring four holes (Equation (1.3)), while the cathodic reaction reduces water to hydrogen, involving the consumption of four electrons (Equation (1.4)). In order to get total PEC water splitting, liquid water molecules must be converted into gaseous oxygen and hydrogen with a minimum light-driven energy input of 1.23 electron volts (eV) per electron (Equation (1.5)).[21, 22]

$$h\nu \rightarrow h^+ + e^- \qquad \text{Eq. (1.2)}$$

$$2H_2O\ (l) + 4h^+ \rightarrow O_2\ (g) + 4H^+(aq) \qquad E_0 = +1.23\ V \text{ versus NHE} \qquad \text{Eq. (1.3)}$$

$$4H^+\ (aq) + 4e^- \rightarrow 2H_2\ (g) \qquad E_0 = 0\ V \text{ versus NHE} \qquad \text{Eq. (1.4)}$$

$$h\nu + 2H_2O\ (l) \rightarrow 2H_2\ (g) + O_2\ (g) \qquad \Delta G°= +237.2\ kJ/mol \qquad \text{Eq. (1.5)}$$

The crucial elements within PEC processes consist of photoelectrodes constructed from photoactive materials. These materials have the unique capability to absorb sunlight and convert it into a photo potential, driving the PEC process forward. A photoelectrode usually

consists of a transparent conductive substrate with a semiconductor layer placed on top of it. A typical PEC cell can have two photoelectrodes or just one photoelectrode (either a photoanode or a photocathode) along with a counter electrode.[23]

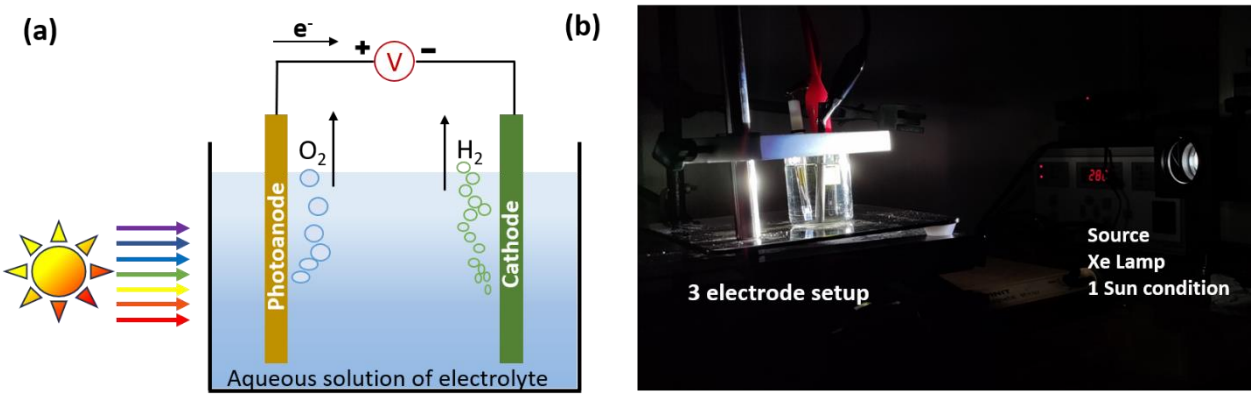

Figure 1.3 (a) A schematic representation of photoelectrolysis processes, (b) A lab-based setup representation of photoelectrolysis processes

In this analysis, we are primarily interested in the OER and possible alternatives, such as low potential oxidation reaction. As a result, we particularly address a PEC process that takes place in a device that only has the photoanode. Photons that are absorbed at energy levels higher than the inherent bandgap energy (Eg) of the photoanode cause electrons in the valence bands (VBs) to change into conduction bands (CBs), which creates holes in the VBs. Following their migration from the bulk to the surface, these charge carriers proceed through redox processes that split water. Hole diffusion to the photoanode surface occurs simultaneously, promoting the water oxidation reaction (see Equation (1.3)). As shown in Equation (1.4), electrons simultaneously move through the external circuit to the cathode interface, where they power the process of cathodic water reduction, producing H_2 gas.[21]

1.5.2 Thermochemical water splitting: Water molecules dissociate into their component components during thermochemical water splitting, often referred to as thermolysis, when they are subjected to high temperatures, usually between 500 and 3000 °C.[24] This thermal decomposition yields various reaction products, predominantly hydrogen (H_2), and oxygen (O_2), and atomic hydrogen (H), atomic oxygen (O), and hydroxyl radicals (OH). The necessary heat for thermochemical water splitting is frequently provided by nuclear power plant waste heat or concentrated solar electricity. An environmentally safe and sustainable method of producing hydrogen is by concentrated solar power. Nonetheless, there are still issues with the longevity and effectiveness of the materials used in such high-temperature environments.

Furthermore, concentrating mirror system implementation costs continue to be a major obstacle to this technology's mainstream adoption. As an alternative, thermolysis powered by nuclear energy offers a way to produce hydrogen with low greenhouse gas emissions. However, major barriers to widespread implementation include the safety of nuclear power facilities and the handling of radioactive waste.

1.5.3 Electrochemical water splitting: Water is electrolyzed by passing a direct current between the cathode and anode, which are separated by a membrane or diaphragm.[25] The electrodes in this configuration, which is depicted in Figure 1.4, are submerged in water, which frequently contains an electrolyte to improve ionic conductivity. OER occurs at the anode, producing oxygen and allowing electrons to move via the external circuit to positively charge the anode. After that, these electrons travel to the cathode, where they negatively polarise it and start the hydrogen-producing reduction process, or HER. The entire water-splitting process is made up of these two half-reactions. To help in the separation of product gases and the transportation of particular ions in the electrolyte, an ion exchange membrane is also frequently used in cells.

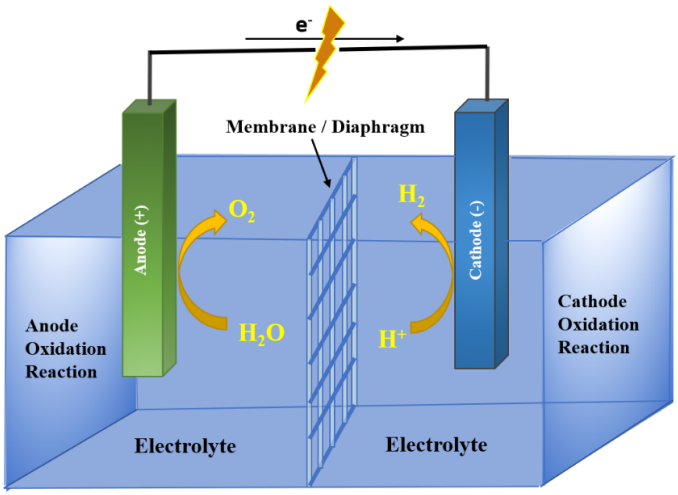

Figure 1.4 A schematic representation of electrolysis processes.

At ambient temperature, 1.23 V is the theoretical minimum voltage needed to power the electrochemical water-splitting reaction. However, overcoming the kinetic barrier of the electrodes necessitates a typically higher potential, denoted as overpotential (η). The term "overpotential" refers to the extra potential required to reach a particular current density. Electrocatalysts work to minimise this overpotential and encourage electrochemical processes. Superior electrocatalytic activity in the reaction of interest is indicated by an electrocatalyst

with a lower overpotential (η). Two electrons are transferred during the cathodic phase of HER, the total water-splitting process. The HER process can be broken down into two phases in an acidic electrolyte. The catalyst's active site (M) is initially exposed to a proton (H^+) adsorption process known as the Volmer reaction (Equation 1.6). This is followed by an electron transfer, which forms adsorbed hydrogen (M-H_{ads}) on the active site. In the second stage, two routes can then appear. In the Tafel reaction, two adsorbed M-H_{ads} directly couple to release an H_2 molecule (Equation 1.7), after which the M-H_{ads} desorb from the catalyst surface. As an alternative, one surface M-H_{ads} unit and one reduced proton combine to generate H_2 in the Heyrovsky reaction (Equation 1.8), which is then followed by desorption from the catalyst surface.

$$\text{Step 1: } M + H^+ + e^- \rightarrow M\text{-}H_{ads} \quad \text{(Volmer reaction)} \quad \text{Eq. (1.6)}$$

$$\text{Step 2: } M\text{-}H_{ads} + M\text{-}H_{ads} \rightarrow 2M + H_2 \quad \text{(Tafel reaction)} \quad \text{Eq. (1.7)}$$

Or

$$M\text{-}H_{ads} + H^+ + e^- \rightarrow M + H_2 \quad \text{(Heyrovsky reaction)} \quad \text{Eq. (1.8)}$$

The primary focus of this thesis is on hydrogen production and the oxidation of small molecules derived from biomass through electrolysis. Therefore, the subsequent sections will provide a detailed examination of water electrolysis.

1.6 Water electrolyzer

The first experimental demonstration of water electrolysis was carried out by William Nicholson and Anthony Carlisle in 1800, although electrolysis was first recorded in 1789.[26] It has been thoroughly studied and applied ever since. Early water electrolyzers used alkaline electrolytes, but subsequent research looked at acidic and even neutral mediums. Nevertheless, it was discovered that the performance in neutral electrolytes was inadequate. A major problem was to find gas-separating membranes that were both electrically and corrosion-resistant. To stop leaks and corrosion, solid electrolyte development took precedence over traditional gas-separating membranes. The first notable development in solid electrolyte membranes was the creation of proton exchange membranes. However, the capital cost of such devices proved to be too costly for large-scale deployment due to the low stability of noble metal-based electrocatalysts in severe acidic conditions. The majority of inexpensive, earth-available metal-based catalysts had good activity and stability, suggesting that the use of alkaline electrolytes was advantageous. However, a significant barrier continued to be the absence of reliable and

effective solid alkaline electrolyte membranes. Large-scale applications are currently primarily focused on alkaline liquid water electrolyzers because of their lower alkali concentration and less corrosive character. However, solid proton exchange membrane (PEM) electrolyzers have also attracted a lot of industry interest due to their ability to build inexpensive catalytic materials and study reaction processes.

There are three main techniques for electrolyzing water that are known: the solid oxide electrolyzer, PEM electrolyzer, and alkaline electrolyzer. While PEM and alkaline electrolyzers have been successfully brought to market, solid oxide electrolyzers are still in the early stages of development despite showing great technological promise. Nevertheless, as commercial solid oxide electrolyzers are not widely available, complete data on this type of device is not available.

1.6.1 Alkaline electrolyzer:

The most well-established method is alkaline water electrolysis, which has been used extensively in the chlor-alkali sector. Equation (1.9) for the reduction half-reaction at the cathode and Equation (1.10) for the oxidation half-reaction at the anode represent the half-cell reactions that take place at the electrodes of an alkaline electrolysis cell, as shown in Figure 1.5(a).

Cathode Reaction: $2H_2O\,(l) + 2e^- \rightarrow H_2\,(g) + 2OH^-(aq)$ Eq. (1.9)

Anode Reaction: $2OH^-\,(aq) \rightarrow H_2O\,(l) + ½\,O_2\,(g) + 2e^-$ Eq. (1.10)

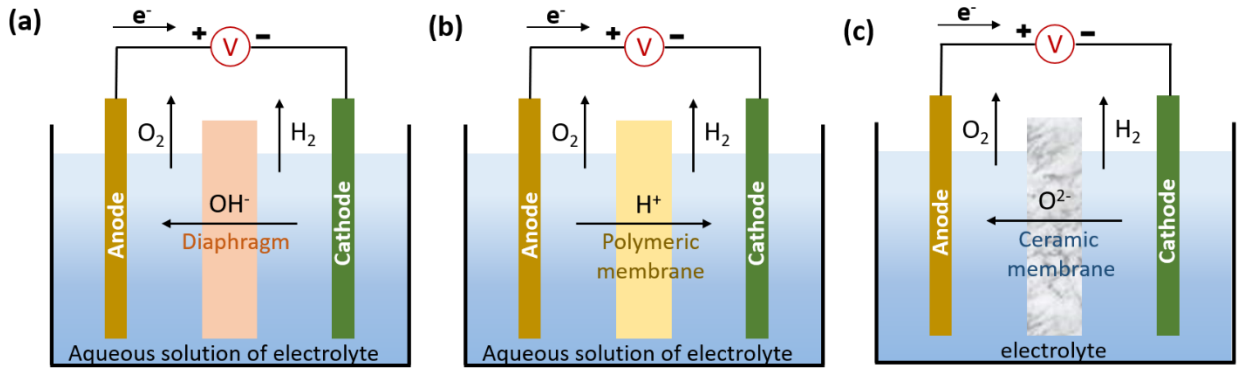

Figure 1.5 A schematic simplified diagram of (a) alkaline electrolyzer, (b) PEM electrolyzer and (c) Solid oxide electrolyzer

The cathode is where water is reduced to hydrogen (H_2), which produces hydroxyl ions (OH^-). These OH^- ions move in the direction of the anode, where they liberate their electrons and

produce oxygen. Under normal circumstances, $U°_{cathode}$ at 0.83 V and $U°_{anode}$ at 0.40 V,[27] govern the potential difference between the electrodes, leading to a $U°_{rev}$ of 1.23 V, which is calculated using the typical change in free energy related to the electrolysis of liquid water.

Two electrodes, an aqueous solution containing a strong, inert electrolyte (usually KOH or NaOH), and a porous medium (diaphragm) acting as a separator between the anode and cathode compartments are the main parts of an alkaline electrolysis cell (shown in Figure 1.5a). Electrocatalysts, including platinum-coated nickel-foam, are frequently used. Cross-contamination, sometimes referred to as crossover, is a phenomenon that can happen at low current densities because the diaphragm employed as a separator is not completely impermeable. This involves the possibility of an explosion as certain gases (H_2 into O_2 and vice versa) flow through the diaphragm. Crossover in alkaline cells requires hydrogen purification, which is mostly pressure swing adsorption-based deoxygenation. An alkaline electrolyzer must have a minimum current density threshold (about 20% of the rated power) when it is linked to an intermittent power supply.

1.6.2 Proton exchange membrane (PEM) electrolyzer:

Figure 1.5(b) shows a diagram that depicts a PEM electrolyzer. The proton-conducting membrane, which is usually made of a sulfonated fluorinated polymer, is the fundamental component of the PEM electrolyzer's operation. Nafion, made by DuPont, is the most widely used membrane. It is available in a range of thicknesses, from 25 to 250 micrometres. The choice of suitable membrane thickness for a given application is contingent upon the electrolyzer’s operational parameters. A larger membrane is frequently required in situations where the membrane may deteriorate more quickly, such as greater pressures or frequent start-stop cycles. This larger membrane can minimise gas crossover, endure higher differential pressures, and act as a buffer against material degradation loss. On the other hand, because membrane resistance decreases with decreasing thickness, thinner membranes provide higher electrolysis process efficiency. Consequently, it's important to strike a careful balance between maximising the membrane's electrochemical qualities and making sure it works well under the specific circumstances of the operation. The goal of ongoing research is to create novel membranes with superior qualities, like stronger mechanical construction and higher proton conductivity.[28-30]

Equations 1.11 and 1.12 reflect the two half-reactions in PEM electrolysis that occur at the cathode and anode, respectively, as shown in Figure 1.5b.

Cathode Reaction: $2H^+ + 2e^- \rightarrow H_2\,(g)$ Eq. (1.11)

Anode Reaction: $2H_2O\,(l) \rightarrow \frac{1}{2}\,O_2\,(g) + 2H^+ + 2e^-$ Eq. (1.12)

The standard potential under normal circumstances is 1.23 V at the anode ($U°_{anode}$) and 0 V at the cathode ($U°_{cathode}$). As a result, the standard change in Gibbs free energy ($\Delta G°$) of liquid water electrolysis yields 1.23 V as the standard reversible potential ($U°_{rev}$).

1.6.3 Solid oxide electrolyzer:

Elevating the temperature during electrolysis procedures can drastically reduce the amount of electricity used, but it also requires the use of thermal energy. Solid Oxide (SO) cells in Figure 1.5(c) serve as an example of high-temperature electrolysis, which is a potentially effective method that works at temperatures that are higher than 700 °C and frequently fall between 800 and 1000 °C. Equation 1.13 shows the half-reaction that is happening at the cathode, and Equation 1.14 shows the half-reaction that is happening at the anode.

Cathode Reaction: $2H_2O\,(g) + 2e^- \rightarrow H_2\,(g) + O^{2-}$ Eq. (1.13)

Anode Reaction: $O^{2-} \rightarrow \frac{1}{2}\,O_2\,(g) + 2e^-$ Eq. (1.14)

In the context of steam electrolysis, at a temperature of 1000 K, the reversible potential (U_{rev}) is measured at 0.94 V.[31] This value is notably lower than the $U°_{rev}$ (1.18 V), primarily due to the significant decrease in electricity demand (ΔG) with increasing temperature.

A ceramic membrane typically yttria-stabilized zirconia, or YSZ is used in the SO electrolyser (SOE), shown in Figure 1.5(c), to function as the electrolyte and separator. Oxygen ions (O^{2-}) may only be transported from the cathode to the anode through this membrane. An air stream, preheated beforehand, is commonly introduced through the anode. This airflow serves the dual purpose of temperature regulation and ensuring proper temperature distribution within the stack, thereby preventing degradation. Leveraging the advantages of elevated temperatures, SOE show promise in reducing electricity consumption, thus attracting researchers. Nevertheless, SOE necessitates the input of steam and process heat, which are considerations to consider when assessing the performance of the system and first law efficiency. Process heat from renewable energy sources (RES) or industrial waste heat has the potential to improve overall efficiency.

In SOE, thermal management is a crucial factor. For them to remain stable and efficient, precise operating temperatures must be maintained. In order to enable efficient ion conduction via the

solid oxide electrolyte, these devices run at high temperatures. In order to avoid overheating, keep electrolyzer cells at constant temperatures, and reduce thermal strain on materials factors that affect longevity and performance effective thermal control is essential. Furthermore, safety depends on efficient thermal regulation because improper handling of high temperatures might result in dangers. Consequently, one notable area of research and innovation in the field of SOE is the development of robust heat management technologies.

1.7 Current status of alkaline water electrolyzer

This thesis aims to advance in alkaline water electrolysis among the three mentioned technologies with low thermodynamic oxidising molecules. Owing to its commercial availability and maturity in the megawatt range, alkaline water electrolysis is the preferred method. Water electrolyzers based on PEM technology usually have a stack life of less than 25,000 hours and a system life of roughly 10-20 years. In contrast, alkaline electrolysis has shown stack life reaching 90,000 hours and a system life of 20-30 years. Presently, alkaline electrolyzers have produced up to 760 Nm^3/h of H_2, while PEM electrolyzers can produce 0.06 to 75 Nm^3/h with this kind of output. However, a significant challenge with alkaline electrolyzers is the susceptibility to CO_2 attack, leading to electrocatalyst poisoning and impurities in the H_2.[16,17]

The Bhabha Atomic Research Centre (BARC), located in Mumbai, has demonstrated the successful use of improved electrolyzers with locally fabricated porous nickel electrodes to produce alkaline water electrolyzers with a greater current density (4500 A m^{-2}). The aim of this work is to improve energy efficiency. Despite advancements, water electrolysis remains a highly energy-intensive process, consuming between 4.5-6.5 kWh/Nm^3. Additionally, the high capital investment associated with electrolysis technology restricts its widespread commercial adoption. To address these challenges, strategic initiatives are required, leveraging government plans that foster collaboration between relevant institutes and industries to bridge the gap and promote the commercialization of water electrolysis technology in India through production linked incentives.[3]

1.8 Strategies to replace the energy extensive water oxidation reaction

The production of hydrogen still requires a minimum voltage of 1.8-2.0 V in industrial alkaline water electrolyzers, despite considerable efforts to improve the kinetics of both half-cell reactions.[32] Therefore, it's critical to investigate alternate approaches for economical and

energy-efficient hydrogen generation in addition to the creation of effective electrocatalysts. Finding and using molecules with reduced thermodynamic oxidation potentials and kinetic favorability as stand-ins for oxygen evolution is one intriguing strategy. To this end, a comprehensive survey has been conducted to investigate various strategies employed for hydrogen generation from water by harnessing alternative forms of waste energy. Within this context, all potential methods for replacing the energy-intensive process of water oxidation can be broadly categorized and explored in further sections.

1.9 Water and Bio-mass electrolysis

Electrolysis of water has been shown as a green method of producing hydrogen for many years. The principles by which it operates, as well as some of the most recent scientific breakthroughs, are discussed at length in other, specialized studies/reviewes.[33-37] The primary factor used to select electrocatalysts is their capacity to drive redox processes with minimal energy loss, which is indicated by the electrochemical cell voltage, V, which is typically provided by

$$V = \Delta E_{eq} + \eta_a + \eta_c + IR \qquad \text{Eq. (1.15)}$$

In this case, η_a and η_c represent the overpotentials at the anode and cathode,[38] respectively, while IR stands for the ohmic drop caused by the electrolyte's intrinsic resistance and bubble effect.[39] The water and biomass oxidation kinetics diagram is shown in Figure 1.6a. Equation (1.15) shows a large overpotential η_a due to the multielectron transfer mechanisms that cause the kinetics of the anodic reaction to be delayed in both water and biomass electrolysis, even with a low $\mathbf{\Delta}E_{eq}$. In order to attain a high H_2 generation rate, a greater cell voltage and current density are necessary. The electrolysis of water requires U_{cell} ~2 V to reach 1 A cm^{-2} current density, while the electrolysis of organic molecules generated from biomass with $\mathbf{\Delta}E_{eq}$ at 0 V needs only 0.4 V, which is an energy-efficient technique.

The kinetics diagram displayed in Figure 1.6(a) outlines the oxidation processes of water and biomass.[40] Despite a low ΔE_{eq}, both water and biomass electrolysis encounter sluggish anodic reactions due to their multielectron transfer nature, resulting in elevated overpotential η_a in Equation (15).[41] Consequently, achieving a high H_2 production rate demands a higher cell voltage at increased current densities. In order to achieve a current density of 1 A cm^{-2}, water electrolysis requires around 2 V, while organic molecules obtained from biomass, which usually have a ΔE_{eq} of about 0 V, require roughly 0.4 V to drive the electrolysis process, which is favourable in terms of energy. The process of electrochemical synthesis by anodic

oxidations includes a series of processes that include reactant molecule adsorption, interatomic bond cleavage, electron transfer, oxidation of intermediates by oxygenated species, and final product desorption (Figure 1.6b).

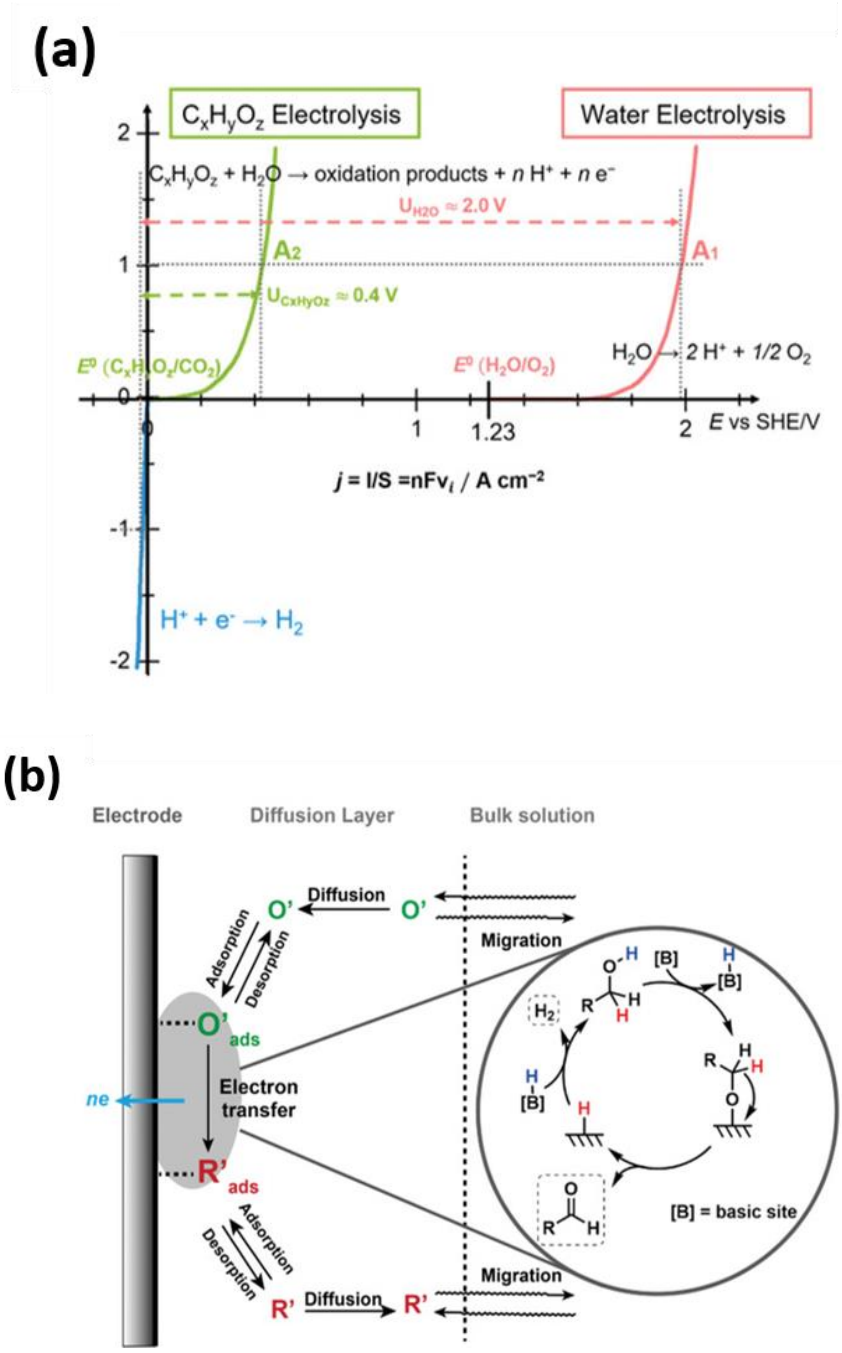

Figure 1.6 (a) Theoretical reaction kinetics controlled by the Butler–Volmer law, U_{CxHyOz}, and U_{H2O} are the cell voltage for $C_xH_yO_z$ and water electrolysis at 1 A/cm^2 Current density.[40] (b) Schematic diagram of the pathway of a general electrode system. Copyright 2021, Wiley.[41]

Comparing different glycerol oxidation processes, for instance, demonstrates the importance

of selectivity as it directly affects the selling price of hydrogen and its impact on global warming. Hence, electrochemical technologies alone cannot provide a complete understanding of the ongoing chemical reaction. Complementary analytical techniques are essential for obtaining comprehensive information. These techniques include nuclear magnetic resonance (NMR), Fourier-transform infrared spectroscopy (FTIR), electrochemical mass spectrometry (MS), and high-performance liquid chromatography (HPLC) with in situ sample collection.

These techniques enable the identification of resultant products and offer qualitative and quantitative information about reactant conversion rate, reaction intermediates, and product distribution. The anode reaction requires precise control, heavily influenced by the structural and electrical properties of the electrocatalysts, particularly the interaction between catalyst and substrate.

Therefore, the quantity, intrinsic activity, and selectivity of each active site determine an electrocatalyst's total performance. While similar to traditional electrocatalysis, parameters including onset potential, overpotential, current density, and selectivity have unique properties for transforming organic molecules.

In conclusion, there are three primary obstacles to the development of biomass-based electrolysis: In order to determine energy consumption for hydrogen production and selectivity towards valuable chemicals, three goals must be achieved: (1) creating high intrinsic activity electrocatalysts to lower the activation energy for both cathode (hydrogen production) and anode (molecule oxidation) reactions; (2) gaining a fundamental understanding of electrocatalytic and interfacial processes for various reactants, enabling precise control of reaction processes and manipulation of selectivity towards desired products; and (3) scaling up these systems for practical applications. The reactions and electrocatalyst needs for various organic compounds will be covered in detail in the section that follows, and views on technology development and scaling up will be covered in the area that follows.

1.10 HER Integrated with Anodic Oxidation Reaction

To maximise energy efficiency, combining electrocatalytic anodic oxidation processes (AOR) with the HER has received significant attention in recent years. Protons and electrons are produced as byproducts by many AORs. Currently, steam reforming technologies account for the majority of hydrogen production from water electrolysis, with just around 4% coming from renewable sources. Nevertheless, hydrogen is becoming more and more acknowledged

as a sustainable and renewable fuel. Against this backdrop, substantial research has been directed towards integrating HER with concurrent generation of valuable chemicals, particularly selective oxidation reactions that are thermodynamically more favorable. This integrated electrocatalytic system primarily revolves around advancing and designing electrocatalysts for both HER and selective oxidation reactions. In some instances, researchers have explored the potential of bifunctional catalysts capable of simultaneously performing both (HER and AOR) tasks.

1.10.1 HER and Alcohol oxidation reaction

There has been significant research focus on chemical-assisted HER. One area of particular interest is the investigation of alcohol-assisted HER for the production of valuable chemicals. By electrochemically oxidizing various alcohols, valuable chemicals can be obtained alongside hydrogen generation at the counter electrode. For instance, the electro-oxidation of methanol or glycerol has been studied to produce formate/formic acid and acetate/ethyl acetate, respectively. Similarly, ethanol can be oxidized to produce acetate or ethyl acetate, isopropanol can be oxidized to produce acetone, and 1,2-propanediol can be converted to lactate or pyruvate. Other examples include the electro-oxidation of 1,3-propanediol to produce acrylate, and the conversion of glycerol to tartronate or mesoxalate. These studies demonstrate the potential for obtaining a variety of valuable chemicals through the electro-oxidation of different alcohols while simultaneously generating hydrogen.

1.10.2 Mono-Alcohol Oxidation

The electrocatalytic methanol selective oxidation process (MOR) in conjunction with the HER has been the subject of extensive investigation, represented by the equation $CH_3OH + OH^- \rightarrow HCOO^- + 2H_2$. This area of study has garnered significant attention due to methanol's affordability and its role as a plentiful platform chemical. Transition metal electrocatalysts, such as those based on nickel, cobalt, or their layered double hydroxides, have been explored for this purpose, enabling the simultaneous production of high-value formate and clean hydrogen. In a particular investigation, as illustrated in Figure 1.7a, carbon nanofibers decorated with nickel selenide (CNFs@NiSe) were synthesized in situ and applied to integrate hydrogen (H_2) production with methanol upgrading.[42]

The presence of methanol was found to significantly enhance the rate of H_2 generation, reaching up to 7.5 times higher compared to conditions without methanol. Researchers proposed a mechanism for MOR leading to formate formation, employing density functional

theory (DFT) calculations (Figure 1.7b, c). Specifically, they identified that the formation of an intermediate species, M/OCH_3, is thermodynamically more favourable on the exposed NiSe (102) surfaces. It was determined that the energy needed to generate $NiSe/OCH_3$ is 0.64 eV less than that of NiSe/HCOOOH, which is a precursor to CO_2/CO_3^{2-} production. This indicates a preference for the formation of $NiSe/OCH_3$. Additionally, the calculated adsorption energy of NiSe/HCOOH was found to be -0.04 eV, suggesting a high selectivity towards formic acid rather than further oxidation to CO_2.

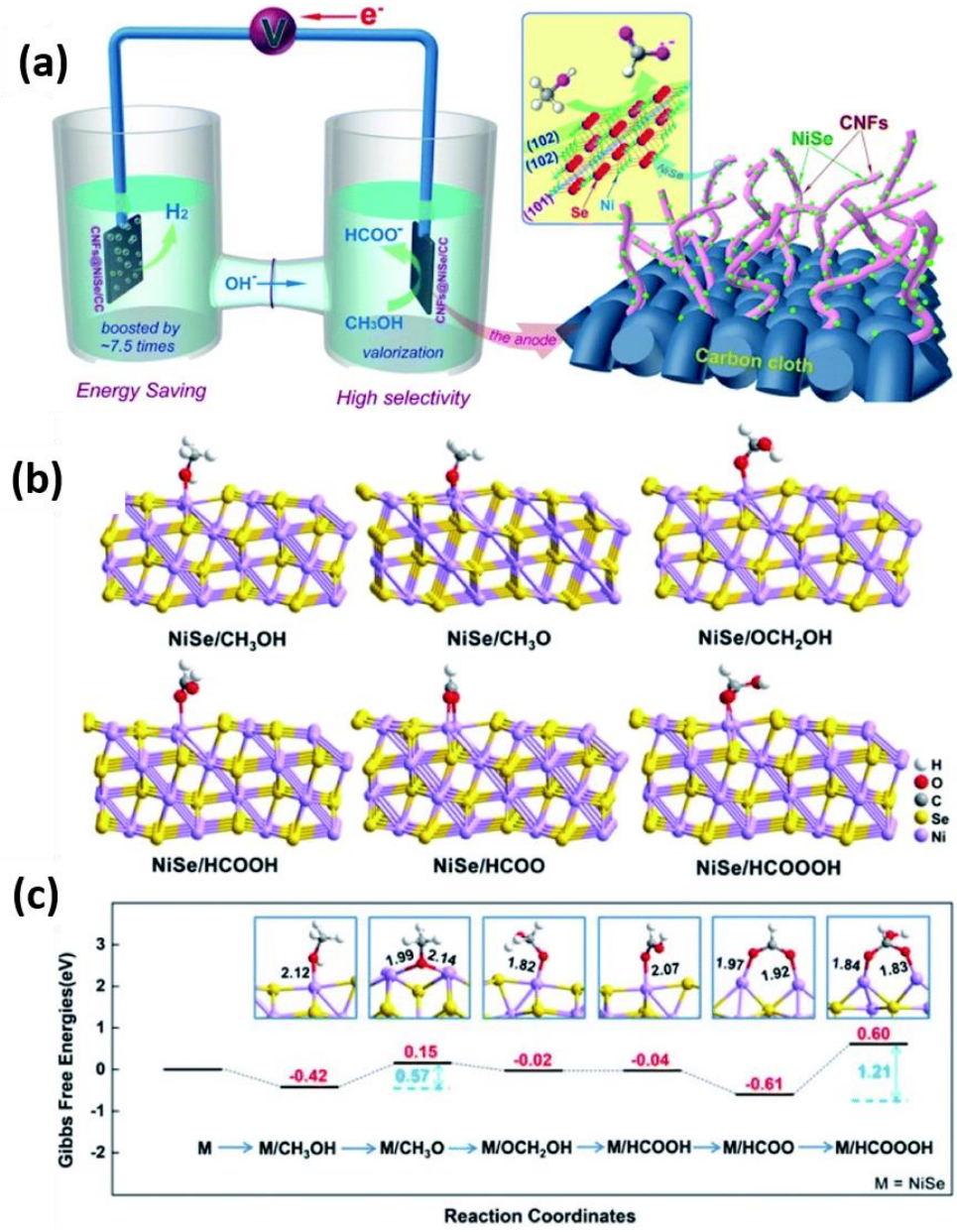

Figure 1.7 HER integrated with MOR for H_2 and formate co-generation. (a) Schematic illustration of bifunctional CNFs@NiSe electrocatalyst for the integration of methanol selective oxidation with H_2 production; Reproduced by permission from Royal Society of

Chemistry; Licence no. 1478253-1 (b) DFT optimized structure; (c) Gibbs free energy diagram. Reproduced by permission from Royal Society of Chemistry; Licence no. 1478257-1[42]

1.10.3 Diol Oxidation

Polyols show great promise for electrocatalytic anodic oxidation, presenting a more streamlined approach compared to their conventional industrial production methods. However, achieving precise selectivity in generating specific chemicals during the partial oxidation of polyols remains a significant hurdle. This challenge underscores the importance of accurately targeting desired product formation. Researchers are actively engaged in unraveling reaction mechanisms, refining operating conditions, and developing efficient catalysts to improve selectivity in the electrochemical oxidation of polyols. By addressing selectivity concerns, the potential for maximizing the production of valuable chemicals is heightened. Tackling selectivity obstacles in polyol oxidation represents a pivotal stride toward establishing sustainable and effective electrocatalytic processes for chemical synthesis.

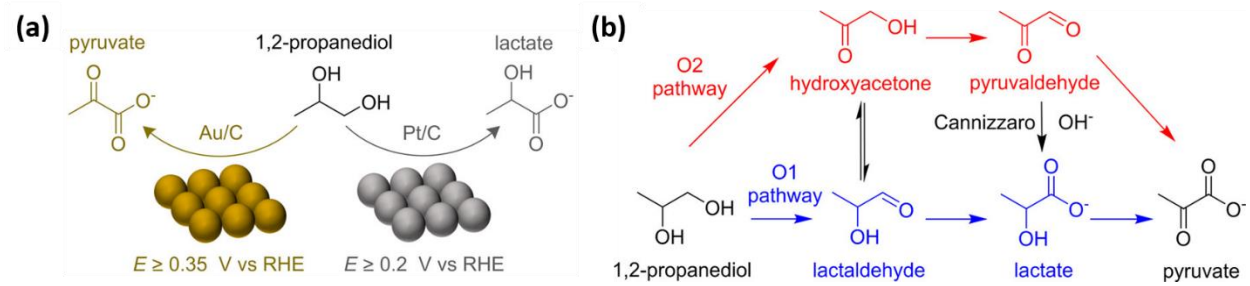

Figure 1.8 HER integrated with polyols electro-oxidation reaction system. a,b) 1,2-propanediol selective oxidation and possible pathway in the alkaline electrolyte; Adapted with permission. (Ref No). Copyright 2015 American Chemical Society.[43]

The selectivity of electrocatalytic oxidation processes has been better understood thanks to these experimental approaches, which have also made it easier to identify and measure desirable products while examining intermediate species. These findings significantly enhance our comprehension of the factors influencing selectivity in electrochemical reactions, with implications for optimizing catalyst design and reaction conditions to synthesize targeted high-value products efficiently.

The impact of the catalyst and the applied potential on the selectivity of valuable products during electrocatalytic oxidation was found to be significant by Chadderdon et al. They found that lactate was preferentially generated with 86.8% selectivity on the Pt/C catalyst, primarily focusing on the oxidation of 1,2-propanediol (PDO). On the other hand, pyruvate was produced from PDO by using an Au/C catalyst. As shown in Figure 1.8a, b, they also noticed

that the selectivity of pyruvate on Au/C varied from 20% to 56% with increasing anode voltage. HPLC was employed for the quantification of lactate or pyruvate generated. Additionally, ^{1}H NMR spectroscopy was utilized to explore potential intermediates, such as hydroxyacetone or lactaldehyde.[43]

1.10.4 Glycerol Oxidation

When it comes to creating useful oxygenated compounds, glycerol has shown great promise as a renewable resource, especially when used in electrocatalytic oxidation (ECO). It is common practice to analyse the intermediates and products produced during glycerol electro-oxidation utilising in situ methods like FTIR spectroscopy and HPLC. Catalyst poisoning, however, poses a significant risk to glycerol oxidation and calls for cautious catalyst material selection. High-value products from glycerol ECO have the potential to be produced using adatom-doped electrocatalysts, in addition to traditional monometallic catalysts and multimetallic alloys.

Electrocatalysts based on non-noble metals have been investigated for the integration of hydrogen production and glycerol selective oxidation, independent of traditional water splitting. Ni-Mo-N/CFC, or nickel-molybdenum-nitride nanoplates mounted on carbon fibre cloth, were used as anode and cathode catalysts by Li et al. With coupled glycerol selective oxidation and HER, this arrangement produced a cell voltage of 1.36 V, which was 260 mV less than that of whole water splitting. With the simultaneous synthesis of high-purity hydrogen and high-value formate made possible by this approach, glycerol ECO can be significantly more efficient. With 99.7% Faradaic efficiency (FE) for hydrogen generation and 95.0% FE for formate generation, the catalyst system showed good performance (Figure 1.9a-c). Moreover, Figure 1.9d suggested a logical chemical route for the synthesis of formate from glycerol oxidation. The generation of formate is facilitated by the sequential process of electrolysis in which the glycerol's primary and secondary carbons play a part. After oxidising to glyceraldehyde, formate and glycolaldehyde are produced via C-C bond cleavage of glyceraldehyde. Formaldehyde and formate are produced when glycolaldehyde is cleaved by subsequent oxidation. Lastly, formate and methanol are produced by the intermolecular Cannizzaro reaction of formaldehyde. This chemical pathway explains the several processes involved in the electro-oxidation of glycerol and how formate, a useful product, is formed through intermediate intermediates.[44]

The electrocatalytic conversion of biomass and plastic waste into value-added chemicals and fuels is gaining momentum in the quest for sustainable resource management. An

electrocatalytic method is presented by Yifan et al. to convert glycerol, a byproduct of biodiesel manufacturing, into lactic acid; ethylene glycol, which comes from waste polyethylene terephthalate (PET), may be converted into glycolic acid (Figure 1.10a, b).[45]

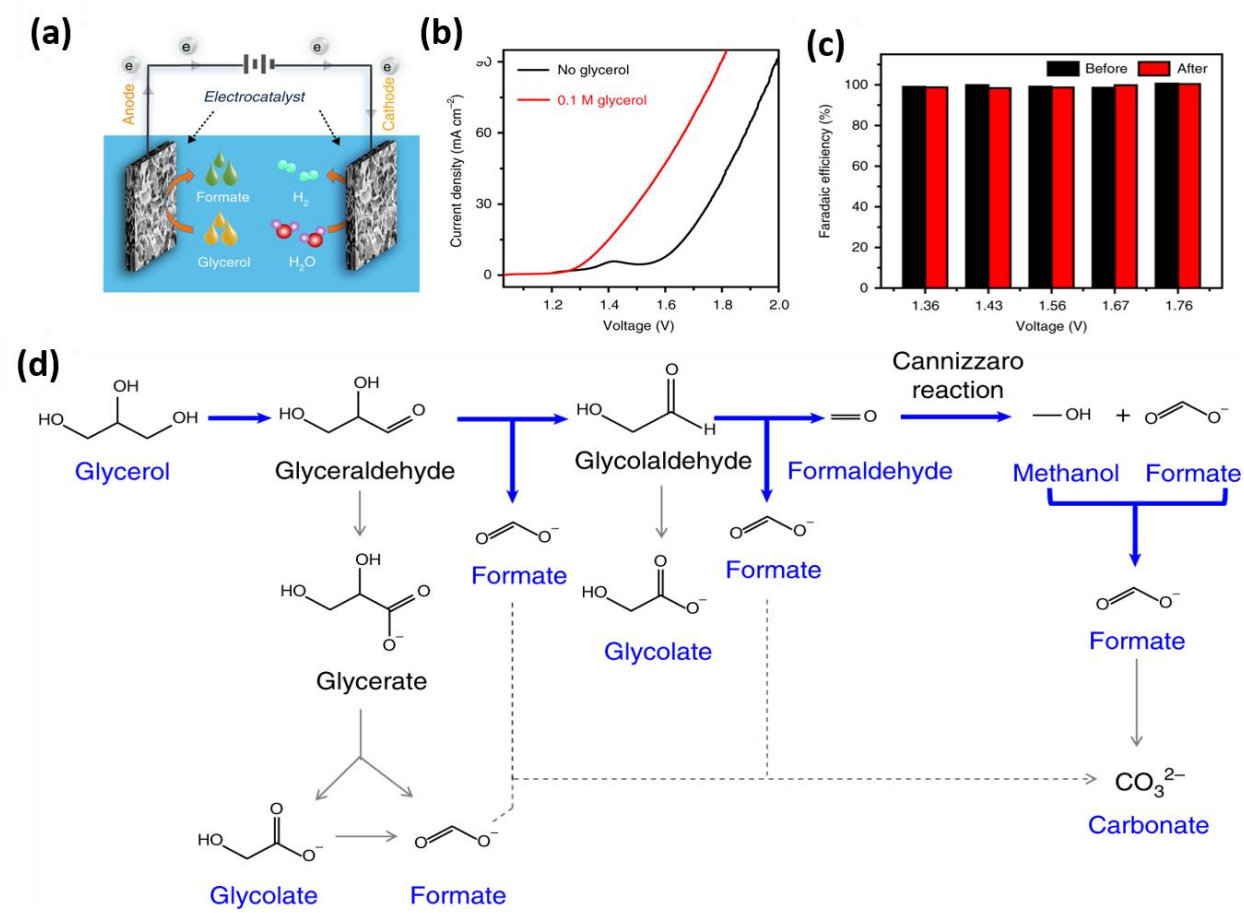

Figure 1.9 a) schematic illustration of glycerol electro-oxidation integrated HER system over bifunctional Ni-Mo-N/CFC catalyst, b) LSV curves, c) FE, d) proposed mechanism of glycerol oxidation.[23] Copyright 2019, Springer Nature [44]

Glycolic and lactic acids are both useful monomers for the manufacture of biodegradable polymers. High current densities and outstanding selectivities of 77% for lactic acid and 91% for glycolic acid are obtained using a nickel hydroxide-supported gold electrocatalyst ($Au/Ni(OH)_2$). For the generation of lactic acid at intermediate potentials, a current density of 317.7 mA/cm^2 at 0.95 V vs RHE and 326.2 mA/cm^2 at 1.15 V vs RHE are reached. For triglyceride and PET bottle upcycling, a membrane-free flow electrolyzer is used to demonstrate practical applicability. 13.7 g of glycolic acid and 9.4 L of H_2 from PET waste and 11.2 g of lactic acid and 9.3 L of H_2 from triglyceride waste are the products of the electrolyzer. This proof of concept highlights the possibility of producing H2 and valuable compounds simultaneously from waste materials in an environmentally responsible and

sustainable way.[45]

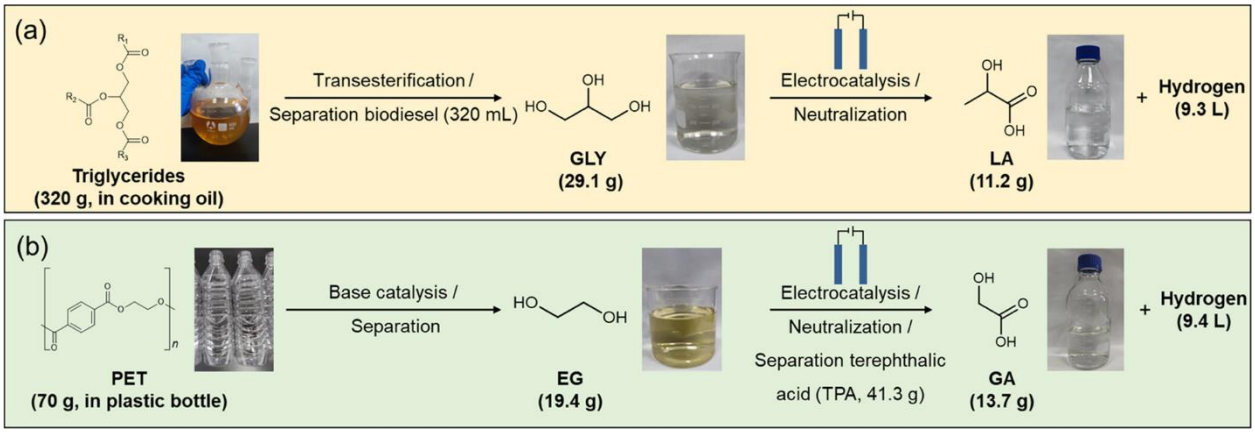

Figure 1.10 Schematic illustrations of the electrocatalytic upgrading process of (a) triglycerides and (b) waste PET bottles. Photographs of the feedstocks and products are shown. Copyright 2023, American Chemical Society.[45]

1.11 HER and Glucose Oxidation Reaction

Highly valued compounds known as glucononic acid (GNA) and its derivatives, such as gluconate, glucaric acid (GRA), and gluconolactone, can be obtained from biomass or by glucose electro-oxidation methods. These compounds can be identified and quantified using HPLC. In glucose oxidation reactions (GLUOR), it has been observed that the actual catalytically active phase comprises metal oxidized species. Energy consumption can be significantly decreased by integrating GLUOR with the HER and employing Pt/C as the cathodic catalyst and Fe2P/SSM as the anodic catalyst. More specifically, under a current density of 10 mA/cm^2, a cell voltage 300 mV lower than that of traditional water electrolysis was achieved in a Fe2P/SSM||Pt/C two-electrode system (Figure 1.11a).[46]

Bifunctional electrocatalysts are pivotal in electrocatalytic reactions as they can concurrently facilitate two distinct reactions, thus markedly decreasing the overall electrolysis process cost. Lin et al. devised the $CoNiO_x$/CC ‖ $CoNiO_x$/CC configuration for GLYOR and HER, which, at 10 mA/cm^2, reduced the cell voltage by 260 mV.[47] Because of the presence of Ni and/or Co metals, the Co-Ni alloy electrocatalyst exhibited better catalytic activity for HER, and oxidised species like NiO, CoO, or Co-NiO were essential for GLUOR (Figure 1.11c, d).

Liu et al. used bimetallic NiFe nitrides (NiFeNx) and NiFe oxides (NiFeOx) to integrate the anodic glucose oxidation reaction (GLUOR) with the cathodic HER, thereby streamlining the electrocatalyst manufacturing process.[29] Both $NiFeN_x$-NF and $NiFeO_x$-NF electrodes were synthesized using a uniform hydrothermal treatment process. NiFeNx-NF exhibited a low overpotential of 40.6 mV to achieve 10 mA/cm^2 in alkaline electrolyte, indicating efficient

electron transfer for HER. $NiFeO_x$-NF catalysts also displayed outstanding performance in catalyzing GLUOR to glucaric acid (GRA). Effective GLUOR was made possible by the NiFeOx-NF anode, which only needed 1.30 V versus RHE to reach a current density of 87.6 mA/cm^2 and a Tafel slope of 19 mV/dec (Figure 1.12, a-c).

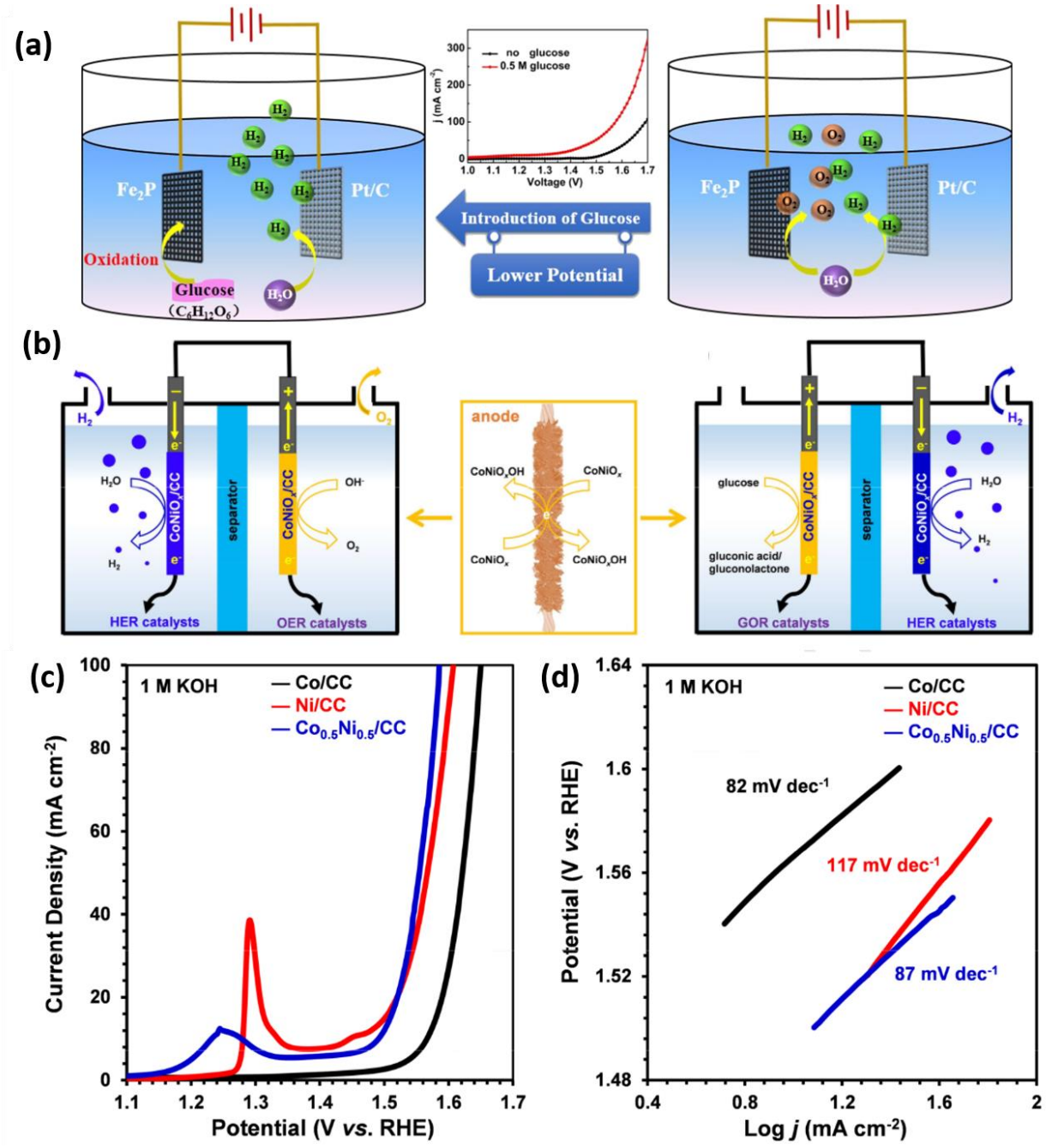

Figure 1.11 HER integrated with GLUOR system. a) Two-electrode system of GLUOR integrated with HER with Fe_2P/SSM and Pt/C as anode and cathode, respectively. Reproduced by permission from Elsevier; License no. 5778161279668.[46] $CoNiO_x$/CC ‖ $CoNiO_x$/CC configuration for GLUOR integrated with HER; c) LSV of Co/CC, Ni/CC, and $Co_{0.5}Ni_{0.5}$/CC in 1 M KOH, d) LSV in 1 M KOH and 0.1 M glucose. Reproduced by permission from Elsevier; License no. 5778170042945.[47]

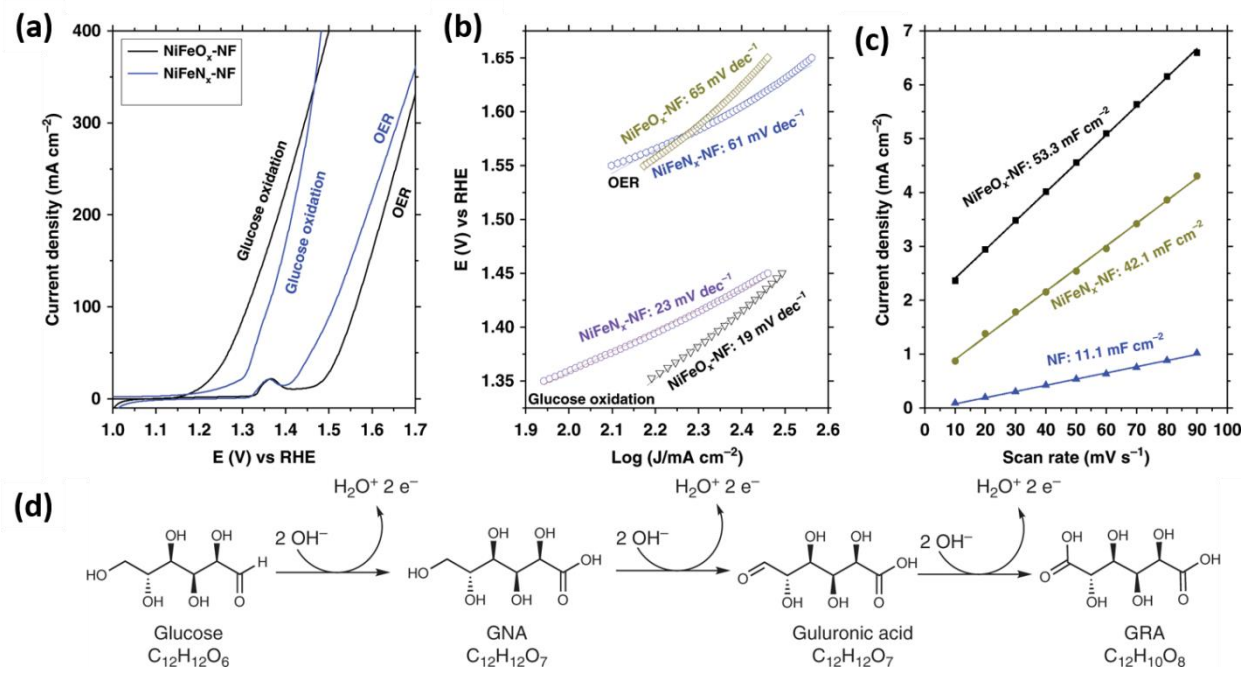

Figure 1.12 Anodic glucose oxidation. a) LSV profiles of the $NiFeO_x$-NF and $NiFeN_x$-NF catalysts for glucose oxidation and OER (scan rate of 5 mV/s; electrolyte: 1 M KOH; glucose concentration 100 mM). b) Corresponding Tafel plots. c) Capacitive current densities of different electrodes for glucose oxidation as a function of scan rate.[29] Copyright 2020, Springer Nature.[48]

The reaction pathway of GLUOR on the $NiFeO_x$-NF electrode involved two steps: glucose conversion to gluconic acid (GNA) via the loss of two electrons, and the subsequent oxidation of GNA to GRA using four electrons shown in Figure 1.12d.[48] A two-electrode electrolyzer using GLUOR and HER integration produced a 200 mA/cm^2 current density and 1.48 V of cell voltage. Higher EF for the manufacture of GNA and GRA was also attained. This process uses easily available raw materials to lower costs while simultaneously producing GRA and H_2 using electrolytic methods, thanks to the use of earth-abundant metal-based electrocatalysts.

In summary, these discoveries underscore the potential of integrating GLUOR with HER to enhance H_2 production. The adoption of GLUOR as an alternative to the OER presents benefits including cost reduction, utilization of readily available materials, and concurrent generation of valuable chemicals alongside hydrogen. Bifunctional electrocatalysts have exhibited promise in facilitating both GLUOR and HER, thus advancing the efficiency and cost-effectiveness of electrocatalytic reactions.

1.12 HER and Other Anodic Oxidation Reactions

1.12.1 Aldehyde Oxidation

The utilization of aldehydes as auxiliary chemicals in conjunction with the HER has been investigated. Aldehydes can undergo oxidation to produce carboxylic acids, rendering them viable candidates for coupled reactions. Extensive research has been conducted on alcohol oxidation reactions coupled with HER in recent decades. This research encompasses the conversion of aldehydes sourced from biomass, such as 5-hydroxymethylfurfural (HMF) [49,50] and the C5 platform derived from cellulosic biomass. The objective of these studies is to exploit the potential of biomass-derived aldehydes for the synthesis of valuable chemicals while simultaneously generating hydrogen through HER.

1.12.2 Amine Oxidation[51]

The integration of the HER with amine oxidation represents a significant type of oxidation reaction, notably due to the lower oxidation potential of most amines compared to water. A vital pathway for the production of numerous significant organic compounds, such as oximes, imines, amides, nitriles, amine oxides, and azo compounds, is catalytic amine oxidation. These compounds have diverse applications in fields such as agrochemicals, pharmaceuticals, and organic synthesis. The capability to concurrently generate hydrogen through HER while conducting catalytic amine oxidation offers an appealing approach for the sustainable synthesis of valuable organic compounds with broad industrial relevance.

1.12.3 Urea Oxidation[52,53]

Since the urea oxidation reaction (UOR) has a theoretical thermodynamic potential that is significantly lower than the OER's (1.23 V) in water electrolysis, it is a desirable substitute for anodic oxidation in this process. Urea ($CO(NH_2)_2$) is a readily available compound commonly found in domestic and industrial wastewater, and its breakdown by-products, such as nitrate and ammonia, can pose environmental concerns as pollutants. However, when urea is electrolyzed in an alkaline aqueous solution, it undergoes a reaction that generates benign products including N_2, CO_2, and H_2, which can be captured using appropriate methods. The reaction can be depicted as follows.:

$$CO(NH_2)_2 + H_2O \rightarrow N_2 + 3H_2 + CO_2$$

The environmental impact of urea can be reduced while increasing the efficiency of H2 production in water electrolysis by merging the HER and UOR. The slow kinetics of anodic UOR, which are caused by the 6-electron transfer mechanism, are one of the main problems

with it. Consequently, in order to accelerate the rate of reaction and improve the overall efficiency of urea electrolysis, high-performance catalysts must be used. The development of such catalysts is essential for realizing the potential advantages of coupling UOR with HER in water electrolysis processes.

$$CO(NH_2)_2 + 6OH^- \rightarrow N_2 + 5H_2O + CO_2 + 6e^-$$

1.12.4 Hydrazine Oxidation[54-56]

Hydrazine, a vital industrial chemical, holds considerable promise as an auxiliary inorganic compound for anodic oxidation processes coupled with the HER owing to its advantageous characteristics. Hydrazine finds extensive application as rocket fuel and as a fuel for hydrazine fuel cells. When subjected to oxidation in alkaline conditions, the hydrazine oxidation process can be symbolized by the following chemical equation:

$$N_2H_4 + 4OH^- \rightarrow N_2 + 4H_2O + 4e^-$$

One advantage of hydrazine electrooxidation lies in its generation of nitrogen and water as by-products, devoid of greenhouse gases or species that could adversely affect catalysts. However, it's crucial to acknowledge that the high reducing nature of hydrazine leads to a lower oxidation potential, favoring the hydrazine oxidation reaction (HzOR) over the OER from a thermodynamic perspective. This characteristic presents a challenge in achieving efficient and selective hydrazine oxidation. Nevertheless, through the development of appropriate catalysts and optimization of reaction conditions, it is feasible to enhance the performance and efficiency of hydrazine electrooxidation, thereby unlocking its potential as a valuable auxiliary compound in anodic oxidation processes coupled with the HER.

1.13 Scientific Endeavours and organisation of the Current Study

Drawing from the preceding discourse, the pursuit of energy-efficient hydrogen production from water emerges as a pivotal stride in shaping a sustainable energy landscape. Nevertheless, the sluggish kinetics inherent in water splitting reactions present a formidable obstacle to transitioning to a hydrogen-based economy from hydrocarbons. A range of catalysts, including precious and non-precious group-metal types, have been created to overcome this difficulty. Accordingly, the goal of this thesis is to make a contribution to the field of energy-efficient hydrogen synthesis from water and biomass oxidation. In order to develop strong materials, this requires optimising the physicochemical features of electrocatalysts and investigating novel, low-energy approaches for affordable hydrogen synthesis.

The third to sixth chapters of the current thesis provide a broad overview of its scope and objectives by describing our method for synthesising and optimising the properties of photo-electrocatalyst and electrocatalyst to catalyse a variety of electrochemical reactions, such as CER, GLYOR, GLUOR, and others, that are necessary for the economically viable production of hydrogen. Six sections serve as a general classification for the chapters.

The **first and second chapters** serve as an introduction to the main area of thesis on electro and photoelectro catalysis and outline the experimental methods employed, respectively.

Third chapter discusses the development of a Co-doped BiVO4 (Co-BV) nanostructured photoanode for the effective and long-lasting photoelectrochemical evolution of chlorine from simulated seawater. We draw attention to the difficulties in producing hydrogen and chlorine sustainably from seawater splitting and stress how crucial it is to use the right photo-electrocatalyst in this process. The study reports on the successful Co-doping in the $BiVO_4$ crystal lattice. By effectively suppressing kinetically slow OER, the Co-BV photoanode demonstrated efficient chlorine evolution with 92% FE at the same potential, exhibiting a photocurrent of 190 $\mu A/cm^2$ at 1.1 V vs. RHE. The study also discusses the broader implications of using renewable resources for efficient fuel/energy production, highlighting the potential of solar energy in producing hydrogen from water through photoelectrochemical or photocatalytic water-splitting processes. Furthermore, the current work emphasizes the significance of operating at low overpotential for sustainability and outlines the challenges and advantages associated with chlorine evolution reaction (CER) in sea/salt water. The study provides insights into the structural and electronic integration of Co-BV, its performance under different chloride concentrations, and its stability up to 20 h, highlighting its potential for practical applications in photoelectrochemical chlorine evolution.

In **fourth chapter** demonstrate the shape-controlled palladium nanocrystals, afforded by colloidal chemistry, and established morphology dependent electrochemical GLYOR performance at significantly low voltage. Although it is known that controlling the shape of electrocatalyst can modulate the activity and selectivity of the products, still it is relatively underexplored area for many reactions, including GLYOR. The Pd-NC (Pd-nanocube) anode exhibits a strong OER onset potential of 1.5 V; however, the GLYOR onset potential sharply drops in the presence of glycerol. Pd-NC has the highest current density recorded for GLYOR, reaching 100 mA/cm^2 at 0.85 V against RHE. Pd-NC has the lowest onset potential at 0.40 V, whereas Pd-PC (Pd-polycrystalline, spherical in morphology) has the lowest GLYOR current

density. Pd-NC, truncated octahedron (Pd-TO), and Pd-PC electrocatalysts all show the best glycerol conversion (85%) and 40% glyceric acid selectivity in 0.1 M glycerol and 1 M KOH at a low applied potential of 0.6 V (vs RHE). Due to the highly advantageous thermodynamics of GLYOR on the Pd-NC surface, the completed electrolyzer needs only ~3.7 kWh/Nm^3 of H_2 at a current density of 100 mA/cm^2, whereas an alkaline/PEM electrolyzer requires ≥5 kWh/Nm^3 of H_2. With GLYOR in water and simulated seawater, sustainability has been successfully proven at 10 and 50 mA/cm^2 and for up to 120 hours.

In **fifth chapter** presents the synthesis of a two-dimensional (2D) ultrathin nanosheet phosphates, specifically with cobalt (CoP; $Co_3(PO_4)_2$), copper (CuP; $Cu_3(PO_4)_2$) and nickel (NiP; $Ni_3(PO_4)_2$) phosphate and a 3D snow-flake structure with iron (FeP: $FePO_4$) phosphate. In an alkaline electrolyte, CoP functions as a high-performance electrocatalyst for the GLYOR. Phosphate nanosheets are easily and safely synthesised by hydrothermal synthesis, which is also easily scalable. In order to achieve a high density of surface-exposed active sites and a large surface area, transition-metal phosphate with a 2D nanosheet structure is used in the design. Compared to all other phosphate groups, CoP exhibits a low onset potential and higher intrinsic stability in alkaline electrolytes. Hence, the 2D CoP nanosheet was selected as the anode material for detailed GLYOR. As a GLYOR catalyst, CoP ultrathin nanosheets with a thickness of ~5 nm exhibit remarkably low overpotential at 1.27 V (vs RHE), than other phosphates. To the best of our knowledge, this is the first investigation using a phosphate-based electrocatalyst for GLYOR, and these values are much lower. Moreover, in demanding alkaline circumstances, the ideal ultrathin CoP catalyst exhibits extremely robust electrochemical stability for 200 hours of continuous GLYOR operation.

In **sixth chapter** is subdivided into two parts: **Chapter 6a** and **Chapter 6b**. Chapter 6a primarily focuses on demonstrating the electrocatalytic glucose oxidation (GLUOR) concurrently with the generation of carbon-negative green hydrogen, utilizing Pd NC. The low onset observed at 0.3-0.4 V vs RHE indicates the efficient oxidation onset with glucose. Furthermore, we synthesized a NiP catalyst as an alternative to graphite or Pt/C catalyst for HER. Both catalysts Pd-NC and NiP were employed in an alkaline electrolyzer for GLUOR to assess their stability over extended hours using pure water and simulated seawater. Glucose oxidation products were characterized by HPLC and 2D NMR.

In chapter 6b, we explore a combined form of palladium- copper -based electrocatalyst for the concurrent electrochemical oxidation of disaccharide into formate and carbon-negative green

hydrogen production in a sustainable manner. Particularly, the present work relates to a process of production of formate (a C-1 oxygenate) by electrochemical oxidation of disaccharide (a C-12 hydrocarbon- lactose and maltose) with said palladium-copper based electrocatalyst.

Chapter 7 describes the overall conclusion and the future prospects.

1.14 References

1. K. W. A. Guy, *Process Saf. Environ. Prot.*, 2000, 78, 324–327.
2. J. O. Bockris, *Science*, 1972, 176, 1323.
3. National green hydrogen mission – Government of India (MNRE)- January 2023 https://cdnbbsr.s3waas.gov.in/s3716e1b8c6cd17b771da77391355749f3/uploads/2023/01/2023012338.pdf
4. B. Obama, *Science*, 2017, 355, 126–129.
5. I. Staffell, D. Scamman, A. V. Abad, P. Balcombe, P. E. Dodds, P. Ekins, N. Shah and K. R. Ward, *Energy Environ. Sci*., 2018, 12, 463–491.
6. AR5 Climate Change 2013: The Physical Science Basis - IPCC, https://www.ipcc.ch/report/ar5/wg1/ , (accessed 24 September 2019).
7. Z. W. She, J. Kibsgaard, C. F. Dickens, I. Chorkendorff, J. K. Nørskov and T. F. Jaramillo, *Science*, 2017, 355, 146– 157.
8. J. A. Turner, *Science*, 2004, 305, 972–974.
9. A Historical Analysis of Hydrogen Economy Research, Development, and Expectations, 1972 to 2020
10. F.P. Miller, A.F. Vandome, J. McBrewster, 1970s Energy Crisis: Petroleum, 1973 Oil Crisis, 1979 Energy Crisis, Organization of Arab Petroleum Exporting Countries, Iranian Revolution, Middle East, Stagflation, Peak Oil, 1980s Oil Glut, 1973–1975 Recession; Alphascript Publishing: Saarbrücken, Germany, 2009; ISBN 9786130253844
11. Hydrogen, Fuel Cells & Infrastructure Technologies Program Multi-Year Research, Development and Demonstration Plan, https://www.nrel.gov/docs/fy08osti/39146.pdf
12. J. O. Bockris, *Science*, 1972, 176, 1322.
13. Hydrogen Council - Path to hydrogen competitiveness A cost perspective, https://hydrogencouncil.com/wp-content/uploads/2020/01/Path-to-Hydrogen-Competitiveness_Full-Study-1.pdf
14. Hydrogen and Fuel Cells Driving Transportation Innovation-September 26, 2018 https://www.act-news.com/news/hydrogen-driving-transportation-innovation/
15. IEA - Low-Emission Fuels, 11 Jul 2023, https://www.iea.org/energy-system/low-emission-fuels
16. M. V. C. Sastri, *Int. J. Hydrogen Energy*, 1989, 14, 507–513.
17. Hydrogen Energy in India | Production techniques and Government policies on Hydrogen energy. - Energy Alternatives India - EAI.in, http://www.eai.in/ref/ae/hyn/hyn.html, (accessed 8 August 2019).

18. India's Green Hydrogen Revolutions – An Ambitious approach, https://static.pib.gov.in/WriteReadData/specificdocs/documents/2024/may/doc2024510336301.pdf
19. National Hydrogen Mission Decarbonising India, Achieving Net-Zero Vision (Ministry of New & Renewable Energy) https://static.pib.gov.in/WriteReadData/specificdocs/documents/2023/jan/doc2023110150801.pdf
20. A. A. Ismail and D. W. Bahnemann, *Sol. Energy Mater. Sol. Cells*, 2014.
21. J. H. Kim, D. Hansora, P. Sharma, J. W. Jang, J. S. Lee, *Chem. Soc. Rev.* 2019, 48, 1908
22. C. Jiang, S. J. A. Moniz, A. Wang, T. Zhang, J. Tang, *Chem. Soc. Rev.* 2017, 46, 4645
23. L. J. Minggu, W. R. Wan Daud, M. B. Kassim, *Int. J. Hydrogen Energy* 2010, 35, 5233
24. Hydrogen Production: Thermochemical Water Splitting-Department of Energy, https://www.energy.gov/eere/fuelcells/hydrogen-production-thermochemical-water-splitting, (accessed 6 August 2019).
25. J. O. M. Bockris, B. E. Conway and E. Yeager, Plenum Press, New York, 1981, 595.
26. Hydrogen and Fuel Cells: Fundamentals, Technologies and Applications, 2010 by Detlef Stolten.
27. N.-T. Suen, S.-F. Hung, Q. Quan, N. Zhang, Y.-J. Xu and H. M. Chen, *Chemical Society Reviews*, 2017, 46, 337-365.
28. R. Chang, J. Overby, Chemistry, 13th ed.; McGraw-Hill Education: New York, NY, USA, 2019; pp. 806–841
29. K.W. Ahmed, M.J. Jang, M.G. Park, Z. Chen, M. Fowler, *Electrochem* 2022, 3, 581-612.
30. International Organization for Standardization. ISO 22734:2019 - Hydrogen generators using water electrolysis — Industrial, commercial, and residential applications. https://www.iso.org/standard/69212.html (accessed on 4 October 2023)
31. R. Foulkes, C. Jiang and J. Tang, in Solar Fuel Generation, CRC Press, Taylor & Francis Group, New York, 2017.
32. A. Nadeema, V. Kashyap, R. Gururaj and S. Kurungot, *ACS Appl. Mater. Interfaces*, 2019, 11, 25917–25927.
33. J. Jia, L. C. Seitz, J. D. Benck, Y. Huo, Y. Chen, J. W. D. Ng, T. Bilir, J. S. Harris, T. F. Jaramillo, *Nat. Commun*. 2016, 7, 13237.
34. T. Hisatomi, J. Kubota, K. Domen, *Chem. Soc. Rev*. 2014, 43, 7520.
35. J. Joy, J. Mathew, S. C. George, *Int. J. Hydrogen Energy* 2018, 43, 4804.
36. Y.-H. Chiu, T.-H. Lai, M.-Y. Kuo, P.-Y. Hsieh, Y.-J. Hsu, *APL Mater.* 2019, 7, 080901.
37. Z. Xing, X. Zong, J. Pan, L. Wang, *Chem. Eng. Sci*. 2013, 104, 125.
38. W. H. Cheng, M. H. Richter, M. M. May, J. Ohlmann, D. Lackner, F. Dimroth, T. Hannappel, H. A. Atwater, H. J. Lewerenz, *ACS Energy Lett.* 2018, 3, 1795
39. C. Moon, B. Shin, *Discovery Mater.* 2022, 2, 5.
40. T. Tran-Phu, Z. Fusco, I. Di Bernardo, J. Lipton-Duffin, C. Y. Toe, R. Daiyan, T. Gengenbach, C.-H. Lin, R. Bo, H. T. Nguyen, G. M. J. Barca, T. Wu, H. Chen, R. Amal, A. Tricoli, *Chem. Mater.* 2021, 33, 3553.

41. B. A. Pinaud, J. D. Benck, L. C. Seitz, A. J. Forman, Z. Chen, T. G. Deutsch, B. D. James, K. N. Baum, G. N. Baum, S. Ardo, H. Wang, E. Miller, T. F. Jaramillo, *Energy Environ. Sci.* 2013, 6, 1983
42. B. Zhao, J.-W. Liu ,Y.-R. Yin, D. Wu, J.-L. Luo, X.-Z. Fu, *J. Mater. Chem. A*, 2019,7, 25878-25886
43. D. J. Chadderdon, L. Xin, J. Qi, B. Brady, J. A. Miller, K. Sun, M. J. Janik and W. Li, *ACS Catal.*, 2015, **5**, 6926–6936.
44. Y. Li, X. Wei, L. Chen, J. Shi and M. He, *Nature Commun.*, 2019, **10**, 5335.
45. Y. Yan, H. Zhou, S.-M. Xu, J. Yang, P. Hao, X. Cai, Y. Ren, M. Xu, X. Kong, M. Shao, Z. Li and H. Duan, *J. Am. Chem. Soc.*, 2023, **145**, 6144–6155.
46. P. Du, J. Zhang, Y. Liu and M. Huang, *Electro. Commun.*, 2017, **83**, 11–15.
47. C. Lin, P. Zhang, S. Wang, Q. Zhou, B. Na, H. Li, J. Tian, Y. Zhang, C. Deng, L. Meng, J. Wu, C. Liu, J. Hu and L. Zhang, *J. Alloys Compd*, 2020, **823**, 153784.
48. W.-J. Liu, Z. Xu, D. Zhao, X.-Q. Pan, H.-C. Li, X. Hu, Z.-Y. Fan, W.-K. Wang, G.-H. Zhao, S. Jin, G. W. Huber and H.-Q. Yu, *Nature Commun.*, 2020, **11,** 265.
49. W.-J. Liu, L. Dang, Z. Xu, H.-Q. Yu, S. Jin and G. W. Huber, *ACS Catal.*, 2018, **8**, 5533–5541.
50. S. R. Kubota and K.-S. Choi, *ACS Sustain. Chem. Eng*, 2018, **6**, 9596–9600.
51. A. K. V. Mruthunjaya and A. a. J. Torriero, *Molecules*, 2023, **28**, 471.
52. G. G. Kumar, A. Farithkhan and A. Manthiram, *Adv. Energ. Sust. Res.*, 2020, **1**, 2000015.
53. R. K. Singh, K. Rajavelu, M. Montag and A. Schechter, *Energy Tech.*, 2021, 9, 210007.
54. R. Miao and R. G. Compton, *J. Phys. Chem. Lett*, 2021, **12**, 1601–1605.
55. Q. Qian, J. Zhang, J. Li, Y. Li, X. Jin, Y. Zhu, Y. Liu, Z. Li, A. El-Harairy, C. Xiao, G. Zhang and Y. Xie, *Angew. Chem.*, 2021, **133**, 6049–6058.
56. K. Ojha, E. M. Farber, T. Y. Burshtein and D. Eisenberg, *Angew. Chem.*, 2018, **57**, 17168–17172.

Chapter 2

Synthesis and Experimental Methods

Image ref: Generated by Canva based on a prompt by Inderjeet Chauhan, 2024.

2.1 Introduction

Developing a stable and highly efficient catalyst for oxidation and reduction reactions is both crucial and demanding. An ideal photo or electrocatalyst must possess significant catalytic efficiency, selectivity towards the desired product, and exceptional durability over extended operation periods. The catalyst synthesis plays a pivotal role in attaining the desired catalytic performance, selectivity, and resilience in heterogeneous catalysis. Physicochemical characterization of the synthesized materials assists in establishing the correlation between the catalyst's structure and its activity, facilitating the design of superior catalysts.

Current chapter provides an overview of the catalyst preparation process for each catalyst system employed in this doctoral dissertation, accompanied by a range of characterization techniques utilized to understand the catalyst's attributes. In the current thesis, bismuth vanadate ($BiVO_4$) and cobalt-doped $BiVO_4$ catalysts were synthesized using a one-step successive ionic layer adsorption and reaction (SILAR) method. Furthermore, synthesis of shape-controlled Pd nanoparticles, PdCu alloy, PdCu bimetal, and NiP, alongside ultrathin 2D 3d metal phosphates, for the oxidation of biomass components toward various value-added products, such as formic acid were conducted. Biomass components includeglycerol (C3-molecule), mono-saccharide molecule (glucose-C6-molecule), and disaccharide molecules (C12 molecule), such as lactose/maltose.

Careful consideration must be given to the structural and textural aspects of catalysts, including crystallinity, phase modifications, crystallite size, surface architecture, active site abundance and structural morphology. Various characterization techniques, including powder X-ray diffraction (PXRD), X-ray absorption spectroscopy (XAS), Raman spectroscopy, X-ray photoelectron spectroscopy (XPS), UV-Visible spectroscopy, atomic force microscopy (AFM) and microscopic investigations were employed to assess the properties of fresh and spent catalysts.

2.2 A compilation of the gases and chemical substances employed in this study.

Table 2.1 The following enumerates the chemicals utilized in the synthesis of different catalyst materials and reactions, along with their corresponding purities.

Chemical name	Formula	Purity	Supplier
Bismuth (III) nitrate pentahydrate	$Bi(NO_3)_3.5H_2O$	99.9%	Thomas Baker
Cobalt (II) nitrate hexahydrate	$Co(NO_3)_2.6H_2O$	99.9%	Thomas Baker
Ammonium meta vanadate	NH_4VO_3	99.9%	TCI chemicals

Potassium tetrachloride palladate	K_2PdCl_4	99.9%	Sigma-Aldrich
Cobalt chloride	$CoCl_2.6H_2O$	99.9%	Merck
Iron chloride	$FeCl_3$	99.95%	Merck
Nickel chloride	$NiCl_2.6H_2O$	99.5%	Merck
copper chloride	$CuCl_2.2H_2O$	99.5%	Merck
monosodium phosphate	$Na_2H_2PO_4$	99.9%	Merck
Potassium chloride	KCl	99.95%	Sigma-Aldrich
Potassium bromide	KBr	99.95%	Sigma-Aldrich
Citric acid	$C_6H_8O_7$	99.95%	Sigma-Aldrich
Ascorbic acid	$C_6H_8O_6$	99.9%	Sigma-Aldrich
Polyvinylpyrrolidone (PVP)	MW 40000	99.9%	Sigma-Aldrich
Glycerol	$C_3H_8O_3$	99.9%	TCI chemicals
Glucose	$C_6H_{12}O_6$	99.9%	TCI chemicals
Lactose	$C_{12}H_{22}O_{11}$	99.9%	TCI chemicals
Maltose	$C_{12}H_{22}O_{11}$	99.9%	TCI chemicals
Potassium hydroxide	KOH	99.9%	TCI chemicals
Deuterium oxide	D_2O	99.9%	TCI chemicals
Potassium hydrogen phthalate	$C_8H_5KO_4$	99.9%	TCI chemicals
Formic acid	HCOOH	99.9%	TCI chemicals
Glycolic acid	$C_2H_4O_3$	99.9%	TCI chemicals
Glyceric acid	$C_3H_6O_4$	99.95%	TCI chemicals
Lactic acid	$C_3H_6O_3$	99.5%	TCI chemicals
Acetic acid	CH_3COOH	99.5%	TCI chemicals
Oxalic acid	$C_2H_2O_4$	99.9%	TCI chemicals
Acetone	C_3H_6O	99.9%	TCI chemicals
Ethanol	C_2H_5OH	99.95%	TCI chemicals
n-hexane	C_6H_{14}	99.95%	TCI chemicals
Pt/C	20%	99.9%	Global nanotech
Hydrochloric acid	HCl	99.9%	Merck
Glacial acetic acid	CH_3COOH	99%	Thomas Baker
Fluorine-doped tin oxide (FTO)	FTO	-	Merck

Table 2.2 Gases used for all reactions and other characterization techniques are shown and supplied all the gas with high purity.

Gas/ Gas mixture	**Purity (%)**	**Usage**
Compressed Air	--	For FID
Argon (Ar)	99.9%	GC carrier gas
Nitrogen (N_2)	99.9%	Carrier gas in the GC
Hydrogen (H_2)	99.9%	Catalyst reduction
Helium (He)	99.9%	Pretreatment in TPD/TPD

5% H_2/Ar	99.9%	Gas GC Calibration
10%CO_2/He	99.95%	^{1}H-NMR

2.3 Catalysis synthesis procedure

2.3.1 Fabrication of bismuth vanadate (BV) and cobalt doped bismuth vanadate (Co-BV) Photoelectrode

SILAR (successive ionic layer adsorption and reaction) method was employed for fabrication of photoelectrode on FTO substrate (Figure 2.1). SILAR method is simple to be practiced in any wet-laboratory and the SILAR requirements are the minimum. In fact, with few beakers along with required chemicals, it can be practiced. For the present studies, FTO substrate of 1*2 cm^2 dimension was chosen; FTO plate was pretreated by ultrasonic cleaning in soap and then isopropyl alcohol, followed by drying in an oven at 333 K. Initially two precursor solutions of Bi^{3+} and (ammonium) meta-vanadate (VO_3^-) were prepared for SILAR. The Bi^{3+} precursor solution was prepared by mixing $Bi(NO_3)_3.5H_2O$ (25 mM) with glacial acetic acid and DI water in a ratio 1:19 at 298 K. Similarly, VO_3^- precursor solution was prepared by adding NH_4VO_3 (25 mM) into 40 ml DI water at 343 K. A single SILAR cycle consists of immersion of the FTO plate into the Bi^{3+} precursor for 20 sec followed by immersion into VO_3^- precursor (at 343 K) for 20 s and then rinsed in the distilled water. For BV electrode fabrication, 15 cycles of SILAR were repeatedly applied on FTO plate to prepare 1±0.05 µm thickness.

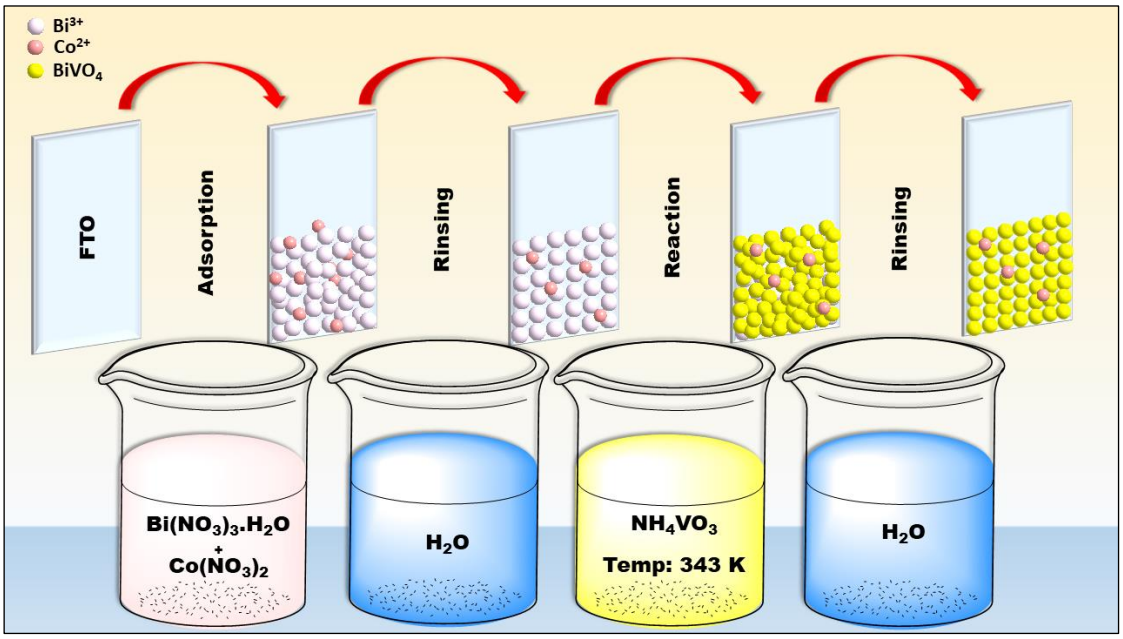

Figure 2.1 Schematic diagram of fabrication of photoanode by SILAR method.

After 15 SILAR cycles, the above electrode was dried at 333 K for 4 h and calcined at 723 K for 2 h in a muffle furnace under static air. For Co-BV electrode fabrication, we modified the cation precursor solution by adding required amount of $Co(NO_3)_2.6H_2O$ (0.01, 0.05, 0.1, 0.5 mol %) to Bi^{3+} ion precursor solution and the same SILAR process was used as that of BV; resulting catalysts are designated as 0.01 Co-BV, 0.05 Co-BV, 0.1 Co-BV and 0.5 Co-BV, respectively, throughout the thesis, unless mentioned otherwise. Thickness of the photoanodes layer is measured by surface profilometer. Typical photoanode (BV and Co-BV) thin film area prepared and utilized for all PEC and characterization measurements is 1 cm^2, and the amount of BV deposited is 100±10 µg/cm^2.[1,2]

2.3.2 Synthesis of Palladium Nanocube (Pd-NC)

In a 25 mL capacity three neck round-bottom flask (RBF), 50 mg of PVP, 60 mg of ascorbic acid, and 300 mg of KCl were added to 8 mL of water. To make sure all the materials were dissolved fully, the flask was sonicated for ten minutes at a temperature of 80-85 °C while being constantly stirred in an Ar environment. To the above solution, 3 mL of water containing 57-60 mg of K_2PdCl_4 was quickly added. For three hours, the solution was continuously stirred and maintained at 85 °C. Following three hours, the acquired black-brown nanoparticles with solution were allowed to cool to ambient temperature before being gathered in centrifuge bottles for subsequent cleaning. The nanoparticles were cleaned by centrifuging the solution containing an excess of acetone and a 1:5 ethanol and hexane mixture at 10000 rpm for 5 minutes.

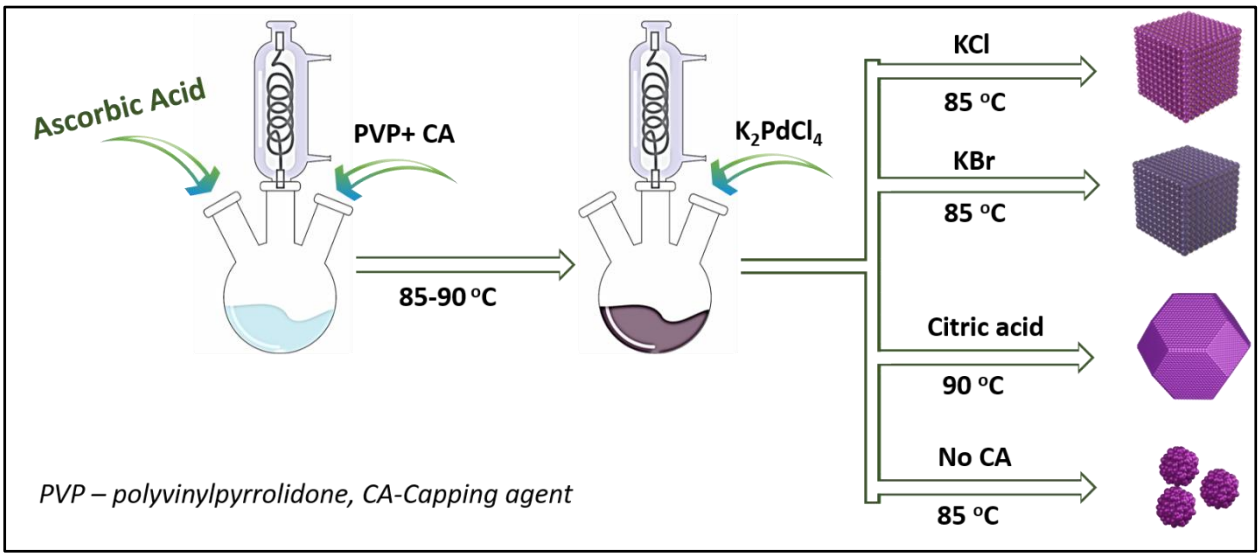

Figure 2.2 Schematic representation of the shape-controlled Pd nanoparticles synthesis with different capping agents, such as KCl, KBr and citric acid.[3,4]

The final black-brown colored material was dried in air oven at 60 °C to remove any solvent molecules. The above-mentioned procedure was also adopted for Pd nanocubes (Pd-NC) with KBr as capping agent; however, 300 mg KBr was employed at 85 °C, instead of KCl. A schematic of synthesis procedure is shown in Figure 2.2.

2.3.3 Synthesis of Palladium-Truncated Octahedra (Pd-TO)

The procedure was the same as that of Pd-NC (Section 2.3.2), except that citric acid (60 mg) was used at 90 °C instead of KCl (300 mg) at 85 °C. The addition of 3 ml Pd precursor solution was carried out slowly, requiring about 10 minutes. A schematic picture shown in Figure 2.2 shows the steps involved in the synthesis of Pd-TO.

2.3.4 Synthesis of Palladium poly-crystalline (Pd-PC)

The procedure was the same as that of Pd-TO (Section 2.2.3), but without the use of any capping agent (citric acid) at 90 °C. A schematic picture shown in figure 2.2 shows the steps involved in the synthesis of Pd-PC.

2.3.5 Fabrication of Pd anode and Pt/C cathode electrode on Ni foam (NF)

Pd nanoparticle anode: All the electrodes were prepared by drop-casting coating method shown in Figure 2.3. NF was first cleaned in an ultrasonication bath using 1 M HCl for 30 minutes. It was then rinsed in a sonication bath using DI water and ethanol in turn for 10 minutes. Finally, it was vacuum-dried for 10 hours at 70 °C. A standard protocol involved dispersing 3 mg of Pd nanocatalyst in 3 ml of iPA, slowly dropping the catalyst over a 1*1 cm^2 NF substrate, and then drying it in a vacuum oven for 12 hours. In electrolyzer, the Pd-NC electrode was prepared by spray coating method and the catalyst loading amount was approximately 1±0.1 mg cm^{-2}.

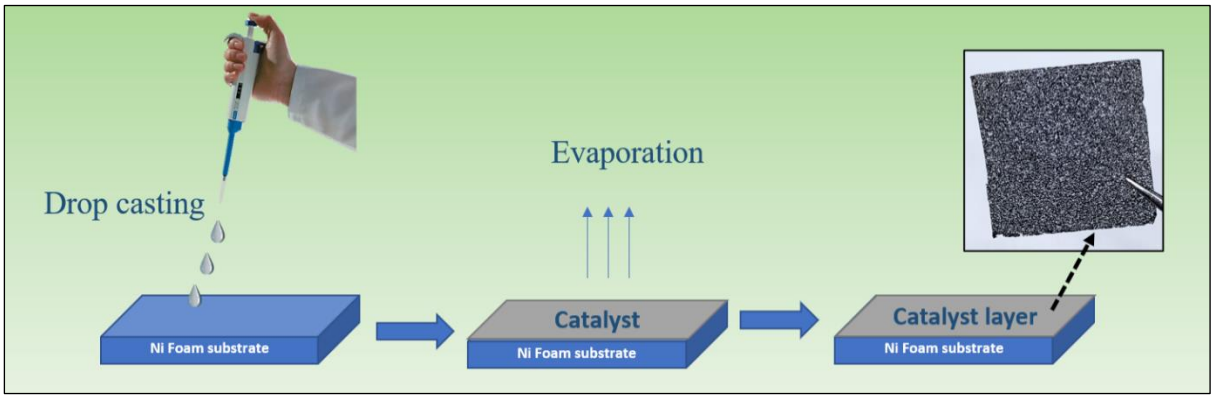

Figure 2.3 A schematic representation of drop casting method on Ni foam.

Pt/C cathode: 20% Pt/C standard catalyst was used as cathode part for HER, by spray coating method; the amount of deposited catalyst was approximately 0.8±0.1 mg.cm^{-2}.

2.3.6 Synthesis of 2D 3d-Metal Phosphates Nanosheet

In this synthesis, metal (M = Co, Cu, Fe and Ni) chloride precursor and monosodium phosphate were utilized for the synthesis of corresponding metal phosphates via a single-step solvothermal process shown in Figure 2.4. A solvent mixture of isopropyl alcohol and ultrapure deionized water in a 2:1 ratio was used to dissolve a total of 10 mM of metal dichlroide and 20 mM of phosphate precursor NaH_2PO_4. The combination produced a uniform slurry that was then put into a 50 mL stainless-steel autoclave with a teflon lining. The autoclave was then placed in a hot air oven and subjected to solvothermal treatment, where it was kept at 140 °C for 14 hours. The autoclave was taken out of the oven once the reaction was finished and allowed to cool down to room temperature. Following the reaction, the products were filtered and subjected to multiple washes with deionized water, concluding with a final wash with ethanol. The collected materials were then dried for 12 h in vacuum oven, and then it was employed to make electrode for GLYOR. As synthesized catalyst exhibits distinct colour namely, CoP (violet), CuP (cyan), FeP (brown) and NiP (lime). It may be noted that the environmentally benign synthesis of phosphate nanosheets by hydrothermal synthesis is easy to scale-up.

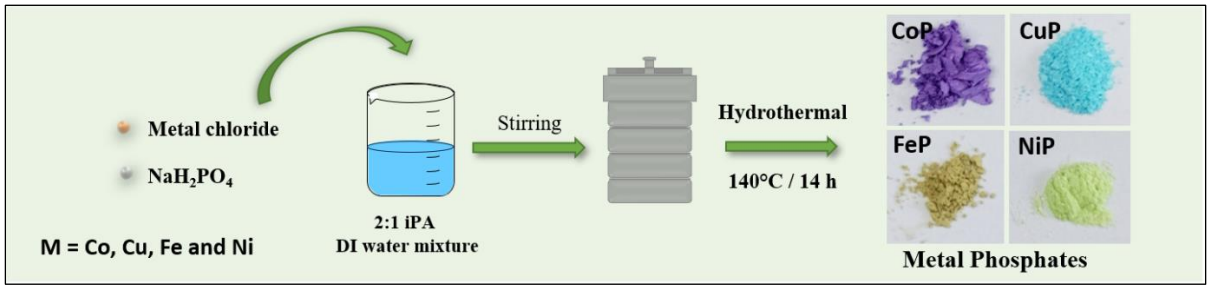

Figure 2.4 Schematic illustration of the M-PO4 synthesis procedure.[5]

2.3.7 Synthesis of NiP

Initially, NF sheets measuring 1 x 3 cm^2 underwent ultrasonic cleaning for 10 minutes sequentially with deionized water, 3 M HCl, and ethanol to eliminate surface oxides and impurities. Electrodeposition took place over a 1 x 1 cm^2 area of the electrode, with the remaining area masked using teflon tape for half-cell reactions. For electrode preparation, solutions of $NiCl_2{\cdot}6H_2O$ (25 mM), and $NaH_2PO_4{\cdot}2H_2O$ (0.5 M), were dissolved in 75 mL of

distilled water. The electro-deposition process occurred within a three-electrode system, using Ag/AgCl as the reference electrode, Pt foil as the auxiliary electrode, and previously cleaned NF as the working electrode. On 1 cm^2 electrodes, electrodeposition was carried out for 20 minutes at a continuous applied current of -0.85 V versus Ag/AgCl.

2.3.8 Synthesis of PdCu Alloy Catalyst

The solution phase method was adopted for the synthesis of PdCu alloy. In a 100 mL capacity 3-neck RBF, 5 mL of 0.25M K_2PdCl_4 solution and 5 mL of 0.25 M $CuSO_4.5H_2O$ were added and diluted the whole solution to 50 mL with water. The flask was sonicated for 30 minutes to ensure that a homogeneous mixture was formed and then heated to 75-85 °C under constant stirring. 0.01 mol (0.486 mL) of hydrazine hydrate was added and stirred the mixture constantly for 1 h under the same temperature. After 1 h, the PdCu alloy solution obtained was cooled to room temperature and collected in centrifuge bottles. Washing or cleaning of the alloy was carried out by centrifuging the solution with Millipore water at 10000 rpm for 5 times. The final precipitate was dried in the oven at 60-70 °C and then used for the catalytic reaction.

2.3.9 Synthesis of PdCu Bimetal Catalyst

Synthesis of PdCu bimetallic nanoparticles was achieved using the solution phase method. In a 25 mL, 3-neck RBF, containing 8 mL of water, variable amounts of PVP (25-150 mg), ascorbic acid (40-100 mg), and KCl (100-300 mg) were dissolved. The flask underwent 10 minutes of sonication to ensure complete dissolution of the components, followed by heating to 75-85 °C under continuous stirring in an inert atmosphere. A solution containing $PdCl_2$ and KCl in a 1:2 mole ratio (20-100 mg), was dissolved in 2-6 mL of water, and $CuCl_2.2H_2O$, in 2-6 mL water was then added to the above solution simultaneously. The temperature was maintained at 75-85 °C for 5-10 minutes, followed by three hours of constant stirring at the same temperature. After 3 hours, the resulting PdCu bimetallic nanoparticle solution was cooled to room temperature and transferred to centrifuge bottles. The nanoparticles were washed by centrifuging the solution with excess acetone once, and then with an ethanol: hexane mixture (in a 1:5 ratio) five times at 10000 rpm. Finally, the precipitate containing the PdCu bimetallic nanoparticles was dried in an oven at 60 °C and subsequently utilized for catalytic reactions.

2.3.10 Synthesis of PdCo Alloy Catalyst

The synthesis of PdCo alloy catalyst followed the same procedure as that of section 2.3.8 (PdCu), except for the use of cobalt chloride hexahydrate as the cobalt precursor.

2.3.11 Synthesis of PdAg Alloy Catalyst

The palladium silver alloy was synthesized using silver nitrate as the metal precursor. The remaining procedure is the same as that of section 2.3.10.

2.3.12 Synthetic process of PdRe Alloy

Rhenium metal powder was used for the preparation of $Re(NO_3)_3$ by dissolving the required amount of Re in nitric acid . This solution was used as Re precursor for PdRe alloy synthesis. Other steps are the same as that of the section 2.3.10.

2.4 Experimental method

2.4.1 Photoelectrochemical (PEC) Measurements

The PEC study was conducted using a Gamry potentiostat (Model 3000) in a single quartz compartment cell with three electrodes. Graphite rod and Ag/AgCl (saturated with 1 M KCl) were utilised as the reference and counter electrodes, respectively. Before doing any PEC measurements, the NaCl electrolyte's pH was brought to 2.3 by adding 0.5 M H_2SO_4 and it was purged by bubbling N_2. Every measurement was taken using a single sun and a 300 W Xe arc lamp from Newport Instruments that had an AM 1.5G filter installed. Utilising a lux-meter certified by NIST, it was verified that the light intensity measured 100 mW/cm^2. The following equation was used to convert the electrode potential from the Ag/AgCl scale to the RHE scale:

$$E_{RHE} = E_{Ag/AgCl} + 0.059pH + 0.197\ V$$

2.4.2 Electrochemical measurements

In electrochemistry, a potentiostat is a crucial instrument that regulates the voltage difference between a working electrode and a reference electrode while keeping track of the current that flows through the working electrode as a result. Here's how it operates: (1) Voltage Regulation: The potentiostat administers a steady voltage, known as the set potential, between the working and reference electrodes. This voltage is meticulously regulated via a feedback loop, ensuring a consistent potential difference. (2) Current Monitoring: Concurrently, the potentiostat gauges the current flow within the working electrode. This current serves as a direct indicator of the rate at which electrochemical reactions transpire on the electrode's surface. (3) Feedback Mechanism: To maintain a stable current, the

potentiostat employs feedback control. It applies a minor voltage to the working electrode and observes the resulting current. Adjustments are made to the voltage until the desired current level is achieved. (4) Data Acquisition: Throughout the process, the potentiostat records both potential and current readings over time. These data sets are invaluable for scrutinizing the electrochemical dynamics of the system under examination.

All of the electrochemical studies including the glycerol oxidation (GLYOR), oxygen evolution reaction (OER), and hydrogen evolution reaction (HER) were carried out in three and two electrode systems utilising a Gamry reference 3000 potentiostat. The functioning electrode on NF was immediately the manufactured electrode. For hydrogen evolution in three and two electrode systems, respectively, graphite rod (5 mm in diameter) and Pt/C on NF were employed as counter electrodes. The reference electrodes were Ag/AgCl electrode and saturated calomel electrode (SCE). In this work, all potentials were expressed in relation to the reversible hydrogen electrode (RHE) using the equation that follows:

$$E_{RHE} = E_{SCE} + 0.05916\ pH + 0.241\ V$$

Each polarisation curve was captured using 85% iR correction, and every LSV curve was gathered at a 5 mV/s sweep rate. the apparent current density determined by utilising the geometric area of the electrode. The electrochemical surface area, or ECSA, was computed using the double-layer capacitance, Cdl, which was obtained from the cyclic voltammetry (CV) curves recorded in a potential range devoid of any Faradaic current. Scan rates of 20, 40, 60, 80, and 100 mV/s were used. The Cdl slope was obtained by plotting the recorded cathodic charging currents against various scan rates, such as 20, 40, 60, 80, and 100 mV/s. The following equation was used to calculate the ECSA.[6]

$$ECSA = C_{dl} + C_{NF}$$

2.4.3 Liquid and gaseous products measurement

The liquid and gaseous products were analyzed and quantified by ^{1}H NMR, HPLC and GC analysis. The chronoamperometry testing in three-electrode system was carried out at 0.6 - 1.2V vs. RHE for 4 h (0.1 M glycerol + 1 M KOH); chronopotentiometry testing with two electrode system was carried out at 10 and 50 mA/cm^2 for 120 h. In 4 h reaction, 450 µL electrolyte was added with 130 µL D_2O and 20 µL KHP (as an internal standard concentration-1mM) for NMR measurements. The FE of various products was determined, as stated in the equation below.

$$FE\ (\%) = \frac{Z\ .\ n\ .\ F}{Q}$$

where F is the Faraday constant, Q is the amount of charge conveyed, Z is the number of electrons transported to create the product, and n is the number of moles formed.

Potassium hydrogen phthalate, or KHP, was used as an internal reference to quantify every product seen in ^{1}H NMR analysis. The following formula was used to determine the concentration of liquid products that were produced following the electrocatalytic reaction:

$$\frac{n_x}{n_y} = \frac{I_x}{I_y} \times \frac{N_y}{N_x}$$

In this case, N_x is the number of nuclei, I_x is the integral area in the ^{1}H NMR spectra for KHP, and n_x is the molar concentration of KHP (4 equivalent protons for KHP occurring at 7.25 ppm). In a similar manner, n_y, or the number of nuclei connected to the peak, is determined using the liquid product's formula above, together with I_y, the integral area of the product generated. Conversion, selectivity, and carbon balance were calculated using the product concentrations found using ^{1}H NMR.

$$\text{Conversion (\%)} = \frac{\text{n}_{\text{glycerol,initial}} - \text{n}_{\text{glycerol,final}}}{\text{n}_{\text{glycerol,initial}}} \times 100$$

$$\text{Carbon balance (\%)} = \frac{\text{n}_{\text{Sum of products}}}{3 \times \text{n}_{\text{glycerol,initial}}} \times 100$$

$$\text{Selectivity (\%)} = \frac{\text{n}_{\text{product}} \times \text{carbon balance}}{\text{n}_{\text{Sum of products}}} \times 100$$

Where n is the number of moles.

Some of the products NMR signals had merged in ^{1}H NMR spectra, for that we have recorded 2D NMR spectra using selective excitation and TOCSY transfer in sample to confirm gluconic and glucaric acid product signals arising from glucose oxidation reaction.

2.4.4 KP-AFM measurement

Atomic force microscopy (AFM) experiment was carried out using Dimension Icon (Bruker) at room temperature. A capacitor is formed between sample surface and tip which is applied DC and AC voltage. The formula for CPD ($\Delta\phi$) is (ϕ_{tip} - ϕ_{film})/q, where q is the charge magnitude and ϕ_{tip} and ϕ_{film} are the work functions of the tip and sample, respectively. The sample was held at ground potential in the current experiment by applying a bias voltage $V_{tip} = V_{dc} + V_{ac} \sin(\omega t)$, where ω is the cantilever resonant frequency, straight to the tip. In order to minimise the force component at a frequency between the cantilever tip and sample surface, a feedback loop continually modifies V_{dc}. This condition is then recorded as a function of location, resulting in a map of the sample surface potential.

In order to generate an electric force for the current set of experiments, the Ti-Ir-tip was

subjected to an AC bias (5 V). Using a lift-off mode, the surface potential pictures acquired by KPM were captured for AC bias at the highest potential of the Pd-NC, Pd-TO, and Pd-PC samples. With this technique, a topographic line scan is first taken at a closer range. Next, the line is rescanned in the lift mode, where short-range forces are not present, with the cantilever tip lifted to a lift height of 30 nm. This allows for the simultaneous retrieval of AFM and KPM data from the same location.

2.4.5 Electrolyzer setup

A continuous flow electrolyzer with a 4 cm^2 geometrical electrode area was used in a two-electrode system, and a sustainion membrane was used to exchange anion and separate anode and cathode compartments for GLYOR (or biomass component oxidation) and HER. A digital photograph of the continuous flow electrolyzer employed is shown in Figure 2.5a, b. H_2 gas was collected by inverted burette method for quantitative measurements.

A constant current was used with the different flow rate for different biomass components molecules for longer hour stability. Due to excessive electrolyte consumption and H_2 generation due to fast kinetics, additional electrolyte and a high flow rate was employed. Along with pure miliQ water, all stability reactions were carried out in saline water (3.5 wt% NaCl solution comparable to sea water).

The FE of hydrogen production was evaluated by the following equation:

$$Faradaic\ efficiency\ (\%) = \frac{n_{experimental}}{n_{theoretical}} \times 100$$

Where $n_{\text{experimental}}$ is the number of moles of H_2 collected experimentally. The theoretical amount of H_2 was calculated by the following equation:

$$n_{theoretical} = \frac{Q}{n \times F}$$

where F is Faraday's constant (96,485 C mol^{-1}), n is the number of electrons transferred to generate each H_2 molecule, and Q is the transferred charge.

The following formula was used to get the electricity usage (W, kW) per m^3 of H_2 produced:

$$W = \frac{n \times F \times V \times 1000}{3600 \times V_m}$$

where V is the applied voltage, m is the molar volume of gas at normal temperature and pressure (22.4 L/mol), and n is the number of electrons transferred to generate each H_2 molecule.

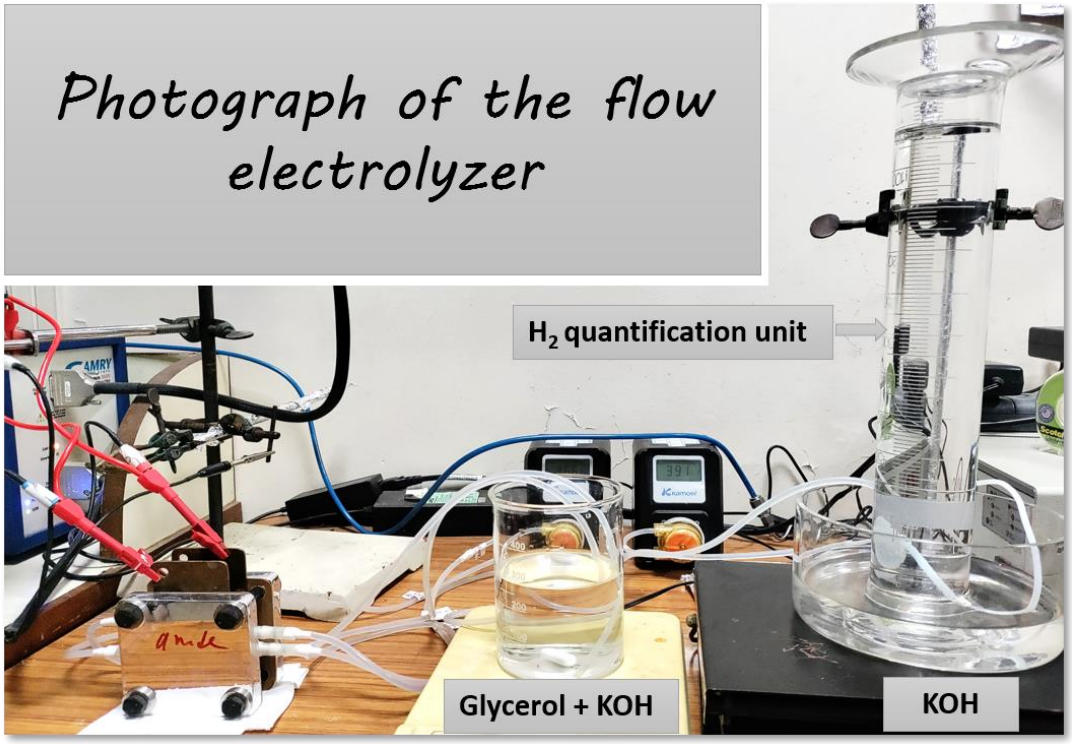

Figure 2.5a Digital photograph of two electrode flow electrolzer and gas collection unit by the inverted burette method.

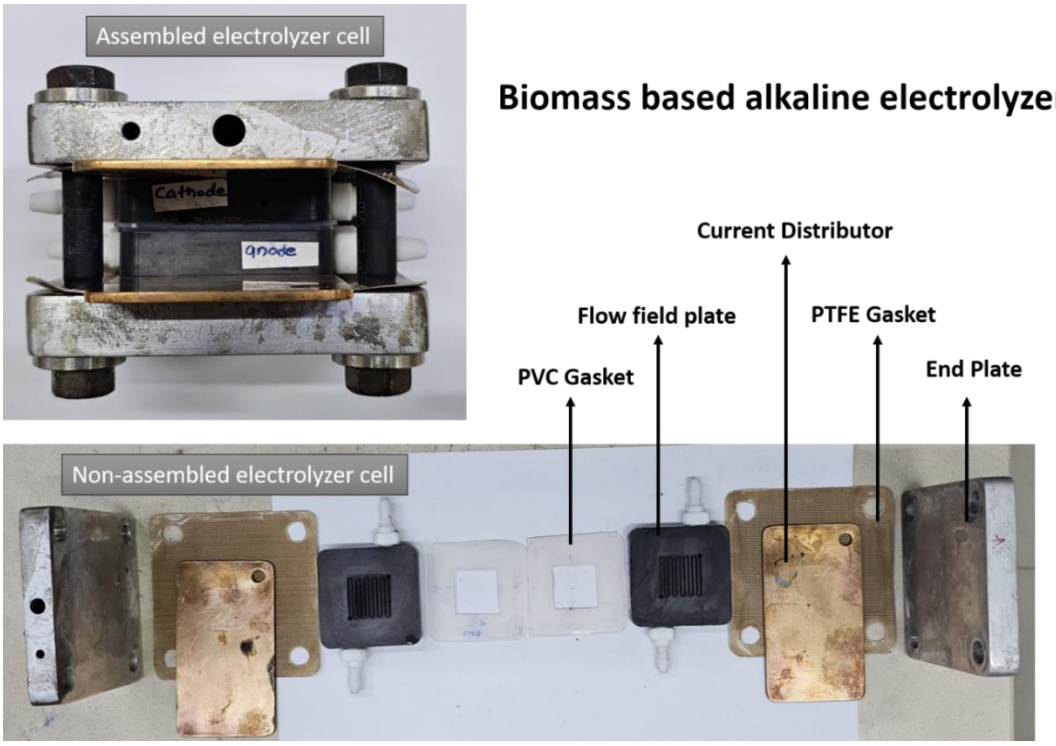

Figure 2.5b Digital photographs showing an electrolyzer in both assembled and non-assembled states, designed for comprehensive two-electrode studies.

2.5 Catalyst characterization methods

The catalyst materials and devices were thoroughly examined using a variety of analytical

techniques.

UV-Visible absorption spectroscopy, a scientific method employed to study the interaction between matter and ultraviolet (UV) and visible (Vis) light, operates on the principle of light absorption. This technique involves the excitation of electrons from lower to higher energy levels within a molecule due to light absorption. A UV-Vis spectrophotometer is used to measure the absorption of light by a sample across different wavelengths. This is achieved by passing a light beam through the sample and recording the absorbed light. The absorption occurs at specific wavelengths, indicating the energy difference between the molecule's ground and excited states. The Beer-Lambert law states that the concentration of the absorbing species in a sample is directly proportional to the observed light absorption. By analyzing the UV-Visible spectrum, which depicts the absorbed light versus wavelength, valuable insights into the electronic configuration of the specimen can be obtained. The position and intensity of spectral absorption peaks are linked to the sample's chemical composition and structure. Additionally, diffuse reflectance, characterized by the scattering of light in various directions upon striking a surface, was also investigated. The UV-Vis measurements were conducted using a Shimadzu spectrophotometer (model-UV2550) with spectral grade $BaSO_4$ serving as a reference material, in the wavelength range of 200 to 800 nm.

X-ray diffraction (XRD) stands as a prevalent method for examining catalyst materials, revealing vital details about their crystal structure, crystalline phases, percentage of crystallinity, and crystallite dimensions. This technique employs X-rays, a form of invisible and electrically neutral electromagnetic radiation, to probe the atomic and molecular arrangement within various materials. XRD operates on the principle of coherent scattering, where X-rays interfere with each other, resulting in distinct bright and dark patterns known as fringes. Bragg's law is fundamental to this process, linking constructive interference with the interplanar distances of crystal planes. XRD measurements yield a plot of diffracted X-rays against incident angle, with sharp intensity peaks indicating points of constructive interference. The width of these peaks reflects the dimensions of the reflecting crystal planes, allowing for estimations of crystallite size using the Scherrer formula. Using a Panalytical X'pert Pro dual goniometer diffractometer and Cu-Kα (1.5418 Å) radiation with a Ni-filter, powder XRD data was collected. The scan rate was set at 0.50 min^{-1} with a step size of 0.02°.

FESEM, or Field Emission Scanning Electron Microscope, utilizes a concentrated stream of high-energy electrons to generate a detailed image of a specimen. Its functionality

hinges on how electrons interact with the sample. FESEM employs either a tungsten filament or a field emission source to emit electrons. These electrons are then focused using electromagnetic lenses and directed onto the specimen. Certain electrons are absorbed or pass through the material, while others scatter as the electron beam interacts with it. By varying the intensity of the electron beam and catching electrons scattered in different directions, detectors gather the scattered electrons to produce an image. The sample's surface characteristics and structure are revealed with remarkable detail through this technique. Energy dispersive X-ray analysis (EDX) and FESEM were performed with the FEI NOVA NANOSEM 450 system, which was fitted with an EDX device. High-Resolution Transmission Electron Microscopy (HRTEM) is a robust imaging method utilized in materials science for scrutinizing the atomic arrangement of substances. Its operation relies on transmitting a stream of electrons through a slender specimen. These electrons are propelled by an electron emitter and directed onto the specimen via a sequence of electromagnetic lenses. Typically, the specimen is prepared by slicing it thinly (less than 100 nm thick) using either a focused ion beam or a diamond saw. The thinness of the sample permits electron penetration, forming an image on a detector positioned on the opposite side. As electrons traverse the sample, they interact with its atoms, causing electron beam scattering and diffraction. The dispersed electrons interfere with each other, generating an intricate pattern of bright and dark spots on the detector known as an electron diffraction pattern. This pattern contains data about the material's atomic structure. By interpreting the electron diffraction pattern, HRTEM can generate a finely detailed image of the material's atomic configuration. This image delineates the spatial arrangement of atoms at the atomic level, facilitating the examination of flaws, interfaces, and other structural attributes. HRTEM and EDS analysis of the materials were carried out using the JEOL JEM F-200 HRTEM operating at 200 kV.

Raman spectroscopy is a technique used to explore the rotational and vibrational movements of molecules by analyzing the inelastic scattering of monochromatic light. This method involves exposing a sample to monochromatic light, typically from a laser, which excites molecular activity within the sample. When the laser light interacts with the sample, some photons scatter, with most maintaining the same energy level as the initial light source (known as elastic or Rayleigh scattering). However, a small portion of the scattered light exhibits different energy levels due to interactions with molecular vibrations and rotations, known as inelastic or Raman scattering. A spectrometer is then employed to collect and analyze the scattered light, separating it into its component wavelengths. The resulting Raman spectrum

depicts the intensity of the inelastically scattered light versus the wavelength shift from the incident light. This spectrum provides insights into the rotational and vibrational behaviors of molecules within the sample, and it can be used to identify both the molecule and its chemical composition. Raman spectra were obtained using the Horiba JY LabRAM HR 800 Raman spectrometer, which utilized a 633 nm excitation source.

X-ray photoelectron spectroscopy (XPS) is a highly surface-sensitive analytical method used to gather chemical insights from the surfaces of various materials. XPS instruments are engineered to function in high vacuum environments to minimize collisions and enhance the detection of photoelectrons emitted from the sample's surface. The resulting spectrum, which shows emission intensity versus electron binding energy, is then analyzed to glean information about the sample's chemical makeup and electronic configuration. The binding energies of the photoelectrons display unique characteristics specific to each element, offering details about surface elemental composition and chemical states. Following ionization, X-ray fluorescence or Auger electron emission occurs, and employing high-resolution X-ray photoelectron spectroscopy enables the retrieval of valuable chemical state details regarding the surface. XPS analysis was performed at Thermo Fisher Scientific Instruments UK using a monochromatic Al K Alpha source with a beam current of 6 mA and 12 kV.

Nuclear magnetic resonance (NMR) occurs when the nuclei of specific atoms experience a secondary oscillating magnetic field while situated in a robust magnetic field. This phenomenon finds application across diverse scientific domains such as chemistry, biochemistry, and medicine, aiding in the elucidation of molecular and material properties. The operational principles of NMR are outlined as follows: (1) Sample placement in a strong magnetic field: Samples containing nuclei with inherent spin are positioned within a potent external magnetic field, causing their magnetic moments to align with the field's orientation. (2) Application of radiofrequency (RF) energy: A secondary magnetic field, perpendicular to the primary magnetic field, is administered to the sample at a precise frequency, inducing the nuclei's precession or rotational motion around the applied field's axis. (3) RF energy absorption: When the oscillating magnetic field's frequency matches the nucleus's resonance frequency precisely, the nucleus absorbs the energy, leading to an increase in its magnetic moment's energy state. (4) Relaxation and emission of RF energy: Subsequently, the excited nucleus returns to its original state, emitting RF energy at the absorbed frequency. This emitted energy is detected by the NMR instrument, and the resulting signal is processed to generate an NMR spectrum. This spectrum furnishes insights into the nucleus's chemical environment and

its interactions with adjacent nuclei. All product quantification was conducted using the Bruker AV 400/500 instrument, employing a water suppression sequence with NS-32, DS-4, SW-24.9934 ppm parameters using Bruker Top Spin. Multiple characterizations were performed with at least three sets of samples/materials prepared in separate batches.

Photoluminescence (PL) signals are generated when light illuminates a material, prompting electrons to move from their ground state to an excited state. As these electrons revert to their original state, they emit energy in the form of light, which is captured as a spectrum. The principle behind PL spectra revolves around the interaction of light with matter. When a material absorbs light of a specific wavelength, it energizes the electrons, causing them to ascend to higher energy levels. Upon relaxation, these excited electrons discharge surplus energy as photons of light. By gauging the intensity of this emitted light across various wavelengths, the PL spectrum is derived. This spectrum offers insights into the material's electron energy levels, facilitating the study of its electronic characteristics. Beyond elucidating electronic properties, PL spectra can also unveil structural attributes of the material. For instance, defects or impurities within the material may manifest as distinct features in the PL spectrum, aiding in their identification and analysis. PL measurements were conducted using the Horiba FluoroMax plus spectrophotometer, with a consistent excitation and emission slit width of 3 and a grating density of 1220.

Gas analysis, the Agilent GC (7890A) equipped with a molecular sieve-coated packed column and a Thermal Conductive Detector (TCD) was employed.

2.6 References

1. I. Chauhan, K. K. Patra, H. Bajpai, N. B. Mhamane, K. N. Salgaonkar and C. S. Gopinath, *Dalton Trans*, 2023, 52, 2051–2061.
2. K. N. Salgaonkar, H. Bajpai, N. B. Mhamane, N. Nalajala, I. Chauhan, K. Thakkar, K. Joshi and C. S. Gopinath, *J. Mater. Chem. A*, 2023, 11, 15168–15182.
3. I. Chauhan, H. Bajpai, B. Ray, S. K. Kolekar, S. Datar, K. K. Patra and C. S. Gopinath, *ACS Appl. Mater. Interfaces*, 2024, 16, 26130–26141.
4. N. Nalajala, K. N. Salgaonkar, I. Chauhan, S. P. Mekala and C. S. Gopinath, *ACS Appl. Energy Mater*, 2021, 4, 13347–13360.
5. J. Yang, Y. Xiao, Q. Zhao, G. Zhang, R. Wang, G. Teng, X. Chen, M. Weng, D. He, S. Mu, Y. Lin and F. Pan, *Nano Energy*, 2019, 59, 443–452.

Chapter 3

Nanostructured Co-doped $BiVO_4$ for Efficient and Sustainable Photoelectrochemical Chlorine Evolution from Simulated Sea-Water

---

A manuscript has been published based on the work described in chapter 3 and the details are: Chauhan, I.; Patra, K. K.; Bajpai, H.; Mhamane, N. B.; Salgaonkar, K. N.; Gopinath, C. S. Nanostructured Co-Doped $BiVO_4$ for Efficient and Sustainable Photoelectrochemical Chlorine Evolution from Simulated Sea-Water. *Dalton Trans.* **2023**, 52, 2051–2061.

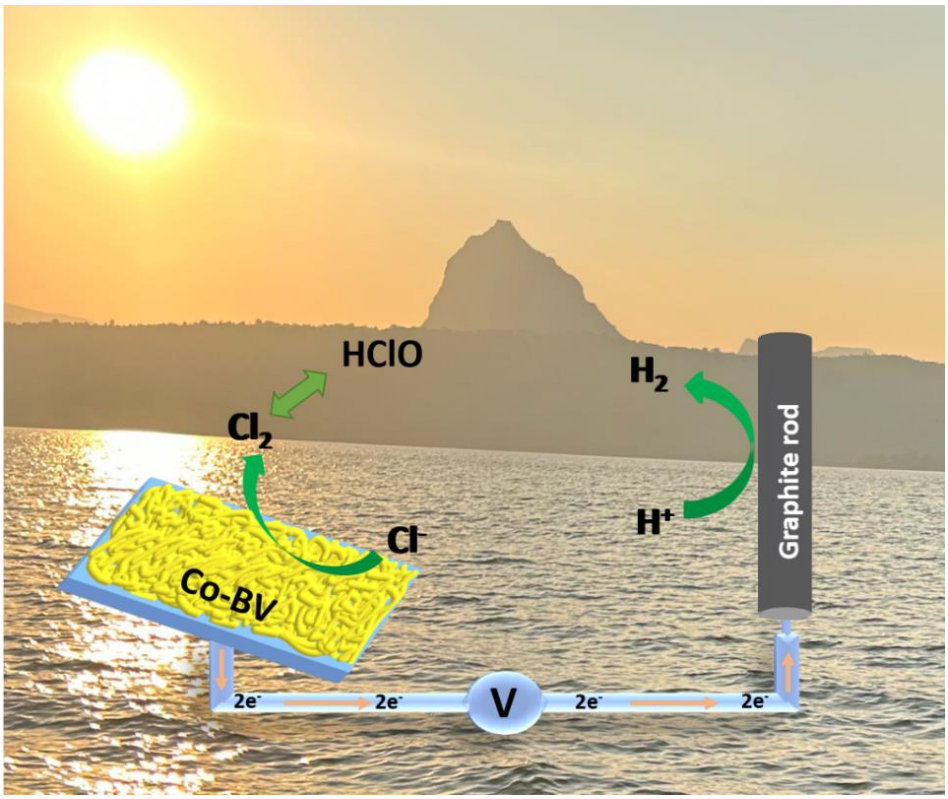

Nanostructured Co-doped $BiVO_4$ for Efficient and Sustainable Photoelectrochemical Chlorine Evolution from Simulated Sea-Water

3.1 Introduction

To address the depletion of fossil fuels, rapid anthropogenic climate change, and severe environmental issues, there is a widening push to use renewable resources, such as solar and wind energy, carbon free chemicals (such as hydrogen), for sustainable and efficient fuel/energy production**.** Solar energy is one of the most appealing methods, and can be used to obtain hydrogen from water via photoelectrochemical (PEC) or photocatalytic water-splitting**.**[1] In PEC water splitting, a semiconductor functions as a photoanode to oxidize water to oxygen up on exposure to sunlight, and H_2 is produced on the cathodic side.[2] This could be an effective and environmentally sustainable way to generate pure hydrogen in a clean, cost-effective, and carbon-free approach. However, a key technical and economically challenging aspect in PEC water splitting is the kinetically-sluggish four electron water oxidation process, and the same is the bottleneck for cost effective green hydrogen production. Moreover, the O_2 produced in this process has limited economic value (Equation 3.1), but produced at a high cost/energy, such as employing high operating potential, noble metal catalyst.[3-6] Replacing the water oxidation with any suitable electro oxidant could potentially reduce the hydrogen production cost along with a value-added oxidized product, and opens up a new pathway to produce two value added chemicals concurrently.

$$2H_2O \rightarrow O_2 + 4H^+ + 4e^-, E^0 = 1.23\ V_{RHE} \qquad (3.1)$$

In contrast to four electron OER, CER is a two electron process, and CER is also kinetically more favorable than OER. However, the theoretical potential required for OER and CER is 1.23 and 1.36 V, respectively. Considering the overpotentials required for both OER and CER, which predominantly depends on the material, a catalyst that works at low (high) overpotential for CER (OER) is a key requirement to demonstrate the selective CER activity with sea/salt water, while fully avoiding OER. It is also well known that there are many advantages of operating at low overpotential, which is, in fact, a pre-requisite for sustainability. Additionally, it is known that CER causes an acidic pH because it dissolves chlorine in water, forming hypochlorous acid (HClO). For sustained activity, the catalyst must be able to survive these circumstances. Since sea water is an abundant source of aqueous NaCl (0.6 M or 3.5 wt %) as electrolyte, few attempts have been made to use sea/salt water as feed stock in PEC device to produce hydrogen and oxygen/chlorine. Moreover, the use of sea water potentially reduced the

operational cost of PEC water splitting device, which otherwise used pure water and chemicals for electrolyte solution. In addition to the above aspect, Cl_2 produced through CER is an industrially important chemical/intermediate for the production of several compounds, such as drugs, disinfectants, polymers etc. Currently, about 53 million metric tons of chlorine is annually produced worldwide, mainly through chlor-alkali process.[7] Due to the sluggish four electron kinetics of OER, if CER can be carried out at low overpotential, there is a good possibility to increase the H_2 production rate also through PEC means with non-precious metal group catalyst/metal.[8-10] (Equation 3.2)

$$H_2O + 2Cl^- \rightarrow H_2 + Cl_2, E^0 = 1.36\ V_{RHE} \qquad (3.2)$$

Very few reports are available to produce hydrogen and/or chlorine by PEC water splitting under visible light irradiation, and this fact highlights the complexity of sea-water splitting. An electrodeposited nanostructured WO_3 shows 70% Faradaic efficiency and a photocurrent of 4.5 mA/cm^2 at 1.3 V (vs RHE) with predominant Cl_2 and significant oxygen generation, while hydrogen is stored in Pd-cathode.[11] A rutile TiO_2 was also reported to be active under UV illumination for photoelectrochemical CER and exhibited 8 mA/cm^2 at relatively higher potential of 1.65 V (vs RHE) at neutral pH (pH = 7) solution.[12] An electrode consisting of nanostructured $BiVO_4/WO_3$ reached a photocurrent density of 2.5 ± 0.3 mA/cm^2 at 1.42 V (vs RHE) and shows 85% Faradaic efficiency for Cl_2 production.[13] Although the above catalysts works with high photocurrent density, either it works at high overpotential, low Faradaic efficiency, with UV light or exhibits poor stability. Hence the challenge is to produce a photoelectrocatalyst system that works for CER at low overpotential, which is also necessarily and significantly lower than that of OER, and possibly with high current density. In addition, the catalyst should absorb visible light and stable in acidic pH conditions, as chlorine dissolution makes the solution acidic and corrode the catalyst. Indeed the real challenge is to bring all the above factors in one catalyst system, to demonstrate a sustainable sea water splitting photoelectrocatalyst, under favorable operating conditions. Since OER is favorable in neutral and alkaline solution, most works reported for CER by PEC process has been carried out in acidic pH (pH< 4). $BiVO_4$ (BV) is known to be a very good light absorbing semiconductor (band gap 2.4 eV) and used as low cost material for CER due to its favorable conduction and valence band edge positions. However, BV is unstable at pH~1 and undergoes anodic dissolution due to loss of V^{5+} ion. For the present studies, we have fabricated a Co-doped $BiVO_4$ (Co-BV) photoanode, which is stable at pH ~2.3 and above, selectively produce

active chlorine by suppressing OER in the PEC system using earth abundant Co-BV. The doping of Co-ions into the $BiVO_4$ lattice decreases the charge transfer resistance, increases the lifetime of charge carriers, and enhances the CER kinetics. Moreover the role of the Co is to provide redox reaction site and acts as a co-catalyst to accelerate the CER. We observed a photocurrent of 67 μA/cm^2 at 1.1 V vs RHE with about 100 μg/cm^2 photoanode material for CER under one sun illumination for virgin BV. In-contrast, 0.05Co-BV photoanode exhibited two-time higher photocurrent density of 190 μA/cm^2 under similar reaction conditions.

3.2 Result and discussion

3.2.1 Powder X-ray diffraction (P-XRD)

Figure 1.1a shows XRD patterns of pristine BV and Co-BV thin films. The bare BV photoelectrode shows a pure monoclinic scheelite (m-s) phase structure (m-s $BiVO_4$, JCPDs-00-014-0688) with high intensity parent peak appearing at 29.4^0 corresponding to (121) facet.[14-16] No diffraction features corresponding to any cobalt oxide(s) was observed for any doping level from 0.01 to 0.5 mol % of Co; as the doping level is less than 0.5 atom %, it may be difficult to detect. The diffraction peak intensities of $BiVO_4$ decreases significantly after Co-doping in BV, and shows that Co-doping reduces the crystallinity of BV and possibly increase the defects in the lattice.[16] XRD measurements made carefully with same quantity of catalyst in thin film form, and hence the results can be compared directly. Although close packing of Co-BV particles increases, compared to BV (as shown in SEM, Figure 3.2a and b), a decrease in diffraction features intensity supports the Co-doping in the lattice of BV. Diffraction angle shifts to higher angle for all xCo-BV, compared to parent BV; Figure 3.1b exhibits an observable shift for (121) and (040) features towards higher diffraction angle compared to that of pure BV. In addition, there is a significant line broadening occurs from 0.218 for BV to 0.260 for 0.5Co-BV for (121) feature. These two observations are typical for introduction of smaller-size ion in the place of bigger ion. Final calcination involved in the synthesis step is expected to oxidize the cobalt to Co^{3+}. HR-TEM result also shows a reduction in inter-layer d-spacing of (121) and the same is explained later (Figure 3.2). This could be explained by the fact that the substitution of a larger cation (Bi^{3+}, ionic radii = 117 pm) by a smaller cation (Co^{2+}/Co^{3+} ionic radii = 79/68 pm) results in a decrease in the lattice parameter or lattice contraction. It is to be noted that although ionic radii of V^{4+}/V^{5+} and Co^{2+}/Co^{3+} (72/68 pm) are comparable, a shift in diffraction features to higher angle and lattice contraction rules out the doping of Co in V-site. Irrespective of the oxidation state of Co, very small size of Co^{3+} (compared to Bi^{3+}) is expected to generate a structural stress in the BV lattice. Moreover the

iso-valent substitution of Bi by Co-ions into the BV lattice not only modulates the crystal structure, but the electronic structure also in Co-BV system. It is to be noted that Bi have unoccupied 5f, 6d orbitals, which are also very diffused; while Co have 4p and 4d unoccupied orbitals, and they are compact in nature. In addition, cobalt vanadate could form locally in the BV crystal lattice.

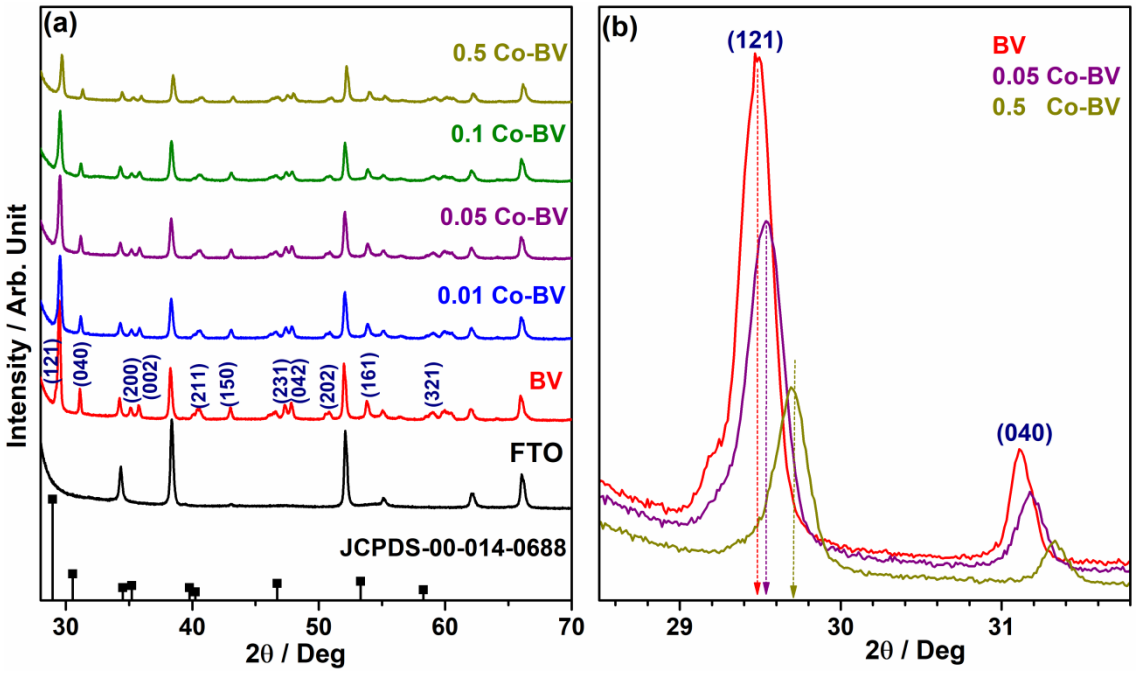

Figure 3.1 (a) XRD patterns of the pristine BV and Co-doped BV catalysts. (b) Enlarged XRD pattern of BV, 0.05 Co-BV and 0.5 Co-BV, to show the gradual shift in diffraction features to higher angle as well as line broadening.

3.2.2 Field Emission Scanning Electron Microscopy (FE-SEM) and Elemental mapping

The freshly fabricated thin films were explored for surface morphology and elemental mapping by FESEM, TEM and HRTEM and the results are shown in Figure 3.2. While the morphology of both the photoanodes (BV and 0.05 Co-BV) are similar, the particle was found to be close-packed in the Co-BV case than the parent BV. The pristine $BiVO_4$ shows a relatively low-density nanoparticles, whereas Co-BV revealed a uniform and high-density coating of porous nano structural units with particle size range observed to be 90-150 nm (Figure 3.3).

It is also reiterated that except adding required Co-precursor to Bi-precursor solution in the preparation by SILAR, no other changes in preparation procedure were adopted for Co-BV. It is interesting to observe that no morphological change due to Co-doping was observed, but rather a density change. The average thickness of the film was found to be 1±0.05 µm (Figure 3.4).

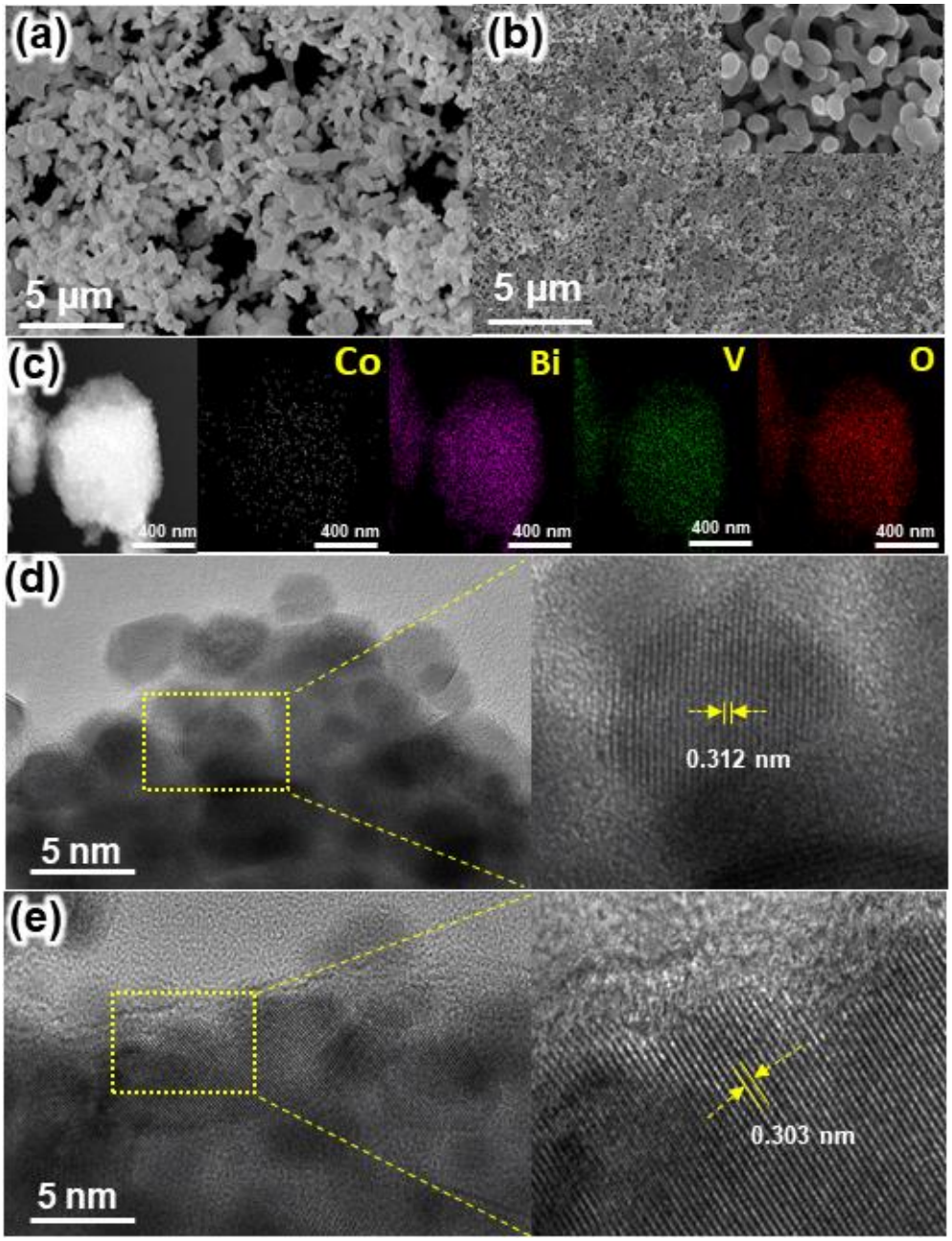

Figure 3.2 Microstructural and elemental mapping characterization of BV and 0.05 Co-BV. FESEM images of (a) pristine $BiVO_4$ and (b) 0.05 Co-BV films are shown. Inset in panel b shows the enlarged view of 0.05Co-BV and demonstrates the similarity of morphology as that of BV. (c) EDS for elemental mapping of 0.05 Co-BV, and it demonstrates an uniform doping of Co throughout the film. HRTEM images recorded are shown for (d) BV, and (e) 0.05Co-BV. A significant decrease in the lattice parameter for (121) facet is observed after Co-doping.

The elemental mapping of Co, Bi, V and O was explored by EDS for 0.05 Co-BV and the results are shown in Figure 3.2c. While Bi, V and O shows an equally dense distribution over the entire particle surface, a uniform and scarce distribution of Co-ions in the 0.05 Co-BV was observed. This also directly supports the uniform doping of Co-ions in the $BiVO_4$ lattice.

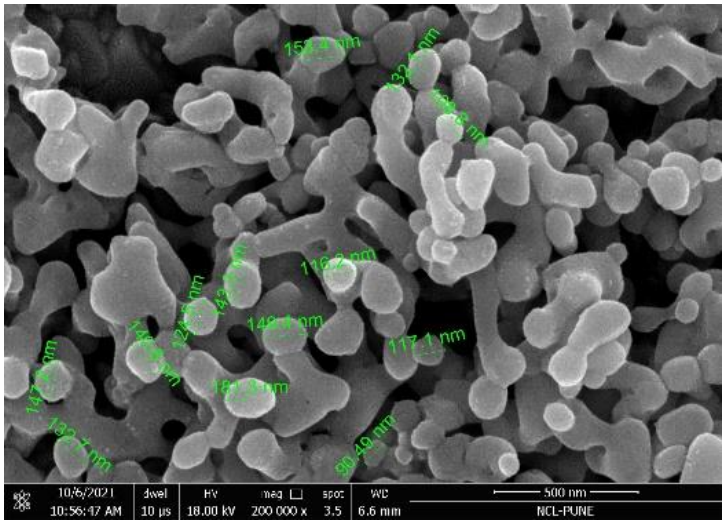

Figure 3.3 FESEM image of 0.05 Co-BV.

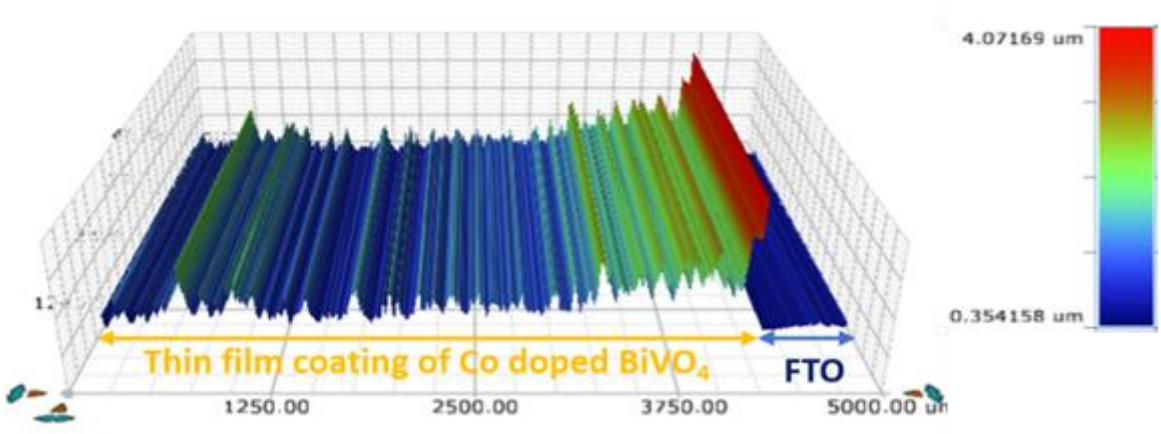

Figure 3.4 The surface roughness and thickness of 0.05 Co-BV.

3.2.3 High-Resolution Transmission Electron Microscopy (HR-TEM)

TEM and HRTEM images recorded for BV and 0.05 Co-BV are shown in Figure 3.2d and e, respectively. Figure 3.2d shows a lattice spacing of 0.312 nm, and this corresponds to (121) facet of $BiVO_4$, which is in good agreement with the reported values.[17-18] However we observed a decrease in the d_{121} lattice spacing of 0.303-0.306 nm for 0.05 Co-BV, which is attributed to the lattice contraction.[19] This is in good correspondence with the XRD results observed in Fig. 3.1. No isolated cobalt oxide was detected in the TEM images, supporting a near complete doping.

3.2.4 X-ray Photoelectron Spectroscopy (XPS)

XPS studies of BV and 0.05 Co-BV catalysts were carried out to understand the electronic structure aspects, such as oxidation states and the effect of Co-doping. Figure 3.5a, b and c shows the XPS core level spectra of Bi 4f, V 2p, and O 1s, respectively. XPS survey spectra shows the presence of Bi 4f, V 2p, O 1s, and C 1s peaks for both BV and 0.05 Co-BV.

Absence of any Co features, especially Co 2p in the 775-810 eV BE range for 0.05 Co-BV is not surprising. This is attributed to the very small amount (0.05 atom %) of doped Co-ions; further, as shown in Figure 3.2c (EDS results), Co is distributed uniformly throughout the bulk and hence the amount of Co present on the surface could be below detection limit. Nonetheless, Co-content measured by ICP method (Table 3.1) is in accordance to the nominal input Co-content.

Table 3.1 Co-content determined from ICP analysis

Photo-electrocatalyst	ICP (mol %)
0.01 Co-BV	0.011
0.05 Co-BV	0.052
0.1 Co-BV	0.104
0.5 Co-BV	0.486

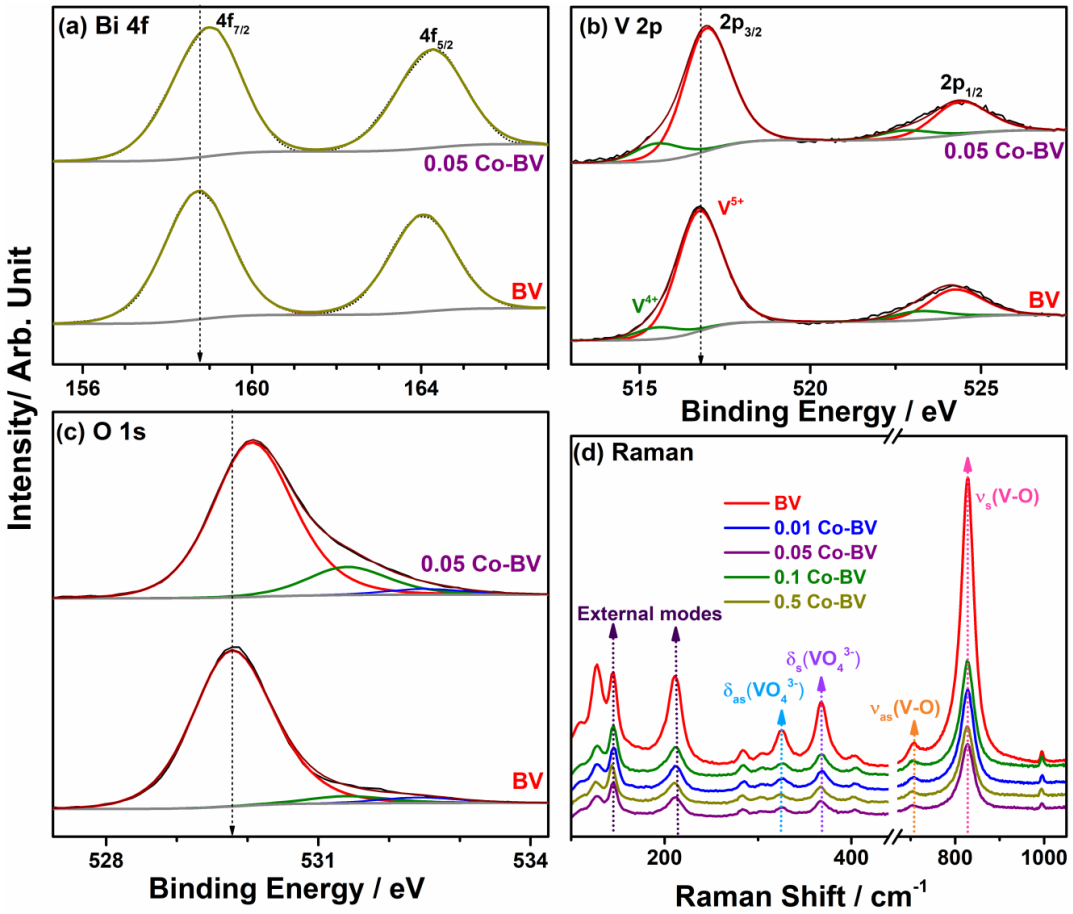

Figure 3.5 (a) Bi 4f, (b) V 2p, and (c) O 1s core level spectra of BV and 0.05 Co-BV catalysts. (d) Raman spectra of BV and xCo-BV catalysts.

Bi 4f spectrum of BV (Figure 3.5a) shows a characteristic spin-orbit doublet of Bi $4f_{7/2}$ and $4f_{5/2}$ core levels at 158.8 and 164.1 eV, respectively (Δ = 5.35 eV), which corresponds to Bi^{3+} in BV. Similarly, 0.05 Co-BV shows Bi $4f_{7/2}$ and $4f_{5/2}$ core levels appearing at 159.1 and 164.35 eV, respectively. The shift in BE by 0.3 eV towards higher BE side observed for 0.05 Co-BV, compared to un-doped BV, shows the change in the surface electronic structure of 0.05 Co-BV after Co-doping.[20] V 2p core level spectrum for BV and 0.05 Co-BV (Figure 3.5b) broadens towards the lower BE side, suggesting the presence of more than one type of vanadium species. For BV, V $2p_{3/2}$ core level shows an intense V^{5+} and a small shoulder peak, due to V^{4+}, at 516.8 and 515.4 eV, respectively.[21] However, for 0.05Co-BV, V^{4+} shows a marginal shift in core level towards the higher BE by 0.25 eV. Along with a shift in BE, an observable increase in V^{4+} intensity is also observed.[21-22] Figure 3.5c shows O 1s spectra for BV and 0.05 Co-BV. O 1s for BV show three peaks corresponding to lattice oxygen, oxygen near defect sites (5 %), and adsorbed species such as -OH, H_2O, at BE of 529.8, 531.5, and 532.5 eV, respectively. For 0.05 Co-BV, an increase in the oxygen defect sites (14 %) and a shift in the lattice oxygen peak are observed. V^{4+} species and oxygen vacancies increased with Co-doping demonstrating a change in electronic structure, which is expected to influence the catalytic activity/process.

3.2.5 Raman spectroscopy

Raman spectroscopy is sensitive towards finding any structural stress factors, such as doping, oxygen vacancy in the crystalline materials, and it also complements the XRD results. In view of this, Raman spectra of all catalysts were recorded and the results are shown in Figure 3.5d. The peak at 145 and 212 cm^{-1} correspond to the external vibration of BV. The peaks at 325 and 368 cm^{-1} were attributed to V–O asymmetric vibration ($\delta_{as}(VO_4^{3-})$, and V–O bending vibration of the VO_4^{3-} tetrahedron unit ($\delta_s(VO_4^{3-})$, respectively.[23] Raman features observed at 708 cm^{-1} (the asymmetric V–O stretching mode ν_{as}(V–O)), and 828 cm^{-1} (the symmetric V–O stretching mode ν_s(V–O)), matches very well to that of m-s $BiVO_4$ phase. It was observed that crystallinity of all Co-BV catalysts decreased significantly, with respect to BV; indeed, this is a clear indication that Co-doping occurs in the BV lattice and this possibly induces oxygen vacancies too. A significant increase in full-width at half maximum (FWHM) of BV (36.9 cm^{-1}) to 0.05 Co-BV (38.3 cm^{-1}) of 828 cm^{-1} (ν_s(V–O)) feature supports the above conclusion. While the XRD data exhibited shift in diffraction features due to Co-doping in BV lattice, the crystalline phase of BV remains observed to be intact. However, a weak deformation of the VO_4 tetrahedron resulted in a decline in the intensity of the symmetric V-O stretching mode that was inversely correlated with the doped ion content. This weak deformation is

attributed to the metal ion substitution at the Bi-site in the BV lattice. Earlier reports on the effect of Fe-doped $BiVO_4$[24] and Ce-doped $BiVO_4$,[25] are in good agreement with the present findings.

3.2.6 UV-Vis absorption and Time correlated single photon counting (TCSPC) decay

Optical absorption of the photoelectrode materials was studied by UV-Vis absorption spectroscopy and the results are shown in Figure 3.6a. Onset of light absorption is observed in the visible region from 530 nm, which is in good correspondence with the earlier reports.[18,19] Although structural changes were observed for Co-doping in BV in the earlier characterization studies, no significant change in the light absorption intensity was observed. Indeed the bright yellow color remains observed to be the same for bare and Co-BV photoelectrodes. The photoinduced electron-hole pair recombination of semiconductor could be explained by photoluminescence spectra (Figure 3.7) recorded with 510 nm excitation wavelength. The PL shows a broad emission peak between 530 and 650 nm for all the photoelectrodes. This indicates that there is no change in the bandgap of BV and 0.05 Co-BV due to doping and no states are created in the forbidden band-gap region. However, 0.05 Co-BV photoelectrode exhibited a lower emission peak intensity with respect to BV photoelectrode, which suggests that the recombination of electron and hole is likely minimized and a greater number of holes could be transferred to the photoelectrode surface to activate the chloride oxidation reaction. However, other dopant concentrations lead to an increment in emission peak intensity, which correspondence to the lower and higher mol % of Co species act as a recombination site and they are suppressing the CER reaction.

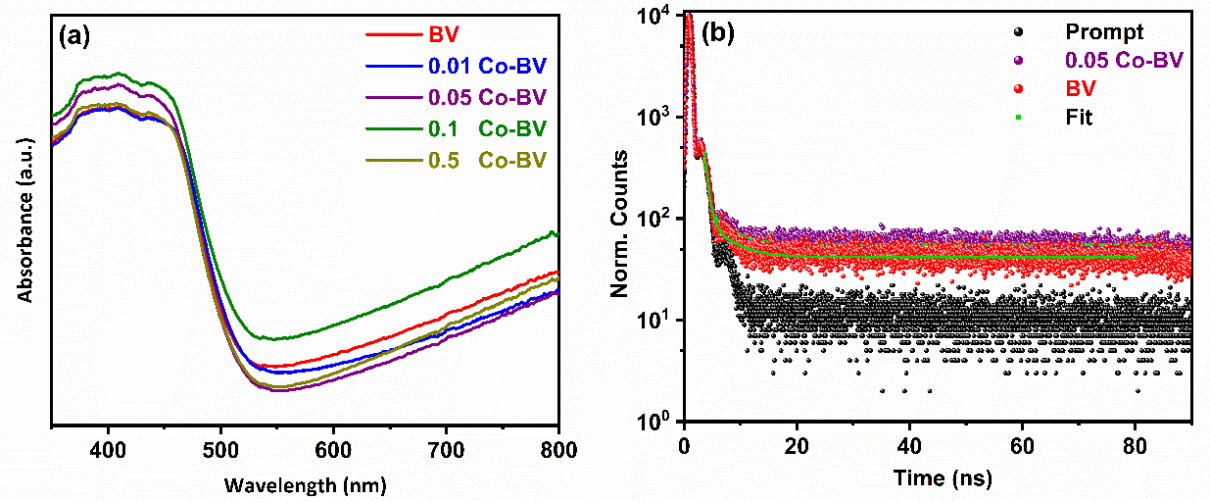

Figure 3.6 (a) UV-visible absorption spectra of xCo-BV photoanodes. (b) TCSPC decay of the BV and 0.05 Co-BV. (λ_{ex} = 377 nm, λ_{mon} = 555 nm).

To confirm the Co doping in BV and consequent increase in charge carrier lifetime, the TCSPC decay measurements were performed and the results are shown in Figure 3.6b. The charge carrier lifetime decay for both samples was fitted using a second-order exponential function. The PL lifetime of the electron and hole pair recombination for 0.05 Co-BV electrode was 4.05 ns, while the BV electrode was 3.61 ns (Table 2).[26-27]

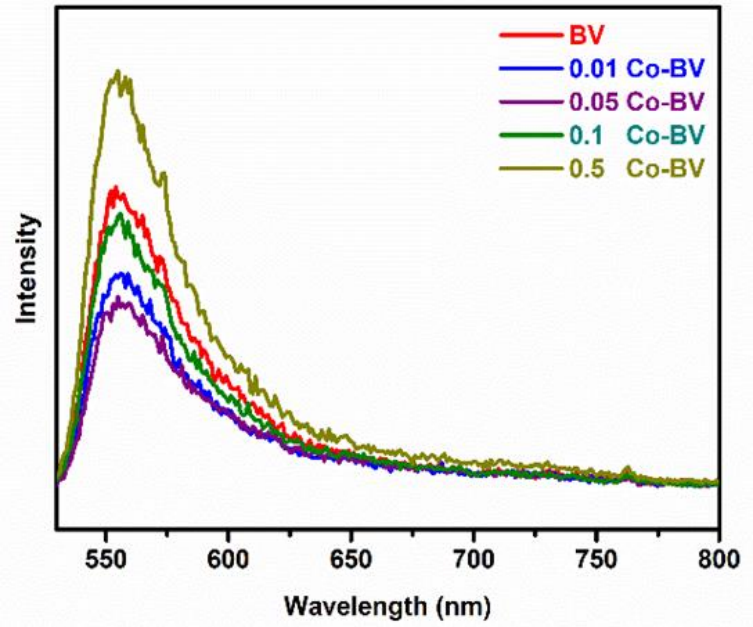

Figure 3.7 The photoluminescence spectra of the pristine BV and all doped sample.

Table 3. Lifetime decay of BV and 0.05 Co-BV.

Catalyst	**Lifetime (ns)**	**CHISQ (χ^2) values**
BV	τ_1 = 0.248; τ_2 = 3.61	1.12
0.05 Co-BV	τ_1 = 0.59; τ_2 = 4.05	1.15

These results confirm that the lifetime of the electron/hole pair of doped Co-BV is significantly higher than that of the pure BV phase, suggesting that Co doping was decreases the electron and hole recombination.

3.2.7 Photoelectrochemical Characterization

CER performance in NaCl solution was evaluated, with pH adjusted to 2.3, in a single compartment photo electrolysis cell (shown in Figure 3.8a) for BV and xCo-BV, and the results obtained are shown in Figure 3.8b-c. The PEC performance of all photoelectrodes was characterized in a three-electrode system with BV or 0.05 Co-BV as working electrode. Photoanode was illuminated from the backside through the FTO plate. The overall redox

process taking place at both the electrodes is shown in Figure 3.8a. Under illumination the photogenerated holes diffuse to the surface of BV and oxidize chloride ions to chlorine over the catalyst surface. Electrons generated from the oxidation step are transferred through the external circuit and reduced H_2O to produce hydrogen on graphite electrode. Although chlorine is sparingly soluble in water (up to 0.7 wt %), it reacts instantly with water and forms HClO.

Preliminary CER study was conducted with BV and all compositions of Co-BV (Figure 3.8b). Figure 3.8b shows photocurrent density vs potential (*j*-V) graph for BV and for all xCo-BV in 1 M NaCl under one sun irradiation condition. Under dark conditions negligible anodic current density (j ~ 1 µA/cm^2) was observed with all the photoanodes. Upon one sun illumination, BV shows a photo current density of 67 µA/cm^2 at 1.1 V vs RHE. In contrast, 0.05 Co-BV photoanode (1 µm thick film), under the same measurement conditions, show a photocurrent density of 147 µA/cm^2 at 1.1 V vs RHE. More than two fold enhancement in photocurrent density after Co-doping is attributed to the enhanced charge separation induced by efficient diffusion of holes onto the catalyst surface as well as its utilization for chloride oxidation. A marginal shift in CER onset potential was observed around 0.9 V RHE for all the anodes. While 0.05 Co-BV shows the lowest onset potential (0.88 V RHE), 0.1 and 0.01 Co-BV shows a marginally higher onset potential (0.96 V RHE). However, the CER current density increases significantly with 0.05 Co-BV as compared to BV photoanode with increase in applied potential. This result demonstrates that after Co-doping, Co-BV behaves as a multifunctional material; Co-BV absorbs visible light as well as an efficient co-catalyst and accelerates the CER activity. Furthermore, different amount of Co was doped in BV and they were evaluated for CER performance. The lowest amount of Co doping (0.01 mol%) shows 34 µA/cm^2, while 0.05 mol% Co-doped system shows the highest current density of 147 µA/cm^2 at 1.1 V vs RHE. However, with further increase in Co amount to 0.1 and 0.5 mol% the photocurrent density decreases to 56 and 75 µA/cm^2 respectively, which underscores the importance of optimum amount of Co-doping towards the best CER performance. 0.05 Co-BV was found to show the best performance; in view of this, 0.05 Co-BV was evaluated in detail and compared with parent BV. Results in Figure 3.8b indicates that excess oxygen vacancies generated by Co-doping could behave as a recombination site for electron-hole pairs and decrease the photocurrent density by hindering the CER performance.[28]

To study the instant photocurrent response of photoanode, the chronoamperometry (*j*-*t*) analysis was performed at an applied potential of 1.2 V vs. RHE under chopped one sun

illumination conditions, and the results are shown in Figure 3.8c. The photocurrent increases instantly under illumination condition and then drops to zero in the dark condition, underscoring the current generation is exclusively due to light absorption. 0.05 Co-BV shows the highest photo response as compared to BV and other xCo-BV, and it is in accordance with the LSV results (Figure 3.8b). High photocurrent response indicates the charge transfer resistance across the working electrode and electrolyte should be lower for 0.05 Co-BV, compared to BV. This was evaluated by electrochemical impedance spectroscopy (EIS) and the results are shown in Figure 3.8d. In fact, it is evident from Nyquist plot shown in Figure 3.8d that Co doping in $BiVO_4$ lattice decreases the charge transfer resistance and increases the charge mobility.[29] The relatively low charge transfer resistance in 0.05 Co-BV can be realized from the smaller radius of the arc.[30-31]

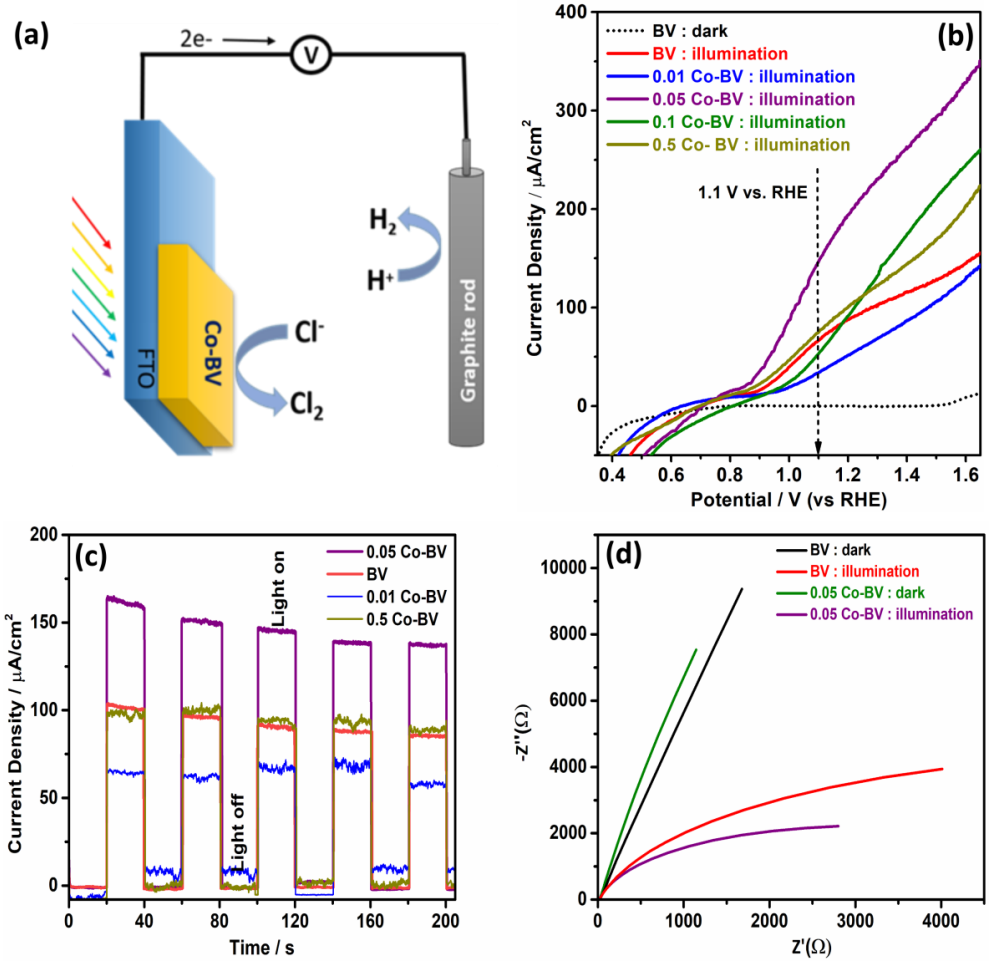

Figure 3.8 Photoelectrochemical performance of pristine BV and xCo-BV. (a) Schematic to show the PEC setup and the overall reaction scheme of seawater splitting. (b) Linear sweep voltammetry in 1 M NaCl solution at pH = 2.3. (c) Transient photocurrent response at 1.2 V vs. RHE. (d) Nyquist plot (or EIS) recorded under dark and illumination conditions.

Furthermore, we studied the effect of chloride ion concentration on CER performance and the results are shown in Figure 3.9a. We observed a gradual increase in oxidation current on increasing the chloride concentration from 1 M to 4 M. Further increase in chloride concentration to 5 M decreased the CER current density significantly, possibly due to decrease in ion mobility into the electrolyte solution. For product quantification, the chronoamperometric (*j*-*t*) analysis was performed with the best active 0.05Co-BV photoelectrode, at different applied potentials (1.1 V, 1.3 V and 1.5 V vs. RHE) under one sun illumination for 2 h, and the results are shown in (Figure 3.9b). The amount of dissolved active chlorine was measured by spectrophotometry using *N*,*N*-diethyl-p-phenylenediamine sulfate (DPD) reagents.[32] Prior to the chronoamperometric evaluation, the electrolytic system was pre-purged with N_2 gas for 1 h. After 2 h of constant photoelectrochemical run, the collected anodic products were analyzed to determine the Faradaic efficiency of the process (Figure 3.9b). For the 0.05 Co-BV electrode the maximum Faradaic efficiency of 92 ± 3 % was observed at 1.1 V vs RHE. However, the Faradaic efficiency decreases to 82 ± 3 % at 1.3 V vs. RHE. It is worth to note that at lower potential the CER current is quite stable in the *j*-t plot; however, higher applied potential leads to a significant decrease in CER activity due to increasing competition from the OER. As a result of low chlorine formation, Faradaic efficiency of only 12 ± 5 % was observed at 1.5 V vs RHE. The increase in current density at higher applied potential is predominantly due to the contribution from OER (Figure 3.10).

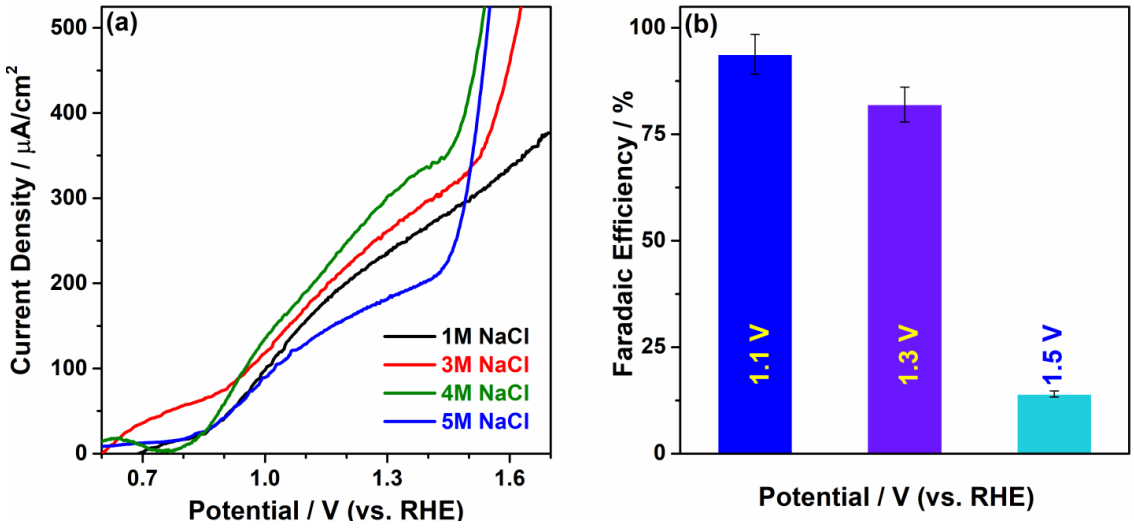

Figure 3.9 (a) Linear sweep voltammetry in different molar NaCl concentration with 0.05 Co-BV, pH 2.3 solution. (b) Faradaic efficiency at three different applied potentials for Cl_2 production. Error bars represent the standard deviation for three different measurements.

Indeed, this result demonstrates that Co-BV system overcome the aspect of lowering the overpotential of chlorine evolution and successfully avoided OER at potential below 1.3 V vs RHE. It is well-known that there are advantages of carrying out the reaction at low applied bias, which is of commercial interest. A comparison of few sea-water splitting PEC CER results reported in the literature is shown in Table 3.3. This comparison underscores the highest Faradaic efficiency (95 %) observed at the lowest applied potential, but at pH = 5.8 with CoO_x-loaded $BiVO_4/WO_3$ catalyst reported by Okunaka et al.[33] and present result is comparable to the above for operating voltage and FE; however, the activity was demonstrated only for 1000 s. Other catalysts are operating at either high applied voltage (>1.1 V), high pH or in UV. However, it is also to be mentioned the lowest current density observed with the present catalyst. Nonetheless, it is to be noted that the amount of catalyst employed in the present work is a mere 100 µg/cm^2, and a fair comparison could not be made with other results currently, as the catalyst content is not available. However, the present work is superior in terms of operating at low pH and demonstrated longer sustainability (shown in next section), which are necessarily required for application aspects.

Table 3.3 Catalysts reported for chlorine and hydrogen evolution

Catalyst	Voltage (vs RHE)	FE (%)	j_{CER} mA/cm^2	Operating pH	Illumination conditions	Stability Demo.	Ref.
$BiVO_4/WO_3$	1.42	85	2.5	1	1 sun	2 h	13
WO_3	1.3	70	4.5	6.5	1 sun	20 h	11
Rutile TiO_2	1.65	NA	8	7	λ =385 nm	NA	12
CoO_x-loaded $BiVO_4/WO_3$	1.0	95	1	5.8	1 sun with L-42 filter	0.27 h	33
Co-BV	**1.1**	**92**	**0.19**	**2.3**	**1 sun**	**20 h**	**Present work**

3.2.8 Sustainability Aspects of 0.05 Co-BV Catalyst

The stability test of the 0.05 Co-BV was performed in 4 M NaCl solution, acidified to pH = 2.3 at a constant applied potential of 1.1 V vs RHE, and the result is shown as red trace in Figure 3.11. We observed a nearly steady photocurrent up to 10 h and indicating the high photo stability of the catalyst. Although the applied potential employed is unfavorable (or not

sufficient) for OER, still some possibility of oxygen formation could hinder the rate of CER.[11] Therefore we observed a slight decrease in the photocurrent with respect to time. Furthermore, the photoanode used in the first experiment is used again for another 10 h, and the result is compared with freshly prepared electrolyte (green line). First and second 10 h experiments exhibited the similar *j*-t behavior, and the observed difference is within the experimental error limit. In fact, the continuous formation of HOCl is expected to decrease the pH significantly, especially during longer duration of reaction, and decrease the stability due to dissolution of Bi^{3+} ion from the catalyst.[13] However, the doping of Co-ion in the $BiVO_4$ lattice seems to prevent the photo corrosion in acidic environment. Continuous flow from a larger reservoir of NaCl solution to the electrochemical set up could be useful to prevent the corrosion caused by decrease in pH during long duration electrolysis.

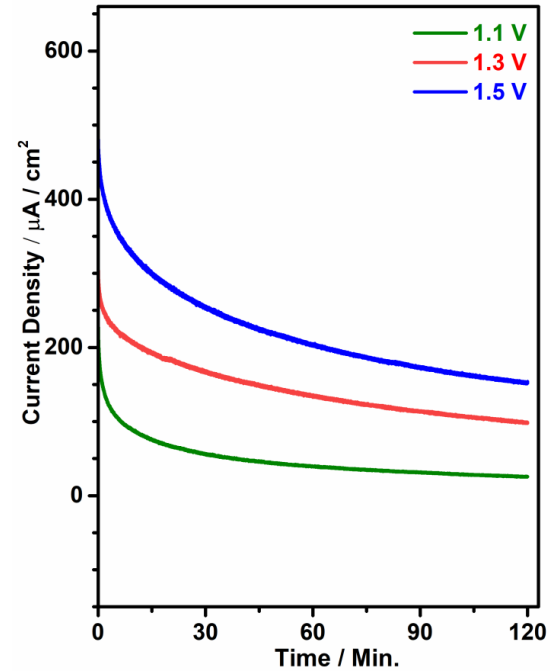

Figure 3.10 The chronoamperometry data of the 0.05 Co-BV at 1.1, 1.3 and 1.5 V Vs. RHE.

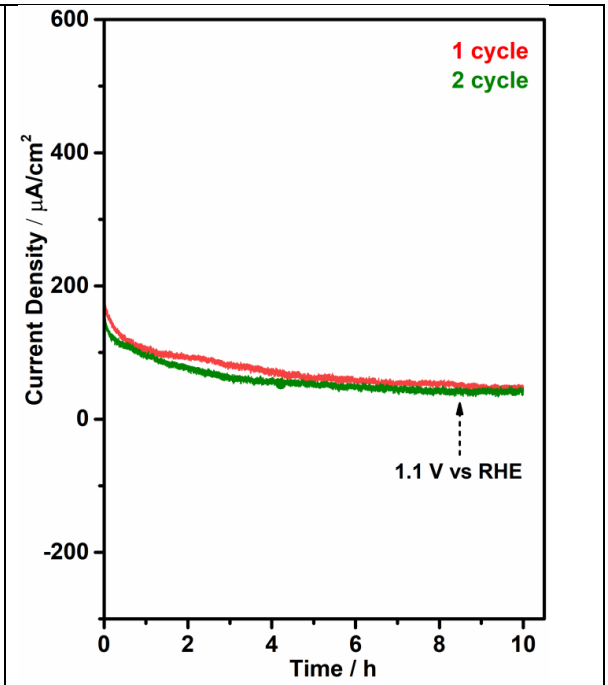

Figure 3.11 Photoelectrochemical stability test for CER of 0.05 Co-BV at 1.1 V RHE under one sun illumination.

3.3 Conclusion

In summary, a simple and scalable SILAR process has been demonstrated to fabricate the earth abundant Co doped BV photoanode to produce Cl_2 and H_2 concurrently. A high photocurrent to chlorine Faradic efficiency of 92 % was observed for the best active 0.05 Co-BV composition with 190 µA/cm^2 at 1.1 V vs. RHE. Co doping in BV facilitate the efficient

utilization of holes and enhances the CER performance. This work demonstrates that molecule/ions having lower oxidation potential than water can reduce the overall cell potential and provides an efficient way for economical solar H_2 production. Simultaneously, use of a HER catalyst in the counter electrode position could further improve the kinetics of overall CER and HER reaction.

The sun-driven photoelectrochemical seawater splitting devices could be particularly useful in isolated areas with plenty of sunshine and seawater, and where only small amounts of hypochlorite or chlorine are required for various critical disinfection tasks, like drinking water purification. For actual sea-water separation, Co-BV evaluation is also worthwhile. It would be worthwhile to investigate the possibility of using the same preparation procedure for scale-up to huge area panels.

3.4 References

(1) (a) C. S. Gopinath and N. Nalajala, *J. Mater. Chem. A* **2021**, *9*, 1353–1371. (b) S. Raja Ambal, K. Sivaranjani and C. S. Gopinath, *J. Chem. Sci.*, **2015**, *127*, 33-47.

(2) S. He, Y. Meng, Q. Wu, J. Yang, S. Huang, X. Li, S. Tong, T. Asefa and M. Wu, **2018**, *10* , 19367–19374.

(3) M. R. Shaner, H. A. Atwater, N. S. Lewis and E. W. McFarland, *Energy Environ. Sci.* **2016**, *9*, 2354–2371.

(4) K. Sayama, *ACS Energy Lett.* **2018**, *3*, 1093–1101.

(5) R. K. B. Karlsson and A. Cornell, *Chem. Rev.* **2016**, *116*, 2982–3028.

(6) C. C. L. McCrory, S. Jung, J. C. Peters and T. F. Jaramillo, *J. Am. Chem. Soc.* **2013**, *135*, 16977–16987.

(7) K. Maeda and K. Domen, *J. Phys. Chem. Lett.* **2010**, *1* , 2655–2661.

(8) N. Melián-Martel, J. J. Sadhwani and S. Ovidio Pérez Báez, *Desalination* **2011**, *281*, 35–41.

(9) M. E. Porter and C. Van Der Linde, *J. Econ. Perspect.* **1995**, *9*, 97–118.

(10) L. D. Schulte, J. R. Fitzpatrick, R. R. Salazar, B. S. Schake, B. T. Martinez, L. D. Schultr, J. R. Fitzpatrick, R. R. Salazarl, B. S. Schake and B. T. Martinezl, **2006**, *30*, 1833–1847.

(11) M. Jadwiszczak, K. Jakubow-Piotrowska, P. Kedzierzawski, K. Bienkowski and J. Augustynski, *Adv. Energy Mater.* **2020**, *10*, 1903213.

(12) T. R. Harris-Lee, Y. Zhang, C. R. Bowen, P. J. Fletcher, Y. Zhao, Z. Guo, J. W. F. Innocent, S. A. L. Johnson and F. Marken, *Electrocatal.* **2021**, *12*, 65–77.

(13) A. M. Rassoolkhani, W. Cheng, J. Lee, A. McKee, J. Koonce, J. Coffel, A. H. Ghanim, G. A. Aurand, C. Soo Kim, W. Ik Park, H. Jung and S. Mubeen, *Commun. Chem.* **2019**, *2:57*, p.1–7.

(14) B. Zhang, H. Zhang, Z. Wang, X. Zhang, X. Qin, Y. Dai, Y. Liu, P. Wang, Y. Li and

B. Huang, *Appl. Catal. B Environ.* **2017**, *211*, 258–265.

(15) B. Zhou, X. Zhao, H. Liu, J. Qu and C. P. Huang, *Appl. Catal. B Environ.* **2010**, *99*, 214–221.

(16) Y. Geng, P. Zhang, N. Li and Z. Sun, *J. Alloys Compd.* **2015**, *651*, 744–748.

(17) Z. Zhu, B. X. Jiang, R. J. Wu, C. L. Huang and Y. Chang, *Catal.* **2022**, *12*, 750.

(18) S. S. Mali, G. R. Park, H. Kim, H. H. Kim, J. V. Patil and C. K. Hong, *Nanoscale Adv.* **2019**, *1*, 799–806.

(19) W. Fang, L. Fu, A. Qin, Y. Lin and R. Xv, *ACS Appl. Energy Mater.* **2022**. 5, 6313-6326.

(20) T. D. Nguyen, Q. T. P. Bui, T. B. Le, T. M. Altahtamouni, K. B. Vu, D. V. N. Vo, N. T. H. Le, T. D. Luu, S. S. Hong and K. T. Lim, *RSC Adv.* **2019**, *9*, 23526–23534.

(21) (a) K. Sivaranjani, A. Verma and C S. Gopinath, *ACS Catal.* **2014**, *4*, 2844-2853.

(22) D. Kong, J. Qi, D. Liu, X. Zhang, L. Pan J. Zou, *Trans. Tianjin Univ.* **2019**, *25*, 340–347.

(23) J. M. Wu, Y. Chen, L. Pan, P. Wang, Y. Cui, D. C. Kong, L. Wang, X. Zhang and J. J. Zou, *Appl. Catal. B Environ.* **2018**, *221*, 187–195.

(24) C. Regmi, Y. K. Kshetri, T. H. Kim, R. P. Pandey and S. W. Lee, *Mol. Catal.* **2017**, *432*, 220–231.

(25) S. Gu, W. Li, F. Wang, H. Li H. Zhou, *Catal. Sci. Technol.* **2016**, *6* , 1870–1881.

(26) J. K. Kim, X. Shi, M. J. Jeong, J. Park, H. S. Han, S. H. Kim, Y. Guo, T. F. Heinz, S. Fan, C. L. Lee, J. H. Park and X. Zheng, *Adv. Energy Mater.* **2018**, *8*, 1701765.

(27) O. F. Lopes, K. T. G. Carvalho, W. Avansi, D. M. B. Milori and C. Ribeiro, *RSC Adv.* **2018**, *8*, 10889–10897.

(28) W. Yao, H. Iwai and J. Ye, *Dalton Trans.* **2008**, 1426–1430.

(29) G. Liu, F. Li, Y. Zhu, J. Li, L. Sun, *RSC Adv.* **2020**, *10*, 28523–28526.

(30) J. Kim, S. Byun, A. J. Smith, J. Yu and J. Huang, *J. Phys. Chem. Lett.* **2013**, *4* , 1227–1232.

(31) K. Sivaranjani, S. Agarkar, S. B. Ogale and C. S. Gopinath, *J. Phys. Chem. C* **2012**, 116, 2581-2587.

(32) Y. Huang, Y. Yu, Y. Xin, N. Meng, Y. Yu and B. Zhang, *Sci. China Mater.*, **2017**, *60*, 193–207.

(33) S. Okunaka, Y. Miseki and K. Sayama, *Catal. Sci. Tech.*, **2021**, *11*, 5467-5471.

Chapter 4

Electrocatalytic Glycerol Conversion: A Low-Voltage Pathway to Efficient Carbon-Negative Green Hydrogen and Value-Added Chemical Production

Chapter 4 has been published and the details are:

Chauhan, I.; Bajpai, H.; Ray, B.; Kolekar, S. K.; Datar, S.; Patra, K. K.; and Gopinath, C. S.; Electrocatalytic Glycerol Conversion: A Low-Voltage Pathway to Efficient Carbon-Negative Green Hydrogen and Value-Added Chemical Production. *ACS Appl. Mater. Interfaces* 2024, ***16***, 26130-26141.

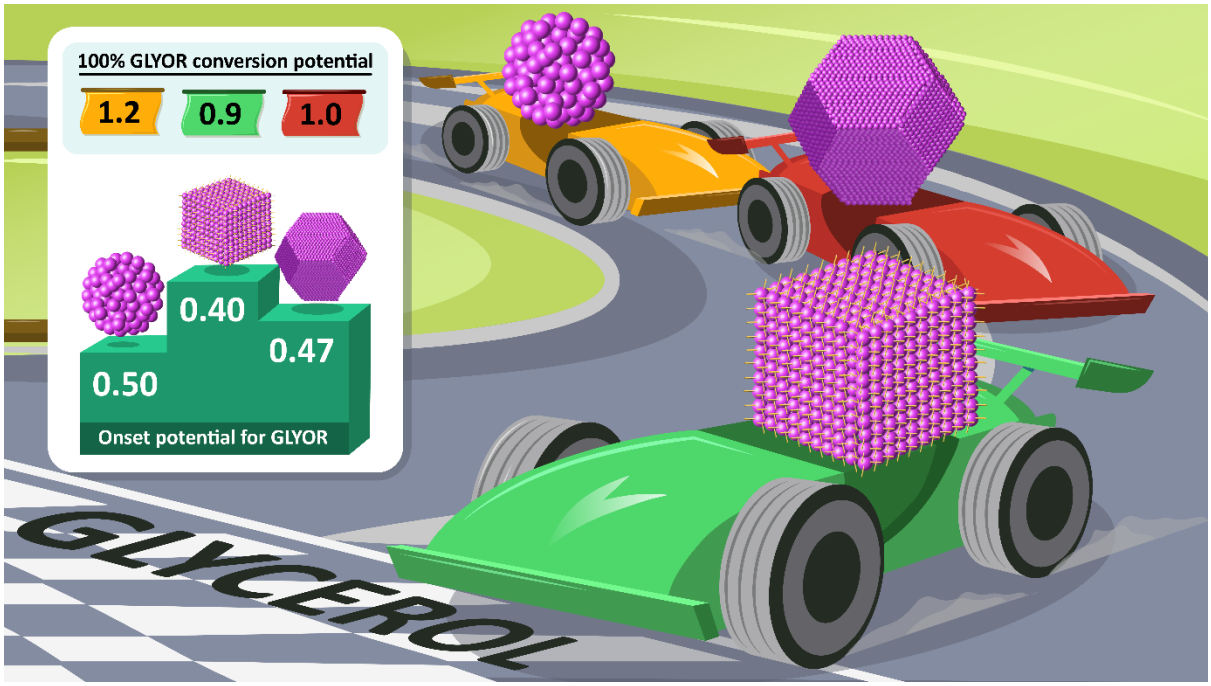

Electrocatalytic Glycerol Conversion: A Low-Voltage Pathway to Efficient Carbon-Negative Green Hydrogen and Value-Added Chemical Production

4.1 Introduction

Biomass up-gradation has the potential to produce sustainable biofuels and carbon-based chemicals.[1] Glycerol is an abundantly available by-product of bio-diesel and can be converted to value added chemicals.[2-5] A large production of biodiesel generates surplus glycerol and subsequent reduction in price is unavoidable.[6] In fact, US DoE recommended glycerol as one of the top ten building blocks for the production of value added chemicals.[7] A survey suggested that the global glycerol production could reach 4 billion litres per year by 2026.[8] Among various approaches, glycerol oxidation reaction (GLYOR) with suitable electrocatalyst provides a green route to synthesize value added chemicals with the simultaneous evolution of hydrogen at the counter electrode.[1] Oxidation products such as glycolic and glyceric acids are important chemicals used in pharmaceuticals, cosmetics and polymer industry.[9-11] Glyceric acid is also present in human body and crucial for glycolytic pathway, and acts as a reagent for variety of biological activities. Thus, electrochemical methods for up-scaling biomass could be intriguing approach to convert low-cost glycerol to valuable chemicals.

Over the years, the electro oxidation reaction of glycerol has been studied with various metal catalysts such as Au, Pd and Pt.[12] In alkaline solution, Au catalysed the partial oxidation of glycerol to glycolic acid efficiently, via C–C bond cleavage.[13,14] Significant progress has been made in nano structuring the Au catalyst to increase the product selectivity and conversion rate. Oh et. al demonstrated the effect of nano structuring of Au catalyst and the local KOH concentration on GLYOR.[13] Many earth-abundant catalyst has been reported for GLYOR with high formic acid selectivity.[15,16] Cobalt oxide nanorod decorated on reduced graphene oxide (RGO) is effective for GLYOR with high formate selectivity; however, high selectivity of formic acid production required longer reaction time and high potential.[17] Other strategy, such as, defect creation on electrocatalyst surface is also suggested to boost the GLYOR performance.[18] Xia et al. reported a vacancy rich NiCrO catalyst, which exhibit GLYOR performance with 99% conversion and 98% selectivity for formic acid production.[19] Furthermore, most of the GLYOR is favorable in alkaline solution, since adsorbed OH^- ion is often a key intermediate for the electrocatlytic biomass oxidation reaction.[14] Interestingly, Li et al. has suggested a manganese oxide catalyst which exhibits high stability for hydrogen production coupled with GLYOR in acidic electrolyte.[20] The use of acidic electrolyte could

reduce the energy consumption. Moreover, engineering the microenvironment at the catalyst-electrolyte interface could steer the GLYOR performance. For example, cation effect via electric double layer forming at the interface boost the product selectivity by interacting with the glycerol oxidation intermediates.[21]

Wang et.al suggested that Au catalysed the formation of glyceric acid and glycolic acid by supressing the C–C bond cleavage.[14] Although Au catalysed the conversion of glycerol to glycolic acid with high selectivity, the potential required to achieve 70% conversion is ~1 V vs RHE.[13] However, achieving high glycerol conversion and high selectivity of desired product at low overpotential is paramount to evaluate the electrocatalyst efficiency, and essential to the feasibility as well as the scalability of the process. Moreover, high applied potential may also lead to the production of CO_2, which should be avoided at all cost. Therefore, finding new and suitable electrocatalyst with high intrinsic activity at low applied potential is a key parameter to improve the efficiency of the GLYOR process. Earlier observation suggested that C–C bond dissociation energy is higher on Pd surface as compared to Au and Pt; as a result glyceric acid is more commonly produced on Pd.[12] Nonetheless, it is also shown that the selectivity and rate of reaction of electrochemical process is strongly dependent on nanocrystal morphology and local electrolyte environment.[22] Especially Pd nanocubes (Pd-NC) with (100) facets exhibit more favourable catalytic performance than truncated octahedra (Pd-TO), with (111) and (100) facets, and polycrystalline Pd.[23-25] Terekhina et. al investigated the effect of different crystallographic facets present on different morphologies (namely, octahedral (~34 nm), rhombic dodecahedral (~69 nm) and cubic (~75 nm)) on the performance of GLYOR and observed that Pd-Octahedral exhibited the highest selectivity for C3 products, particularly glycerate. However, the glycerol conversion (≤21 %) and selectivity are very low at room temperature.[26] Hence rational design of Pd catalyst with high intrinsic activity is required to improve the GLYOR activity, possibly with smaller particle size.

Green H_2 is a vital and carbon-less clean energy feedstock, and often referred as future fuel. However, currently ~95% of H_2 is produced from steam reforming of methane which is unsustainable and non-eco-friendly, due to associated emission of 10-12 kg of CO_2 for every kg of H_2 produced.[27] Although water electrolysis is an efficient technology to produce clean and green H_2, the high voltage requirement in commercial electrolyzer increase the cost of hydrogen (US$ 5-12/kg) and limits its large scale applications.[28] The sluggish kinetics of oxygen evolution reaction (OER) at high applied potential mainly consumed the input

electricity and results in increased electrolyzer potential.[29] Various organic and inorganic oxidation strategies have been employed to decouple the OER. [30-32] Suitable coupling of organic oxidation with different cathodic reaction can further maximize the energy efficiency of the overall electrochemical process. Although biomass components, such as, furfural,[33] 5-hydroxymethyl furfural (HMF)[25,34,35] and glucose[36] are employed to decouple OER, glycerol and glucose are particularly appealing because of their low cost and availability. Moreover, furfural and HMF are valuable platform chemicals, and derived from glucose oxidation and follows complex reaction pathways.[37,38] Therefore, replacing anodic water oxidation with GLYOR in alkaline electrolyzer could be a more effective approach to improve the energy efficiency of H_2 production and generates value added chemicals and fuels on both sides of the cell. If value added products are also produced through non-fossil resources, green H_2 produced through GLYOR should be considered as carbon-negative.

Herein, we demonstrate that the selectivity and conversion of glycerol could be improved by controlling the facets of Pd nanocrystals. We synthesized various morphologies of Pd NPs (Pd-NC (nanocube), Pd-TO (truncated octahedron), and spherical and polycrystalline (Pd-PC)) and investigated the GLYOR activity and made an attempt to correlate them. The Pd-NC electrocatalyst deposited on a Ni foam achieved impressive 85 % glycerol conversion with 42 % glyceric acid selectivity at an exceptionally low applied potential (0.6 V vs RHE) in 0.1 M glycerol and 1 M KOH in 4 h. In contrast, Pd-TO and Pd-PC exhibited 70-75% glycerol conversion under similar conditions; this demonstrates the high intrinsic activity for GLYOR associated with Pd-NC than that of Pd-TO and/or Pd-PC catalyst. At 1.2 V vs RHE, Pd-NC catalyst exhibits near 100% conversion along with 40% glycolic and 34% formic acid selectivity. The morphology and active sites of the Pd-NC was controlled by the structure directing chloride and bromide anion. Further, it has been demonstrated that how the selection of capping agent (KCl and KBr) in Pd-NC synthesis is crucial for achieving better GLYOR performance. Moreover, when the Pd-NC electrocatalyst was assembled in to a two-electrode alkaline electrolyzer, the input electricity consumed is only 3.7 kWh per m^3 of H_2, in contrast to the requirement of ≥5 kWh per m^3 of H_2 with commercial electrolyzers at a current density of 100 mA/cm^2. Finally, we have also leveraged a facet dependent concept to maximize GLYOR activity and concurrent carbon-negative H_2 production by designing different morphologies of Pd NPs with distinct structural characteristics.

4.2 Results and Discussion

4.2.1 Structural and Morphological analysis

Different morphology of Pd nano structures were synthesized with favourable reducing and structure directing agent with K_2PdCl_4 as Pd precursor shown in experimental section Figure 2.2.[41] The experimental section contains a full description of the synthesis process. Please take note that, unless otherwise specified, Pd-NC stated in the paper refers to Pd-NC synthesised with KCl as a capping agent. Using TEM, HRTEM, and SEM, the Pd nanocrystals' morphology and structure were initially described. The HRTEM pictures of the Pd nanoparticles (NC, TO, and PC) with the selected area electron diffraction (SAED) pattern as they were synthesised are displayed in Figure 4.1. The Pd-NC nanoparticles, which range in size from 8 to 10 nm, are seen in Figure 4.1a. The HRTEM images of Pd-NC nanoparticles synthesized using KBr as capping agent is included in Figure 4.2 for the comparison. The measured d-spacing is found to be 0.19 nm and it corresponds to the interplanar spacing of (200) facet of face centered cubic (*fcc*) lattice (Figure 4.1b).[41] The corresponding SAED patterns of Figure 4.1b is shown in Figure 4.1c represent that the Pd-NC was a single nano crystal with (200) facets. Figure 4.1d shows the TEM image of Pd-TO nanoparticles with a uniform TO morphology with 7-10 nm particle size range. The lattice d-spacing of Pd-TO is 0.22 nm and it corresponds to the (111) facets of Pd (Figure 4.1e). The corresponding SAED pattern was recorded and shown in Figure 4.1f, which represents that the Pd-TO was a single nano crystal. Pd-TO exhibits (111) as the dominant facet, along with (200) facet too. Figure 4.1g shows the TEM image of Pd-PC nanoparticles with uniform spherical particles of 3-5 nm size. HRTEM image of Pd-PC is shown in Figure 4.1h and the corresponding SAED pattern (Figure 4.1i) represent the polycrystalline nature of the NPs due to presence of various facets, including (110), (111), and (100). All the Pd nanostructures were drop cast on a NF and used for electrochemical measurements. SEM images shows a uniform coating of Pd on NF (Figure 4.3).

4.2.2 Electrochemical Glycerol oxidation performance

Figure 4.4a shows the LSV plots of various morphologies of Pd nanostructure with different geometric current density. For water electrolysis (in the absence of glycerol), Pd-NC anode drive the OER and exhibited a significantly high onset potential at 1.5 V. In the presence of glycerol, the catalytic onset of GLYOR decreases dramatically to the low potential with all the three morphologies of Pd catalyst anode. Notably, Pd-NC shows the highest current density in the entire potential range, than the other two morphologies. The catalytic current

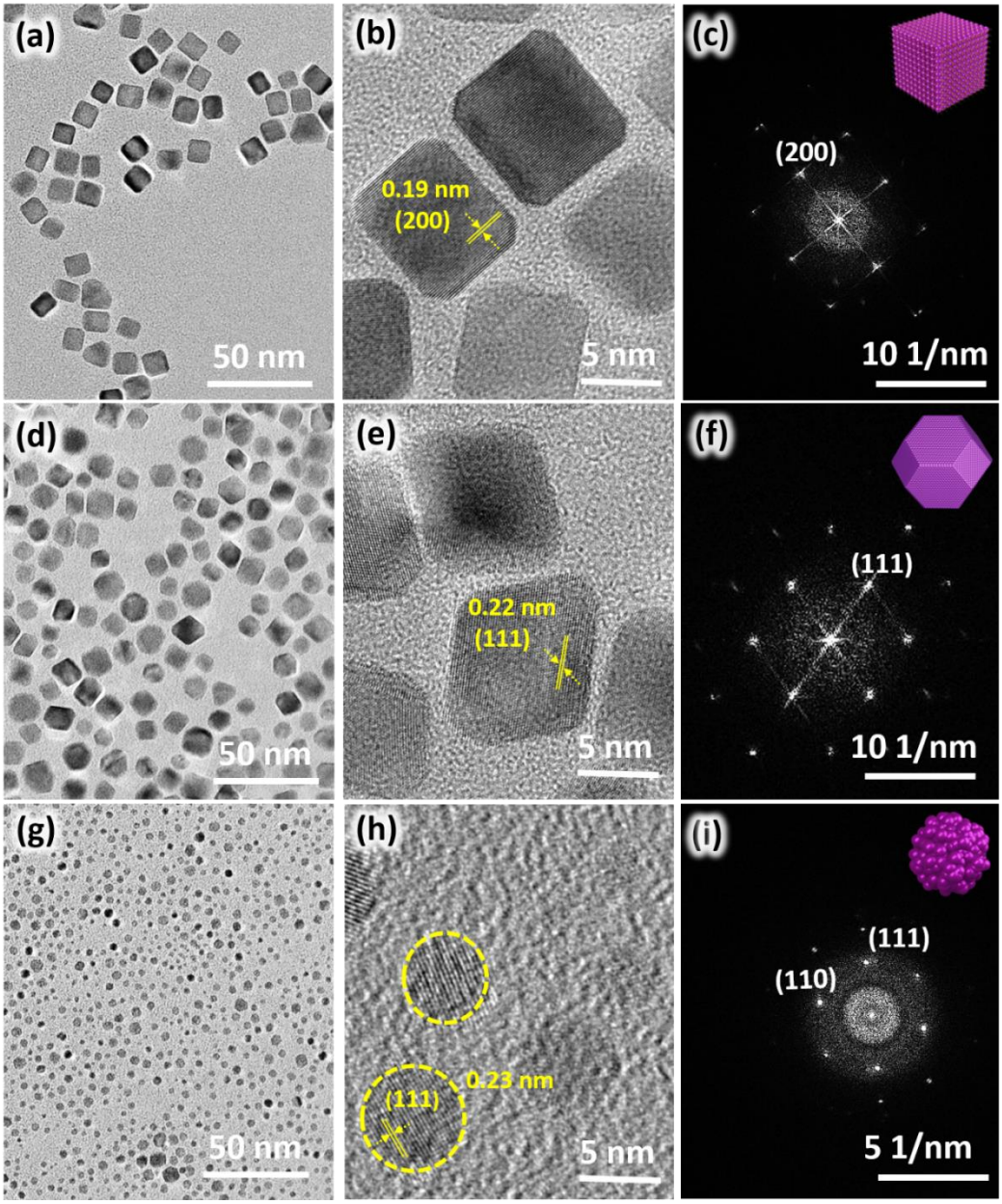

Figure 4.1 Figure (a, d and g) TEM images of homogenously dispersed as-prepared Pd-NC, Pd-TO and Pd-PC, and corresponding high resolution TEM image of Pd nanoparticles are given in b, e and h. Figure (c, f and i) displays selected-area-electron diffraction (SAED) patterns of an individual Pd-NC, Pd-TO and Pd-PC.

density of 100 (250) mA/cm^2 was achieved at low potential of 0.85 (1.22) V vs RHE; to the best of our knowledge, this is the best GLYOR geometric current density reported for Pd-based and any electrocatalyst. In contrast, Pd-PC exhibit lower GLYOR current density among all three morphologies of Pd. Critically, Pd-NC shows the lowest onset potential at 0.40 V, while Pd-TO and Pd-PC exhibit an onset at 0.47 and 0.50 V vs RHE for GLYOR, respectively.

Furthermore, the choice of the capping agent during Pd-NC synthesis also influences the GLYOR performance.

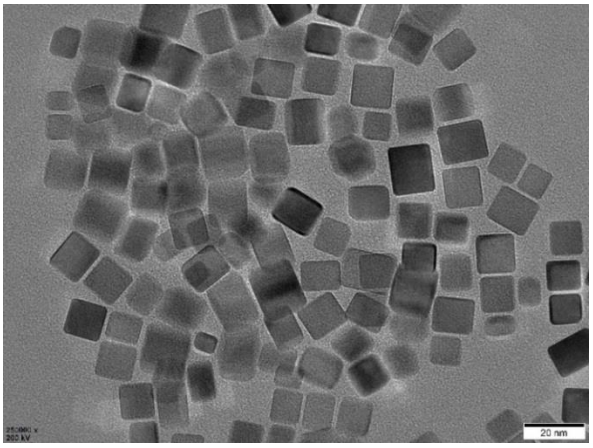

Figure 4.2 HRTEM images of highly dispersed Pd-NC with KBr capping agent which is similar to Pd-NC (KCl) and the average particle size 7-10 nm.

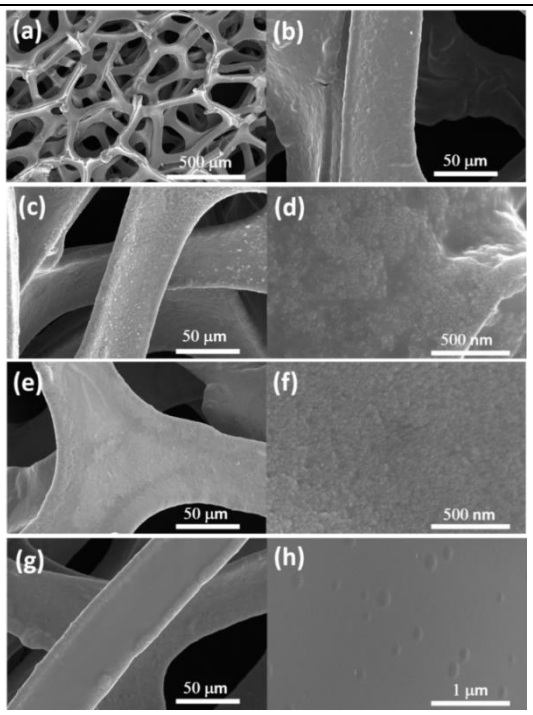

Figure 4.3 FESEM image of Pd loaded Ni foam electrode. **(a-b)** Typical images of the bare Ni foam. **(c-d)** Pd-NC/NF, **(e-f)** Pd-TO/NF, and **(g-h)** Pd-PC/NF.

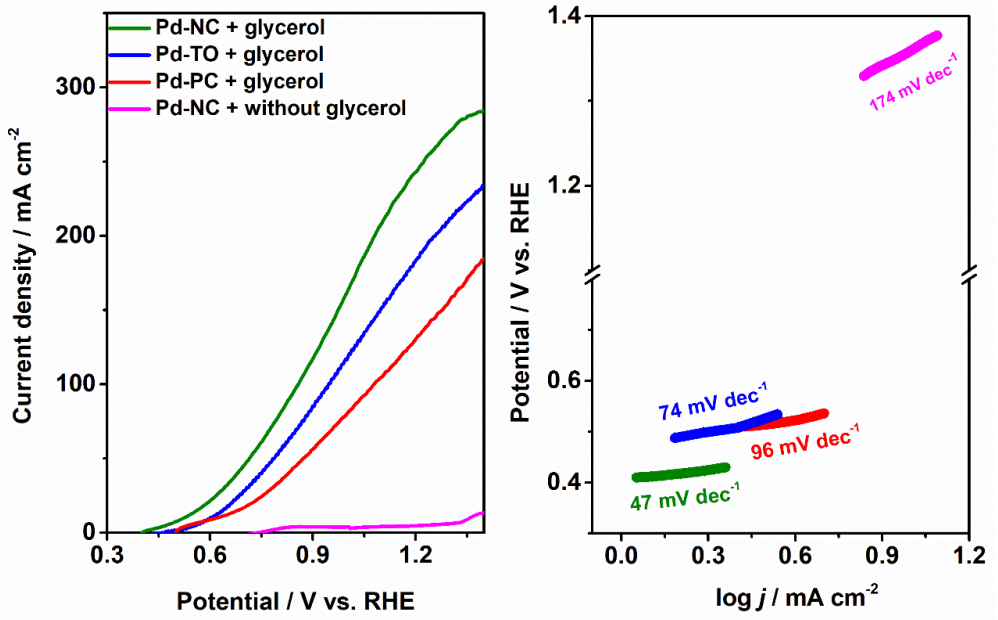

Figure 4.4 (a) Linear sweep voltammogram of various morphology of Pd in 1 M KOH with and without 0.1 M glycerol (scan rate, 5 mV s^{-1}). (b) Tafel slope given for the measurements shown in panel (a).

4.2.3 Effect of capping agent in the synthesis of Pd-NC

A detailed discussion about the role of capping agent on GLYOR performance has been given in Figures 4.5. Pd-NC was synthesized with two different counter halides, namely Cl and Br, and employed for GLYOR performances. Removal of binder and capping agent to obtain clean metal surface is crucial for any catalytic application. Particularly in Pd-NC synthesis, the nature of counter anion in structure directing agent (KCl and KBr) and amount of binder (PVP) influence the structural and electronic properties of nano cubes surface. The adsorption of halide on the Pd-NC surface follows the order $F^- < Cl^- < Br^- < I^-$. Therefore, the extent of poisoning on Pd surface was found to be in the order I− > Br− > Cl− > F−.[1] Since Br− is a strong binding agent, compared to Cl^- ion, and the removal of Br^- from Pd-NC surface is relatively difficult. As a result, Pd-NC synthesized with KBr exhibited poor GLYOR activity. Moreover, our earlier observation shows that the binding of I− is even more strong than the Br− and exhibited very poor catalytic activity.

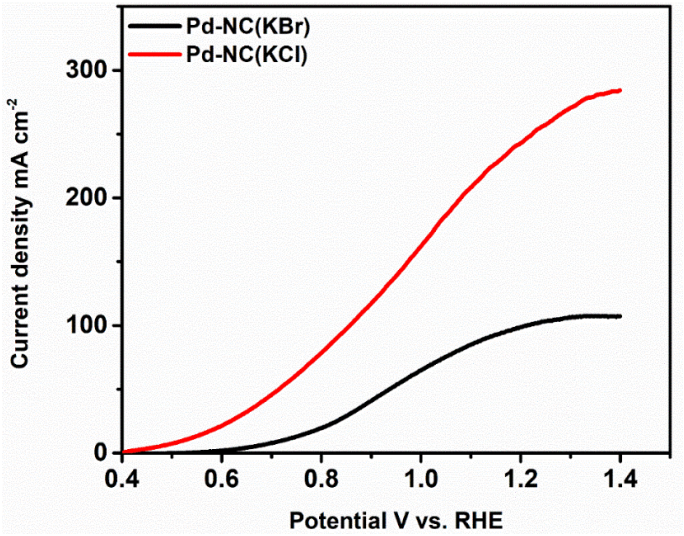

Figure: 4.5 LSV graph of Pd-NC with different capping agent in 1 M KOH + 0.1 M glycerol (scan rate, 5 mV s^{-1}).

4.2.4 X-ray photoelectron spectroscopy and X-ray Valance band spectroscopy

Different morphologies of Pd exhibit almost similar Pd 3d core level spectra (Figure 4.6a, c - 4.7a, b). XPS analysis was performed to understand the oxidation state of Pd in Pd-NC synthesized with KCl and KBr. Figure 4.6a shows the Pd 3d core-level spectrum of Pd-NC synthesized with KBr along with the spin−orbit doublet states of 3d (3d5/2 and 3d3/2). Figure 4.6b shows the Br- present in the surface of Pd atom. The Pd 3d5/2 spin state can be deconvoluted into two peaks. The core level feature appearing at binding energies (BE) of

335.3 and 336.1 ± 0.1 eV are assigned to the metallic Pd and Pd^{2+} at surface defect sites, such as edges and corners. Same features for oxidation level of Pd were observed with Pd-NC with KCl (Figure 4.6c). The Pd 3d5/2 peak at 337.8 eV is ascribed to Pd^{4+}. Although Cl^- is a weak binding ligand still we observed the Cl 2p features in the XPS spectra (Figure 4.6d). The relative % of Pd^{4+} species was 4.7% in Pd-NC synthesized with KCl as compared to 12% in Pd-NC synthesized with KBr. The bromide ion is known to have a largely diffused 4p orbital which results in facile charge transfer from Pd to Br. Therefore, the Pd-NC synthesized with KBr is relatively less metallic in nature as compared to KCl capping agent.

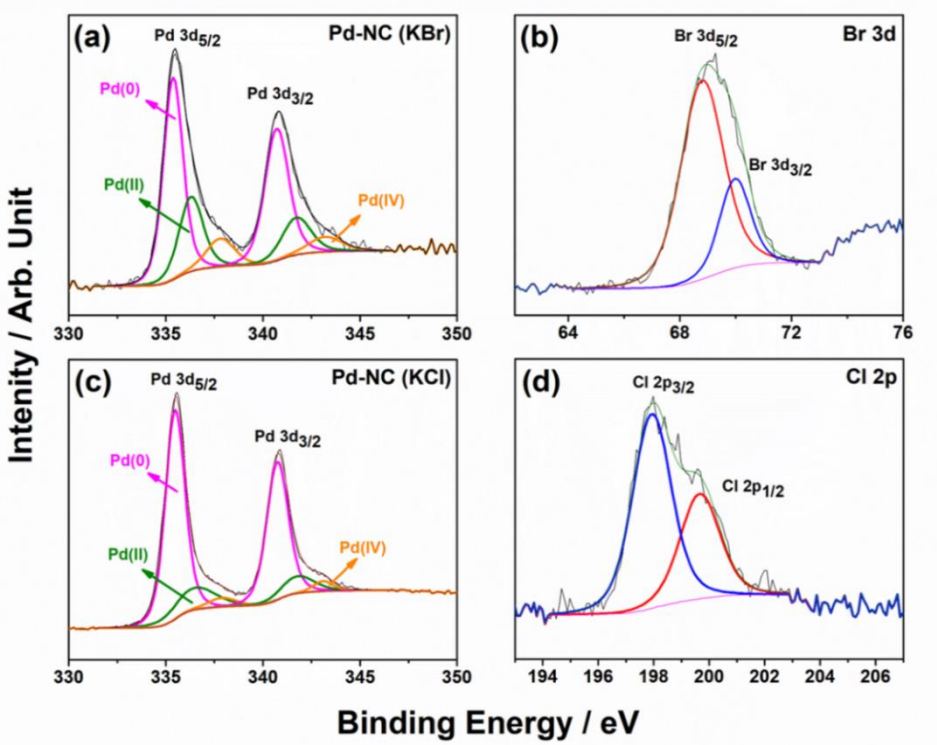

Figure 4.6 XPS core level spectra recorded for (top panels, a-b) Pd-NC with KBr, and (bottom panels, c-d) Pd-NC with KCl. Pd 3d, Cl 2p and Br 3d core level spectra are shown.

However, X-ray valence band spectra (XVB) in Figure 4.7c shows a characteristic change. Interestingly, Pd-NC shows a distinct onset of VB at Fermi level (E_F = 0 eV), compared to all other morphologies, truly representing metallic surface. Compared to Pd-NC, VB onset of Pd-TO is shifted by 0.3 eV to the higher BE. In general, VB feature appearing at low energy corresponds to higher activity. Pd-PC shows ultra-low intensity below 2 eV, indicating a non-metallic behaviour, which is worth exploring further. This could be a reason for a relatively low activity observed with Pd-PC. These observations signify the enhanced catalytic activity associated with Pd-NC, and attributed to its unique electronic structure.

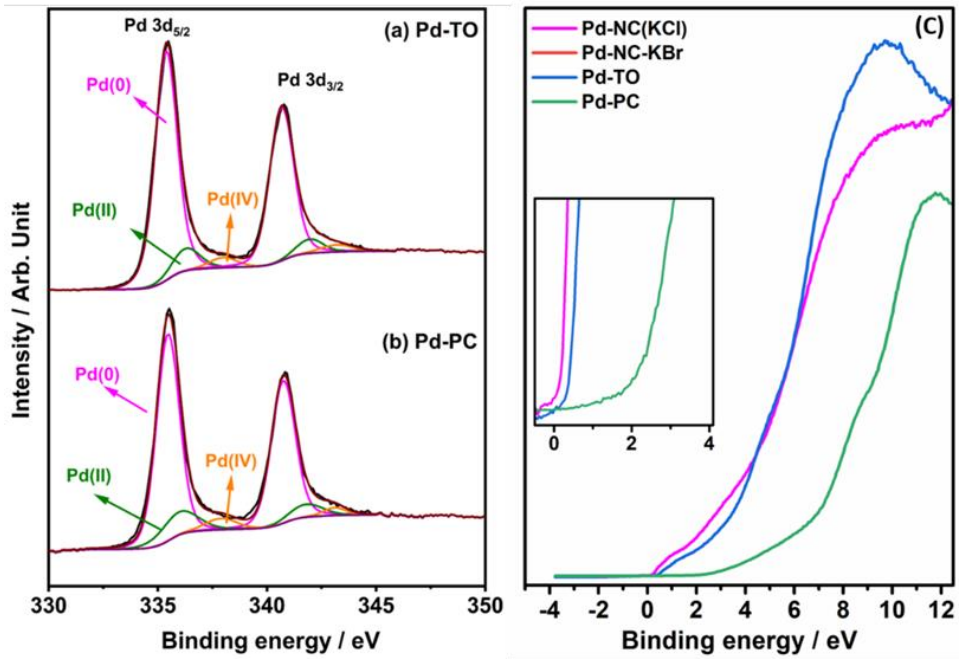

Figure 4.7 Pd 3d core level spectra recorded for (a) Pd-TO and (b) Pd-NC. (c) X-ray valence band spectra recorded for all three morphologies of Pd and a clear shift in the onset of valence band could be seen.

4.2.5 Effect of glycerol concentration

Using Pd-NC as a function of glycerol concentration, LSV analysis was carried out to investigate the impact of glycerol concentration on GLYOR (Figure 4.8). Using a scan rate of 5 mV s^{-1}, LSV was observed in the potential range of 0.3 to 1.3 V versus RHE. The peak in LSV of GLYOR is caused by the oxidation of glycerol that has been chemisorbed on the Pd surface. The concentration of glycerol increased from 0.05 to 0.2 M, causing a rise in GLYOR current density. But when the glycerol concentration was between 0.5 and 1 M, there was no discernible change in the peak current density. Moreover, it is worth to mention that the onset potential of GLYOR was shifted to lower potential, when the glycerol concentration was kept at 0.05 to 0.2 M. However, the onset potential remains same at 0.5 and 1 M glycerol. This indicates that an optimum surface concentration of glycerol is required for oxidation. However, for the entire set of GLYOR experiments, 0.1 M glycerol concentration was chosen for a fair comparison with reported literature.

The Tafel plot generated from the LSV data was used to examine the reaction kinetics (Figure 4.4b). Pd-NC electrode was found to have the lowest Tafel slope (47 mV/dec), followed by Pd-TO (74 mV/dec) and Pd-PC (96 mV/dec). Furthermore, the Tafel slope of 174 mV/dec for OER indicates that, in the absence of glycerol, Pd-NC exhibited substantially slower kinetics at the anode.

The GLYOR rate is high on all six (200) facets of the NC, as indicated by the low Tafel slope value with Pd-NC electrode.

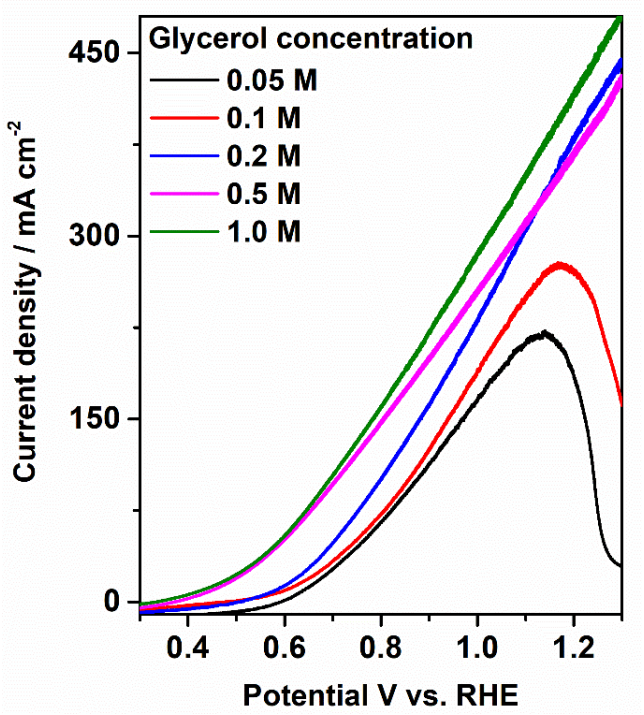

Figure 4.8 LSV profiles of GLYOR on Pd-NC as a function of Glycerol concentration with 1 M KOH at a scan rate of 5 mV s^{-1}.

The GLYOR activity was evaluated with different morphologies of Pd NPs by chronoamperometry measurement as a function of applied potential in 1 M KOH and 0.1 M glycerol. All the chronoamperometry measurements were carried out for 4 h. The chronoamperometry results revealed that the current density of the GLYOR continuously declined as the reaction proceeds with time, and it reached to as low as 3-5 mA/cm^2 at the end of the reaction in 4 h (Figure 4.9). The rate of decrease of current density is significantly high in the case of Pd-NC, suggesting the high rate of GLYOR at low overpotential. The decrease in catalytic current density with all the three morphologies is mainly due to the depletion of the glycerol content and increase in value added products content.

Figure 4.10 shows the products selectivity pattern from GLYOR at a potential range, from 0.6 to 1.2 V vs RHE, with three Pd nano crystals. A similar selectivity pattern was observed with all three morphologies of Pd. At the lowest potential of 0.6 V vs RHE, glyceric acid was observed to be the major product, along with glycolic acid, lactic acid, oxalic acid and formic acid as the minor products. Notably, no appreciable change in products distribution was

observed from GLYOR with various morphologies of Pd nanocrystals. At 0.6 V, the maximum selectivity of ~ 65% was achieved for C3 products (glyceric and lactic acids)

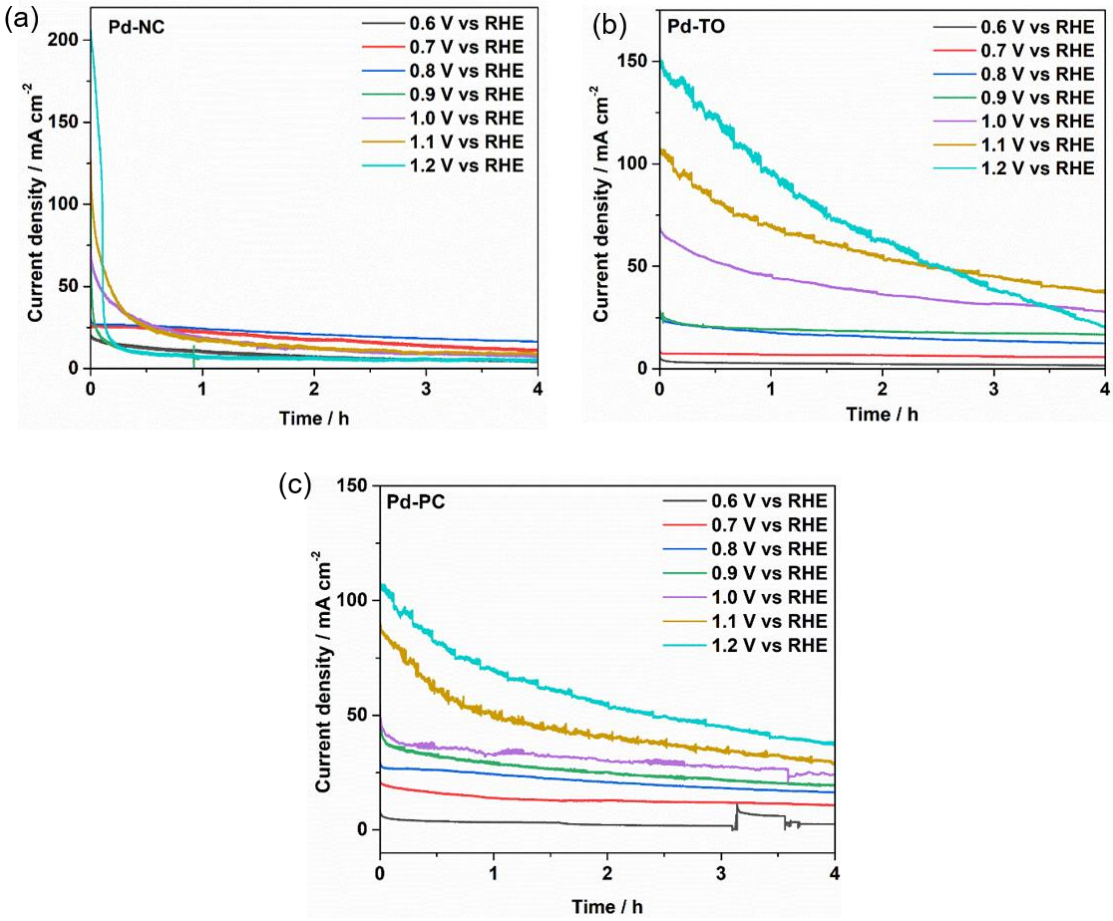

Figure 4.9 Chronoamperometry plots for GLYOR recorded at different potentials with Pd-NC, Pd-TO and Pd-PC catalysts for the reaction time of 4 h.

formation with Pd-TO (Figure 4.10b). When the potential increased to 1.2 V, the C2 products (glycolic, oxalic and acetic acid) reached the maximum selectivity of ~50% with Pd-NC (Figure 4.10a), indicating that higher overpotential is required for the oxidative cleavage of C–C bond. The selectivity towards glycolic acid started to enhance at 1.0 V vs RHE with all three Pd morphologies. The formation of glycolic acid originated from the oxidative C–C bond cleavage of glyceric acid with simultaneous production of formic acid. Indeed, the total amount of glycolic and oxalic acids produced with all three Pd morphologies are almost equal to the amount of formic acid production, at high potentials (1.0-1.2 V). Critically, no carbonate feature was observed in ^{13}C NMR spectrum even at the highest applied potential. This reiterates that no further oxidation of formic aid to CO_2 taking place during GLYOR process even at the highest potential (1.2 V vs RHE). A detailed carbon balance study was conducted at each

applied potential of the GLYOR process and the results are given in Table 4.1. Our results are reproduced in 5-10 % error margin in the carbon balance calculation.

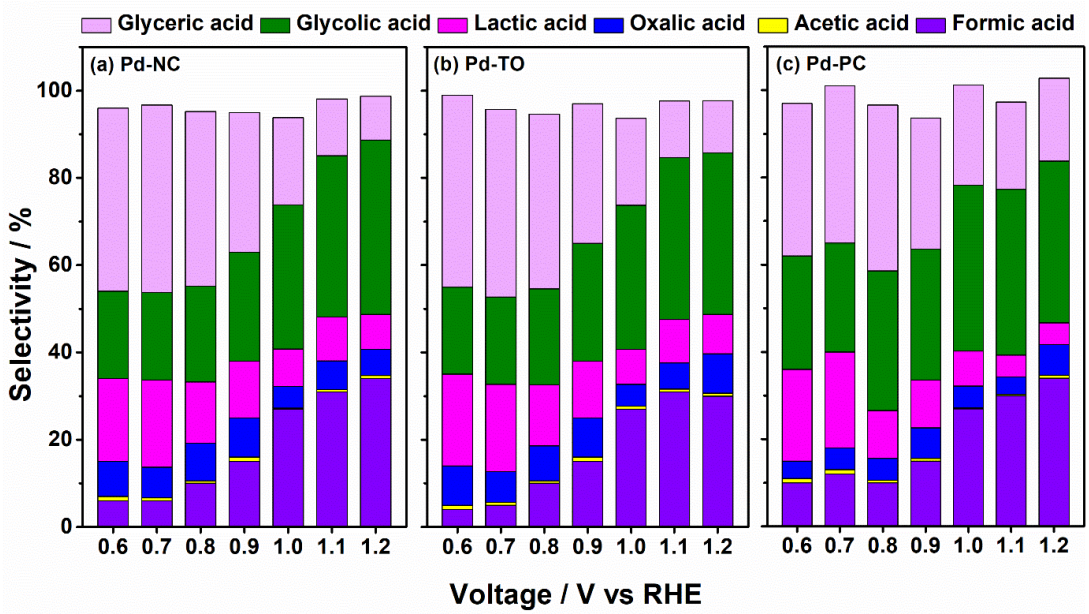

Figure 4.10 Product selectivity as a function of applied potential observed for (a) Pd-NC, (b) Pd-TO, and (c) Pd-PC catalyst after 4 h of reaction.

1 mM KHP was used as an internal standard with each NMR sample for the quantitative determination of various products; hence, we attribute the relevant carbon balance error to sampling and measurement, rather than carbonate formation. In the GLYOR process, it is likely that some of the glycolic acid could get further oxidised to oxalic acid.[13] In fact, less than 5% of oxalic acid was observed throughout the potential range with any of the Pd nano crystals supports the above conclusion. Electron withdrawing effect of the –COOH group with glycolic acid restricts the further oxidation of carbon atom containing hydroxyl group. It is likely that the partial reduction of glyceric acid to lactic acid was observed at lower applied potential, rather than from glycerol. The selectivity towards lactic acid was found to decrease at higher applied potential, due to further oxidation to formic acid and acetic acid. Therefore, a small amount of acetic acid was observed in the entire applied potential window. A schematic of the above discussed points is shown as a possible mechanism in the Figure 4.11. Since the amount of lactic acid production is low (< 10%) the contribution from the lactic acid pathway to the overall formic acid production is minimal. Finally, the GLYOR process could eventually stop at the stage of formic acid and oxalic acid, as higher potential is required to oxidise formic acid to CO_2.

Table 4.1 Carbon balance, conversion and selectivity values obtained at each applied potential for the GLYOR process. It is worth to notice that no CO_2 was observed within the applied potential range, and near 100% carbon balance was obtained.

Pd-NC								
Potential	**Formic acid**	**Acetic acid**	**Oxalic acid**	**Lactic acid**	**Glycolic acid**	**Glyceric acid**	**Conversion %**	**Carbon balance**
0.6	6	1	8	19	20	42	85	96.1
0.7	6	0.7	7	20	20	43	85	96.9
0.8	10	0.6	8.6	14	22	40	96	97.6
0.9	15	1	9	13	25	32	99	96.7
1.0	27	0.2	5	8.6	33	20	99	91.3
1.1	31	0.5	6.6	10	37	13	99	96.1
1.2	34	0.7	6	8	40	10	99	90.6
Pd-TO								
Potential	**Formic acid**	**Acetic acid**	**Oxalic acid**	**Lactic acid**	**Glycolic acid**	**Glyceric acid**	**Conversion %**	**Carbon balance**
0.6	4	1	9	21	20	44	74	100
0.7	5	0.7	7	20	20	43	80	96.4
0.8	10	0.6	8	14	22	40	83	95.6
0.9	15	1	9	13	27	32	83	97.1
1.0	27	0.7	5	8	33	20	98	96.1
1.1	31	0.6	6	10	37	13	98	96.2
1.2	30	0.7	9	9	37	12	99	95.8
Pd-PC								
Potential	**Formic acid**	**Acetic acid**	**Oxalic acid**	**Lactic acid**	**Glycolic acid**	**Glyceric acid**	**Conversion %**	**Carbon balance**
0.6	10	1	4	21	26	35	72	98.6
0.7	12	1	5	22	25	36	78	100
0.8	10	0.6	5	11	32	38	81	97.9
0.9	15	0.6	7	11	30	30	85	93.8
1.0	27	0.2	5	8	38	23	87	100
1.1	30	0.3	4	5	38	20	93.7	98.0
1.2	34	0.7	7	5	37	19	98	100

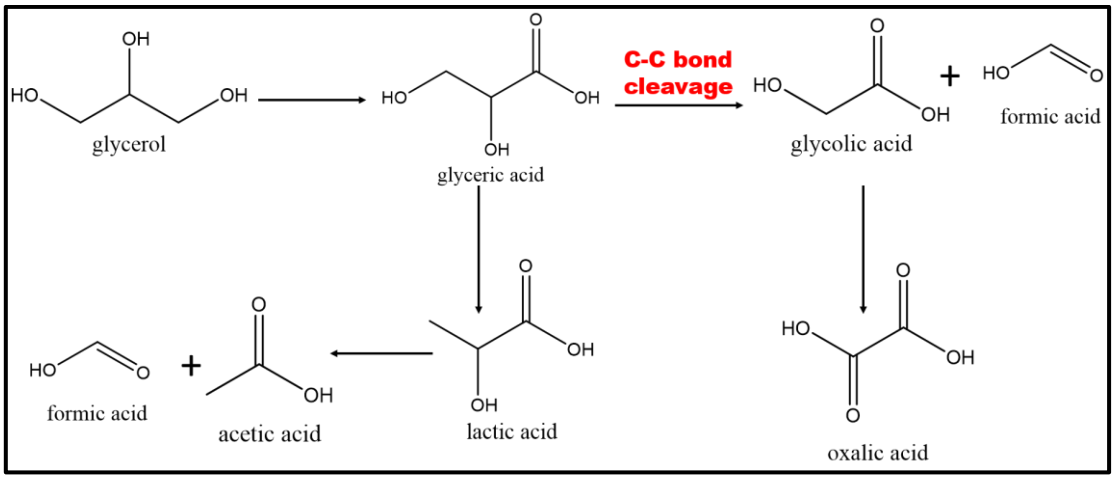

Figure 4.11 Possible reaction pathway for different C2 and C3 oxidation products from GLYOR.

4.2.6 GLYOR products selectivity and glycerol conversion

To further gain insights into the mechanistic aspects, the products selectivity and glycerol conversion has been measured as a function of reaction time, and GLYOR performance was monitored periodically for every 1 h interval at 1.2 V RHE (Figure 4.12a). It was observed that the product distribution not only depends on the applied potential, but also on the reaction time. Pd-NC afforded outstanding conversion of 47% in just 1 h. However, Pd-TO and Pd-PC exhibited 30 and 28% glycerol conversion, respectively, under same experimental conditions. This result confirms that more rapid electron transfer occurs with the Pd-NC electrode, and it is in good agreement with Tafel plot analysis (Figure 4.4b).

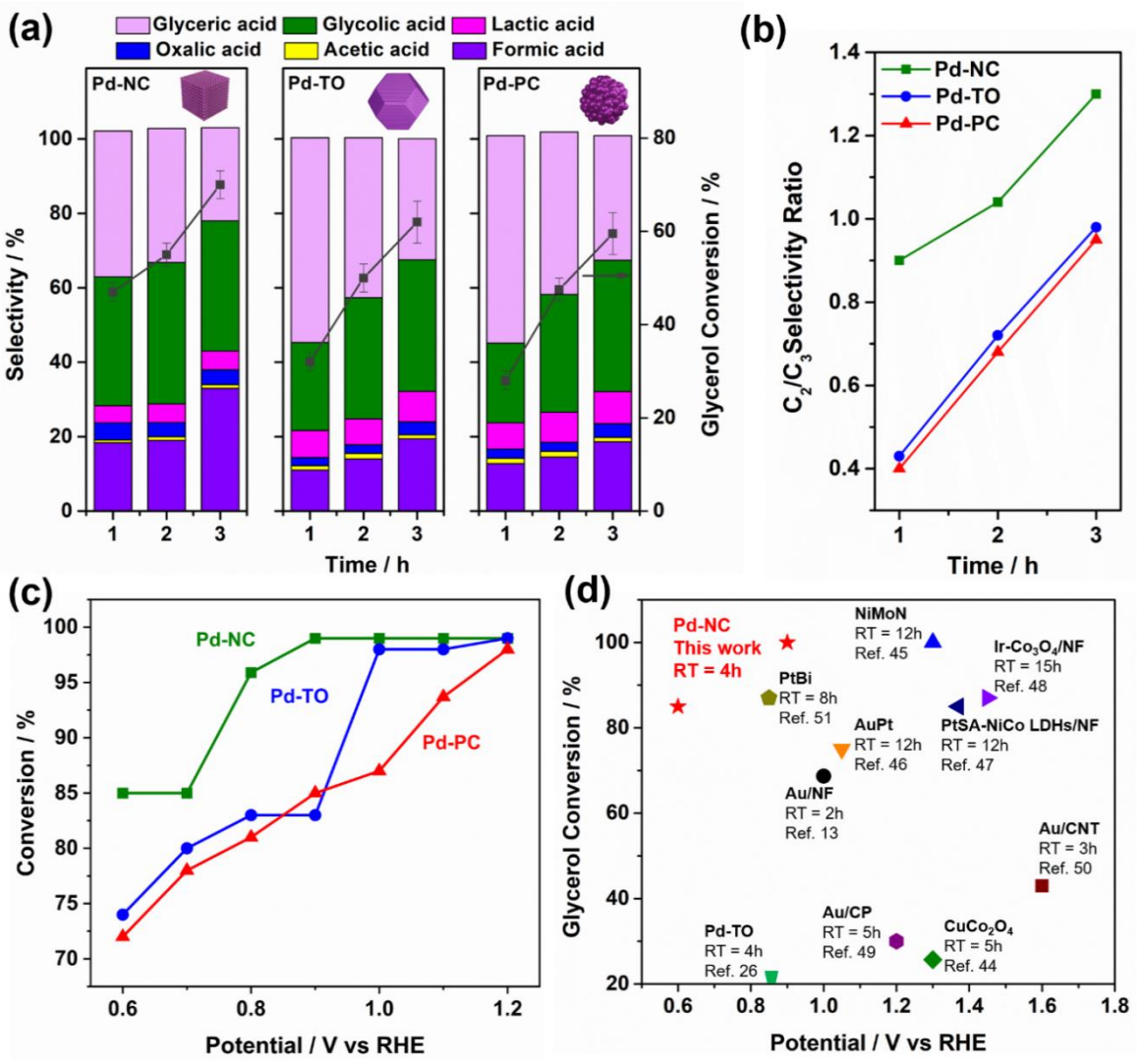

Figure 4.12(a) Glycerol conversion and selectivity of different products as a function of reaction time at 1.2 V vs RHE over different morphologies of Pd catalysts. (b) Change in ratio of C2/C3 products selectivity as a function of GLYOR time at 1.2 V vs RHE. (c) Comparison of glycerol oxidation performance over different catalyst surfaces in alkaline solution, as a

function of applied potential. (d) A comparison of top-performing catalysts results from the literature with present result from Pd-NC under comparable conditions.

It is worth to note that the glyceric acid selectivity after the first hour of the rection is only 38% with Pd-NC, compared to 57 and 60% with Pd-TO and Pd-PC, respectively. The total C2 oxidation products in Pd-NC were 42% after 1 h of the reaction. However, Pd-TO and Pd-PC exhibited 27 and 25% of C2 selectivity, respectively (Figure 4.12a). Moreover, carbon balance studies were conducted after every hour of GLYOR process and the results are given in Table 4.2.

Table 4.2 Carbon balance, selectivity of different products and glycerol conversion as a function of reaction time at 1.2 V vs RHE over different morphologies of Pd catalysts.

Pd-NC								
Time (h)	**Formic acid**	**Acetic acid**	**Oxalic acid**	**Lactic acid**	**Glycolic acid**	**Glyceric acid**	**Conversion %**	**Carbon balance**
1	18.4	0.7	4.6	4.6	34.6	39.2	47	102
2	19	1	3.8	5	38	36	55	103
3	33	1	4	5	35	25	70	103
Pd-TO								
Time (h)	**Formic acid**	**Acetic acid**	**Oxalic acid**	**Lactic acid**	**Glycolic acid**	**Glyceric acid**	**Conversion %**	**Carbon balance**
1	11	1.2	2.2	7.3	23.6	55	32	102
2	14	1.5	2.3	7	32.5	43	50	100
3	19.4	1.1	3.5	8.2	35.3	32.6	62	100
Pd-PC								
Time (h)	**Formic acid**	**Acetic acid**	**Oxalic acid**	**Lactic acid**	**Glycolic acid**	**Glyceric acid**	**Conversion %**	**Carbon balance**
1	12.8	1.4	2.5	7	21.4	55.8	28	101
2	14.5	1.6	2.4	8.1	31.6	43.7	47.5	102
3	18.6	1.2	3.7	8.6	35.3	33.5	59.5	101

As the reaction proceeds, the ratio of C2 to C3 selectivity increases with all the three morphologies (Figure 4.12b), and attain almost similar product distribution after 3 h of reaction for Pd-TO and Pd-PC; while Pd-NC shows higher C2 products selectivity along with formic acid. This result confirms that the rate of oxidative cleavage of C-C bond is the highest with Pd-NC compared to other morphologies. Earlier studies proposed that the adsorption of OH^- ions on the catalyst surface is the rate determining step for GLYOR.[13]

This suggested the competitive oxidative pathway of adsorbed glycerol and glyceric acid with hydroxide ion on catalyst surface through a Langmuir-Hinshelwood mechanism.[42] Wang et al observed that the cubic NPs with (100) facets were found to be more active for oxidative

cleavage of C-C bonds and the oxidation of acetyl group (CH_3CO) to acetic acid is significantly inhibited on Pt (100) compared to Pt (111) surface and accelerate the formation of CO_2 due to more feasible breaking of C-C bond on (100) surface.[43]

Although the selectivity of different products are similar after 3 h of reaction, the glycerol conversion is significantly different with different morphology of Pd nanocrystals at a given applied potential (Figure 4.12c). For instance, Pd-NC exhibited 85% glycerol conversion after 4 h of reaction time at a low potential of 0.6 V compared to 72 and 74% conversion with Pd-PC and Pd-TO, respectively, under same experimental conditions. The GLYOR process catalysed by Pd-NC shows near 100 % conversion at 0.8 V; however, Pd-TO and Pd-PC exhibited near 100% conversion at 1 and 1.2 V, respectively.

The complete conversion at this respective potential is fully supported by the disappearance of glycerol peak in the NMR spectrum (Figures 4.13-4.15). Furthermore, the formation of different products was confirmed from HPLC by comparing with the standard samples (Figure 4.16). This reiterates that the rate of partial oxidation of glycerol is high on (100) facets of Pd-NC compared to additional (111) facets of Pd-TO and multiple crystalline facets of Pd-PC.

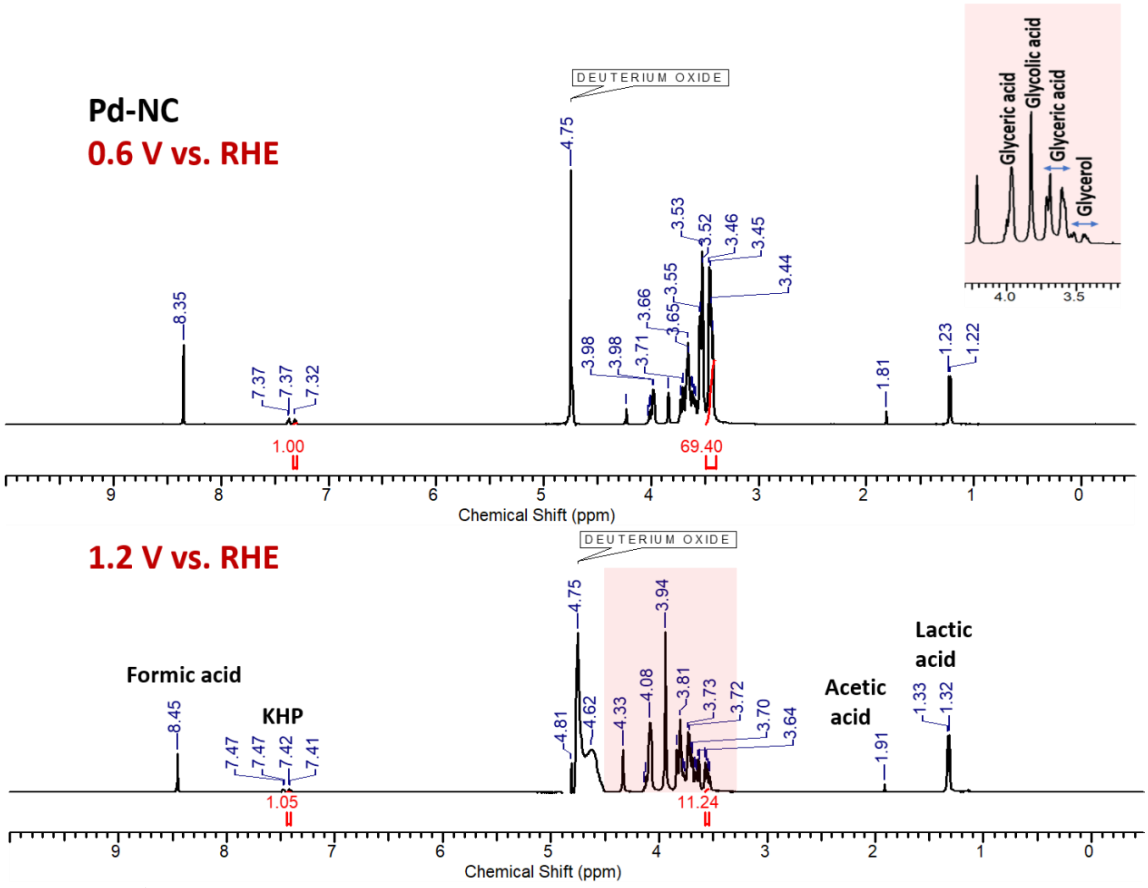

Figure 4.13 ^{1}H NMR data of 4 h chronoamperometry data of Pd-NC at 0.6 V and 1.2 V vs. RHE.

High GLYOR activity reported for different catalysts in alkaline solution are compared in Figure 4.12d and to the best of our knowledge Pd-NC shows the highest conversion at the lowest overpotential among all the catalysts. Han et al. demonstrated 29.7% electrocatalytic conversion of glycerol at 1.3 V vs RHE by integrating $CuCo_2O_4$ catalyst with carbon fibre electrode.[44] The NiMoN loaded on a carbon cloth exhibit 100% conversion at 1.3 V, but requires a long reaction time (12 h) for complete conversion.[45] AuPt[46] and Au[13] on NF shows comparable GLYOR activity of 70% conversion at an applied potential of 1 V (RHE); however, the latter (former) catalyst requires 2 h (12 h) reaction time. Furthermore, many precious metal catalysts exhibit near 100 % conversion only at higher potential (≥ 1V) and longer reaction time.[47–51] A similar report by Terekhina et al. observed the highest glycerol conversion to be 82 % with Pd-octahedral morphology at 60 °C; while the same catalyst at 20 °C exhibits a mere 21 % glycerol conversion to be noted.[26] It may be noted that KI capping agent was employed to synthesize Pd-cubic nanocatalyst, while the present work with highest GLYOR performance employed KCl; further KCl is also removed to the maximum level in the present work, as supported by LSV results shown in Figure 4.4. In addition, a large difference in particle size to be noted in the present work (Pd-NC ~7-10 nm), while Pd-Octahedral[26] shows ~34 nm.

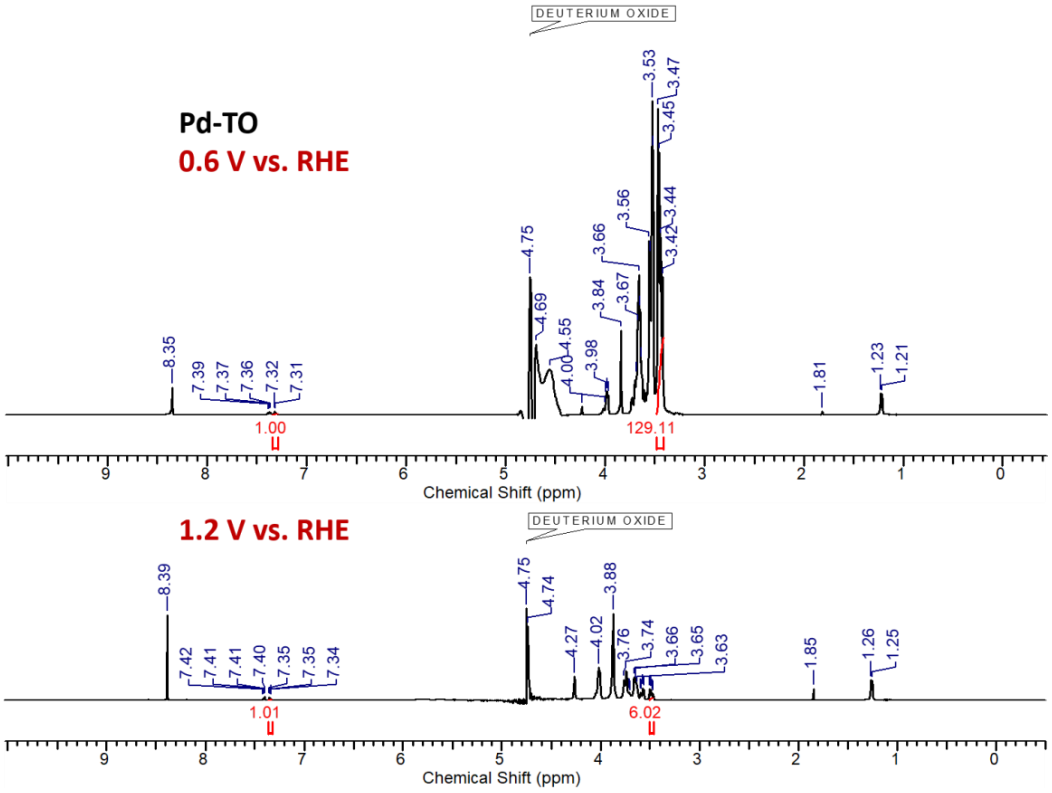

Figure 4.14 ^{1}H NMR data of 4 h chronoamperometry data of Pd-TO at 0.6 V and 1.2 V vs. RHE.

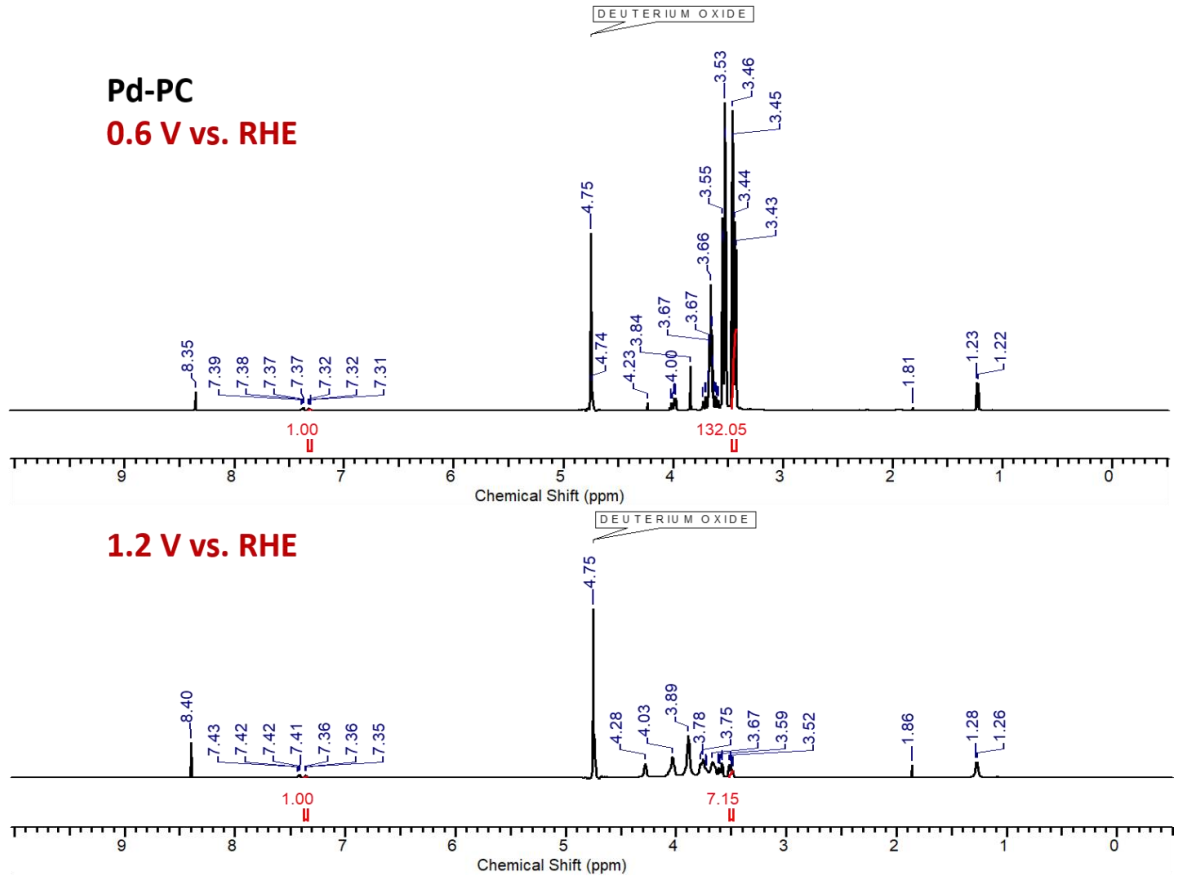

Figure 4.15 ^{1}H NMR data of 4 h chronoamperometry data of Pd-PC at 0.6 V and 1.2 V vs. RHE.

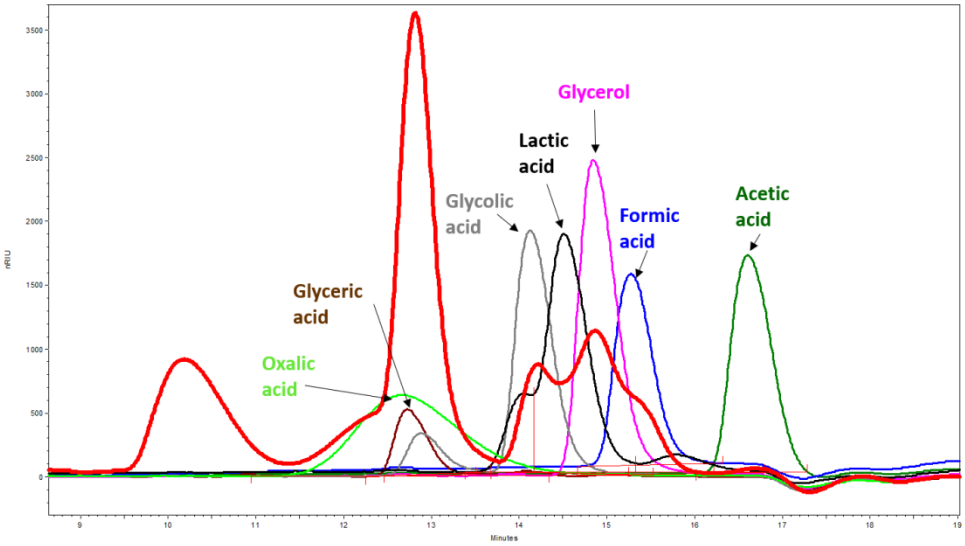

Figure 4.16 HPLC chromatogram of the electrolyte solution after 4 h reaction (Pd-NC at 1.2 V vs. RHE). As oxalic acid can not be quantified by ^{1}H NMR, HPLC was employed to quantify the oxalic acid, which appears at 12.67 minutes retention time. Along with oxalic acid, glyceric acid (12.73 min.), glycolic acid (14.12 min.), lactic acid (14.55 min.), glycerol (14.84 min.), formic acid (15.34 min.) and acetic acid (16.61 min.) are also present and identified. Bold red line represents the after reaction sample and thin lines repredent standard/reference samples.

4.2.7 ECSA study

To probe the morphology dependent GLYOR activity, the ECSA of different catalysts was compared by deriving their C_{dl} values from CV. The CV profile was recorded in the non-faradaic potential range of -0.7 to -0.9 V vs Ag/AgCl (Figure 4.17). The C_{dl} of the Pd-NC was calculated to be 9.3 mF/cm^2, which is higher than that of Pd-TO (5.5 mF/cm^2) and Pd-PC (0.9 mF/cm^2). Therefore, the ECSA of the different morphology of Pd NPs follows the order Pd-NC (232.5 cm^2) > Pd-TO (137.5 cm^2) > Pd-PC (22.5 cm^2). High ECSA of Pd-NC indeed enhances the glycerol conversion without changing the product selectivity.

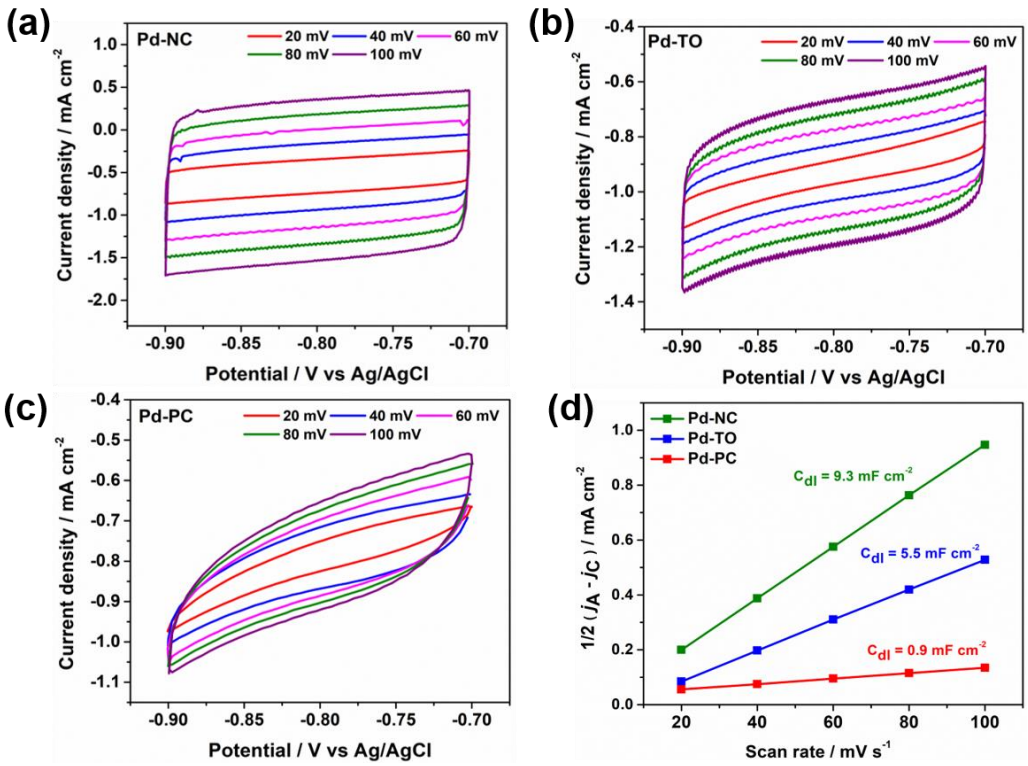

Figure 4.17 C_{dl} measurement of different shape of Pd NPs. Cyclic voltammetry (CV) profile (a) Pd-NC (b) Pd-TO and (c) Pd-PC in the non-faradaic region of potential range -0.7 V to -0.9 V vs Ag/AgCl. (d) Comparison of derived C_{dl} value are shown.

4.3 KPFM studies of Pd-NC, Pd-TO, Pd-PC

To further gain insight into understanding the structure-activity correlation, Kelvin probe force microscopy (KPFM) analysis of was carried out. KPFM is a powerful tool for visualizing the surface properties and correlate the electrocatalytic activity.[52] The surface charge on the active sites of catalyst regulates adsorption of reactant and used as a descriptor for correlating electrocatalytic activity.[53,54] In fact, the surface potential could be altered by the different arrangement of atoms on the surface. In KPFM, electrostatic force between the tip and the

sample gives information about the contact potential difference (CPD) ($\Delta\phi$) between the conducting Ti-Ir-tip and the sample surface. The measured CPD is related to the surface potential. KPFM measurements were carried out to measure topographic surface aspects of Pd-NC, Pd-TO, Pd-PC on SiO_2 surface and its corresponding surface potential (Figure 4.18). The standard AFM topography image and matching surface potential are displayed by Pd-NC and Pd-TO NPs (Figure 4.18a-d). However, Pd-PC NPs shows triangular shape with non-uniform surface structure (Figure 4.18e-f). Significant agglomeration was likely due to the polycrystalline nature of the particles. Compared to Pd-TO and Pd-PC, the surface potential is higher with Pd-NC (Figure 4.18g). (100) facet is known to be unsaturated and exhibit open structure, then (111) or (110), and the same is attributed to high surface charge on Pd-NC. Reproducible surface potential values were found, and any artefacts resulting from line-by-line fitting are eliminated by repeating the set of experiments over multiple cycles and on various batch materials. It is evident from the line profile analysis that edges of the NPs exhibited higher surface potential. Moreover, the diffusion of subsurface oxygen in (100) facets are relatively higher compared to (111) and (110) facets, as (100) facets are lower in Pd atomic density.[55]

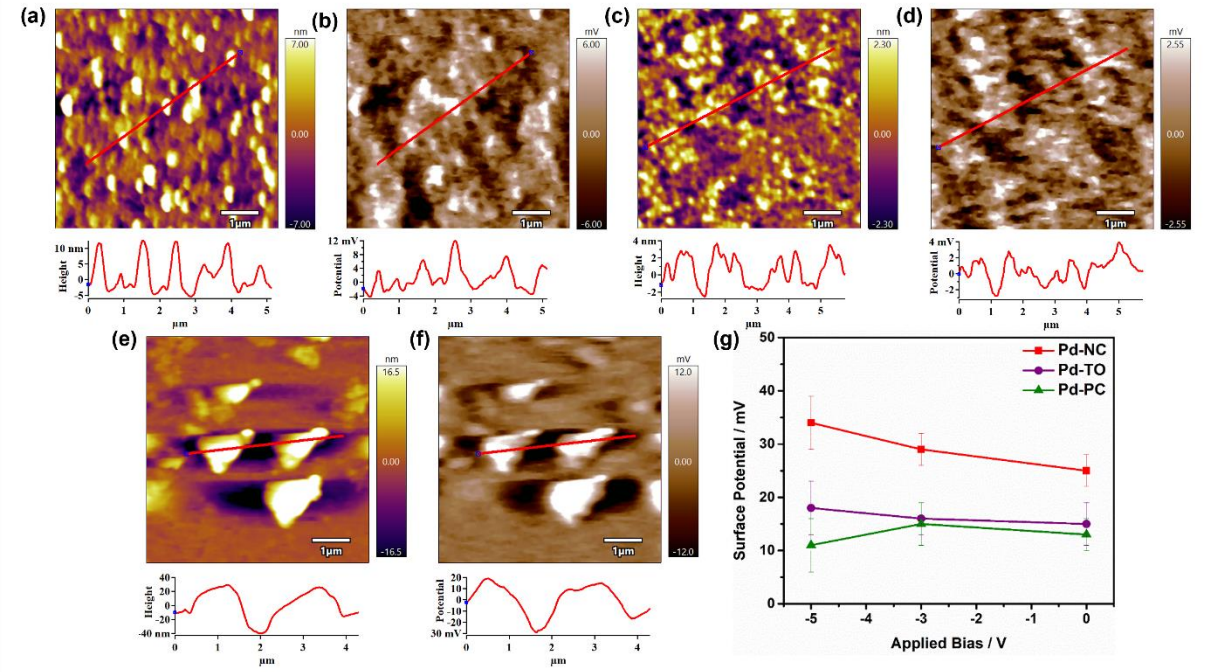

Figure 4.18 AFM topography and line profile analysis of (a-b) Pd-NC, (c-d) Pd-TO, and (e-f) Pd-PC. (g) KPM surface potential at different applied bias shows Pd-NC has higher surface potential then Pd-TO and Pd-PC.

Prior research indicates a linear relationship between the surface potential and either the catalytic activity for CO oxidation or the capacity to store oxygen. The atomic oxygen diffusion generates partial positive charges on the surface and enhanced the catalytic activity for many applications.[56,54] By controlling the crystallographic facets of catalysts, activity modulation is possible, as it alters the surface potential, which in turn alters the charge transfer.

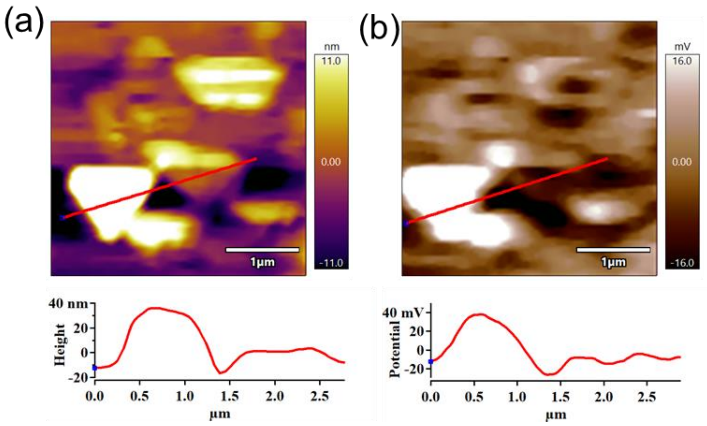

Figure 4.19 (a) AFM topography of Pd-NC (KBr), (b) KPM surface potential image, line profile analysis of AFM figure (a)

Furthermore, we studied the surface potential of Pd-NC NPs synthesized with KBr capping agent and a significant decrease in surface potential was observed as compared to Pd-NC synthesized with KCl (Figure 4.19). Since Br^- is a strong binding agent, the extent of poisoning of catalyst surface is more, as indicated earlier. This result suggested that great care must be taken in choosing and removal of halide, given that these halide ions can inhibit GLYOR performance.

4.4 Electrolyzer performance

One of the critical challenges in water electrolysis is the reduction of operating potential to bring down the electricity consumption. Due to high overpotential associated with OER from water splitting, it will be nearly impossible to bring down the power consumption beyond certain level. Nonetheless, the same was easily realized by coupling GLYOR and HER in a two-electrode electrolyzer (Figure 4.20a). Pt/C served as the cathode and Pd-NC served as the anode in the electrolyzer, which was set up with an anion exchange membrane separating them. The experimental part includes information and a digital photo of the electrolyzer setup. The LSV curve for GLYOR in the alkaline electrolyzer is shown in Figure 4.20b with and without 0.1 M glycerol. To reach 100 mA/cm^2, 1.54 V of power is needed. However, when the experiment was conducted without glycerol, a noticeably modest OER current 1.54 V was

noted. Additionally, GLYOR was able to attain a current density of 10 and 50 mA/cm^2 at applied potentials of 0.62 and 1.13 V, respectively, which is lower than OER's thermodynamic potential of 1.23 V.

A comparison of top-performing catalysts results from the literature with the present electrolyzer result from Pd-NC is summarised in Table 4.3. It is apparent that Pd-NC is far superior in electrocatalytic performance than all other catalysts listed. Even with 3.5 wt% of NaCl solution (simulated sea water), the chloride oxidation is fully avoided; however, a marginal decrease in GLYOR current density was observed and could be due to the adsorption of chloride ions on Pd-NC surface. This observation enables further opportunity for, chlorine free, sea water splitting coupled with GLYOR. Indeed, it is worth evaluating this reaction with real sea water, which contains many other ions.

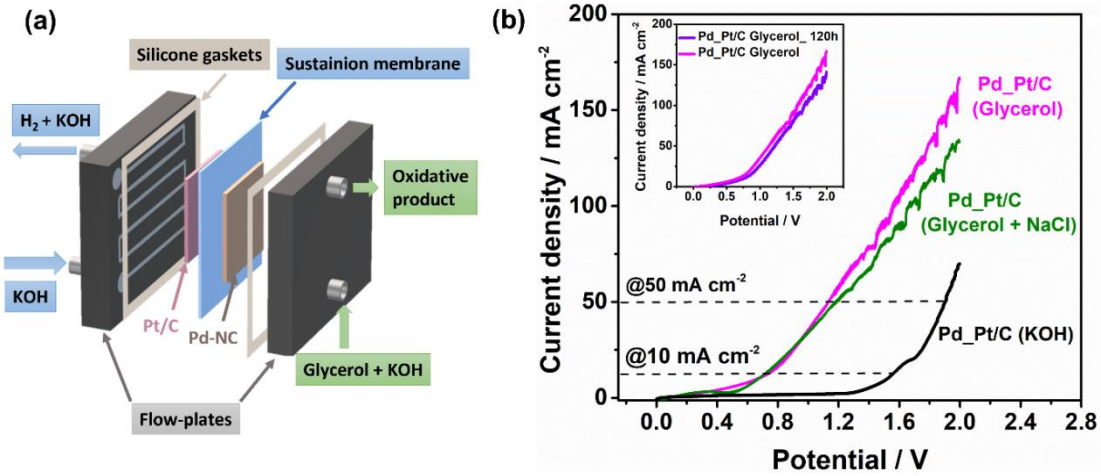

Figure 4.20 (a) Schematic of two-electrode alkaline electrolyzer performing GLYOR at the anode and HER at the cathode (b) LSV curve obtained for GLYOR in the electrolyzer using Pd-NC and Pt/C on Ni foam as anode and cathode, respectively.

A chronoamperometry experiment for 50 h was conducted at 10 mA/cm^2 current density to investigate the stability of the Pd-NC catalyst and the result is shown in Figure 4.21a. The voltage remains constant at ~0.8 V throughout the 50 h operation and it shows the stability of the catalyst. We also evaluated the long-term operation of the electrolyzer with 3.5 wt% of NaCl solution at 10 mA/cm^2 current density and observed a marginal increase in operating potential. It is to be noted that the same catalyst was employed for both the above reactions continuously (GLYOR and GLYOR in simulated sea water), except the change in NaCl containing solution after 50 h. The electrolyzer continuously produced hydrogen at a rate of 0.71 mmol/h over 50 h and the faradaic efficiency (FE) of HER was observed to be ~95%

(Figure 4.21b). The FE of HER was calculated from the theoretical and experimental H_2 production and the detailed calculation is discussed in the experimental section. Moreover, we have also carried out the stability test of the Pd-NC catalyst at 50 mA/cm^2 current density for 10 h (inset in Figure 4.21a). It can steadily work at 1.1 V and produced hydrogen at a rate of 1.1 mmol/h over 10 h. It is noteworthy to mention that the identical catalyst was utilized for a continuous duration of 120 hours in all electrolyzer experiments.

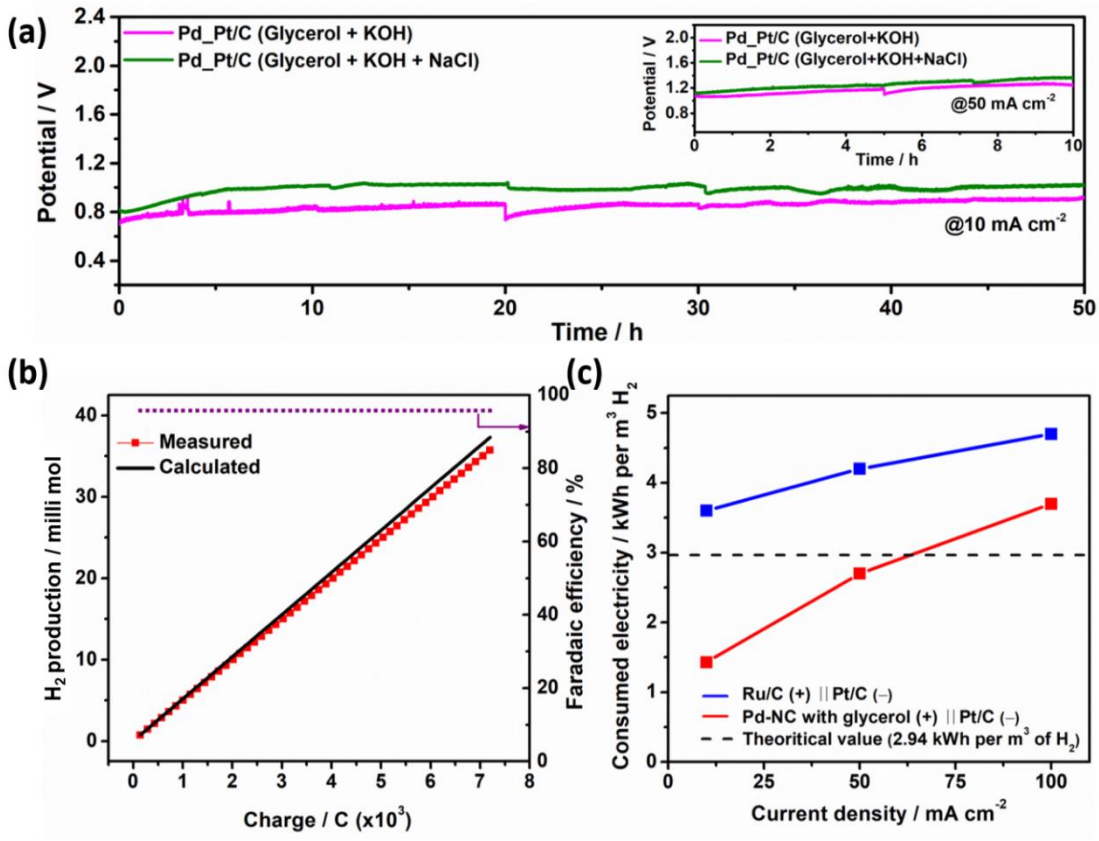

Figure 4.2 (a) Sustainability study of glycerol oxidation at 10 mA/cm^2 current density with two-electrode electrolyzer using Pd-NC as the anode, and Pt/C as the cathode. GLYOR and GLYOR with 35 wt% of NaCl solution was continuously performed one after another for 50 h each. (b) Amount of H_2 measured experimentally at the cathode and the corresponding theoretically calculated value. (c) Electricity consumed per m^3 H_2 production from GLYOR system and using conventional alkaline elctrolyzer.

The aforementioned results clearly show that an electricity input of around 3.7 kWh per m^3 of H_2 at a current density of 100 mA/cm^2 is needed for the GLYOR-based hydrogen production system (Figure 4.21c). On the other hand, a typical electrolyzer with the same current density needs 4.8 kWh per m^3 of H2 (Figure 4.22).[57] In addition, only 1.13 kWh of power are needed for every m^3 of H_2 to reach a current density of 50 mA/cm^2, which is much less than the 2.94

theoretical estimate for the water splitting reaction at 1.23 V. This is possible by completely avoiding OER, and concurrently oxidizing glycerol to value added products.

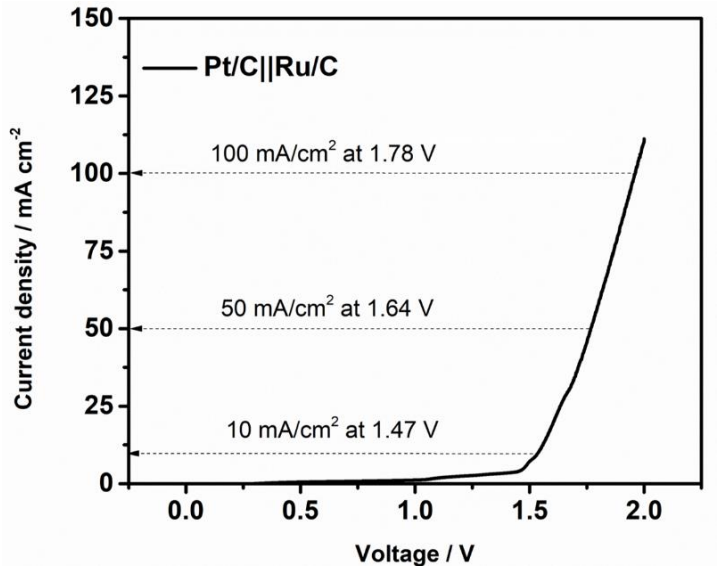

Figure 4.22 LSV curve obtained for water electrolysis in the electrolyzer using Ru/C and Pt/C on Ni foam as anode and cathode, respectively.

Table 4.3 Electrochemical glycerol upcycling for H_2 production and VAPs in alkaline medium.

Anodic catalyst	Electrolyte	Applied potential at 10 mA cm^{-2} (V)	Ref.
Pd-NC	**1 M KOH + 0.1 M Glycerol**	**0.62**	**This work**
NC/Ni-Mo-N/NF	1 M KOH + 0.1 M Glycerol	1.38	58
Ni-Mo-N/CFC	1 M KOH + 0.1 M Glycerol	1.36	59
E- NiV-LDH	1 M KOH + 0.1 M Glycerol	1.25	60
MoO_X/Pt	1 M KOH + 0.1 M Glycerol	0.70	61
PdNCs/NiO – uNPs	1 M KOH + 0.5 M Glycerol	1.62	62
NiCo Hydroxide	1 M KOH + 0.1 M Glycerol	1.33	63
$Ni(OH)_2$	1 M KOH + 0.1 M Glycerol	1.42	64
N-CoO_X	1 M KOH + 0.1 M Glycerol	1.59	65
PW-NiCo-NC	1 M KOH + 0.2 M Glycerol	1.125	66
Au/CP	0.1 M NaOH + 0.1 M Glycerol	1.0	67
NiVRu-LDHs	1 M KOH + 0.1 M Glycerol	1.35	68
Ir-Co_3O_4/NF	1 M KOH + 0.1 M Glycerol	1.40	69
CoP-Cu_3P/CC	1 M KOH + 0.1 M Glycerol	1.21	70
Ni_3N-$Ni_{0.2}Mo_{0.8}N$/CC	1 M KOH + 0.1 M Glycerol	1.40	71
Pt_{SA}-NiCo LDHs/NF	1 M KOH + 0.1 M Glycerol	1.25	72

4.5 Conclusion

In summary a unique morphology dependent selectivity and conversion of GLYOR has been demonstrated with Pd NPs. Pd-NC selectively and efficiently upgrades glycerol to glyceric acid and glycolic acid at a high conversion rate; global glycolic acid market size was projected to be USD 281.2 million in 2022, and from 2023 to 2030, it is expected to grow at a 9.1% CAGR, and electrochemical routes can certainly play a major role.[50] The electrochemical oxidative cleavage of C‑C bond is more favourable on Pd-NC compared to Pd-PC and Pd-TO morphology, suggesting the intrinsic activity of Pd (100) facets. Especially, when Pd-NC and Pt/C assemble as anode and cathode respectively, the electrolyzer requires an electricity input of only ~3.7 kWh/m^3 H_2 at a current density of 100 mA/cm^2 in contrast to 4.8 kWh/m^3 H_2 required for conventional alkaline electrolyzer. Importantly, no run-away reaction occurs to CO_2 formation and a near 100 % carbon balance was obtained. The reported electrocatalytic system provides a promising opportunity for the production of valuable chemicals from glycerol oxidation with concurrent high-purity hydrogen, and it can be considered as carbon-negative hydrogen.

4.6 Reference

(1) Lucas, F. W. S.; Grim, R. G.; Tacey, S. A.; Downes, C. A.; Hasse, J.; Roman, A. M.; Farberow, C. A.; Schaidle, J. A.; Holewinski, A., *ACS Energy Lett* **2021**, 1205–1270.

(2) Gallezot, P., *Chem. Soc. Rev.* **2012**, *41* (4), 1538–1558.

(3) Pagliaro, M.; Ciriminna, R.; Kimura, H.; Rossi, M.; Della Pina, C. *Angew. Chem. Int. Ed.* **2007**, *46*, 4434–4440.

(4) Quispe, C. A. G.; Coronado, C. J. R.; Carvalho Jr., J. A. *Renewable Sus. Energy Rev.* **2013**, *27*, 475–493.

(5) Bajpai, H.; Chauhan, I.; Salgaonkar, K. N.; Mhamane, N. B.; Gopinath, C. S. *RSC Sustainability* **2023**, *1* (3), 481–493.

(6) Monteiro, M. R.; Kugelmeier, C. L.; Pinheiro, R. S.; Batalha, M. O.; da Silva César, A. *Renewable Sustainable Energy Rev.* **2018**, *88*, 109–122.

(7) Werpy, T.; Petersen, G. *Top Value Added Chemicals from Biomass: Volume I -- Results of Screening for Potential Candidates from Sugars and Synthesis Gas*; Golden, CO (United States), 2004.

(8) Chong, C. C.; Aqsha, A.; Ayoub, M.; Sajid, M.; Abdullah, A. Z.; Yusup, S.; Abdullah, B. *Environ Technol Innov* **2020**, *19*, 100859.

(9) Sharad, J. *Clin Cosmet Investig Dermatol* **2013**, 281.

(10) Kim, K.-T.; Lee, J.-Y.; Kim, D.-D.; Yoon, I.-S.; Cho, H.-J. *Pharmaceutics* **2019**, *11*, 280.

(11) Jem, K. J.; Tan, B. *Adv. Ind. Eng. Poly. Res.* **2020**, *3*, 60-70.

(12) Li, T.; Harrington, D. A. *ChemSusChem* **2021**, *14*, 1472–1495.

(13) Kim, D.; Oh, L. S.; Tan, Y. C.; Song, H.; Kim, H. J.; Oh, J. *ACS Catal* **2021**, *11* (24), 14926–14931.

(14) Wang, H.; Thia, L.; Li, N.; Ge, X.; Liu, Z.; Wang, X. *Appl Catal B: Environ.* **2015**, *166–167*, 25–31.
(15) Wu, G.; Dong, X.; Mao, J.; Li, G.; Zhu, C.; Li, S.; Chen, A.; Feng, G.; Song, Y.; Chen, W.; Wei, W. *Chem. Eng. J.* **2023**, *468*, 143640.
(16) Zhang, J.; Shen, Y.; Li, H. *ACS Appl Energy Mater* **2023**, *6* (10), 5508–5518.
(17) Sapner, V. S.; Tanwade, P. D.; Munde, A. V.; Sathe, B. R. *ACS Appl Nano Mater* **2023**, *6* (18), 16414–16423.
(18) Han, X.; Sheng, H.; Yu, C.; Walker, T. W.; Huber, G. W.; Qiu, J.; Jin, S. *ACS Catal* **2020**, *10* (12), 6741–6752.
(19) Xia, Z.; Ma, C.; Fan, Y.; Lu, Y.; Huang, Y.-C.; Pan, Y.; Wu, Y.; Luo, Q.; He, Y.; Dong, C.-L.; Wang, S.; Zou, Y. *ACS Catal* **2024**, *14* (3), 1930–1938.
(20) Li, Y.; Wei, X.; Han, S.; Chen, L.; Shi, J. *Angew. Chem. Int. Ed.* **2021**, *60* (39), 21464–21472.
(21) Wu, J.; Li, J.; Li, Y.; Ma, X.; Zhang, W.; Hao, Y.; Cai, W.; Liu, Z.; Gong, M. *Angew. Chem. Int. Ed.* **2022**, *61* (11).
(22) Patra, K. K.; Gopinath, C. S. CO_2 *Chem. Commun.* **2023**, *59* (45), 6774–6795.
(23) Zhang, J.; Feng, C.; Deng, Y.; Liu, L.; Wu, Y.; Shen, B.; Zhong, C.; Hu, W. *Chem. Mater.* **2014**, *26* (2), 1213–1218.
(24) Zhang, H.; Jin, M.; Xiong, Y.; Lim, B.; Xia, Y. *Acc Chem Res* **2013**, *46* (8), 1783–1794.
(25) Antolini, E. *Energy Environ Sci* **2009**, *2* (9), 915.
(26) Terekhina, I.; White, J.; Cornell, A.; Johnsson, M. *ACS Appl Nano Mater* **2023**, *6* (13), 11211–11220.
(27) Gopinath, C. S.; Nalajala, N. *J Mater Chem A* **2021**, *9* (3), 1353–1371.
(28) Nikolaidis, P.; Poullikkas, A. *Renewable and Sustainable Energy Reviews* **2017**, *67*, 597–611.
(29) Oener, S. Z.; Foster, M. J.; Boettcher, S. W. *Science (1979)* **2020**, *369* (6507), 1099–1103.
(30) Chen, Y. X.; Lavacchi, A.; Miller, H. A.; Bevilacqua, M.; Filippi, J.; Innocenti, M.; Marchionni, A.; Oberhauser, W.; Wang, L.; Vizza, F. *Nat Commun* **2014**, *5* (1), 4036.
(31) Huang, H.; Yu, C.; Han, X.; Huang, H.; Wei, Q.; Guo, W.; Wang, Z.; Qiu, J. Ni, Co *Energy Environ Sci* **2020**, *13* (12), 4990–4999.
(32) Sun, F.; Qin, J.; Wang, Z.; Yu, M.; Wu, X.; Sun, X.; Qiu, J. *Nat Commun* **2021**, *12* (1), 4182.
(33) Jiang, N.; Liu, X.; Dong, J.; You, B.; Liu, X.; Sun, Y. *ChemNanoMat* **2017**, *3* (7), 491–495.
(34) Wang, T.; Tao, L.; Zhu, X.; Chen, C.; Chen, W.; Du, S.; Zhou, Y.; Zhou, B.; Wang, D.; Xie, C.; Long, P.; Li, W.; Wang, Y.; Chen, R.; Zou, Y.; Fu, X.-Z.; Li, Y.; Duan, X.; Wang, S. *Nat Catal* **2021**, *5* (1), 66–73.
(35) Jiang, N.; You, B.; Boonstra, R.; Terrero Rodriguez, I. M.; Sun, Y. *ACS Energy Lett* **2016**, *1* (2), 386–390.
(36) Liu, W.-J.; Xu, Z.; Zhao, D.; Pan, X.-Q.; Li, H.-C.; Hu, X.; Fan, Z.-Y.; Wang, W.-K.; Zhao, G.-H.; Jin, S.; Huber, G. W.; Yu, H.-Q. *Nat Commun* **2020**, *11* (1), 265.
(37) Guo, W.; Heeres, H. J.; Yue, J. *Chem. Eng. J.* **2020**, *381*, 122754.
(38) He, O.; Zhang, Y.; Wang, P.; Liu, L.; Wang, Q.; Yang, N.; Li, W.; Champagne, P.; Yu, H. *Catalysts* **2020**, *11* (1), 11.
(39) Xiong, T.; Zhu, Z.; He, Y.; Balogun, M. -Sadeeq; Huang, Y. *Small Methods* **2023**, *7* (4).
(40) Zhu, Z.; Luo, L.; He, Y.; Mushtaq, M.; Li, J.; Yang, H.; Khanam, Z.; Qu, J.; Wang, Z.; Balogun, M. -Sadeeq. *Adv Funct Mater* **2024**, *34* (8).

(41) Nalajala, N.; Salgaonkar, K. N.; Chauhan, I.; Mekala, S. P.; Gopinath, C. S. *ACS Appl Energy Mater* **2021**, *4* (11), 13347–13360.
(42) Busó-Rogero, C.; Grozovski, V.; Vidal-Iglesias, F. J.; Solla-Gullón, J.; Herrero, E.; Feliu, J. M. *J Mater Chem A* **2013**, *1* (24), 7068.
(43) Wang, H.-F.; Liu, Z.-P. *J Am Chem Soc* **2008**, *130* (33), 10996–11004.
(44) Han, X.; Sheng, H.; Yu, C.; Walker, T. W.; Huber, G. W.; Qiu, J.; Jin, S. *ACS Catal* **2020**, *10* (12), 6741–6752.
(45) Li, Y.; Wei, X.; Chen, L.; Shi, J.; He, M. *Nat Commun* **2019**, *10* (1), 5335.
(46) Dai, C.; Sun, L.; Liao, H.; Khezri, B.; Webster, R. D.; Fisher, A. C.; Xu, Z. J. *J Catal* **2017**, *356*, 14–21.
(47) Yu, H.; Wang, W.; Mao, Q.; Deng, K.; Wang, Z.; Xu, Y.; Li, X.; Wang, H.; Wang, L. *Appl Catal B* **2023**, *330*, 122617.
(48) Xu, Y.; Liu, T.; Shi, K.; Yu, H.; Deng, K.; Wang, Z.; Li, X.; Wang, L.; Wang, H. *Chemical Communications* **2023**, *59* (13), 1817–1820.
(49) Xie, Y.; Sun, L.; Pan, X.; Zhou, Z.; Zheng, Y.; Yang, X.; Zhao, G. *Carbon N Y* **2023**, *203*, 88–96..
(50) Zhang, Z.; Xin, L.; Qi, J.; Wang, Z.; Li, W. *Green Chem.* **2012**, *14*, 2150.
(51) Liu, L.; Liu, B.; Xu, X.; Jing, P.; Zhang, J. *J Power Sources* **2022**, *543*, 231836.
(52) Wang, Y.; Skaanvik, S. A.; Xiong, X.; Wang, S.; Dong, M. *Matter* **2021**, *4* (11), 3483–3514.
(53) Tao, L.; Qiao, M.; Jin, R.; Li, Y.; Xiao, Z.; Wang, Y.; Zhang, N.; Xie, C.; He, Q.; Jiang, D.; Yu, G.; Li, Y.; Wang, S. *Angew. Chem. Int. Ed.* **2019**, *58*, 1019–1024.
(54) Mhamane, N. B.; Panchal, S.; Kolekar, S. K.; Ranjan, R.; Salgaonkar, K. N.; Burange, A. S.; Nalajala, N.; Datar, S.; Gopinath, C. S. *Phys. Chem. Chem. Phys.* **2023**, *25*, 22040–22054.
(55) Kolekar, S. K.; Dubey, A.; Date, K. S.; Datar, S.; Gopinath, C. S. *Phys. Chem. Chem. Phys.* **2016**, *18*, 27594–27602.
(56) Cheon, J. Y.; Kim, J. H.; Kim, J. H.; Goddeti, K. C.; Park, J. Y.; Joo, S. H. *J Am Chem Soc* **2014**, *136* (25), 8875–8878.
(57) Ursua, A.; Gandia, L. M.; Sanchis, P. *Proc. IEEE* **2012**, *100*, 410–426.
(58) Xu, Y.; Liu, M.; Wang, S.; Ren, K.; Wang, M.; Wang, Z.; Li, X.; Wang, L.; Wang, H. *Appl. Catal. B.* **2021**, 298, 120493.
(59) Li, Y.; Wei, X.; Chen, L.; Shi, J.; He, M. *Nat. Commun.* **2019**, 10, 5335.
(60) Dong, L.; Chang, G.-R.; Feng, Y.; Yao, X.-Z.; Yu, X.-Y. *Rare Metals* **2022**, 41, 1583–1594.
(61) Yu, X.; dos Santos, E. C.; White, J.; Salazar-Alvarez, G.; Pettersson, L. G. M.; Cornell, A.; Johnsson, M. *Small* **2021**, 17, 2104288.
(62) Ma, G.; Yang, N.; Zhou, G.; Wang, X. *Nano Res.* **2022**, 15, 1934–1941.
(63) He, Z.; Hwang, J.; Gong, Z.; Zhou, M.; Zhang, N.; Kang, X.; Han, J. W.; Chen, Y. *Nat. Commun.* **2022**, 13, 3777.
(64) Wu, J.; Li, J.; Li, Y.; Ma, X.; Zhang, W.; Hao, Y.; Cai, W.; Liu, Z.; Gong, M. *Angew. Chem. Int. Ed.* **2022**, 61.
(65) Ke, Z.; Williams, N.; Yan, X.; Younan, S.; He, D.; Song, X.; Pan, X.; Xiao, X.; Gu, J. *J. Mater. Chem. A.* **2021**, 9, 19975–19983.
(66) Cao, H.; Wei, T.; Liu, Q.; Zhang, S.; Qin, Y.; Wang, H.; Luo, J.; Liu, X. *ChemCatChem* **2023**, 15.
(67) Xie, Y.; Sun, L.; Pan, X.; Zhou, Z.; Zheng, Y.; Yang, X.; Zhao, G. *Carbon* **2023**, 203, 88–96.
(68) Qian, Q.; He, X.; Li, Z.; Chen, Y.; Feng, Y.; Cheng, M.; Zhang, H.; Wang, W.; Xiao, C.; Zhang, G.; Xie, Y. *Adv. Mater.* **2023**, 35.
(69) Xu, Y.; Liu, T.; Shi, K.; Yu, H.; Deng, K.; Wang, Z.; Li, X.; Wang, L.; Wang, H. *ChemComm* **2023**, 59, 1817–1820.
(70) Xie, Z.; Wang, K.; Zou, Y.; Ying, G.; Jiang, J. *Energy Adv.* **2023**, 2, 161–169.

(71) Liu, X.; Fang, Z.; Teng, X.; Niu, Y.; Gong, S.; Chen, W.; Meyer, T. J.; Chen, Z. *J. Energy Chem.* **2022**, *72*, 432–441.
(72) Yu, H.; Wang, W.; Mao, Q.; Deng, K.; Wang, Z.; Xu, Y.; Li, X.; Wang, H.; Wang, L. Pt *Appl. Catal. B.* **2023**, *330*, 122617.

Chapter 5

Electrocatalytic and Selective Glycerol Oxidation to Formate on 2D 3d-Metal Phosphates Nanosheet and Carbon-Negative Hydrogen Generation

Chapter 5 has been Published and details are:

Chauhan, I.; Vijay, P.M.; Ranjan, R.; Patra, K. K.; and Gopinath, C. S.; Electrocatalytic and Selective Glycerol Oxidation to Formate on 2D 3d-Metal Phosphates Nanosheet and Carbon-Negative Hydrogen Generation. *ACS Mater. Au.*, **2024**, (***Just accepted***) https://doi.org/10.1021/acsmaterialsau.4c00024

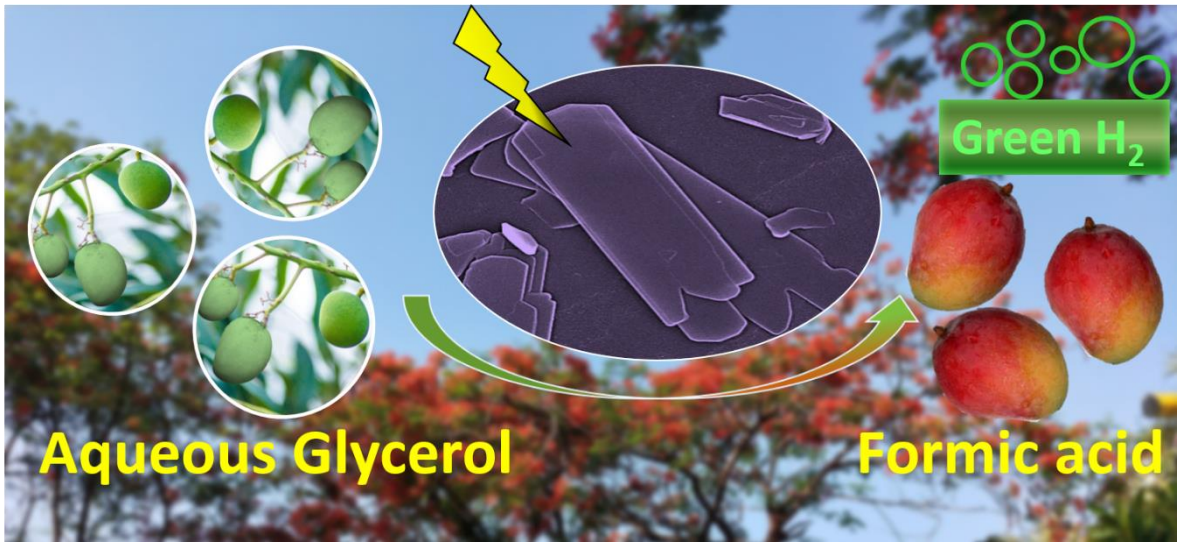

Electrocatalytic and Selective Glycerol Oxidation to Formate on 2D 3d-Metal Phosphates Nanosheet and Carbon-Negative Hydrogen Generation

5.1 Introduction

The imperative quest for clean and renewable energy sources, driven by the escalating challenges of environmental damages and energy crises, has spurred intense research into viable alternatives. Solar, wind, and green hydrogen energy have emerged as pivotal contenders, garnering widespread attention for their potential to mitigate the adverse impacts of conventional energy production methods.[1-3] Molecular hydrogen is a clean energy carrier that is both appealing and carbon-neutral. It holds great potential for a sustainable future.[4,5] Steam methane reforming, the current standard method for producing hydrogen, is not sustainable due to its heavy reliance on fossil fuels and high CO2 emissions.[6] Electrocatalytic water splitting is a compelling solution due to its capability of generating high-purity hydrogen, except for the cost. Nonetheless, this method is envisioned as a key player in the future hydrogen economy, providing an environmentally favourable alternative.[7-9] However, the current challenges in electrocatalytic water splitting lie in the high overpotentials required for the anodic oxygen evolution reaction (OER), leading to suboptimal energy conversion efficiency. Despite the theoretical voltage requirement of 1.23 V for OER, commercial electrolyzers typically operate at voltages around 2.0 V and higher.[10] Moreover, the co-production of O_2 at the anode introduces the risk of hazardous mixing with H_2 at the cathode, even in the presence of high-cost/sophisticated membranes due to cross-over. Furthermore, the formation of reactive oxygen species in the presence of H_2, O_2, and catalysts poses a threat to the longevity of the electrolyzer, as it may degrade the membrane and reduce its operational lifespan.[11,12] These challenges underscore the necessity for innovative solutions that address the efficiency, safety, and longevity aspects of electrocatalytic water splitting. Realising hydrogen's full potential as a clean energy carrier and easing the shift to a sustainable energy landscape depend on the development of advancements in this area.

The escalating global demand for sustainable energy resources has spurred intensive research into the development of efficient and environmentally benign catalysts for energy conversion processes. In this context, the selective electrocatalytic oxidation of glycerol holds particular significance due to its abundant availability as a by-product in biodiesel production.[13] As a possible energy carrier and renewable feedstock for the production of value-added products, glycerol is a trihydroxy sugar alcohol that offers a special possibility. It has been

demonstrated that glycerol oxidation may be electrochemically converted to produce a variety of commercial products, including lactic acid, formic acid, glycolic acid, and glyceric acid. Of these compounds, formic acid (HCOOH) has the largest industrial market value.[14] Methyl formate hydrolysis, which is one of the classic commercial processes for manufacturing formic acid, is often a difficult multistep process that operates at moderately high temperature (90-140 °C) and pressure (between 2 and 7 bar of methyl formate with steam) conditions.[15] Crucially, 0.69 V (vs. RHE) is the theoretical oxidation potential required to fully oxidise one glycerol molecule into three formic acid molecules. This is significantly less than the 1.23 V required for OER under typical circumstances.[16]

Until far, the majority of catalysts utilised for the glycerol oxidation reaction (GLYOR) have been based on noble metals, such as Au,[17] AuPt,[18] Pt,[19] Pd,[20] PtSb,[21] and PtRuSn[22] and non-noble metal-based catalysts, like, NiOOH,[23],[24],[25] amorphous CoO_x,[26] $NiCo_2O_4$/NF,[27] Co-doped Ni-Fe,[28] $CuCo_2O_4$[29] and $Ni_{0.33}Co_{0.67}(OH)_2$@HOS/NF.[30] However, the reaction pathways of GLYOR are intricate, resulting in the production of various C1–C3 intermediates due to the difficulties in efficient C–C bond cleavage. This complexity necessitates the development of nonprecious earth-abundant electrocatalysts for a highly efficient, low onset/overpotential and selective GLYOR to possibly a single product. Therefore, it is crucial to explore alternatives to noble metals, considering their cost and availability constraints. Developing nonprecious metal catalysts could enhance the economic and environmental sustainability of the GLYOR process, addressing the challenges associated with the current noble metal-dominated catalyst landscape. Transition metal-based catalysts have emerged as promising candidates for catalysing GLYOR, offering a diverse range of active sites and redox capabilities. Among them, the synthesis of ultrathin 2D nanosheets has garnered substantial attention for their intrinsic properties, including high surface area, tuneable composition, and enhanced catalytic activity.[31-35]

In this work, we synthesise ultrathin nanosheet phosphates in two dimensions (2D) with Co, Cu, or Ni, and in three dimensions (3D) with Fe in a structure resembling a snowflake. In an alkaline electrolyte media, CoP functions as a high-performance electrocatalyst for the GLYOR. In order to achieve a high density of surface-exposed active sites and a large surface area, transition-metal phosphate with a 2D nanosheet structure is used in the design. CoP exhibits the lowest onset potential and the best inherent stability in an alkaline electrolyte when compared to other phosphates. Compared to other phosphates, CoP ultrathin nanosheets with a thickness of about 5 nm show an exceptionally low onset at 1.12 V against RHE when acting

as a GLYOR catalyst. To the best of our knowledge, this is the first phosphate-based investigation on glycerol oxidation, and this figure is far lower. In addition, the ideal ultrathin CoP catalyst exhibits extremely robust electrochemical stability for an extended 200 hours of GLYOR in an alkaline environment.

5.2 Result and Discussions

5.2.1 Procedure of catalyst synthesis

In this study, metal (M = Co, Cu, Fe and Ni) chloride precursor and monosodium phosphate were utilized for the synthesis of corresponding metal phosphates via a single-step solvothermal process, as shown in schematic diagram (Figure 5.1a). A solvent mixture of isopropyl alcohol and ultrapure deionized water in a 2:1 ratio was used to dissolve a total of 10 mM of metal chloride and 20 mM of phosphate precursor NaH_2PO_4 during the synthesis process. After this mixture produced a homogenous solution, it was put into a 50 ml stainless-steel autoclave with a teflon lining. After that, the autoclave underwent solvothermal treatment, which involved keeping it in a hot air oven for 14 hours at 140 °C. After the reaction was finished, the autoclave was taken out of the oven and left cool to room temperature. After the reaction, the products were filtered and went through several deionized water washes before getting one last wash with ethanol. After that, the samples were dried for 12 hours under vacuum oven, and then it was employed to make electrode for GLYOR. As synthesized catalyst colour was shown in Figure 5.1a and the catalysts are designated as CoP (violet), CuP (cyan), FeP (brown) and NiP (lime). Phase purity and crystallographic structure of CoP, CuP, FeP and NiP catalysts was conducted through XRD. It may be noted that the environmentally benign synthesis of phosphate nanosheets by hydrothermal synthesis is easy to scale-up.

5.2.2 Microstructure and morphological analyses

Narrow XRD patterns presented in Figure 5.1b demonstrate that as-prepared metal phosphates exhibit a crystalline structure**.** CoP shows the formation $Co_3(PO_4)_2.8H_2O$ (JCPDS No.33-0432) with two major diffraction peaks at 10.57° and 12.09°, corresponding to (001) and (020) crystallographic facets, respectively.[36] While CuP (JCPDS No. 01-070-0494) displays the major diffraction peaks at 12.71°, 29.64° and 33.44° which can be indexed to the (001), (012), and (121) facets, respectively.[37] The FeP (JCPDS No. 85-2386) shows two major diffraction peaks at 26.62° and 27.8° and they are indexed to (103) and (112) facets, respectively. NiP shows the major diffraction peak at 18.14° and indexed to (200) facet.[38] Layered 2D structure is evident from the XRD pattern, especially with high intensity for (00z) or (x00) with narrow features, for all phosphates, except FeP. While NiP displays (200) facet at 18.14°, CoP shows

(001) at 10.57°. Nanosheet morphology feature diminishes in intensity for CuP and low intensity (001) feature was observed. Conversely, $FePO_4$ displays no specific features for 2D morphology and supported by FESEM images (Figure 5.1e).

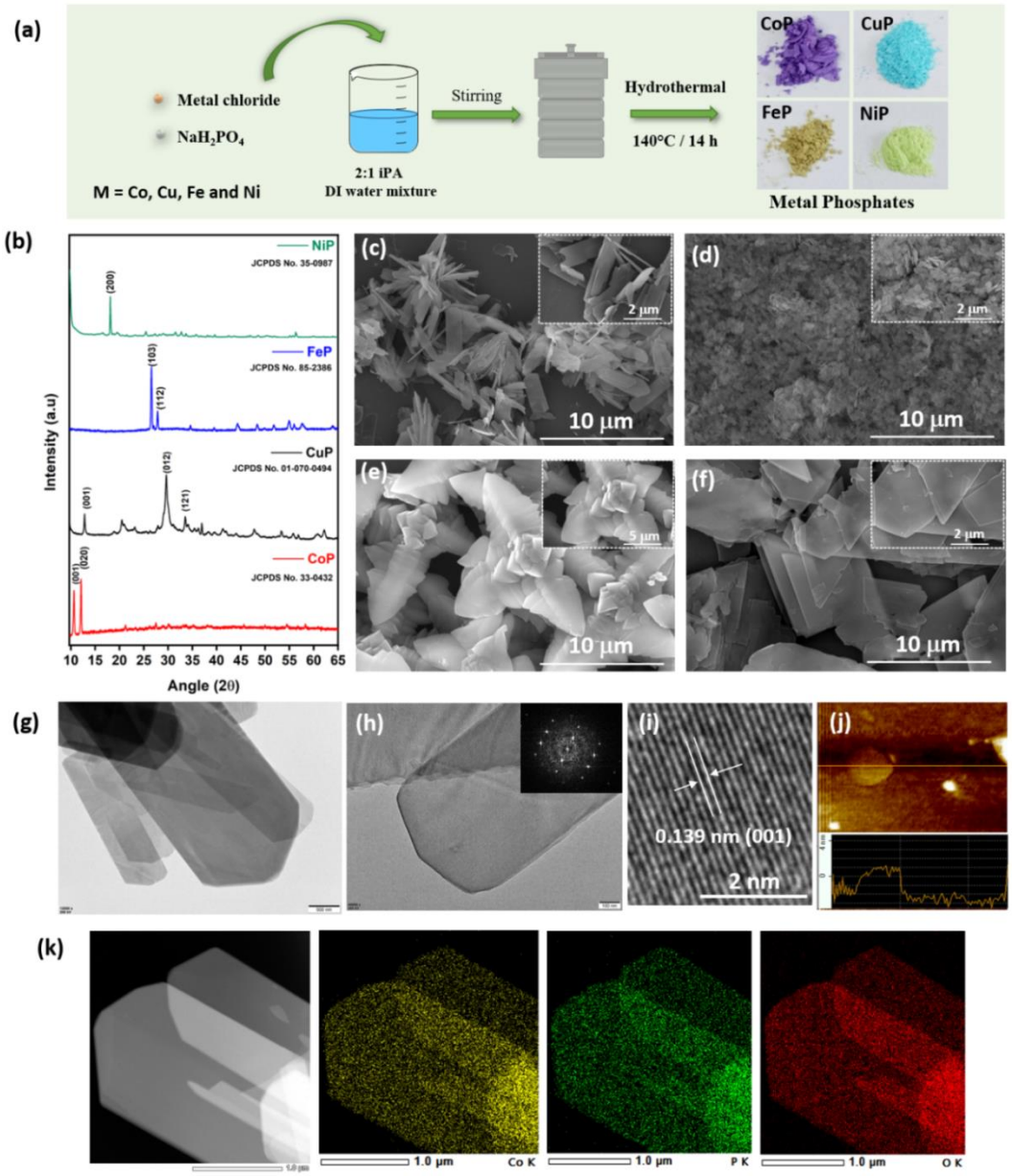

Figure 5.1 Synthesis and microscopy characterization of the M-PO_4 (M = Co, Cu, Ni and Fe) catalysts. a) Schematic illustration of the M-PO_4 synthesis procedure. b) XRD patterns of the as-prepared M-PO_4 samples. The FE-SEM images of c) CoP, d) CuP, e) FeP and f) NiP; inset in all these panels shows FESEM recorded at higher magnification. g) TEM image of CoP, h-i) HRTEM image of CoP, and SAED pattern (inset) obtained from the Figure (i), j) AFM image of single sheet of CoP, to display the nanolevel (~3-4 nm) thickness. k) HADDF-STEM-EDS elemental maps of CoP nanosheet for Co, P and O and their uniform distribution observed all over the nanosheet.

Morphological and microstructure analyses were conducted using FE-SEM and HRTEM. Even a cursory look at the FESEM images reveals the influence of cations on the morphology of metal phosphates. Figure 5.1c and 5.1f reveals the bundles of sheet-like ultrathin 2D nanosheet structure for CoP and NiP, respectively; ultrathin nanosheets provide an almost transparent (for electron) appearance. CoP appears to be cactus-ovoid morphology with thin layers of CoP protruding out from the center of cacti. Square nanosheet and random morphology of CuP, depicted in Figure 5.1d, exhibits a mixed morphological feature. Nevertheless, a distinct morphological transformation is evident in the case of FeP, as shown in Figure 5.1e, where a 3D snowflake morphology is observed. Figure 5.1g presents a TEM image providing detailed insights into the rectangular nanosheet structure of CoP. Figure 5.1h-i show HRTEM images of CoP. In Figure 5.1i, distinct lattice fringes are observed, revealing an interplanar spacing of 0.139 nm and attributed to the (001) facet of CoP, which is matching with XRD data.[39] Selected area electron diffraction (SAED) pattern (inset) recorded is shown in Figure 5.1i. To garner more compositional information and understand the distribution of constituent elements, additional investigations were conducted. Figure 5.1j shows the thickness of one single nanosheet of CoP, and it is measured to be 3-4 nm; observation of such thin nanosheet indicates the stacking of very few unit cells; considering the unit cell parameters of CoP (a = b = 12.63 Å, and c = 5.017 Å), 3–4-unit cells of CoP could be stacked in a single sheet. Hexagonal structure is evident from the nanosheet shown in TEM (Figure 5.1g and h) and suggest (001) facet on it. HADDF- STEM and elemental mapping in Figures 5.1k demonstrated the presence of cobalt (Co), along with phosphorus (P) and oxygen (O), as constituent elements in CoP. Moreover, a uniform distribution of all elements throughout the nanosheets was observed. Analogous patterns of HRTEM images and elemental mappings were observed for other phosphates, as shown in supporting information (Figures 5.2, 5.3, and 5.4 for CuP, FeP, and NiP, respectively).

5.2.3 Electronic Structure of Metal Phosphates

XPS was used to examine the surface chemical properties of all metal phosphates. Figure 5.5 shows the high-resolution XPS spectra of the core levels of (a) Co 2p, (b) Cu 2p, (c) Fe 2p, and (d) Ni 2p for CoP, CuP, FeP, and NiP, respectively, and (e) P 2p. The deconvolution was carried out using Casa XPS software, and Shirley background removal procedure was applied to all spectra.

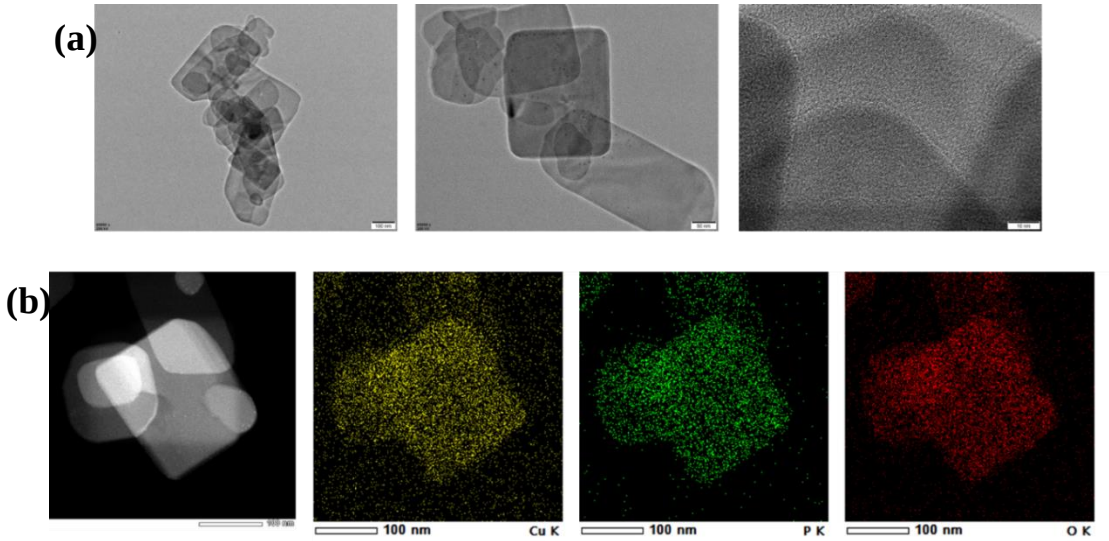

Figure 5.2 (a)TEM and HRTEM image of CuP. (b) HADDF-STEM-EDS elemental maps of CuP nanosheet.

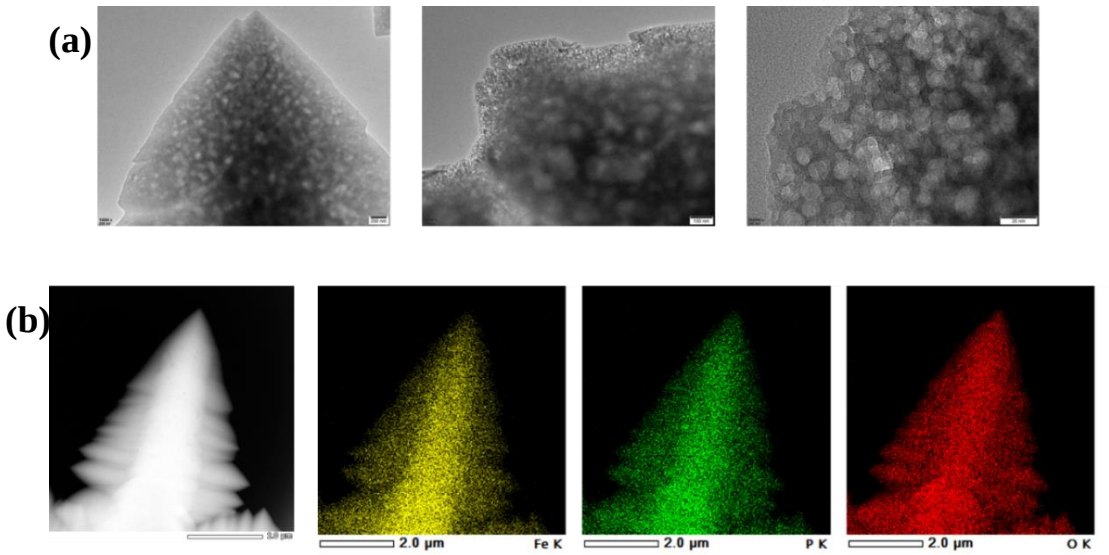

Figure 5.3 (a)TEM and HRTEM image of FeP. (b) HADDF-STEM-EDS elemental maps of FeP 3D snowflake's structure.

The Co 2p core level spectra (Figure 5.5a) exhibit spin-orbit doublet along with prominent satellite features. However, deconvolution indicates the presence of Co^{3+} ($2p_{3/2}$ at 779.6 eV) and Co^{2+} ($2p_{3/2}$ at 780.6 eV) oxidation states along with a sub peak at 782.3 eV and satellite features at high binding energy (BE).[40] Similarly, minor amount of Cu^{1+} ($2p_{3/2}$ at 932.2±0.2 eV) and majority of Cu^{2+} ($2p_{3/2}$ at 935.2±0.2 eV) were observed with CuP in Figure 5.5b. A low intensity feature observed at 932.2 eV is attributed to a possible reduction of Cu^{2+} to Cu^{1+} due to x-ray exposure.[41] The Fe $2p_{3/2}$ and $2p_{1/2}$ spin-orbit doublet exhibits multiple splitting and very weak satellite, as depicted in Figure 5.5c for FeP. For FeP, the presence of Fe^{3+} (as in

Fe_3O_4), Fe^{3+} (as in Fe-PO_4), and $Fe_3(PO_4)_2$ is observed at BE 711.2±0.2, 712.4±0.1 eV and 714.2±0.1 eV, respectively.[42] A minor peak observed at 709.6±0.2 eV is attributed to reduction of Fe^{3+} to Fe^{2+} due to x-ray exposure. In contrast, XPS spectrum of Ni shows characteristic peaks for Ni^{2+} and Ni^{3+} at BE= 853.5±0.2 eV and 855.0±0.2 eV, respectively, in Figure 5.5d along with a broad satellite feature around 861 eV.[43]

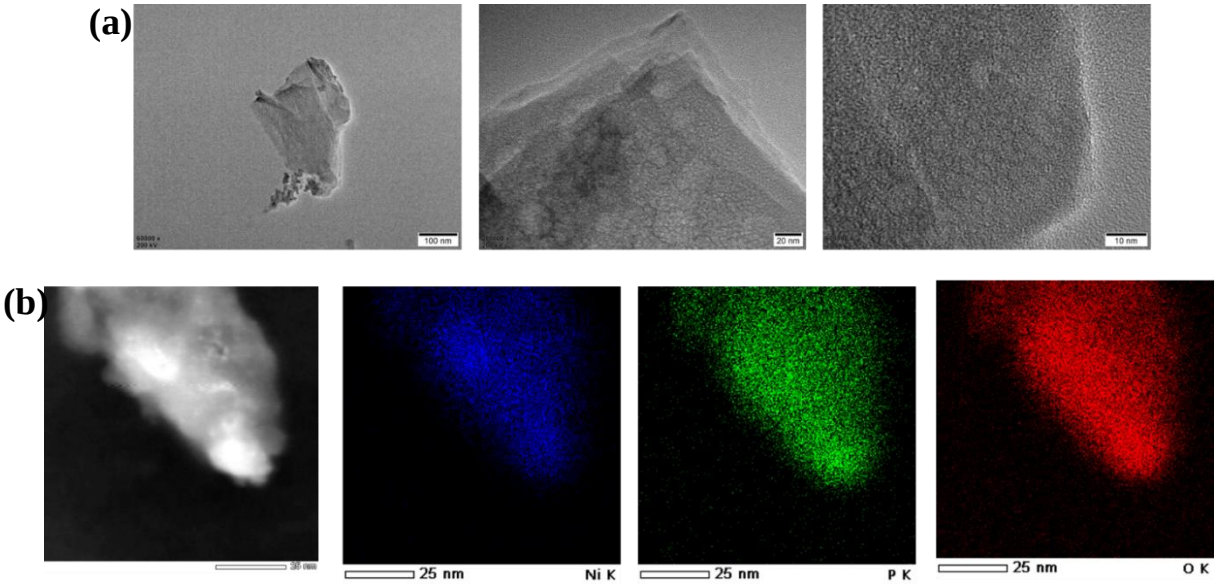

Figure 5.4 (a)TEM and HRTEM image of NiP. (b) HADDF-STEM-EDS elemental maps of NiP nanosheet.

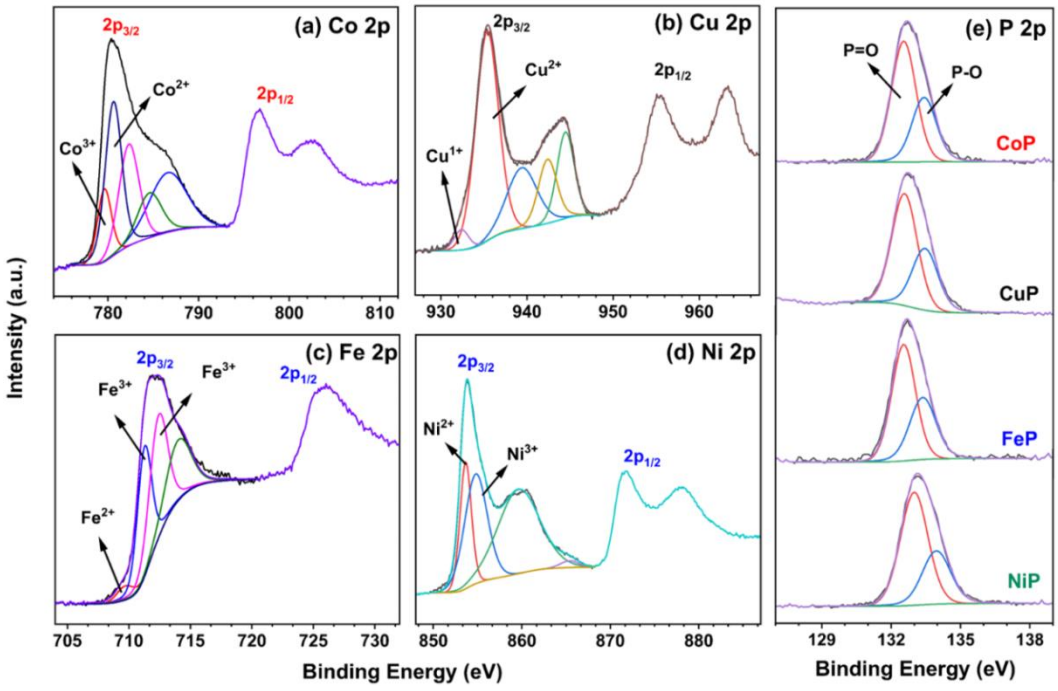

Figure 5.5 High-resolution XPS of a) Co 2p, b) Cu 2p, c) Fe 2p, d) Ni 2p and e) P 2p of the as-prepared CoP.

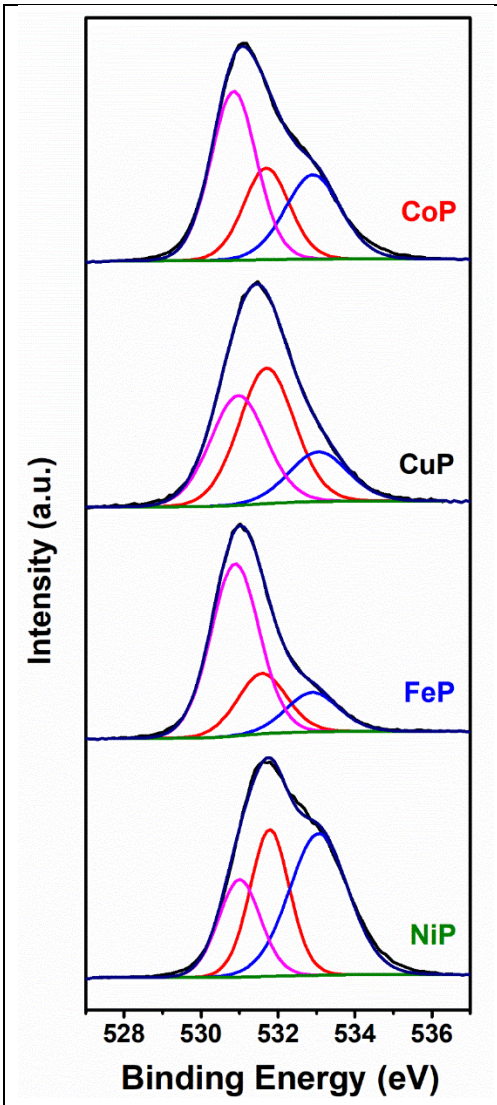

Figure 5.6 O1s spectra for all M-PO_4

Figure 5.5e shows P 2p core level spectrum for all catalysts. The spectra show a broad peak, which upon deconvolution, reveals the $2p_{3/2}$ and $2p_{1/2}$ spin-orbit doublet centered at 133.0 eV and 133.9 eV, respectively, for all M-PO_4, except NiP. O 1s spectra recorded for all phosphates are shown in Figure 5.6; deconvolution shows three peaks at 530.5±0.2, 531.5±0.2, and 532.8±0.2 eV. First two features are attributed to the O-atoms predominantly associated to octahedral and tetrahedral coordination, respectively. Third feature at 532.8 eV is attributed to atmospheric contamination components, like water, CO_2.[44]

5.2.4 X-ray valence band spectroscopy study of M-PO_4

X-ray valence band (XVB) spectral results of all M-PO_4 catalysts are shown in Figure 5.7a. In the XVB spectra, the highest occupied VB appears between 1 and 5 eV for all catalysts. However, the presence of intense main VB is attributed to the contribution from M (Co, Cu, Fe and Ni) 3d and O 2p orbitals. Interestingly, CoP shows a distinct onset of VB at the lowest BE, compared to all other phosphates. Compared to the VB onset of NiP, the same for CoP is shifted by 0.7 eV to the lower BE. In general, VB feature appearing at low energy corresponds to higher activity, while the high BE features indicate the reduced activity or more stability of material. Co metal oxidation to various oxides states by in-situ XPS reveal the presence of Co^{3+} 3d feature at lower BE in the VB, followed by Co^{2+} 3d feature.[45] This asserts the predominant contribution of Co 3d orbitals to the electronic structure, while CuP and FeP exhibit a combination of metal 3d along with O 2p orbitals.

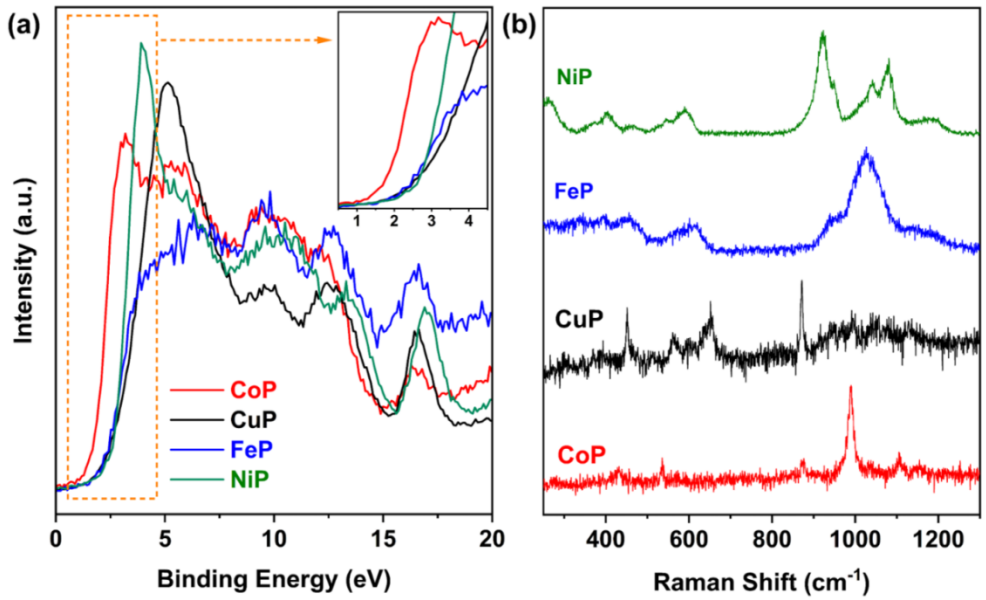

Figure 5.7 (a) X-ray valence band spectra of metal phosphates; inset shows the enlarged view of VB-onset. (b) Raman spectra recorded for all metal phosphates.

NiP exhibits an intermediate character between the two sets. Further, the VB-onset of NiP, FeP and CuP is at the same BE, VB-maximum appears at the lowest for NiP, followed by CuP and FeP. This indicates a trend in activity from high to low (CoP-NiP-CuP~FeP), which is in conformity with the LSV results, shown later.

5.2.5 Raman spectral studies

Raman spectra were recorded for M-PO_4, mainly to understand the structural aspects. Raman results recorded are shown in Figure 5.7b. Distinct peaks corresponding to the vibrational modes of the free oxo-anion $(PO_4)^{3-}$ were observed in the metal phosphates, encompassing a singlet (A_1) at approximately 971 cm^{-1}, a doublet (E) around 465 cm^{-1}, and two triply degenerate (F_2) modes, namely υ_3 at 1027 and υ_4 at 567 cm^{-1}. The symmetric and asymmetric stretching modes of the P-O bonds were associated with (υ_1 and υ_3), while (υ_2 and υ_4) primarily involved O-P-O symmetric and asymmetric bending modes, with a minor contribution from P vibration.[46] In CoP, the most prominent symmetric stretching peak identified at 989 cm^{-1}, with corresponding antisymmetric and bending modes appearing weak at approximately 1100 and 420 cm^{-1}, respectively.[47] CuP exhibited only faint characteristic peaks related to vibrations of $(PO_4)^{3-}$. FeP displayed a broad and intense symmetric stretching peak at 1025 cm^{-1}, indicating a non-distorted $(PO_4)^{3-}$ tetrahedral structure. Notably, FeP showed typical bulk characteristics in morphology and Raman spectra, whereas other phosphates demonstrated either shifts or low-intensity Raman features, suggesting their 2D nature.[48] On the other hand, NiP exhibited both features of antisymmetric modes between 1050 and 1100 cm^{-1}, with a red-shifted symmetric

stretching peak at around 900 cm^{-1}. The correlation effect brought about by the coupling of the Ni-O units in the structure was identified as the cause of the split in the asymmetric stretching mode.[46]

5.2.6 GLYOR Performance in Alkaline Media

As stated in the experimental section, electrochemical studies for GLYOR were carried out using electrocatalysts after a thorough examination of the physical and chemical properties of the metal phosphates. An ideal GLYOR electrocatalyst should show strong activity towards glycerol oxidation and negligible (or minimal) activity towards the OER because the OER from water oxidation is the main competitive anodic process. Water oxidation on these metal phosphate catalysts was also studied under the identical circumstances without glycerol to aid in comparison. Figure 5.8a's LSV polarisation curves show how metal phosphates perform in terms of OER both with and without 0.1 M glycerol. The metal phosphates showed an exceptionally high onset potential in the range of 1.55 to 1.68 V (vs RHE) applied potential needed to reach a current density of 10 mA/cm2 when glycerol was not present. All metal phosphates showed a considerable decrease in the beginning of GLYOR in the presence of glycerol, suggesting a kinetically favourable glycerol oxidation over the OER. In particular, CoP showed the lowest onset potential (1.12 V vs RHE), while the next lowest values were 1.24, 1.24, and 1.27 V vs RHE for NiP, FeP, and CuP, in that order. Figure 5.8b's iR-corrected polarisation curves confirm the trend seen in electrocatalysts' catalytic activity towards GLYOR. It is crucial to note that the catalytic performances of the metal phosphates are intrinsic to the catalysts themselves, as the bare Ni foam exhibits poor catalytic activity for GLYOR. Figure 5.8c presents a comparison of voltage required by all the metal phosphate catalysts to achieve current densities of 10, 50, 100 and 200 mA/cm^2. The disparity in the potentials towards GLYOR has been shown in the Figure 5.8c. In Figure 5.9, at current densities of 10, 20 and 50 mA/cm^2, CoP exhibits a potential difference of 340, 350 and 350 mV between GLYOR and OER, respectively. Additionally, an assessment of the electrocatalytic kinetics for both GLYOR and OER was conducted through Tafel plots analysis derived from LSV data, as shown in Figure 5.8d. This result highlights a considerably reduced Tafel slope value of 113.2 mV/dec specifically for GLYOR with CoP nanosheet, among the metal phosphates. These findings underscore the superior electrocatalytic GLYOR performance of CoP among the metal phosphates. It may be noted that the Tafel slope for GLYOR and OER are comparable, except for CuP, but at different potentials.

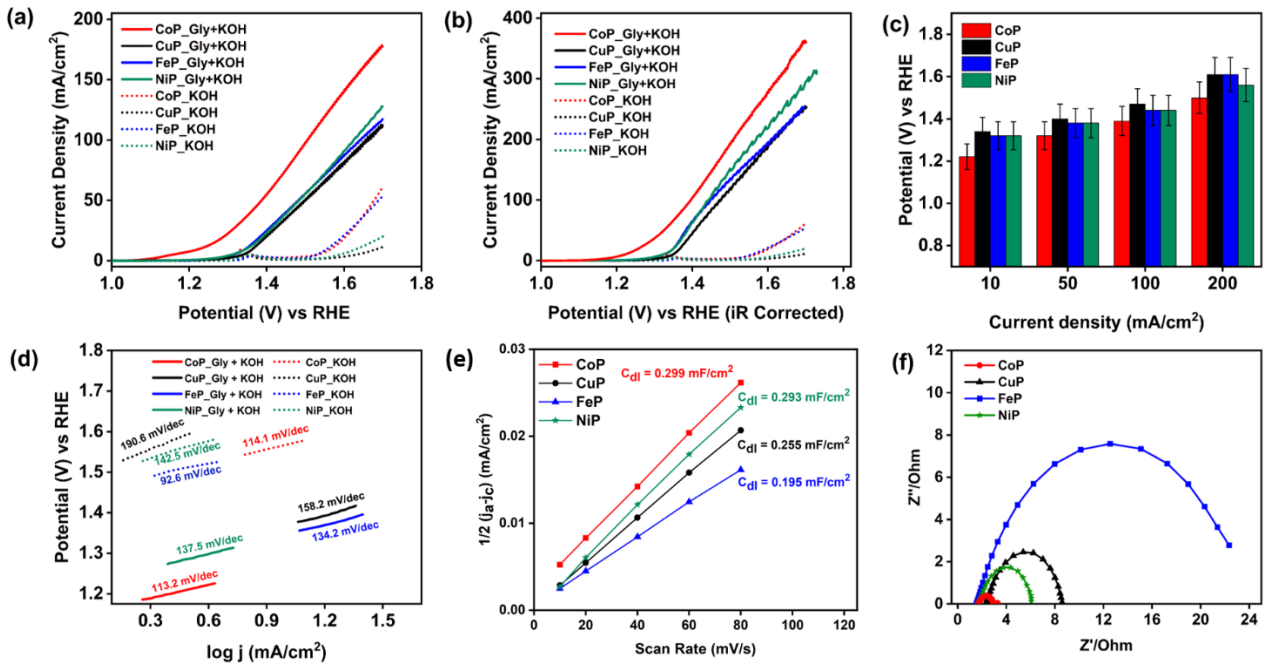

Figure 5.8 a) Glycerol Oxidation Reaction (GLYOR) Linear Sweep Voltammetry (LSV) curves (based on geometric current densities, mA/cm^2) for the series (Co, Cu, Fe, and Ni phosphate) on Ni foam at 5 mV/s in 0.1 M glycerol + 1 M KOH (solid line) and without glycerol in 1 M KOH (dotted line). b) 85% iR corrected LSV curve. c) Bar graph comparing current densities for all phosphates. d) Tafel plots of CoP, CuP, FeP, and NiP in 1 M KOH with and without 0.1 glycerol. e) Capacitive current densities of different catalysts plotted against the scan rate 10-80 mV/s and corresponding Double-Layer Capacitance (Cdl) values estimated through linear fitting of the plots. f) Nyquist plots of different catalysts recorded at a given potential of 0.35 V (vs SCE) with a frequency range of 0.1–100 kHz.

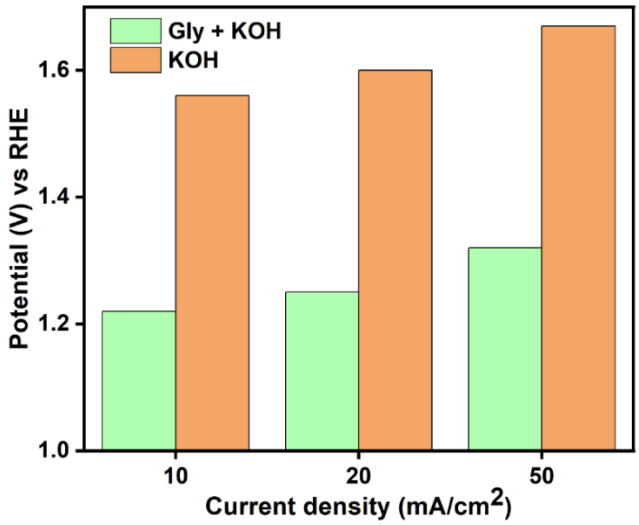

Figure 5.9 A bar graph of potential-difference between GLYOR and OER in CoP nanosheet

5.2.7 ECSA calculation

The C_{dl} measurement (Figure 5.8e) shows that the (C_{dl}) for CoP is 0.299 mF/cm^2. However, the capacitance values observed for NiP (0.293 mF/cm^2), CuP (0.255 mF/cm^2), and FeP (0.195 mF/cm^2) are almost similar to that of CoP. The C_{dl} values are calculated from CV graphs at different scan rate, as shown in Figure 5.10. The measured C_{dl} value and corresponding ECSA values CoP (7.475 cm^2), NiP (7.325 cm^2), CuP (6.375 cm^2) and FeP (4.875 cm^2) indicates that all of the electrocatalysts have almost same number of active sites.[49,50] However, the intrinsic activity of the CoP is significantly high as compared to other metal phosphate catalyst, which resonates in XPS-VB spectra (Figure 5.7a); CoP exhibits the lowest VB energy among phosphates, which leads to enhanced GLYOR activity.

To further gain in to the interfacial reaction behaviour of catalyst, electrochemical impedance spectroscopy (EIS) was carried out. The EIS Nyquist plots presented in Figure 5.8f shows that a notable reduction in charge transfer resistance (R_{ct}) for CoP in comparison to the other catalysts. Specifically, the R_{ct} of CoP (3 Ω) is significantly smaller than that of NiP (6.06 Ω), CuP (8.59 Ω), and FeP (24.62 Ω), indicating accelerated charge-transfer kinetics between the CoP electrode and electrolyte. Despite almost similar number of active sites in all the electrocatalyst, CoP possessed accelerated charge transfer behaviour and is mainly due to the high intrinsic activity of active sites present, which enhanced GLYOR activity.

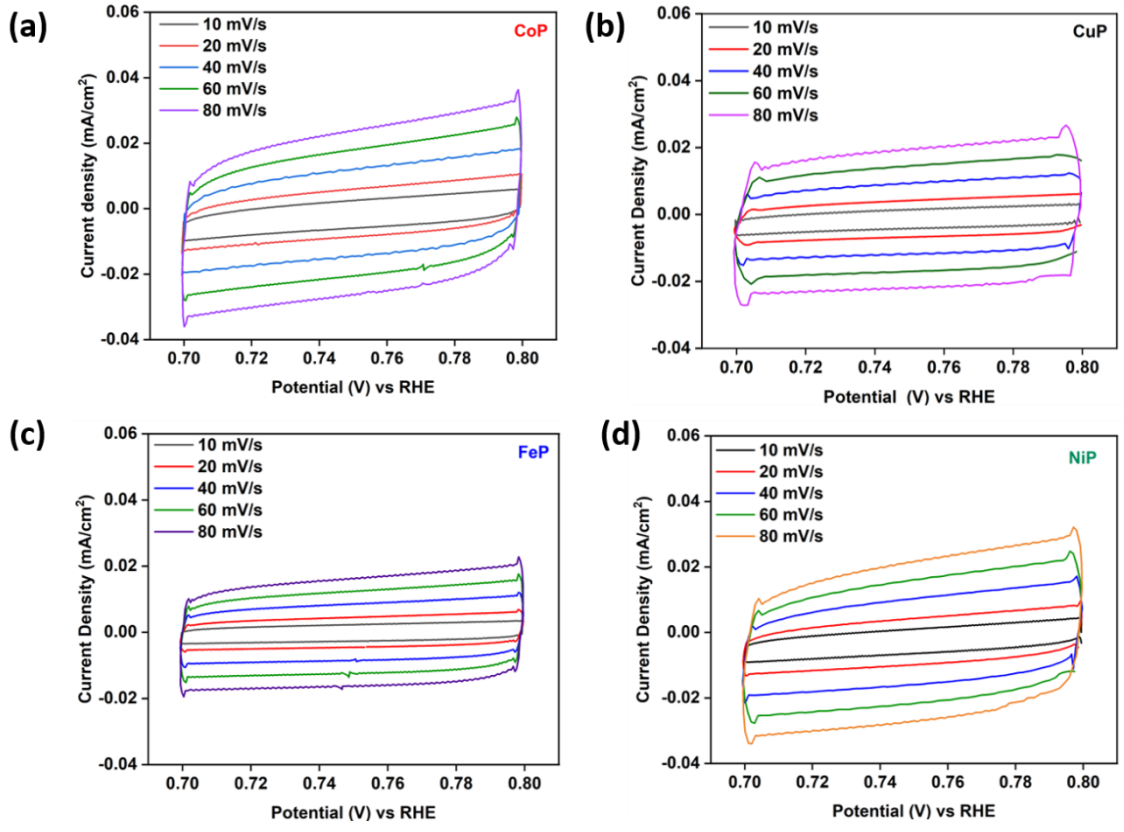

Figure 5.10 Double-layer capacitances (C_{dl}) measurement of different metal phosphates. Cyclic voltammetry (CV) profile (a) CoP (b) CuP, (c) FeP and (d) NiP in the non-faradaic region of potential range 0.7 V to 0.8 V vs RHE.

5.2.8 Glycerol product selectivity and conversion study

To assess the long-term GLYOR performance and its anodic products, constant chronopotentiometry (CP) at 10 mA/cm^2 was conducted for a duration of 15 h. The stability of CoP was observed for the initial 12 h of CP, after which formate oxidation commenced (to carbonate) due to decrease in glycerol concentration and an increase in OER. Consequently, achieving and maintaining the 10 mA/cm^2 required an increase in potential (Figure 5.11a). A significant potential increase during glycerol oxidation after about 12 h, suggests the onset of formate oxidation to carbonate. Furthermore, the reaction mechanism was investigated by quantifying 3 h interval samples through ^{1}H NMR analysis, as depicted in Figure 5.11b.

A detailed carbon balance study was also conducted after each 3 h time duration of the GLYOR process, and the results are given in Table 5.1.

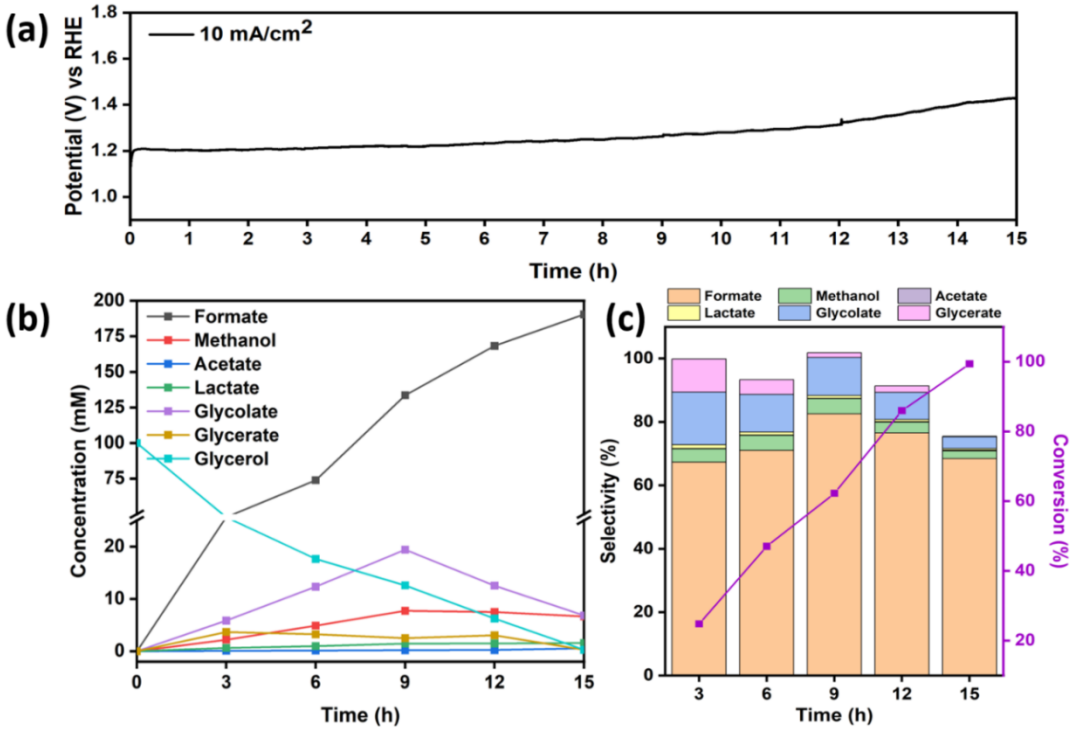

Figure 5.11 (a) Time dependent chronopotentiometry (CP) reaction carried out at constant 10 mA/cm^2 for the glycerol conversion with CoP electrocatalyst. (b) Quantification of glycerol conversion and reaction products by ^{1}HNMR with CoP. (c) Glycerol conversion and products selectivity observed over a period of 15 h at constant CP.

A decrease in glycerol content and a concurrent increase in formate concentration as a function of reaction time along with near 100 % carbon balance in 9 h and suggesting an efficient 100%

conversion of glycerol to formate in 15 h (Figure 5.11b). Major intermediates detected in GLYOR include glycerate, glycolate, and methanol, while acetate and lactate are minor intermediates, as shown in ^{1}H NMR (Figure 5.12).

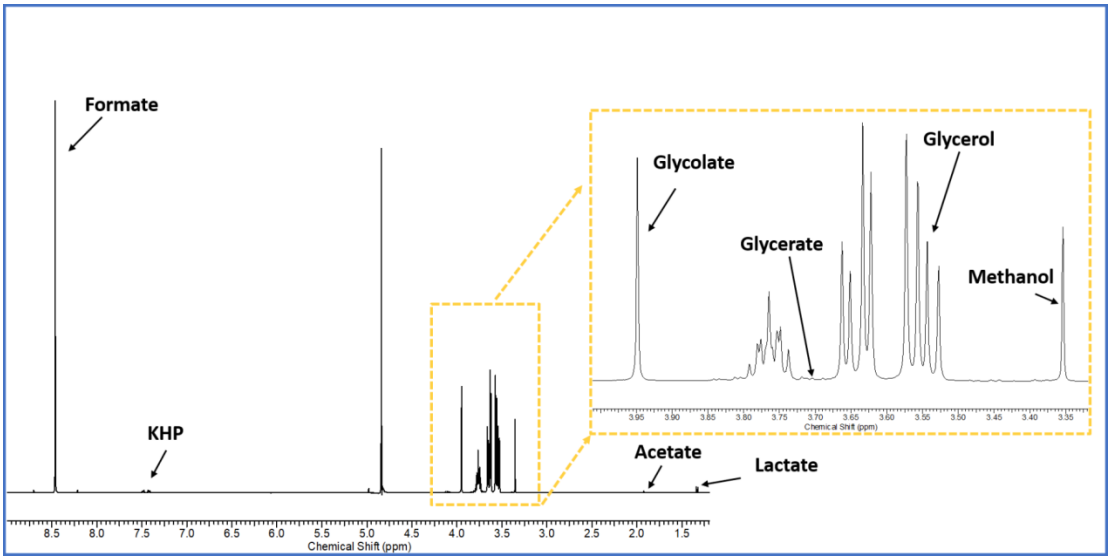

Figure 5.12 ^{1}H NMR spectra for intermediate products from GLYOR.

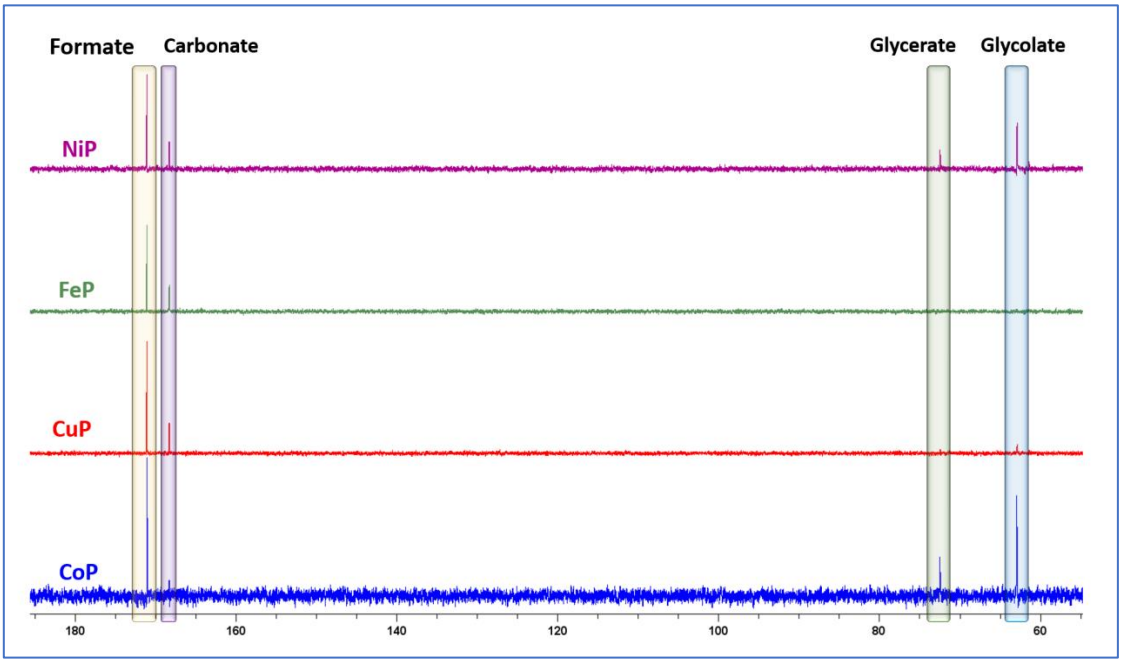

Figure 5.13 ^{13}C NMR spectrum of 15 h GLYOR sample for all M-PO_4.

In Figure 5.11c, at 9 h, formate selectivity reaches 82%, and glycerol conversion stands at ~62%. Over time, formate undergoes further oxidation to carbonate due to decreasing reactant availability, leading to a conversion exceeding 80% and formate selectivity reaching 78% at 12 h. By the end of 15 h, 100 % glycerol conversion was achieved, although the carbon balance

is less than 100% due to a significant formation of carbonate, through continued oxidation of formate; this is evident from a small carbonate peak observed in ^{13}C NMR data (Figure 5.13).

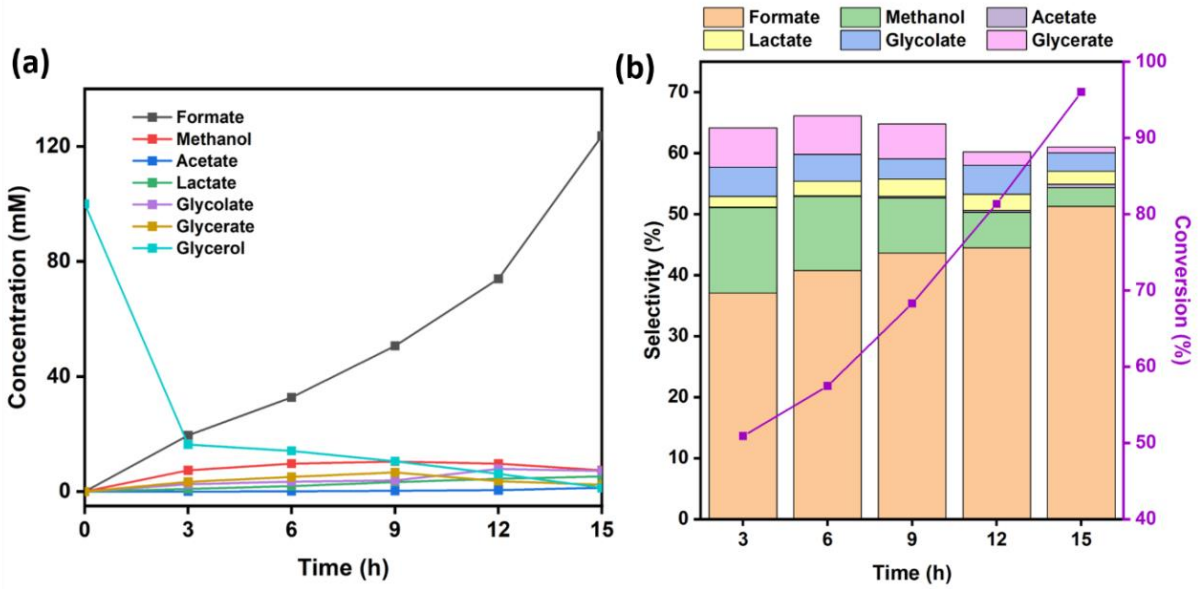

Figure 5.14 (a) Quantification of glycerol conversion and reaction products by ^{1}H-NMR with CuP. (b) The selectivity and conversion of 15 h constant CP.

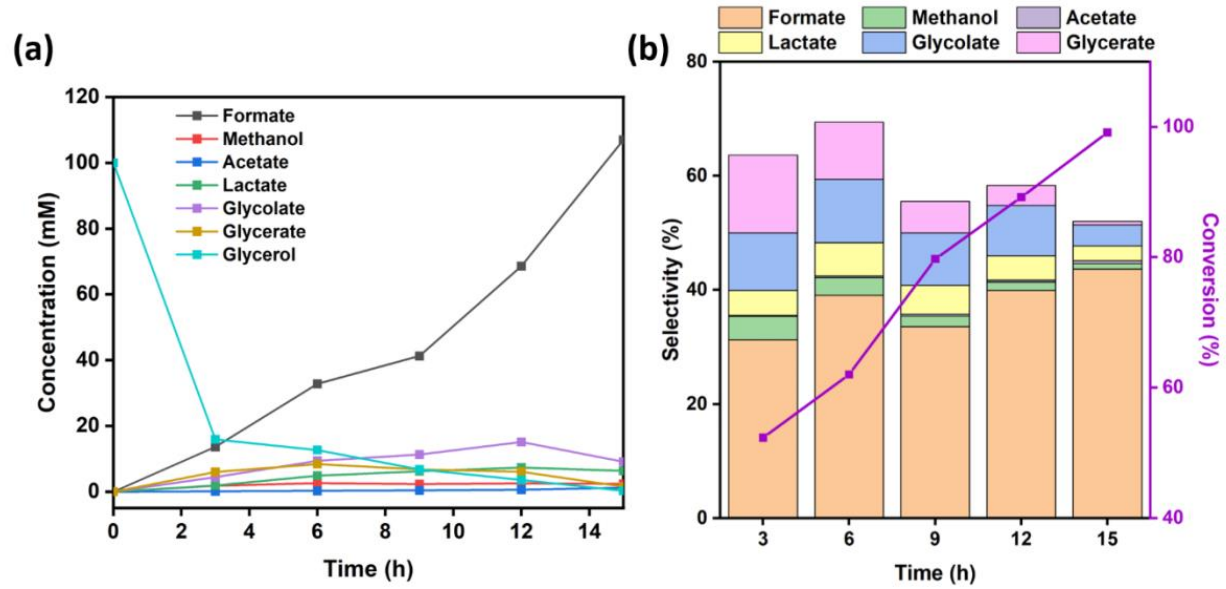

Figure 5.15 (a) Quantification of glycerol conversion and reaction products by ^{1}H-NMR with FeP. (b) The selectivity and conversion of 15 h constant CP.

A similar kinetic study was conducted for CuP, FeP, and NiP, with quantification and the glycerol conversion and products selectivity results are provided in Figure 5.14-5.16 and table 5.1. With NiP, under comparable conditions at a current density of 10 mA/cm^2, a noteworthy 93 % glycerol conversion and 64% formate selectivity was observed in 12 h reaction time.

However, the carbon balance diminished beyond this duration due to the continued oxidation of formate (Table 5.1). Conversely, CuP and FeP exhibited lower conversion rates, with approximately 50% selectivity for formate observed during a 15 h constant current at 10 mA /cm^2. Notably, CuP and FeP necessitated an increment in potential to achieve the desired 10 mA/cm^2 current density, leading to the oxidation of formate to CO_2 (Figure 5.17).

Table 5.1 Selectivity, conversion and carbon balance of all metal phosphate. (a) CoP (b) CuP, (c) FeP and (d) NiP

(a) CoP

Time (h)	Formate	Methanol	Acetate	Lactate	Glycolate	Glycerate	Conversion %	Carbon balance
3	67.32	4.14	0.15	1.19	16.56	10.46	24.82	99.8
6	71.03	4.71	0.12	0.92	11.85	4.67	47.05	93.3
9	82.53	4.77	0.11	0.89	11.98	1.53	62.25	100
12	76.54	3.41	0.10	0.67	8.56	2.06	85.96	91.3
15	68.47	2.39	0.19	0.56	3.69	0.14	99.38	75.4

(b) CuP

Time (h)	Formate	Methanol	Acetate	Lactate	Glycolate	Glycerate	Conversion %	Carbon balance
3	37.08	14.00	0.11	1.70	4.79	6.41	50.89	64.11
6	40.77	12.12	0.13	2.40	4.34	6.32	57.47	66.11
9	43.64	9.01	0.22	2.87	3.32	5.72	68.29	64.81
12	44.49	5.81	0.29	2.67	4.75	2.19	81.34	60.22
15	51.26	3.06	0.54	2.19	2.97	1.00	96.02	61.04

(c) FeP

Time (h)	Formate	Methanol	Acetate	Lactate	Glycolate	Glycerate	Conversion %	Carbon balance
3	31.23	4.12	0.20	4.31	10.11	13.65	52.33	63.64
6	39.07	3.08	0.28	5.79	11.14	10.02	62.01	69.42
9	33.58	1.85	0.30	5.07	9.18	5.50	79.76	55.50
12	39.92	1.46	0.33	4.25	8.81	3.51	89.20	58.31
15	43.65	0.97	0.48	2.59	3.72	0.61	99.16	52.03

(d) NiP

Time (h)	Formate	Methanol	Acetate	Lactate	Glycolate	Glycerate	Conversion %	Carbon balance
3	65.49	3.78	0.57	8.61	12.49	17.43	11.60	98.19
6	62.39	2.30	0.67	9.13	11.15	12.97	37.82	98.64
9	56.15	1.40	0.70	6.89	9.36	8.65	61.09	83.17
12	64.61	0.54	1.03	3.95	4.16	4.12	93.92	78.43
15	22.96	0.33	0.29	2.05	2.49	2.26	93.43	30.41

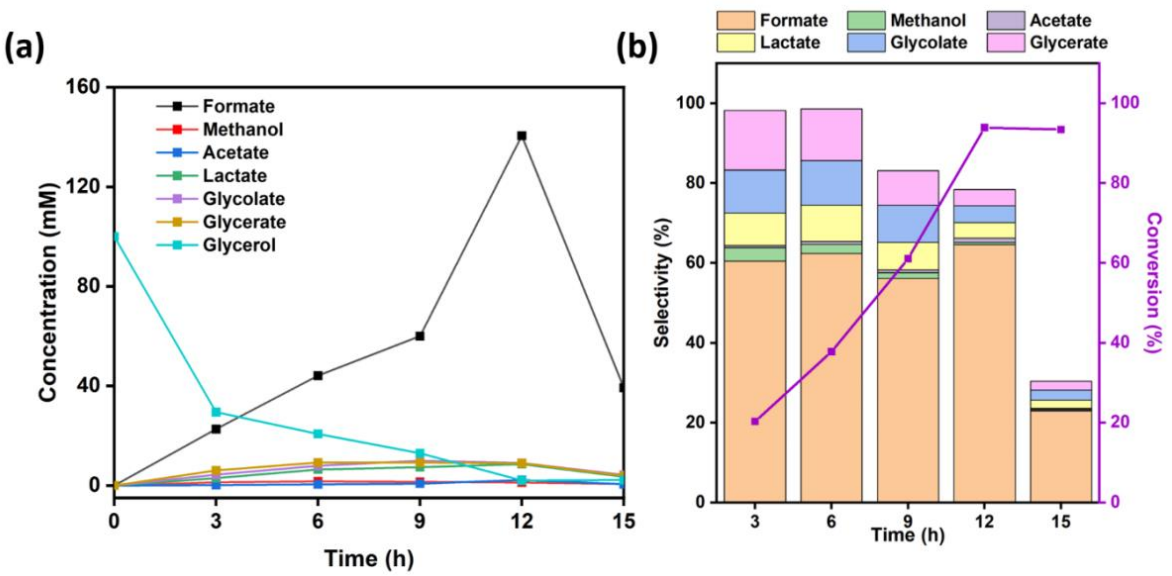

Figure 5.16 (a) Quantification of glycerol conversion and reaction products by ^{1}H-NMR with NiP. (b) The selectivity and conversion of 15 h constant CP.

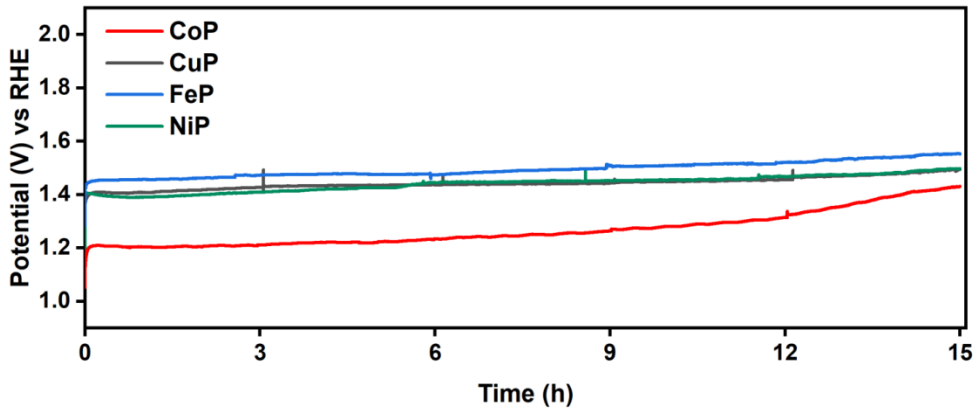

Figure 5.17 Time dependent chronopotentiometry (CP) reaction carried out at constant 10 mA/cm^2 for the GLYOR with all M-PO_4 electrocatalyst.

5.2.9 Proposed mechanism pathway for glycerol oxidation

Typical glycerol oxidation mechanism on metal oxide or noble metal in an alkaline medium reported in the literature is as follows. First a glycerol molecule adsorbs on the catalyst surface, initiating dehydrogenation. This process leads to the formation of glycolaldehyde (GALD) or dihydroxyacetone (DHA), with subsequent reversible inter-conversion facilitated by base-catalysis. Through a dehydration step, DHA could transform into pyruvaldehyde or 2-hydroxypropenal. These intermediates may undergo conversion into lactate via the Cannizzaro rearrangement, and subsequently, acetate and formate are produced through C−C cleavage (Figure 5.18).[51,52]

In the current work, it is evident from Figure 5.11 that high formate selectivity with significant selectivity for glycolate and glycerate underscores the oxidation occurs from the either end of terminal carbon. Although no glyceraldehyde was observed in the present work, it is very likely to undergo fast oxidation to glycerate and subsequently to glycolate and formate.

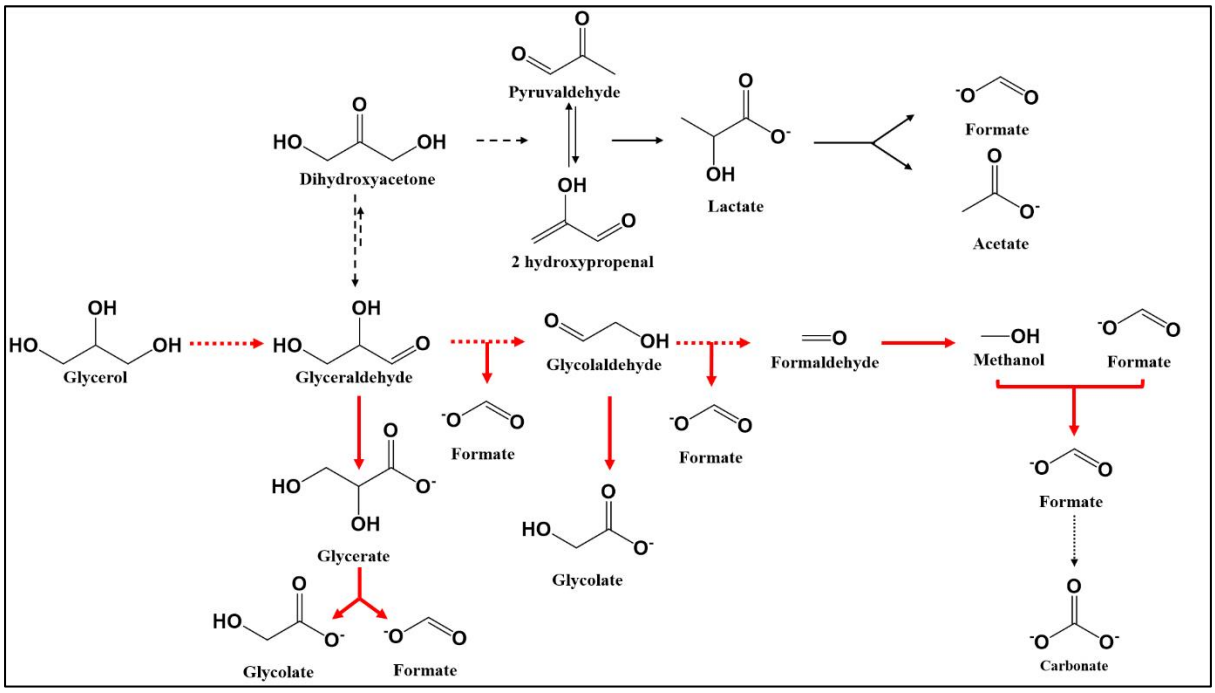

Figure 5.18 Illustrates the proposed mechanistic pathway for the electro-catalytic oxidation of glycerol to formate on CoP in an alkaline medium, with emphasis on the suggested dominant pathways indicated by thick red arrows and dotted arrows shows unobserved intermediates. Solid and dashed black arrows indicates a minor and alternate pathway for products formation.

Minor amount of lactate and acetate formation in the current reaction (Figure 5.11c) also indicates a parallel mechanism, to a small extent, occurs through DHA, pyruvaldehyde. The major conclusion that could be derived is the efficient oxidative C-C cleavage of glycerol and all intermediates, such as glycerate and glycolate, followed by preferential/selective oxidation to formate, on the CoP catalyst under the current experimental conditions. It is also evident from Figure 5.11c that irrespective of the nature of intermediates all of them undergo oxidation to formate. This concept may be extended to bigger molecules with suitable catalysts under relevant conditions and more efforts in this direction is desired.

5.2.10 Sustainable performance study for CoP catalyst

In the realm of water electrolysis, a critical hurdle lies in the imperative reduction of the operational potential to curtail input electricity consumption. The substantial overpotential inherent with the OER in water splitting renders it exceptionally challenging to achieve a

noteworthy reduction in power consumption beyond a certain threshold. Nevertheless, this obstacle was effectively surmounted by the synergistic coupling of GLYOR and HER in a two-electrode electrolyzer configuration, as delineated in Figure 5.19a.

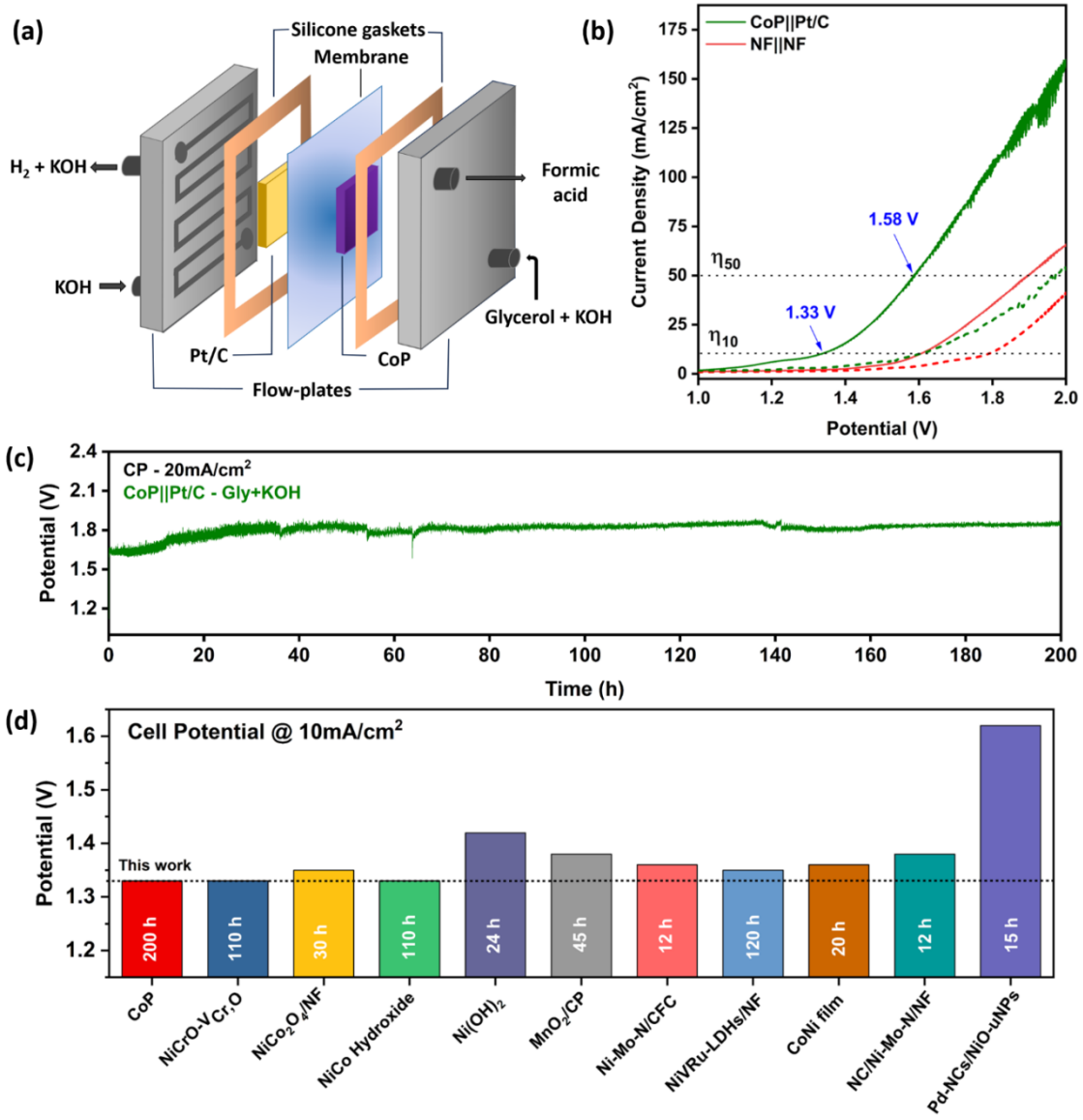

Figure 5.19 (a) Schematic of a two-electrode alkaline electrolyzer engaged in GLYOR to formate at the anode and HER at the cathode. (b) LSV plot observed for GLYOR in the electrolyzer, utilizing CoP/NF as the anode and Pt/C as the cathode (Solid line – Glycerol + KOH and dash line – KOH). Same measurement was made on NF also to rule out the GLYOR contribution from it. (c) A sustainability investigation of GLYOR at 20 mA/cm² was conducted using a two-electrode electrolyzer employing CoP||Pt/C. (d) Comparison of electrolytic efficiency of GLYOR at 10 mA/cm^2 for CoP with alternate electrocatalysts reported in the literature.

The electrolyzer architecture featured a Pt/C cathode and a CoP anode, spatially segregated by an anion exchange membrane, with specific details provided in the experimental section.

Figure 5.19b shows the LSV plot for GLYOR in the alkaline electrolyzer, revealing the concurrent electrochemical generation of hydrogen and formate at room temperature. At higher temperatures, between 60 and 75 °C, a large enhancement in electrolyzer activity performance is expected; it is worth performing this experiment. Within the electrolyzer setup at room temperature, a current density of 10 mA/cm^2 (50 mA/cm^2) was achieved at a notably low potential of 1.33 V (1.58 V), as shown in Figure 5.19b. Under these operational conditions, the system manifested simultaneous HER and glycerol oxidation performance. In contrast, a conventional water electrolysis experiment, employing a two-electrode setup with the same CoP||Pt/C cell, but devoid of glycerol supplementation, necessitated a higher potential of 1.60 V (1.89 V) to attain an identical current density of 10 (50) mA/cm^2. Due to the significantly more advantageous thermodynamics of GLYOR on CoP surface, the constructed electrolyzer necessitates just ~4.2 kWh/m^3 of H_2 at a current density of 100 mA/cm^2. This stands in stark contrast to the about 5.5 kWh/m^3 of H_2 needed by conventional alkaline electrolyzers. The remarkable low cell voltage exhibited by the CoP||Pt/C system in the context of biomass-component-assisted water splitting distinguishes it as an attractive feature relative to the majority of reported systems, as outlined in Table 5.2. Importantly, it is noteworthy that hydrogen constituted the exclusive gaseous product observed, with no oxygen or carbon-containing by-products, such as CO and CO_2. In addition, sustainable performance of biomass component-based electrolysis was demonstrated via a chronoamperometry experiment for 200 h conducted at 20 mA/cm^2 current density and the result is shown in Figure 5.19c. It shows the voltage remains constant at ~1.63 V throughout the 10 h operation for glycerol oxidation and further the ~200 mV potential has been increased for secondary molecule oxidation, which is constant throughout the reaction and shows the stability of the catalyst. During the on-going reaction within a 25 h time frame, the GLYOR sample was subjected to analysis via ^{1}H NMR. The results confirmed an increase in formate concentration, as depicted in Figure 5.20, alongside glycerol conversion. Subsequently, after 75 h, there was a decline in formate concentration attributed to its further oxidation to carbonates. To enhance the prolonged efficacy of the catalyst, electrolyte was introduced into the solution after the 75 h mark. Under constant current density (CP) of 20 mA/cm^2, hydrogen production rate remained consistent at an average of 32.5 mL/h throughout the continuous operation of the overall reaction. The Faradaic efficiency of the HER was determined to be approximately 98%. The calculation of the FE for HER involved a thorough analysis comparing theoretical and experimental H_2 production, and detailed calculations are expounded upon in the experimental section. Catalytic

performance exhibited by CoP is either comparable or better than that of other electrocatalysts documented in the literature for overall electrolysis with GLYOR under same conditions (Figure 5.19d).

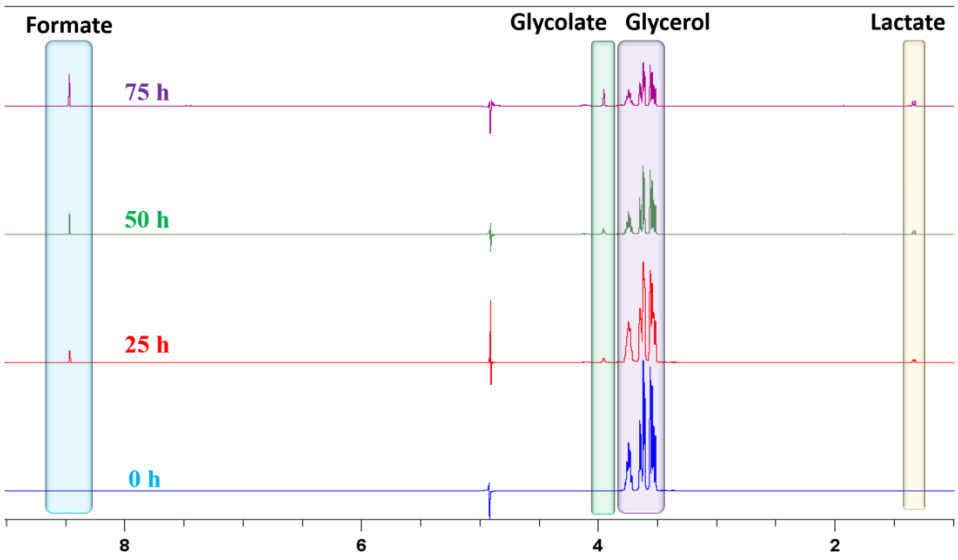

Figure 5.20 ^{1}H-NMR spectrum of GLYOR in electrolyzer system with CoP||Pt/C.

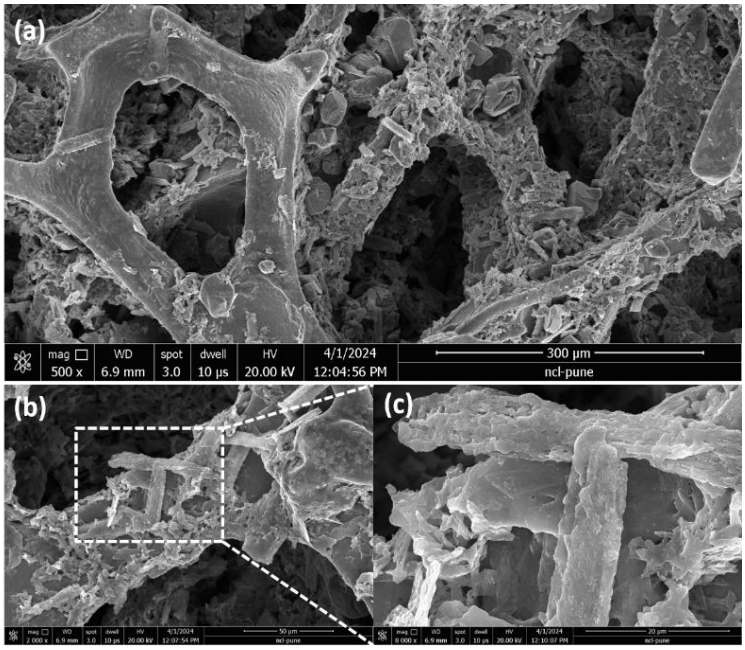

Figure 5.21 FESEM recorded after the sustainability studies carried out for 200 h (shown in Fig. 5.21c). Except for some agglomeration, nanosheet morphology remains intact, as seen in panel c.

However, current study shows the sustainability for longer hours, along with very high selectivity for formate production. This is depicted in Figure 5.19d and many other catalysts are listed in Table 5.2. FESEM characterization (Figure 5.21) carried out after 200 h GLYOR

(Figure 5.19c) exhibits the nanosheet morphology and it is intact, except for some agglomeration. XRD pattern remains the same as observed in Figure 5.1b. These results testify that CoP catalyst remains stable and did not undergo any changes due to prolonged reaction.

Table 5.2 Comparsion table of recent reported work in GLYOR and other low oxidizing molecules.

Catalyst	**Electrolyte 1 M KOH + 0.1 M Glycerol**	**Cell Potential at 10mA/cm^2**		**Selective Product**	**Ref.**
		3-electrode system (vs RHE)	**2-electrode system (V)**		
$Co_3(PO_4)_2$ (CoP)	**Yes**	**1.22**	**1.33**	**Formate**	**This work**
$CuCo_2O_4$	0.1 M KOH + 0.1 M Glycerol	1.26	-	Formate	53
NiCrO-$V_{Cr,O}$	Yes	1.37	1.33	Formate	54
$NiCo_2O_4$/NF	1 M NaOH with 0.1 M Glycerol	1.23	1.35	Formate	55
NiO	0.1 M KOH + 0.1 M Glycerol	1.28	-	Formate	56
Co/Co_3O_4-rGO	Yes	1.42	-	Formate	57
NiCo hydroxide	Yes	-	1.33	Formate	58
Anode: $Ni(OH)_2$ Cath.: $NiCrO_x$/Ni	2 M LiOH+0.1 M Glycerol	1.23	1.42	Formate	59
CuCo oxide	0.1 M KOH + 0.1 M Glycerol	1.25	-	Formate and Glycolic acid	60
MnO_2-CuO/CF	1 M KOH + 0.1 M Glycerol	1.3	-	DHA	61
MnO_2/CP	0.005 M H_2SO_4 + 0.2 M Glycerol	1.36	1.40	Formate	62
NiO/NF	Yes	1.3	-	Formate	63
Ni-Mo-N/CFC	Yes	1.30	1.36	Formate	64
NiO_x/MWCNTs-O_x	1.0 M KOH + 1 M Glycerol	1.31	-	Oxalate	65
NiVRu-LDHs/NF	Yes	1.24	1.35	Formate	66
MnO_2/NF	0.1 M $Na_2B_4O_7$ + 0.1 M Glycerol	1.45	-	DHA	67
$Co(OH)_2$@HOS/ CP	1 M KOH + 3 M methanol	1.385	1.497	Formate	68
NiMn LDH	1 M KOH + 3 M methanol	1.33	1.33	Formate	69
$Ni(OH)_2$/NF	1 M KOH + 0.5 M methanol	1.36	1.52	Formate	70
Co-P/CF	1 M KOH + 50 mM HMF	-	1.4	FDCA	71
NiSe@NiOx	1 M KOH + 10 mM HMF	1.35	1.50	FDCS	72

Ni_2P/Ni/NF	1 M KOH + 0.3 M Furfural	1.34	1.48	2-Furoic acid	73
$CoMn/CoMn_2O_4$	1 M KOH + 0.5 M urea	1.32	1.51	CO_2, N_2	74
Ni_3S_2/NF	1 M KOH + 0.01 M HMF	1.35	1.46	FDCA	75
Co/Ni Film	1 M KOH + 0.33 M Glycerol	1.30	1.36	Hydroxy pyruvate	76
NC/Ni-Mo-N/NF	Yes	1.16	1.38	Formate	77
PdNCs/NiO-uNPs	1 M KOH + 0.5 M Glycerol	-	1.62	Glyceraldehyde	78

5.3 Conclusion

In conclusion, this study elucidates a distinctive morphology-dependent selectivity for formate and glycerol conversion on metal phosphates, showcasing simultaneous and highly efficient electrocatalytic hydrogen generation. Significantly, cobalt phosphate (CoP) has been identified as a novel and proficient catalyst, demonstrating both efficiency and stability in selectively producing formate through glycerol oxidation in alkaline conditions at ambient temperature. Particularly, ultrathin 2D-CoP nanosheets exhibit very high selectivity, achieving 82% formate yield compared to other phosphates. The electrochemical oxidative cleavage of the C–C bond proves more favourable on CoP, surpassing NiP, FeP, and CuP catalysts. In the CoP||Pt/C two-electrode electrolyzer, the coupling of anodic GLYOR and cathodic HER results in a current density of 10 mA/cm2 with a minimum cell voltage of 1.33 V. GLYOR ran continuously for more than 8 days (24x7), demonstrating the CoP catalyst's long-term stability in the current experimental setup. By using transition metal phosphate, which is readily available on Earth, for the electrocatalytic oxidation of glycerol, creative solutions and cost-effective approaches to addressing the GLYOR are made possible. These catalysts offer efficient and selective electrochemical glycerol oxidation, yielding formate and other value-added chemicals, along with the production of environmentally friendly hydrogen resources.

The engineered CoP catalyst exhibits remarkable efficiency in catalysing the conversion of glycerol to formate, thereby demonstrating promising prospects for its application in the conversion of diverse biomass feedstocks, including glucose, starch, cellulose, etc. Selective C-C cleavage strategy presented in the present manuscript is worth exploring with any of the bigger molecules listed above and may be evaluated for depolymerisation of low molecular weight polymers. Further, carrying out the electrocatalytic conversions at significantly higher temperatures (50-75 °C) is expected to improve the performance substantially. Another

important aspect is the production of hydrogen under such conditions, which prudently employ a waste/abundant carbon-containing molecules towards producing value added products and hence the hydrogen generated becomes carbon-negative green hydrogen. This type of routes may prove to be helpful to achieve net-zero targets sooner. Nonetheless, more work is desired in these directions.

5.4 References

(1) Dresselhaus, M. S.; Thomas, I. L. *Nature* **2001**, *414*, 332–337.
(2) Zhang, J.; Wang, H.; Tian, Y.; Yan, Y.; Xue, Q.; He, T.; Liu, H.; Wang, C.; Chen, Y.; Xia, B. Y. *Angew. Chemie Int. Ed.* **2018**, *57* (26), 7649–7653.
(3) Gopinath, C. S.; Nalajala, N. *J. Mater. Chem. A* **2021**, *9* (3), 1353–1371.
(4) Zhang, J.; Wang, T.; Liu, P.; Liao, Z.; Liu, S.; Zhuang, X.; Chen, M.; Zschech, E.; Feng, X. *Nat. Commun.* **2017**, *8* (1), 15437.
(5) Rajaambal, S.; Sivaranjani, K.; Gopinath, C. S. *J. Chem. Sci.* **2015**, *127* (1), 33–47.
(6) Navarro, R. M.; Peña, M. A.; Fierro, J. L. G. *Chem. Rev.* **2007**, *107* (10), 3952–3991.
(7) Holladay, J. D.; Hu, J.; King, D. L.; Wang, Y. *Catal. Today* **2009**, *139* (4), 244–260.
(8) Li, X.; Hao, X.; Abudula, A.; Guan, G. *J. Mater. Chem. A* **2016**, *4* (31), 11973–12000.
(9) Zheng, D.; Li, J.; Ci, S.; Cai, P.; Ding, Y.; Zhang, M.; Wen, Z. *Appl. Catal. B Environ.* **2020**, *277*, 119178.
(10) Qin, D.-D.; Tang, Y.; Ma, G.; Qin, L.; Tao, C.-L.; Zhang, X.; Tang, Z. *Int. J. Hydrogen Energy* **2021**, *46* (51), 25771–25781.
(11) Rausch, B.; Symes, M. D.; Chisholm, G.; Cronin, L. *Science (1979)* **2014**, *345* (6202), 1326–1330.
(12) Wei, X.; Wang, S.; Hua, Z.; Chen, L.; Shi, J. *ACS Appl. Mater. Interfaces* **2018**, *10* (30), 25422–25428.
(13) Kim, D.; Oh, L. S.; Tan, Y. C.; Song, H.; Kim, H. J.; Oh, J. *ACS Catal.* **2021**, *11* (24), 14926–14931.
(14) Quispe, C. A. G.; Coronado, C. J. R.; Carvalho Jr., J. A. *Renew. Sus. Energy Rev.* **2013**, *27*, 475–493.
(15) Bulushev, D. A.; Ross, J. R. H. *ChemSusChem* **2018**, *11* (5), 821–836.
(16) Rizk, M. R.; Abd El-Moghny, M. G. *Int. J. Hydrogen Energy* **2021**, *46* (1), 645–655.
(17) Xie, Y.; Sun, L.; Pan, X.; Zhou, Z.; Zheng, Y.; Yang, X.; Zhao, G. *Carbon N. Y.* **2023**, *203*, 88–96.
(18) Dai, C.; Sun, L.; Liao, H.; Khezri, B.; Webster, R. D.; Fisher, A. C.; Xu, Z. J. *J. Catal.* **2017**, *356*, 14–21.
(19) Zhang, Z.; Xin, L.; Li, W. *Appl. Catal. B. Environ.* **2012**, *119–120*, 40–48.
(20) Chauhan, I.; Bajpai, H.; Ray, B.; Kolekar, S. K.; Datar, S.; Patra, K. K.; and Gopinath, C. S. *ACS Appl. Mater. Interfaces* 2024, **16**, 26130-26141.
(21) Lee, S.; Kim, H. J.; Lim, E. J.; Kim, Y.; Noh, Y.; Huber, G. W.; Kim, W. B. *Green Chem.* **2016**, *18* (9), 2877–2887.
(22) Kim, H. J.; Choi, S. M.; Green, S.; Tompsett, G. A.; Lee, S. H.; Huber, G. W.; Kim, W. B. *Appl. Catal. B Environ.* **2011**, *101* (3–4), 366–375.
(23) Choi, S.; Balamurugan, M.; Lee, K.-G.; Cho, K. H.; Park, S.; Seo, H.; Nam, K. T. *J. Phys. Chem. Lett.* **2020**, *11* (8), 2941–2948.
(24) Taitt, B. J.; Nam, D.-H.; Choi, K.-S. A *ACS Catal.* **2019**, *9* (1), 660–670.
(25) Li, J.; Wei, R.; Wang, X.; Zuo, Y.; Han, X.; Arbiol, J.; Llorca, J.; Yang, Y.; Cabot, A.; Cui, C. *Angew. Chemie Int. Ed.* **2020**, *59* (47), 20826–20830.

(26) Vo, T.-G.; Ho, P.-Y.; Chiang, C.-Y. *Appl. Catal. B Environ.* **2022**, *300*, 120723.
(27) Wu, G.; Dong, X.; Mao, J.; Li, G.; Zhu, C.; Li, S.; Chen, A.; Feng, G.; Song, Y.; Chen, W.; Wei, W. *Chem. Eng. J.* **2023**, *468*, 143640.
(28) Zhong, Z.; Li, M.; Wang, J.; Lin, J.; Pan, J.; Jiang, S.; Xie, A.; Luo, S. *Int. J. Hydrogen Energy* **2022**, *47* (29), 13933–13945.
(29) Han, X.; Sheng, H.; Yu, C.; Walker, T. W.; Huber, G. W.; Qiu, J.; Jin, S. *ACS Catal.* **2020**, *10* (12), 6741–6752.
(30) Pei, Y.; Pi, Z.; Zhong, H.; Cheng, J.; Jin, F. *J. Mater. Chem. A* **2022**, *10* (3), 1309–1319.
(31) Wang, Y.; Zhang, M.; Liu, Y.; Zheng, Z.; Liu, B.; Chen, M.; Guan, G.; Yan, K. *Adv. Sci.* **2023**, *10* (13) 2207519.
(32) Xie, H.; Li, Z.; Cheng, L.; Haidry, A. A.; Tao, J.; Xu, Y.; Xu, K.; Ou, J. Z. *iScience* **2022**, *25* (1), 103598.
(33) Yang, J.; Xiao, Y.; Zhao, Q.; Zhang, G.; Wang, R.; Teng, G.; Chen, X.; Weng, M.; He, D.; Mu, S.; Lin, Y.; Pan, F. *Nano Energy* **2019**, *59*, 443–452.
(34) Li, N.; Ai, L.; Jiang, J.; Liu, S. *J Colloid Interface Sci.* **2020**, *564*, 418–427.
(35) Anantharaj, S.; Ede, S. R.; Sakthikumar, K.; Karthick, K.; Mishra, S.; Kundu, S. *ACS Catal.* **2016**, *6* (12), 8069–8097.
(36) Katkar, P. K.; Marje, S. J.; Kale, S. B.; Lokhande, A. C.; Lokhande, C. D.; Patil, U. M. *CrystEngComm* **2019**, *21* (5), 884–893.
(37) Pujari, S. S.; Kadam, S. A.; Ma, Y.-R.; Jadhav, S. B.; Kumbhar, S. S.; Bhosale, S. B.; Gunjakar, J. L.; Lokhande, C. D.; Patil, U. M. *J. Energy Storage* **2022**, *52*, 105037.
(38) Sharma, P.; Radhakrishnan, S.; Khil, M.-S.; Kim, H.-Y.; Kim, B.-S. *J. Electroanal. Chem.* **2018**, *808*, 236–244.
(39) Bu, X.; Chiang, C.; Wei, R.; Li, Z.; Meng, Y.; Peng, C.; Lin, Y.; Li, Y.; Lin, Y.; Chan, K. S.; Ho, J. C. *ACS Appl. Mater. Interfaces* **2019**, *11* (42), 38633–38640.
(40) Ranjan, R.; Tekawadia, J.; Jain, R.; Mhamane, N. B.; Raja, T.; Gopinath, C. S. *Chem. Eng. J.* **2023**, *471*, 144459.
(41) Roy, K.; Gopinath, C. S. *Anal Chem* **2014**, *86* (8), 3683–3687.
(42) Wang, Y.; Asunskis, D. J.; Sherwood, P. M. A. *Surf. Sci. Spectra* **2002**, *9* (1), 91–98.
(43) Velu, S.; Suzuki, K.; Vijayaraj, M.; Barman, S.; Gopinath, C. S. *Appl. Catal. B Environ.* **2005**, *55* (4), 287–299.
(44) Jain, R.; Reddy, K. P.; Ghosalya, M. K.; Gopinath, C. S. *J. Phys. Chem. C* **2017**, *121* (37), 20296–20305.
(45) Reddy, K. P.; Jain, R.; Ghosalya, M. K.; Gopinath, C. S. *J. Phys. Chem. C* **2017**, *121* (39), 21472–21481.
(46) Ramana, C. V.; Ait-Salah, A.; Utsunomiya, S.; Becker, U.; Mauger, A.; Gendron, F.; Julien, C. M. *Chem. Mater.* **2006**, *18* (16), 3788–3794.
(47) Mahmoud, B. A.; Mirghni, A. A.; Oyedotun, K. O.; Momodu, D.; Fasakin, O.; Manyala, N. *J. Alloys Compd.* **2020**, *818*, 153332.
(48) Zhang, L.; Brow, R. K. *J. Am. Ceram. Soc.* **2011**, *94* (9), 3123–3130.
(49) Jeon, S. S.; Kang, P. W.; Klingenhof, M.; Lee, H.; Dionigi, F.; Strasser, P. *ACS Catal.* **2023**, *13* (2), 1186–1196.
(50) Patra, K. K.; Gopinath, C. S. *Chem. Commun.* **2023**, *59* (45), 6774–6795.
(51) Terekhina, I.; White, J.; Cornell, A.; Johnsson, M. *ACS Appl. Nano Mater.* **2023**, *6* (13), 11211–11220.
(52) Li, Y.; Wei, X.; Chen, L.; Shi, J.; He, M. *Nat. Commun.* **2019**, *10* (1), 5335.
(53) Han, X.; Sheng, H.; Yu, C.; Walker, T. W.; Huber, G. W.; Qiu, J.; Jin, S. *ACS Catal.* **2020**, *10* (12), 6741–6752.
(54) Xia, Z.; Ma, C.; Fan, Y.; Lu, Y.; Huang, Y.-C.; Pan, Y.; Wu, Y.; Luo, Q.; He, Y.; Dong,

C.-L.; Wang, S.; Zou, Y. *ACS Catal.* **2024**, *14* (3), 1930–1938.
(55) Wu, G.; Dong, X.; Mao, J.; Li, G.; Zhu, C.; Li, S.; Chen, A.; Feng, G.; Song, Y.; Chen, W.; Wei, W. *Chem. Eng. J.* **2023**, *468*, 143640.
(56) Zhang, J.; Shen, Y.; Li, H. *ACS Appl. Energy Mater.* **2023**, *6* (10), 5508–5518.
(57) Sapner, V. S.; Tanwade, P. D.; Munde, A. V.; Sathe, B. R. *ACS Appl. Nano Mater.* **2023**, *6* (18), 16414–16423.
(58) He, Z.; Hwang, J.; Gong, Z.; Zhou, M.; Zhang, N.; Kang, X.; Han, J. W.; Chen, Y. *Nat. Commun.* **2022**, *13* (1), 3777.
(59) Wu, J.; Li, J.; Li, Y.; Ma, X.; Zhang, W.; Hao, Y.; Cai, W.; Liu, Z.; Gong, M. *Angew. Chem Int. Ed.* **2022**, *61* (11).
(60) Oh, L. S.; Park, M.; Park, Y. S.; Kim, Y.; Yoon, W.; Hwang, J.; Lim, E.; Park, J. H.; Choi, S. M.; Seo, M. H.; Kim, W. B.; Kim, H. J. *Adv. Mater.* **2023**, *35* (4).
(61) Zijian Huang, H. R. J. G. Y. T. D. Y. J. Z. H. Z. *Appl. Catal. B Environ. Energy* **2024**, *351* (123986).
(62) Li, Y.; Wei, X.; Han, S.; Chen, L.; Shi, J. *Angew. Chemie Int. Ed.* **2021**, *60* (39), 21464–21472.
(63) Li, S.; Liu, D.; Wang, G.; Ma, P.; Wang, X.; Wang, J.; Ma, R. *Nano-Micro Lett.* **2023**, *15* (1), 189.
(64) Li, Y.; Wei, X.; Chen, L.; Shi, J.; He, M. *Nat. Commun.* **2019**, *10* (1), 5335.
(65) Morales, D. M.; Jambrec, D.; Kazakova, M. A.; Braun, M.; Sikdar, N.; Koul, A.; Brix, A. C.; Seisel, S.; Andronescu, C.; Schuhmann, W. *ACS Catal.* **2022**, *12* (2), 982–992.
(66) Qian, Q.; He, X.; Li, Z.; Chen, Y.; Feng, Y.; Cheng, M.; Zhang, H.; Wang, W.; Xiao, C.; Zhang, G.; Xie, Y. *Adv. Mater.* **2023**, *35* (25).
(67) Tran, G.-S.; Vo, T.-G.; Chiang, C.-Y. *J. Catal.* **2021**, *404*, 139–148.
(68) Xiang, K.; Wu, D.; Deng, X.; Li, M.; Chen, S.; Hao, P.; Guo, X.; Luo, J.; Fu, X. *Adv. Funct. Mater.* **2020**, *30* (10).
(69) Zhu, B.; Dong, B.; Wang, F.; Yang, Q.; He, Y.; Zhang, C.; Jin, P.; Feng, L. *Nat. Commun.* **2023**, *14* (1), 1686.
(70) Hao, J.; Liu, J.; Wu, D.; Chen, M.; Liang, Y.; Wang, Q.; Wang, L.; Fu, X.-Z.; Luo, J.-L. *Appl. Catal. B Environ.* **2021**, *281*, 119510.
(71) Jiang, N.; You, B.; Boonstra, R.; Terrero Rodriguez, I. M.; Sun, Y. *ACS Energy Lett.* **2016**, *1* (2), 386–390.
(72) Gao, L.; Liu, Z.; Ma, J.; Zhong, L.; Song, Z.; Xu, J.; Gan, S.; Han, D.; Niu, L. *Appl. Catal. B Environ.* **2020**, *261*, 118235.
(73) Jiang, N.; Liu, X.; Dong, J.; You, B.; Liu, X.; Sun, Y. *ChemNanoMat* **2017**, *3* (7), 491–495.
(74) Wang, C.; Lu, H.; Mao, Z.; Yan, C.; Shen, G.; Wang, X. *Adv. Funct. Mater.* **2020**, *30* (21).
(75) You, B.; Liu, X.; Jiang, N.; Sun, Y. *J. Am. Chem. Soc.* **2016**, *138* (41), 13639–13646.
(76) Rizk, M. R.; Abd El-Moghny, M. G.; Abdelhady, H. H.; Ragheb, W. M.; Mohamed, A. H.; Fouad, H. F.; Mohsen, M.; Kamel, A. S.; El-Deab, M. S. *Int. J. Hydrogen Energy* **2022**, *47* (75), 32145–32157.
(77) Xu, Y.; Liu, M.; Wang, S.; Ren, K.; Wang, M.; Wang, Z.; Li, X.; Wang, L.; Wang, H. *Appl. Catal. B Environ.* **2021**, *298*, 120493.
(78) Ma, G.; Yang, N.; Zhou, G.; Wang, X. *Nano Res.* **2022**, *15* (3), 1934–1941.

Chapter 6

Chapter 6(a) - Electrocatalytic Glucose Oxidation: Insights from Palladium

Chapter 6(b) - Electrocatalytic Disaccharide Oxidation: Synergistic Activity of PdCu Alloy Catalysts

---

Two disclosures have been filed based on the work described in Chapters 4 and 6: (1) C. S. Gopinath, Kshirodra kumar Patra, Inderjeet Chauhan, Electrocatalytic conversion of biomass component(s) into value added chemicals and concurrent green hydrogen production, Provisional Appl. No. 202311042901. C. S. Gopinath, Kshirodra Kumar Patra, Inderjeet Chauhan, P. M. Vijay, Electrocatalytic conversion of disaccharides into value added chemicals and parallel carbon negative green hydrogen production, (NCL Invention Disclosure No. INV-2024-0002).

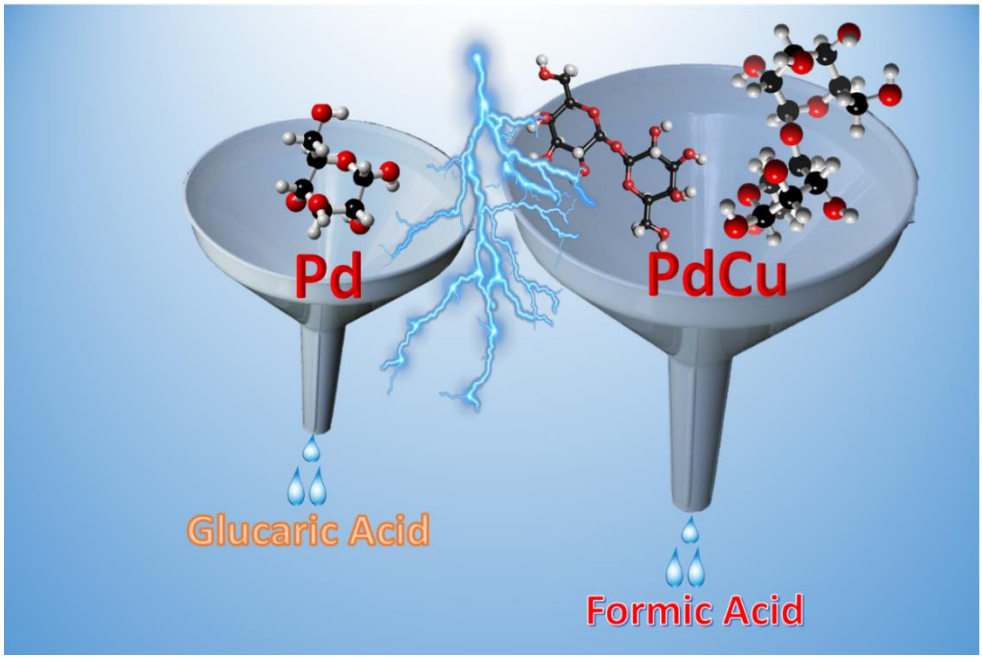

Electrocatalytic Glucose Oxidation: Insights from Palladium

6.1 Introduction

Hydrogen serves as a critical feedstock for next-generation clean fuels and towards a hydrogen-based economy.[1-3] Currently, 95% of H_2 is produced from fossil fuels via steam methane reforming, naphtha reforming, and coal gasification.[4,5] These fossil fuel-derived energy sources are neither sustainable nor environmentally friendly, primarily due to substantial CO_2 emissions. Water electrolysis offers an alternative pathway for generating high-purity hydrogen with minimal CO_2 emissions.[6-10] However, the high electricity consumption required for conventional water electrolysis, driven by the high overpotential in addition to the high anodic theoretical potential of 1.23 V for the OER, remains a critical challenge. Despite ongoing technological advancements, achieving the green hydrogen price target of US$2/kg through electrolysis appears to be a formidable challenge due to numerous obstacles.[1]

Replacing the OER with suitable organic oxidation, such as biomass derivatives, at low potential is an effective strategy to reduce hydrogen production costs. Oxidizing biomass derivatives, like glucose, not only lower energy requirements but also generate value-added chemicals, thereby increasing the efficiency and economic attractiveness of the overall process. This method results in carbon-negative hydrogen production, which is highly attractive commercially.[12]

The glucose electrooxidation reaction (GLUOR) can be coupled with HER to enhance hydrogen production at lower over-potentials compared to traditional water splitting in alkaline electrolyzers. Conventional organic electrolyzers typically utilize organic feeds such as furfural and 5-hydroxymethylfurfural (HMF)[13-15], which are valuable platform chemicals in numerous organic transformations. However, converting starch and cellulose to HMF and furfural with high selectivity and yield is an economically challenging process. Decoupling the OER from GLUOR offers significant advantages for sustainable hydrogen production due to the abundant availability and cost-effectiveness of glucose.[16,17] This approach addresses the economic and technical challenges associated with traditional methods, leveraging biomass derivatives to create a more efficient and commercially viable hydrogen production pathway. By utilizing glucose, which is more readily available and less economically taxing to convert compared to other organic feeds, the process becomes more feasible and attractive for large-scale implementation. The conversion rate is a crucial metric for assessing hydrogen formation in GLUOR and related processes. Higher conversion rates lead to increased production of oxidation products concurrently with accelerated hydrogen generation at the cathode.

However, hydrogen production in GLUOR and similar processes has historically been limited due to low conversion rates at low overpotentials.[18] Therefore, effective catalyst design should aim for near-complete conversion at lower potentials and high current densities (100 mA/cm^2 and above) to enhance hydrogen production and reduce costs simultaneously. In essence, GLUOR-related processes should operate at significantly lower potentials compared to those required for OER, ideally achieving full avoidance of OER. In the earlier chapter, glycerol was utilized as a biomass component for oxidation; however, for the present chapter, glucose is utilized as a biomass component, which is also a bigger and complex molecule. Nevertheless, most of the challenges encountered for glycerol oxidation applies to glucose oxidation too, which is in addition to later's bigger size and complex molecular nature.

Electrocatalytic GLUOR is a promising strategy for converting glucose into various chemicals such as gluconolactone (GCL), gluconic acid (GNA), glucaric acid (GRA), 5-HMF, and sorbitol.[19-21] GCL is the lactone of GNA and these products are considered a valuable chemical derived from glucose oxidation. It finds applications in food additives as a curing and pickling agent, as well as in personal care products like conditioners, moisturizers, facial cleansers, and sunscreens. GRA is highly valued as a "top pricing compound" sourced from biomass[22], owing to its importance as an intermediate in the creation of biodegradable polymers, detergents, and metal complexing agents.[23,24] Moreover, GRA and its derivatives, such as GRA-Ca and GRA-1,4-lactone, are utilized in healthcare for applications like cancer treatment and cholesterol management.[25-27] According to a report by Grand View Research, Inc., the global market for GRA was estimated at around US$ 550.4 million in 2016 and is anticipated to grow to US$ 1.30 billion by 2025.[28]

GRA production is currently practiced through enzymatic or chemical oxidation of glucose, underpinning the concept of glucose-based biofuel cell technology.[29-34] However, microbial oxidation of glucose suffers from challenges such as the generation of large amounts of microbial biomass and lengthy fermentation times. In contrast, electrochemical GLUOR involves the oxidation of glucose at the anode using suitable electrocatalysts and concurrent reduction of water to hydrogen at the cathode. This approach aims to mitigate the substantial electricity consumption associated with conventional water electrolysis, primarily due to the high anodic potential (>1.23 V) required for OER.[35-40]

Recent advancements in non-noble metal-based catalysts for GLUOR have been explored by limited research groups. Liu et al. successfully utilized a NiFeN catalyst in 1M KOH for the oxidation of glucose to glucaric acid, achieving a current density of 100 mA cm^{-2} at a potential

of 1.39 V.[41] Wu et al. developed bifunctional Co@CoO heterojunction catalysts with various structural configurations for simultaneous hydrogen evolution and GLUOR. Specifically, for GLUOR reaction, they shown 20 mA cm^{-2} current density at 1.12 V vs RHE.[42] Similarly, Kang et al. presented a bifunctional nickel copper double hydroxide (NiCu-DH) electrocatalyst on a three-dimensional (3D) CuNi current collector, efficiently catalyzing both GLUOR and HER. In this the catalyst used as sensor and shows the GLUOR current the potential range 0.5 to 0.75 V vs Ag/AgCl.[43] Men et al. introduced WO_3-decorated carbon nanotubes (WO_3/CNT60) with robust W−C bonds for glucose oxidation to gluconate and the onset for GLUOR is nearly 1.25 V vs RHE.[44] Dey et al. reported the use of Bi_2O_3-incorporated carbon-supported bismuth-silver (Bi@Ag/C) nanoparticles for the conversion of glucose to 2-keto-gluconate[45], while Shu et al. demonstrated the efficacy of two-dimensional (2D) ultrathin nickel−cobalt phosphate nanosheets for glucose sensing application.[46]

Despite the low cost of non-noble metal catalysts, their operational potentials are high. To mitigate this, various noble metal-based catalysts have been investigated but still many catalysts used as glucose sensors only. Ham et al. investigated the impact of the Pt oxidation state on the activity and selectivity of glucose oxidation, operating at 0.4 V vs. RHE. They achieved 100% conversion for the GLUOR after 6 hours. Additionally, they utilized advanced techniques such as high-pressure liquid chromatography and high-pressure anion exchange chromatography to address the challenges in product quantification.[47] Ulas et al. examined PdIn alloy catalysts supported on hydroxyapatite (PdIn/HAp) with different atomic ratios and shows 0.62 V vs Ag/AgCl onset potential for GLUOR.[48] Mojarrad et al. proposed a cost-effective graphite electrode adorned with Mo–Pd nanoalloys, which offers high surface area and excellent mechanical strength for glucose oxidation at 0.06 V vs Ag/AgCl.[49] Li et al. developed dual-structured Pt-Ni hydrogels with interlinked networks of PtNi nanowires and $Ni(OH)_2$ nanosheets, showcasing significant electrocatalytic activity and stability in neutral glucose biosensing.[50] Wang et al. demonstrated that Pd@Pt nanocatalysts can be used for GLUOR, with an onset potential of -0.05 V vs. Ag/AgCl under neutral conditions,[51] and Xu et al. reported Pt nanoflower (Pt NF) catalysts for use in abiotic glucose fuel cells at physiological glucose concentrations with an onset potential of -0.6 V vs. Ag/AgCl (pH 7.4).[52] Although noble metal-based catalysts have successfully lowered the onset potential for glucose oxidation, challenges in quantification and sustainable performance remain. Additionally, the current densities achieved by these catalysts are lower compared to those observed in this study.

In this study, we successfully synthesized palladium nanocubes (Pd-NCs) and conducted a comprehensive investigation of their electrochemical performance in both the anodic GLUOR and the cathodic HER. The Pd-NCs demonstrated exceptional selectivity towards the production of GNA and GRA, achieving nearly 100% conversion at a potential of 0.6 V (vs. RHE). This indicates a substantial enhancement in catalytic activity and efficiency. To the best of our knowledge, these Pd-NCs represent the most effective catalysts for electrocatalytic GLUOR at such low overpotentials. Our findings underscore the potential of Pd-NCs to significantly improve the efficiency of electrochemical systems, facilitating sustainable hydrogen production and the synthesis of valuable chemicals from biomass derivatives.

6.2 Result and Discussions

6.2.1 Morphological analysis

As shown in Figure 2.2 of the experimental section, the synthesis of Pd-NCs was performed according to the protocol described in Section 2.3.2, utilising KCl as a structure-directing agent and ascorbic acid as a reducing agent. K_2PdCl_4 was used as the palladium precursor. In Chapter 2 of the experimental portion, the entire synthesis process is covered in detail. HRTEM was initially used to study the Pd nanocrystals' shape and structure. The synthesised Pd nanotube's selected area electron diffraction (SAED) patterns and TEM images are shown in Figure 6.1. The diameters of the Pd-NC nanoparticles range from 8 to 10 nm, as seen in Figure 6.1a, b. The homogeneous dispersion of Pd atoms in the Pd-NCs, as shown in Figure 6.1c, is revealed by HAADF-STEM and elemental mapping.[53]

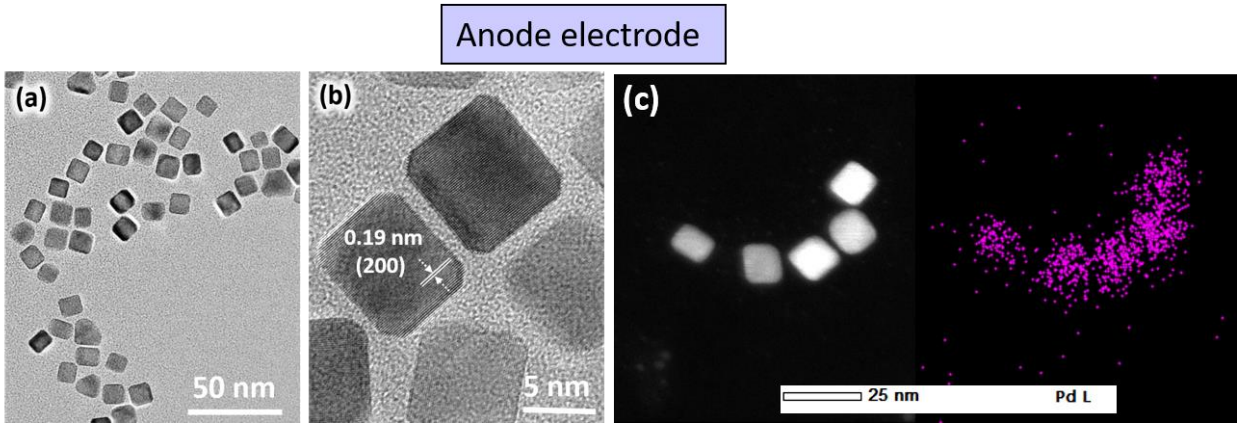

Figure 6.1 (a) TEM images of as-prepared Pd-NC and corresponding HRTEM image of Pd nanoparticles is given in (b). (c) HAADF-STEM image and chemical mappin of Pd-NC.

The Pd-NC catalyst served as the anode electrode for the oxidation of glucose and was drop-cast onto Ni foam. Pd-NC served as the working electrode in all half-cell reactions, while a graphite rod served as the counter electrode and a saturated calomel electrode served as the reference electrode. In the electrolyzer configuration, since graphite is not an effective catalyst for the HER, Pt/C and NiP were employed as HER catalysts in a two-electrode system. A 20 wt% Pt/C catalyst was dispersed in water and isopropanol mixture and spray-coated onto Ni foam, while the NiP catalyst was synthesized via an electrodeposition method. The various parameters adopted for the synthesis of the NiP catalyst are detailed in Table 6.1.

Table 6.1 Optimization parameter for NiP electrodeposition.

Sr. No.	Electrodeposition method (Chronoamperometry)	Applied Potential V vs Ag/AgCl	Time (min)
1	LSV 1	-0.75	10
2	LSV 2	-0.75	20
3	LSV 3	-0.75	30
4	LSV 4	-0.80	10
5	LSV 5	-0.80	20
6	LSV 6	-0.80	30
7	LSV 7	-0.85	10
8	LSV 8	-0.85	20
9	LSV 8 – iR corrected	-0.85	20
10	LSV 9	-0.85	30

The electrodeposited NiP on Ni foam was evaluated using LSV. As shown in Figure 6.2a, the electrode deposited at -0.85 V versus Ag/AgCl exhibited the best performance among all the electrodes that were evaluated for electrolysis. To investigate the microstructure of this optimal electrode, a small amount of the deposited material was scraped from the electrode surface and subjected to TEM and HRTEM analysis, as depicted in Figures 6.2b and 6.2c. Figure 6.2b reveals hexagonal-shaped nanoparticles, while Figure 6.2c indicates an average particle size ranging from 5 to 8 nm.

6.2.2 Electrocatalytic glucose oxidation reaction

The LSV profile for both GLUOR and OER using the Pd-NC electrocatalyst in 1 M KOH solution is presented in Figure 6.3a.

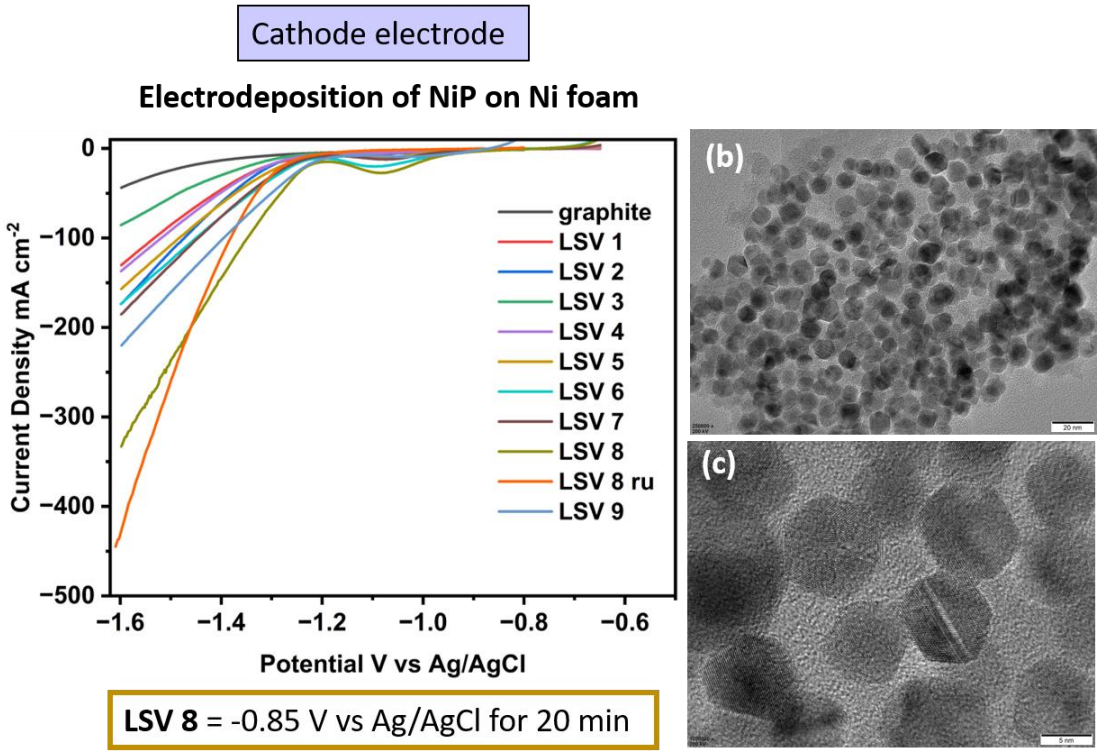

Figure 6.2 Figure (a) LSV graph for all optimized electrode, (b) & (c) HRTEM images of NiP nanoparticles.

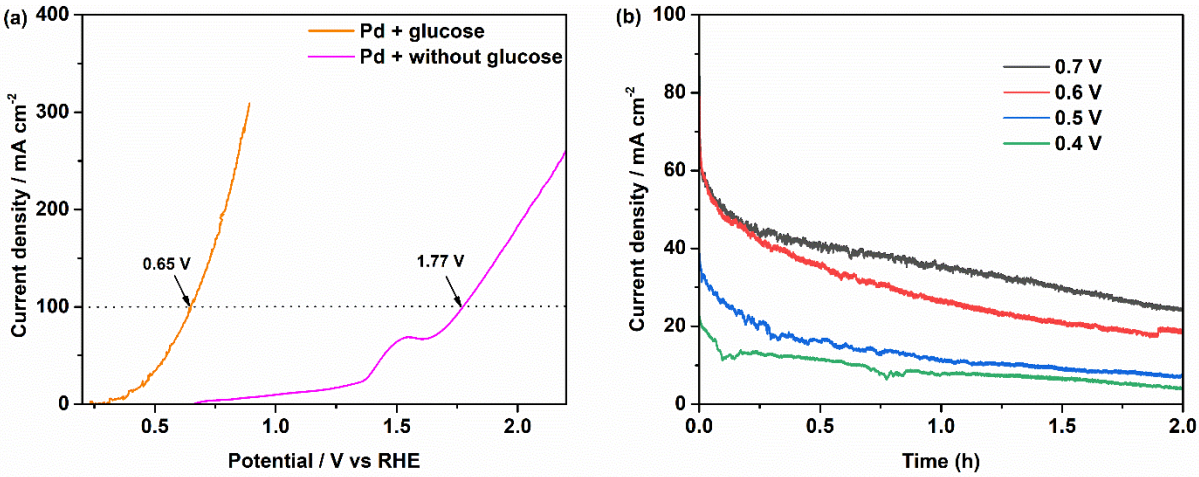

Figure 6.3 (a) LSV profile of Pd-NC with and without glucose in 1M KOH solution (b) the corresponding chronoamperometry at different applied potential for 2 hours.

With the addition of 0.1 M glucose, a catalytic current density of 100 mA cm^{-2} is achieved at only 650 mV. In contrast, the OER requires 1.77 V to reach the same current density with the Pd-NC catalyst, due to the slow kinetics of the four-electron process. This substantial reduction in anodic potential is advantageous for hydrogen production and overall cell-functioning, as it reduces the electricity consumption. The feature observed at 1.5 V during the OER is attributed

to the oxidation of metallic Ni. Figure 6.3b depicts the chronoamperometry results for GLUOR at various applied potentials.

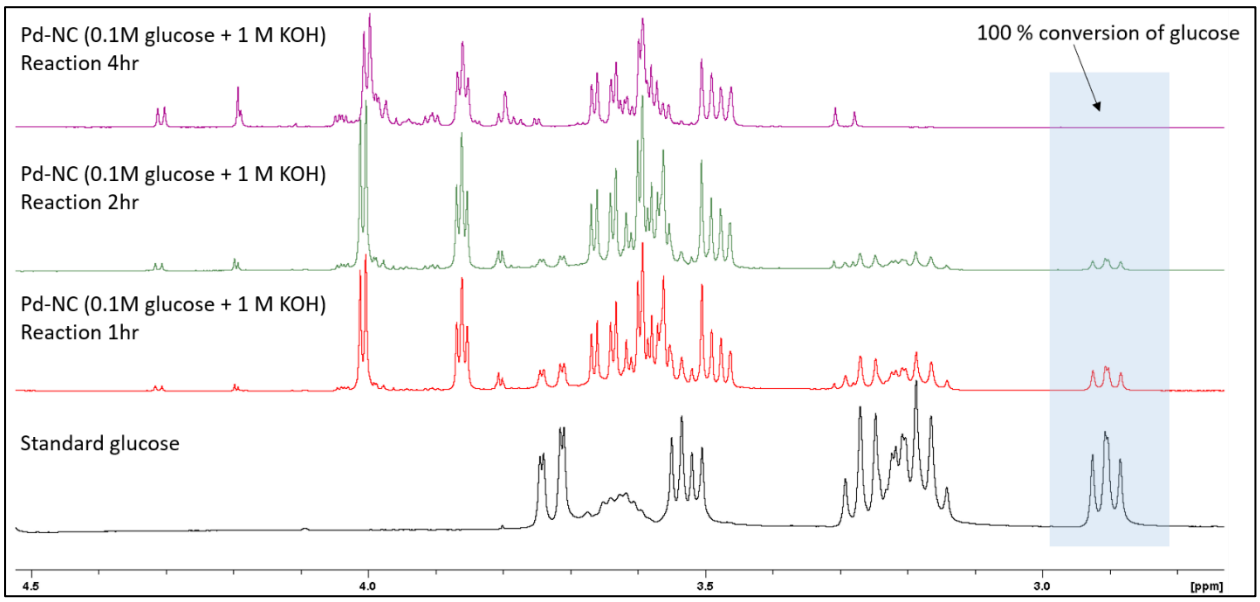

Figure 6.4 ^{1}H NMR data of glucose conversion and oxidation products at 0.6 V vs RHE for 4 h of reaction.

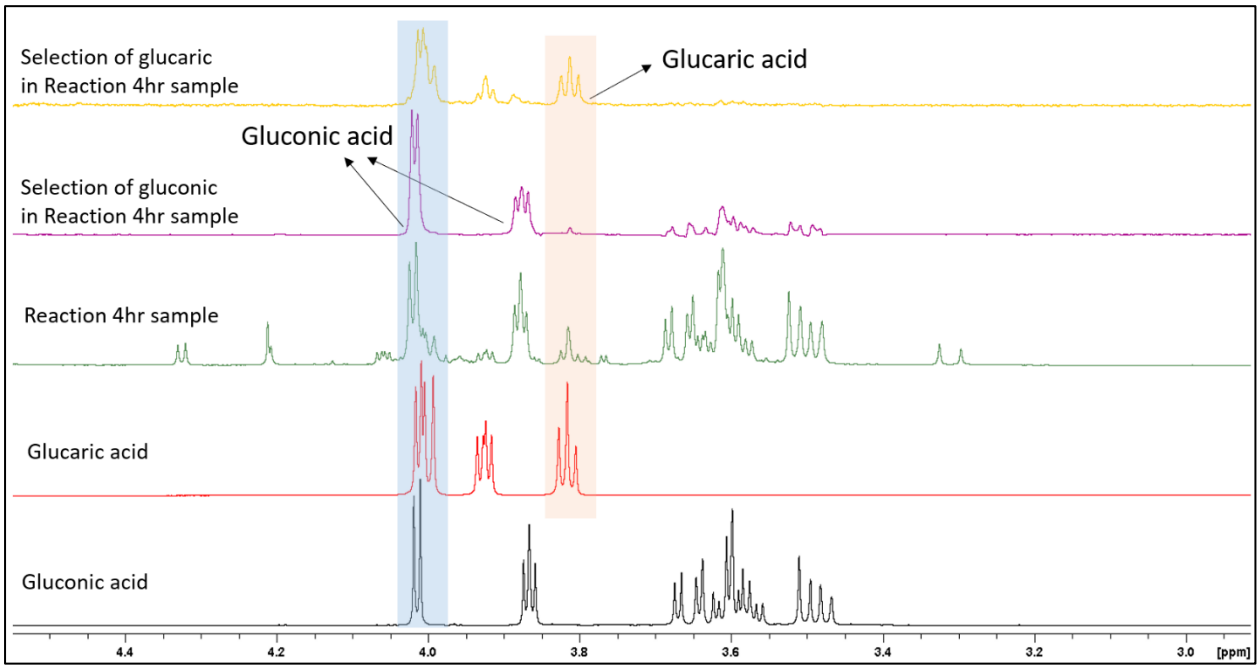

Figure 6.5 ^{1}H NMR data of gluconic acid, glucaric acid and glucose oxidation product distribution at 0.6 V vs RHE for 4 h of reaction.

Product analysis for the experiment conducted at 0.6 V vs. RHE is illustrated in Figures 6.4 and 6.5. Even at this lower potential, approximately 90% selectivity was observed for the production of GNA and GRA, with complete glucose conversion after four hours of reaction.

Figure 6.4 shows a systematic decrease in glucose signal intensity over time (1 hour, 2 hours), culminating in its complete disappearance at 4 hours, confirming 100% glucose conversion to value-added products. The products from glucose oxidation were characterized using 2D NMR (Total Correlation Spectroscopy - TOCSY), as shown in Figure 6.5. Selective excitation and TOCSY transfer from the sample obtained after 4 hours of reaction confirm the formation of gluconic and glucaric acids. Approximately 20-30% selectivity for gluconic acid and 70-80% for glucaric acid was observed across the entire potential range. *These initial experimental results are promising, and further experiments are worth doing to analyze reactions at higher potentials, such as 1-1.2 V vs. RHE, which is well below theoretical potential of OER. Applying higher potential may enable glucose conversion faster to other value-added products (VAPs), potentially altering the selectivity pattern as well as fast kinetics.*

6.2.3 A Possible Reaction Pathway from Glucose to GRA

Given that C6 is the predominant oxidation product across the potential range, it suggests that oxidative cleavage of the C–C bond necessitates a higher applied potential. A plausible reaction pathway for the production of glucaric acid (GRA) is depicted in Figure 6.6. In the initial step, the oxidation of the aldehyde group in glucose proceeds via a two-electron oxidation process, converting glucose to gluconic acid. This intermediate can further form a lactone. The lactone formation is initiated by the nucleophilic attack of the hydroxyl group at the C5 position on the carbonyl carbon of the carboxylic acid group (–COOH), resulting in the removal of a water molecule. In the subsequent step, the alcohol group undergoes oxidation to an aldehyde and subsequently to an acid, leading to the formation of GRA, which has carboxyl groups at both ends.[41]

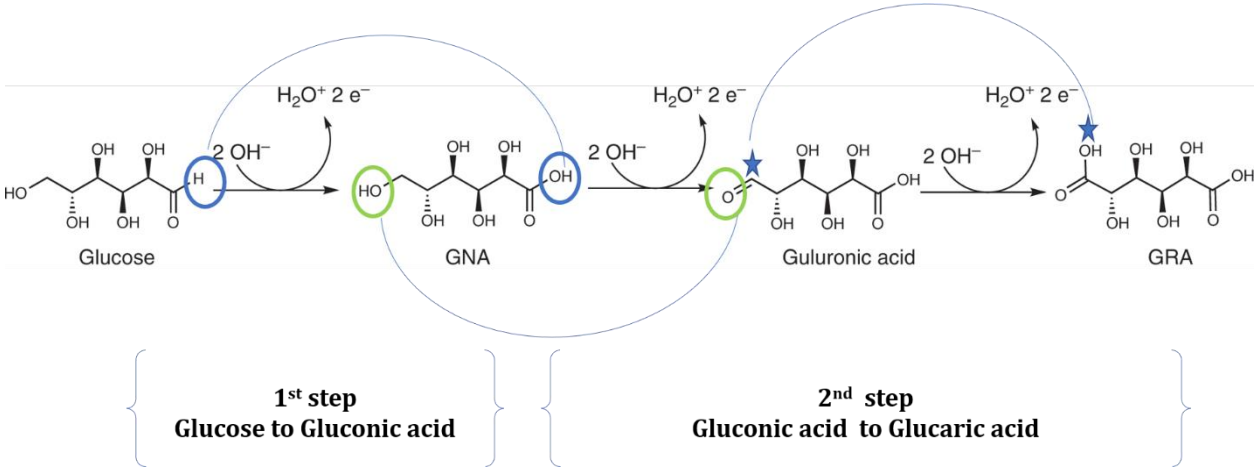

Figure 6.6 Schematic illustration of the potential electrochemical oxidation pathway for converting glucose to gluconic acid (GNA) and glucaric acid (GRA).

6.2.4 Electrolyzer study for GLUOR

In addition to the glucose oxidation experiments, a two-electrode study was conducted to generate carbon-negative green hydrogen at lower potentials. For the GLUOR experiments, the electrolyzer was configured with Pt/C and/or nickel phosphide (NiP) as the cathode, while Pd-NC served as the anode. The LSV plot for GLUOR in the alkaline electrolyzer, presented in Figure 6.7a, indicates that a current density of 100 mA/cm^2 was achieved at applied voltages of 1.4 V and 1 V with NiP and Pt/C as the cathode, respectively. Similar to GLUOR, no oxygen evolution reaction (OER) current was observed at these voltages in the presence of glucose for both NiP and Pt/C. The energy input required for hydrogen production was significantly low. When NiP was used as the cathode, an electricity input of approximately 3.35 kWh per m^3 of H_2 was needed to achieve a current density of 100 mA/cm^2 (Figure 6.7b). In comparison, the Pt/C cathode required only about 2.39 kWh per m^3 of H_2 to reach the same current density. These findings highlight the potential of using earth-abundant catalysts like NiP for the long-term operation of electrolyzers, offering enhanced techno-economic performance.

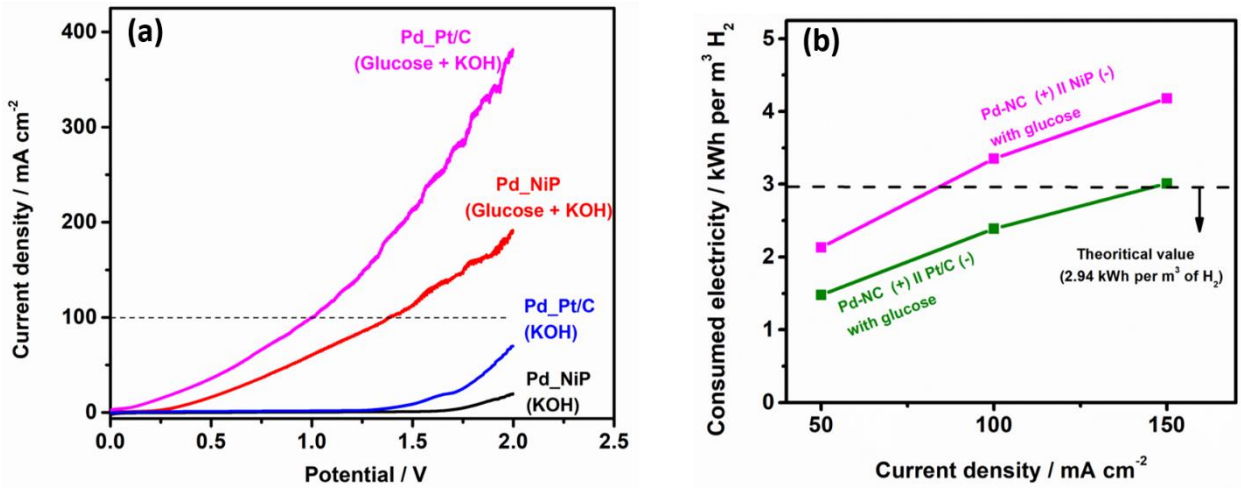

Figure 6.7 Figure (a) shows LSV of GLUOR in 2 electrode alkaline electrolyzer with Pd-NC as a anode, Pt/C and/or NiP as a cathode. Figure (b) shows electricity consumed for hydrogen production in GLUOR when Pt/C and NiP used as cathode and Pd-NC as anode in the electrolyzer.

A chronopotentiometry experiment was conducted over 50 hours at a current density of 100 mA cm^{-2} to evaluate the long-term performance of the electrolyzer using NiP and Pt/C as cathodes (Figure 6.8). Despite the presence of 0.34 M NaCl, chlorine oxidation was completely avoided, and only a marginal decrease in GLUOR current was observed. The voltage remained

stable throughout the 50-hour operation with both NiP and Pt/C as cathodes, as depicted in Figure 6.8a.

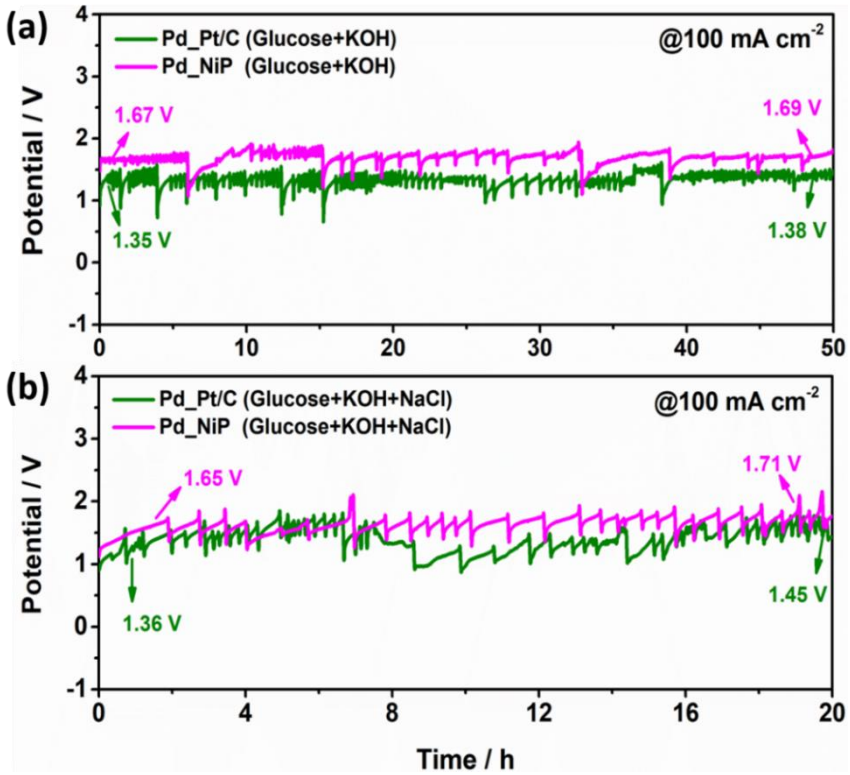

Figure 6.8 (a) shows sustainable operation of GLUOR process at 100 mA cm^{-2} for 50 h in pure DI water and figure (b) shows sustainable operation of GLUOR process at 100 mA cm^{-2} for 20 h in simulated sea water.

The electrolyzer consistently produced hydrogen at a rate of approximately 180 mL/h over the 50-hour period. Additionally, a stability test for the Pd-NC catalyst was performed in a NaCl solution at a current density of 100 mA cm^{-2} for 20 hours (Figure 6.8b). No change in cell voltage was detected, and chlorine oxidation was entirely prevented during GLUOR. These results suggest significant potential for chlorine-free seawater splitting coupled with GLUOR, offering a sustainable approach for hydrogen production.

6.3 Conclusion

This study highlights the exceptional performance of palladium nanocubes (Pd-NCs) as catalysts for glucose oxidation. The Pd-NCs demonstrated high selectivity for gluconic and glucaric acid, achieving nearly 100% conversion at a low potential of 0.6 V vs. RHE. In practical electrolyzer applications, Pd-NCs along with Pt/C or NiP as cathode facilitated efficient hydrogen production with low energy consumption, showing robust stability over

prolonged operation periods. These findings underscore the potential of Pd-NCs to significantly enhance the efficiency of sustainable hydrogen production and the valorization of biomass derivatives.

6.4 Reference

1. S. Chu, & A. Majumdar, *Nature*, 2012, 488, 294–303.
2. L. Lin, W. Zhou, R. Gao, S. Yao, X. Zhang, W. Xu, S. Zheng, Z. Jiang, Q. Yu, Y.-W. Li, C. Shi, X.-D. Wen and D. Ma, *Nature*, 2017, **544**, 80–83.
3. X. Tian, X. Zhao, Y.-Q. Su, L. Wang, H. Wang, D. Dang, B. Chi, H. Liu, E. J. M. Hensen, X. W. Lou and B. Y. Xia, *Science*, 2019, **366**, 850–856.
4. K. Gong, F. Du, Z. Xia, M. Durstock and L. Dai, *Science*, 2009, **323**, 760–764.
5. P. Nikolaidis and A. Poullikkas, *Renewable & Sustainable Energy Reviews*, 2017, **67**, 597–611.
6. F. Lin, Z. Dong, Y. Yao, L. Yang, F. Fang and L. Jiao, *Advanced Energy Materials*, 2020, 31, 202002176.
7. Wu, L. et al. Heterogeneous bimetallic phosphide Ni2P-Fe2P as an efficient bifunctional catalyst for water/seawater splitting. Adv. Funct. Mater., 2020, 31, 2006484
8. J. Mahmood, F. Li, S.-M. Jung, M. S. Okyay, I. Ahmad, S.-J. Kim, N. Park, H. Y. Jeong and J.-B. Baek, *Nature Nanotechnology*, 2017, **12**, 441–446.
9. H. Li, C. Tsai, A. L. Koh, L. Cai, A. W. Contryman, A. H. Fragapane, J. Zhao, H. S. Han, H. C. Manoharan, F. Abild-Pedersen, J. K. Nørskov and X. Zheng, *Nature Materials*, 2015, **15**, 48–53.
10. B. Zhang, L. Wang, Z. Cao, S. M. Kozlov, F. P. G. De Arquer, C. T. Dinh, J. Li, Z. Wang, X. Zheng, L. Zhang, Y. Wen, O. Voznyy, R. Comin, P. De Luna, T. Regier, W. Bi, E. E. Alp, C.-W. Pao, L. Zheng, Y. Hu, Y. Ji, Y. Li, Y. Zhang, L. Cavallo, H. Peng and E. H. Sargent, *Nature Catalysis*, 2020, **3**, 985–992.
11. https://www.irena.org/-/media/Files/IRENA/Agency/Publication/2020/Dec/IRENA_Green_hydrogen_cost_2020.pdf
12. F. W. S. Lucas, R. G. Grim, S. A. Tacey, C. A. Downes, J. Hasse, A. M. Roman, C. A. Farberow, J. A. Schaidle and A. Holewinski, *ACS Energy Letters*, 2021, 1205–1270.
13. N. Jiang, B. You, R. Boonstra, I. M. T. Rodriguez and Y. Sun, *ACS Energy Letters*, 2016, **1**, 386–390.
14. B. You, N. Jiang, X. Liu and Y. Sun, *Angewandte Chemie*, 2016, **55**, 9913–9917.
15. B. You, X. Liu, N. Jiang and Y. Sun, *Journal of the American Chemical Society*, 2016, **138**, 13639–13646.
16. W.-J. Liu, Z. Xu, D. Zhao, X.-Q. Pan, H.-C. Li, X. Hu, Z.-Y. Fan, W.-K. Wang, G.-H. Zhao, S. Jin, G. W. Huber and H.-Q. Yu, *Nature Communications*, 2020, 11, 265.
17. P. Du, J. Zhang, Y. Liu and M. Huang, *Electrochemistry Communications*, 2017, **83**, 11–15.

18. K. Wang, Z. Guo, M. Zhou, Y. Yang, L. Li, H. Li, R. Luque and S. Saravanamurugan, *Journal of Energy Chemistry*, 2024, **91**, 542–578.
19. L. T. Mika, E. Cséfalvay and Á. Németh, *Chemical Reviews*, 2017, **118**, 505–613.
20. Z. Zhang and G. W. Huber, *Chemical Society Reviews*, 2018, **47**, 1351–1390.
21. R.-J. Van Putten, J. C. Van Der Waal, E. De Jong, C. B. Rasrendra, H. J. Heeres and J. G. De Vries, *Chemical Reviews*, 2013, **113**, 1499–1597.
22. A. J. Ragauskas, C. K. Williams, B. H. Davison, G. Britovsek, J. Cairney, C. A. Eckert, W. J. Frederick, J. P. Hallett, D. J. Leak, C. L. Liotta, J. R. Mielenz, R. Murphy, R. Templer and T. Tschaplinski, *Science*, 2006, **311**, 484–489.
23. M. F. Mangiameli, J. C. González, S. Bellú, F. Bertoni and L. F. Sala, *Dalton Transactions*, 2014, **43**, 9242.
24. T. Mehtiö, M. Toivari, M. G. Wiebe, A. Harlin, M. Penttilä and A. Koivula, *Critical Reviews in Biotechnology*, 2015, **36**, 904–916.
25. B.-A. Khaw, J. Narula and W. Hartner, *Current Molecular Imaging*, 2015, **4**, 20–28.
26. H. A. Houson, G. N. Nkepang, A. F. Hedrick and V. Awasthi, *Nuclear Medicine and Biology*, 2018, **59**, 9–15.
27. Calcium glucarate prevents tumor formation in mouse skin, https://pubmed.ncbi.nlm.nih.gov/12747003/.
28. Glucaric Acid Market Size, Share & Trends Analysis by product (Pure glucaric acid, D-Glucaric acid-1,4-lactone), by application (Food ingredients, detergents, corrosion inhibitors), & Segment forecasts, 2017 - 2025, https://www.grandviewresearch.com/industry-analysis/glucaric-acid-market.
29. E. Derrien, P. Marion, C. Pinel and M. Besson, *Organic Process Research & Development*, 2016, **20**, 1265–1275.
30. T. R. Boussie, E. L. Dias, Z. M. Fresco, V. J. Murphy, J. Shoemaker, R. Archer, H. Jiang and R. Inc, US20100317823A1 - Production of Adipic Acid and Derivatives from Carbohydrate-Containing Materials - Google Patents, https://patents.google.com/patent/US20100317823A1/en.
31. M. Kunz, A. Schwarz, J. Kowalczyk and S. Ag, CA2190308A1 - Method and apparatus for producing di- and more highly oxidized carboxylic acids - Google Patents, https://patents.google.com/patent/CA2190308A1/en.
32. T. S. Moon, S.-H. Yoon, A. M. Lanza, J. D. Roy-Mayhew and K. L. J. Prather, *Applied and Environmental Microbiology*, 2009, **75**, 589–595.
33. T. S. Moon, J. E. Dueber, E. Shiue and K. L. J. Prather, *Metabolic Engineering*, 2010, **12**, 298–305.
34. Y. Liu, X. Gong, C. Wang, G. Du, J. Chen and Z. Kang, *Enzyme and Microbial Technology*, 2016, **91**, 8–16.
35. G.-F. Chen, Y. Luo, L.-X. Ding and H. Wang, *ACS Catalysis*, 2017, **8**, 526–530.
36. Y. X. Chen, A. Lavacchi, H. A. Miller, M. Bevilacqua, J. Filippi, M. Innocenti, A. Marchionni, W. Oberhauser, L. Wang and F. Vizza, *Nature Communications*, 2014, 5, 4036.
37. B. You, X. Liu, X. Liu and Y. Sun, *ACS Catalysis*, 2017, **7**, 4564–4570.

38. J. Zheng, X. Chen, X. Zhong, S. Li, T. Liu, G. Zhuang, X. Li, S. Deng, D. Mei and J. Wang, *Advanced Functional Materials*, 2017, 27, 1704169.
39. H. Huang, C. Yu, X. Han, H. Huang, Q. Wei, W. Guo, Z. Wang and J. Qiu, *Energy & Environmental Science*, 2020, **13**, 4990–4999.
40. S. Chen, J. Duan, A. Vasileff and S. Z. Qiao, *Angewandte Chemie*, 2016, **55**, 3804–3808.
41. W.-J. Liu, Z. Xu, D. Zhao, X.-Q. Pan, H.-C. Li, X. Hu, Z.-Y. Fan, W.-K. Wang, G.-H. Zhao, S. Jin, G. W. Huber and H.-Q. Yu, *Nature Communications*, 2020, 11, 265.
42. M. Wu, J. Zhao, C. Li and R. Liu, *Journal of Materials Chemistry. A*, 2022, **10**, 4791–4799.
43. K.-N. Kang, S.-I. Kim, J.-C. Yoon, J. Kim, C. Cahoon and J.-H. Jang, *ACS Applied Materials & Interfaces*, 2022, **14**, 33013–33023.
44. Y.-L. Men, P. Liu, Y. Liu, X.-Y. Meng and Y.-X. Pan, *Industrial & Engineering Chemistry Research*, 2022, **61**, 4300–4309.
45. S. Dey, M. K. Mandal, S. Pramanik, S. Atta and S. Basu, *Ionics*, 2022, **29**, 1101–1113.
46. Y. Shu, B. Li, J. Chen, Q. Xu, H. Pang and X. Hu, *ACS Applied Materials & Interfaces*, 2018, **10**, 2360–2367.
47. M. P. J. M. Van Der Ham, E. Van Keulen, M. T. M. Koper, A. A. Tashvigh and J. H. Bitter, *Angewandte Chemie*, 2023, 62, e202306701.
48. B. Ulas, Y. Yilmaz, S. Koc and H. Kivrak, *International Journal of Hydrogen Energy*, 2023, **48**, 6798–6810.
49. A. Mojarrad, R. E. Sabzi and M. Faraji, *Journal of Applied Electrochemistry*, 2022, **53**, 861–874.
50. G. Li, C. Wang, Y. Chen, F. Liu, H. Fan, B. Yao, J. Hao, Y. Yu and D. Wen, *Small*, 2023, 19, 2206868.
51. S.-S. Wang, W.-J. Qiu, T.-P. Wang and C.-L. Lee, *Applied Surface Science*, 2022, **605**, 154670.
52. X. Xu, X. Dong, D. Li, M. Qi and H. Huang, *ACS Applied Materials & Interfaces*, 2023, **15**, 17969–17977.
53. I. Chauhan, H. Bajpai, B. Ray, S. K. Kolekar, S. Datar, K. K. Patra and C. S. Gopinath, *ACS Applied Materials & Interfaces*, 2024, **16**, 26130–26141.

Chapter 6(b) - Electrocatalytic Disaccharide Oxidation: Synergistic Activity of PdCu Alloy Catalysts

6.5 Introduction

All technological advancements and communications in the modern world rely heavily on energy.[1-3] The escalating energy consumption across various facets of daily life has led to an exponential increase in energy demand.[4-6] In this context, the identification and establishment of sustainable and renewable energy sources are critical. Among renewable energy resources, green hydrogen has garnered significant attention due to its numerous advantages. As an eco-friendly and clean energy source, green hydrogen boasts a plentiful supply and is considered one of the most promising alternatives to fossil fuels, offering nearly three times higher energy per unit mass compared to petrol or diesel with no pollution.[7-9] Currently, 95% of hydrogen is produced via steam reforming of methane/naphtha and coal gasification processes, which are neither sustainable nor environmentally friendly.[10] As a result, electrocatalytic water splitting, specifically the HER at the cathode, is gaining substantial attention and is widely regarded as a viable technology for hydrogen production. However, the anodic OER, which complements HER, requires a high overpotential and proceeds at a slow rate. This significantly increases the energy needed for the overall water-splitting process, contributing to the high operational costs of electrolyzers and limiting their large-scale industrial applications. In practice, the energy consumption in electrolyzers is 1.5 to 2.2 times higher than the theoretical energy consumption, with actual efficiencies ranging between 48% and 70% in current commercial electrolyzers.[11,12] Additionally, compared to H_2, the O_2 generated at the anode is a low-value byproduct.[13]

Over the past decade, there has been growing interest in electrolytic hydrogen generation by replacing the anodic OER with the oxidation of biomass-derived components.[14,15] This approach aims to enhance the overall efficiency and economic viability of the hydrogen production process. Many biomass-derived organic molecules can be oxidized into VAPs, and by optimizing various parameters, high selectivity for specific products can be achieved. In thermal catalytic processes, overoxidation to carbon dioxide, known as the run-away reaction, is a significant issue. Electrocatalysis offers a powerful yet underutilized method for upgrading biomass to desired products. Instead of water oxidation to oxygen, biomass components could be oxidized at the anode, while water splitting to hydrogen occurs at the cathode. This process produces carbon-negative hydrogen, which is commercially attractive.[16-18] Several organic molecules like methanol,[19] ethanol,[20] ethylene glycol,[21] hydrazine hydrate[22] etc. have been used

for this method; however, due to high cost of these molecules, alternative biomass derived molecules lactose/maltose have been studied in this work. The lactose electrooxidation reaction (LacOR) and maltose electrooxidation reaction (MalOR) can be coupled with the HER to enhance hydrogen production at low overpotentials in alkaline electrolyzers. Other biomass components, like, furfural, 5-hydroxymethylfurfural (HMF), are expensive yet highly valuable chemicals used in organic transformations.[23,24] Therefore, it is prudent to utilize difficult-to-handle, waste biomass components, which are abundant and low-cost, in electrocatalytic processes.[25]

It is important to note that cellulose, a polymer consisting of thousands of D-glucose units, is the most abundant biomass component. Hemicellulose, the next most abundant biomass component, is a heterogeneous polymer composed of various sugars such as xylose, arabinose, and galactose. Both cellulose and hemicellulose, being composed of thousands of C6 and/or C5 sugar units, are considered fundamental building-block structures.[26] The dimerization of two C6 sugars results in disaccharides, like, maltose, lactose. Lactose, formed from galactose and glucose subunits, is commonly found in milk, while maltose, composed of two glucose subunits, is present in sweet potatoes, honey, and other sources.[27] Any biomass catalysis commences following the depolymerization of woody and non-woody biomass into glucose-level components, which can be achieved through high-temperature pyrolysis, acid/base treatments, or enzymatic treatments. The extent of biomass component conversion is a crucial parameter for evaluating hydrogen production in biomass oxidation reactions and related processes. As conversion increases, more oxidation products are formed, which concurrently accelerates hydrogen generation at the cathode. However, at low overpotential, the decreased conversion results in relatively low hydrogen production during biomass component oxidation reactions and related activities. To maximize hydrogen generation while minimizing costs, rational catalyst design must ensure near-complete conversion (up to 100%) of biomass components, such as, lactose, maltose at low potentials with high current densities (100 mA/cm^2 and higher). Specifically, compared to the high potentials and current densities required for the OER, LacOR and MalOR should occur at significantly lower potentials by completely circumventing OER, while still operating at high current densities. Sami Ben Aoun et al.,[28] demonstrated Au(111) single crystal surface modification with metals such as Ag, Cu, Co, Ru, Cd, Ir and Pt for the electrooxidation of monosaccharides (glucose, mannose and xylose) and disaccharides (maltose, lactose and sucrose). Ag on Au (111) showed activity better than other metals. They studied the activation of mono as well as disaccharides without

indicating any stability studies, reactant conversion and product distribution.[28] Parpot et al., illustrated the electrooxidation of trehalose, maltose, isomaltulose and cellobiose using gold electrode and selectivity observed for the maltobionic acid after MalOR, which is the major product, is only 27%. Furthermore, the conversion is only 50% even after 8 h of electrolysis, which makes it less attractive.[29] However, both studies demonstrate a proof of concept for the utilization of saccharide molecules in alkaline electrolysis. What is required to achieve higher catalytic activity and selective production of one VAP is the electrocatalyst with high intrinsic activity for such saccharide conversion along with H2 production. Such research is also required to be continued to directly convert much bigger biomass components, like cellulose, and possibly microplastic waste. For the present study, PdCu alloy without capping agent was used as electrooxidation of MalOR and LacOR, which results in the selective formation of formic acid (65 %) along with ≥80 % conversion at high current densities.

6.6 Result and discussion

6.6.1 Synthesis and characteristics of the catalyst materials

The catalysts were synthesized via a solvothermal method without the use of a capping agent, as the presence of a capping agent often reduces catalytic activity.[30] Detailed synthesis procedures are provided in Chapter 2. Figure 6.9 displays the XRD patterns of all synthesized materials. The XRD patterns of the PdCu catalysts in alloy and bimetal forms are shown in Figure 6.9a. The bimetallic PdCu XRD pattern exhibits characteristic diffraction peaks corresponding to the face-centered cubic (fcc) phases of nanoparticles of Pd and Cu. Nonetheless, the diffraction peaks for the PdCu alloy appear at 40.99°, 47.54°, 70.23°, and 84.87°, corresponding to the (111), (200), (220), and (311) crystallographic planes, respectively (Pd-PDF#46-1043, Cu-PDF#04-0836). [31-33] The bimetallic PdCu shows sharp diffraction features, whereas the PdCu alloy exhibits broad diffraction features, indicative of near-atomic level mixing of Pd and Cu in the alloy. The narrow XRD peaks observed for the bimetallic PdCu suggest significant segregation of individual metals within the bimetallic catalyst. The FWHM values for the Pd (111) facet are 1.59 for the PdCu alloy and 0.23 for the PdCu bimetal, highlighting this difference. Notably, the PdCu bimetal displays features of both Pd and Cu, while Cu features are absent in the PdCu alloy.

The XRD patterns of various PdCu alloy ratios with pure Pd and Cu nanoparticles are illustrated in Figure 6.9b. For the face-centered cubic (fcc) phase of pure Pd nanoparticles, the

diffraction peaks at 40.15°, 46.62°, 68.10°, and 82.22° correspond to the (111), (200), (220), and (311) crystallographic facets, respectively.

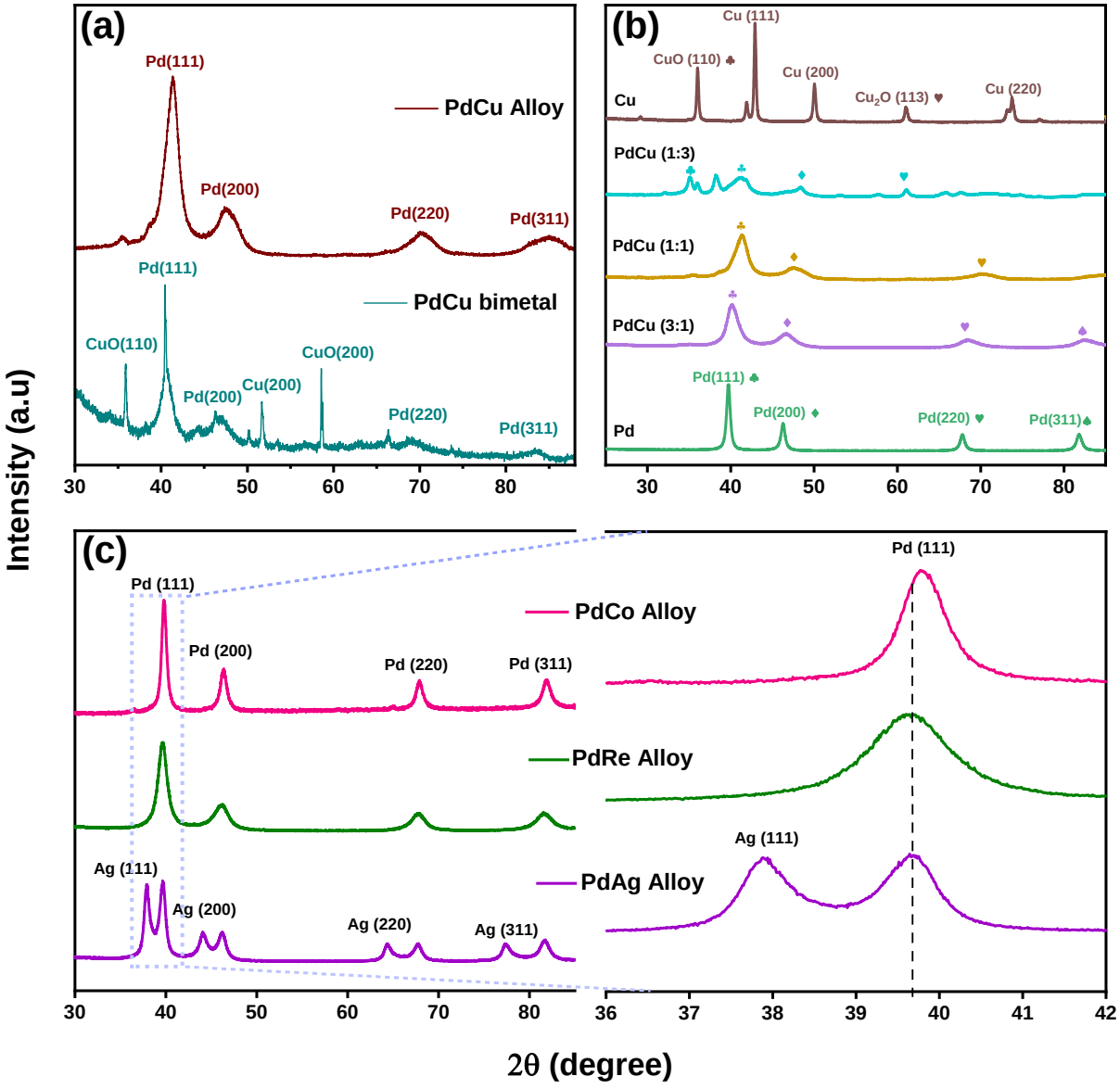

Figure 6.9 XRD patterns of (a) 1:1 PdCu alloy and PdCu bimetal system, (b) various ratios of PdCu alloy with pure Pd and Cu nanoparticles, and (c) 1:1 PdM alloys (M=Co, Re, Ag).

The XRD peaks for the PdCu(3:1) alloy appear at 40.24°, 46.89°, 68.21°, and 82.63°, indicating that the diffraction peaks from the (111), (200), (220), and (311) planes shift towards higher 2θ values, compared to pure Pd, due to the incorporation of Cu atoms. Similarly, for the PdCu(1:1) alloy, the diffraction peaks appear at higher 2θ angles due to a larger incorporation of Cu atoms into the Pd fcc lattice, with peaks observed at 40.99°, 47.54°, 70.23°, and 84.87°. In the XRD pattern of the PdCu(1:3) alloy, in addition to the aforementioned Pd features, peaks corresponding to Cu nanoparticles are also observed due to the high Cu content. The peaks at

35.10° and 61.03° correspond to the (111) and (113) facets of monoclinic CuO and Cu_2O, respectively. Diffraction peaks corresponding to the (111) and (200) planes of fcc Pd nanoparticles are also present. The FWHM for the Pd (111) plane is 0.57 for pure Pd, 1.54 for the PdCu(3:1) alloy, 1.59 for the PdCu(1:1) alloy, and 1.97 for the PdCu(1:3) alloy. Notably, the FWHM values increase with the increasing percentage of Cu. As the weight percent of copper increases, the atomic percentage of Cu also increases, leading to a decrease in net Pd-Cu alloy content, and an increase in the amount of Cu without Pd (i.e., bimetal), resulting in a mixture of alloy, bimetal and possibly some highly enriched Cu-metal; particularly the last enriched Cu is susceptible to oxidation and hence some amount of copper oxides also appears in XRD.

Figure 6.9c presents the XRD patterns of various PdM alloys (M = Co, Re, Ag). It is noteworthy that in addition to Pd features, Ag features are also observed for the Pd-Ag alloy. However, PdCo (3:1) and PdRe (1:1) forms alloy, without any bimetal formation. Atomic radii of Cu, Co and Re is reported to be 1.35 Å, while Pd is 1.4 Å; while Ag exhibits a atomic radius of 1.60 Å. It is possible that very similar radius helps in alloy formation, while significantly different radius hinders the alloy formation, in the case of PdAg.

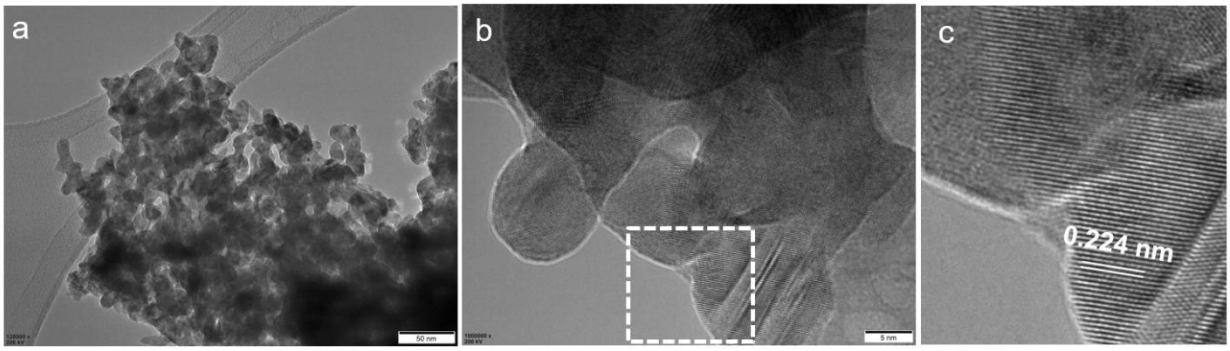

Figure 6.10 HRTEM study of PdCu alloy at (a) 50 nm (b) 5 nm (c) PdCu alloy d spacing.

Figure 6.10 shows the HRTEM images of as prepared PdCu (1:1) alloy. It shows the agglomerated spherical morphology (Figure 6.10a) of the PdCu alloy and an HRTEM image of the alloy is shown in Figure 6.10b and c. The PdCu alloy d-spacing is found to be ~0.224 nm (Figure 6.10c) which corresponds to the (111) facet of the alloy.[34]

6.6.2 Electrochemical LacOR and MalOR in alkaline medium

The electrolysis experiments for the LacOR and MalOR were conducted using both three-electrode and two-electrode configurations, utilizing batch and flow reactors, respectively, as

depicted in Figure 6.11. Electrolysis experiments conducted with glycerol, monosaccharides are similar to the present set of experiments and more details can be found in the earlier chapters. For the three-electrode half-cell reactions, a Pd-M catalyst coated on Ni foam served as the working electrode, a saturated calomel electrode (SCE) was employed as the reference electrode, and a graphite rod functioned as the counter electrode. This setup facilitated precise electrochemical measurements of LacOR and MalOR. In the two-electrode full-cell reactions, a zero-gap electrolyzer flow reactor was used. Here, a PdCu(3:1) catalyst acted as the anode for LacOR/MalOR, while a Pt/C electrode was employed as the cathode for the HER. This configuration enabled efficient and scalable electrolysis under practical conditions.

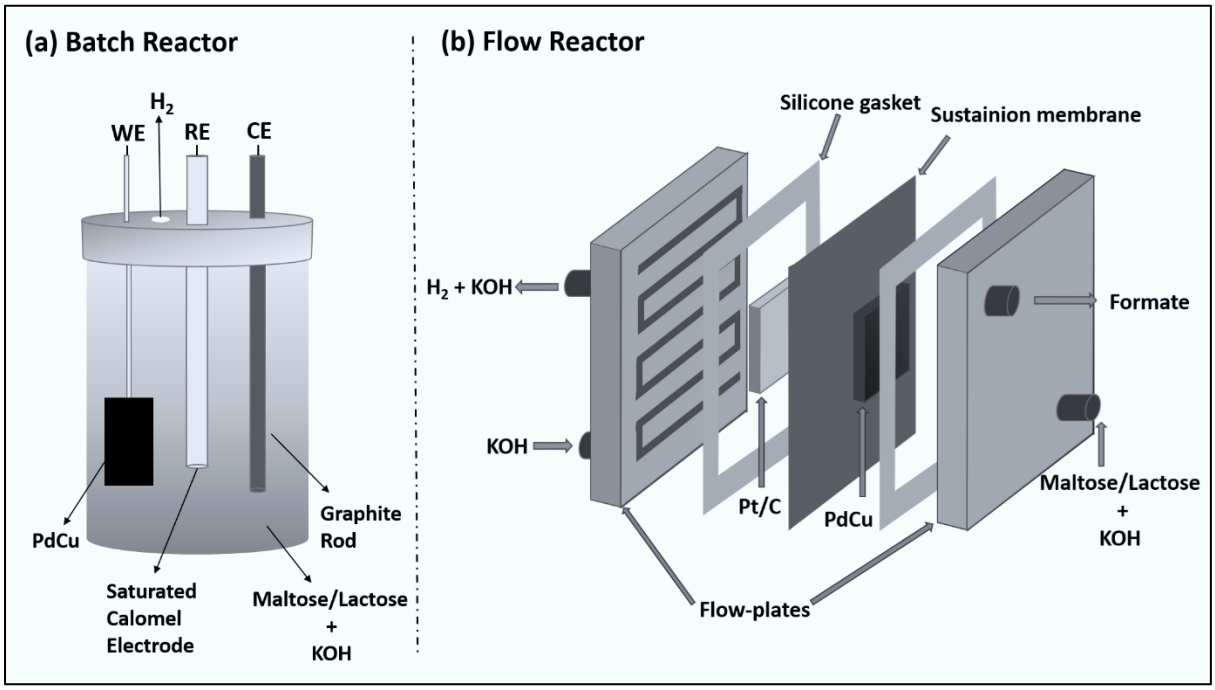

Figure 6.11 Schematic representation of the (a) batch reactor and (b) flow reactor.

Figure 6.12a presents the LSV results for various Pd-based electrocatalysts at different geometric current densities for the LacOR. In the absence of lactose, the PdCu (1:1) alloy anode facilitates the OER from water splitting, exhibiting a high potential of 1.75 V vs. RHE (overpotential of 0.5 V) at a current density of 50 mA/cm^2. With the addition of lactose, the onset potential for LacOR decreases significantly. Notably, the PdCu alloy demonstrates the highest current density even at low applied potentials; for example, a catalytic current density of 100 mA/cm^2 was achieved at a low applied potential of 0.87 V vs. RHE. This represents the first reported LacOR geometric current density for any catalyst. In contrast, the PdCu (1:1) bimetallic combination exhibits a lower LacOR current density. Additionally, the PdCu (1:1)

alloy exhibits the lowest onset potential of 0.12 V vs. RHE, whereas the PdCu (1:1) bimetal exhibits an onset potential of 1.3 V vs. RHE. It is also noteworthy that OER occurs at comparable potentials for both alloy and bimetal forms of PdCu (1:1), while the addition of lactose in LacOR results in a significant difference in activity. Figure 6.12b displays the LSV results for various Pd-based electrocatalysts at different geometric current densities for the MalOR. In the absence of maltose, the PdCu (1:1) alloy anode drives the OER, exhibiting a high potential of 1.75 V vs. RHE at a current density of 50 mA/cm^2. With the addition of maltose, the onset potential for MalOR significantly decreases for the PdCu alloy catalyst anode. The PdCu alloy demonstrates the highest current density even at low applied potentials; a catalytic current density of 100 mA/cm^2 was achieved at 0.91 V vs. RHE. This is also the first reported MalOR geometric current density for any catalyst. Conversely, the PdCu (1:1) bimetal form exhibits lower MalOR current density. The PdCu (1:1) alloy shows the lowest onset potential of 0.09 V vs. RHE, while the PdCu bimetal exhibits an onset potential of 1.3 V vs. RHE. Similar to LacOR, the addition of maltose in MalOR results in a substantial increase in activity compared to OER for both forms of PdCu.

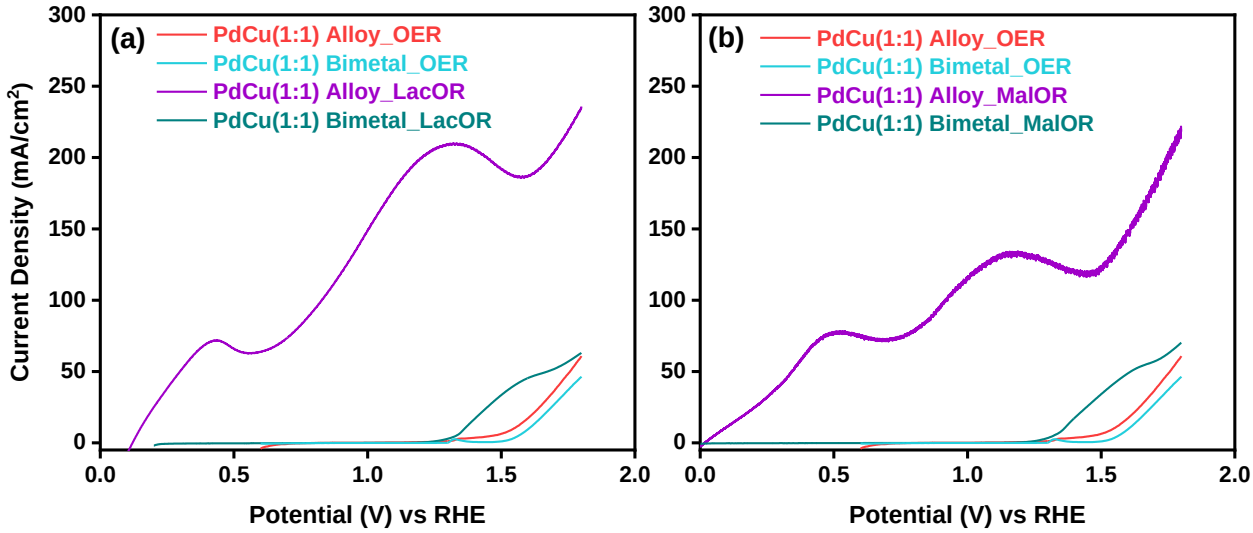

Figure 6.12 (a) Linear sweep voltammetry (LSV) results of Pd-Cu alloy and bimetal electrocatalysts for (a) Lactose electrooxidation (LacOR) and (b) Maltose electrooxidation (MalOR).

Further investigations were conducted on various ratios of PdCu catalysts for LacOR and MalOR, and the results are depicted in Figure 6.13. Figure 6.13a presents the LSV results of different PdCu alloy ratios (1:3, 1:1 and 3:1) for LacOR. The onset potentials of all PdCu alloys are significantly lower compared to pure Pd and Cu. Among the PdCu alloys, the PdCu (3:1) composition exhibited the lowest onset potential of 0.07 ± 0.01 V vs. RHE, marking the lowest

potential reported to date. The PdCu (3:1) catalyst demonstrated catalytic current densities of 50, 100, and 250 mA/cm^2 at applied potentials of 0.1, 0.67, and 1.29 V vs. RHE, respectively, which is significantly superior to the performance of PdCu (1:1) for LacOR (Figure 6.13a). In contrast, pure Pd and Cu exhibited onset potentials at 1.3 V vs. RHE.

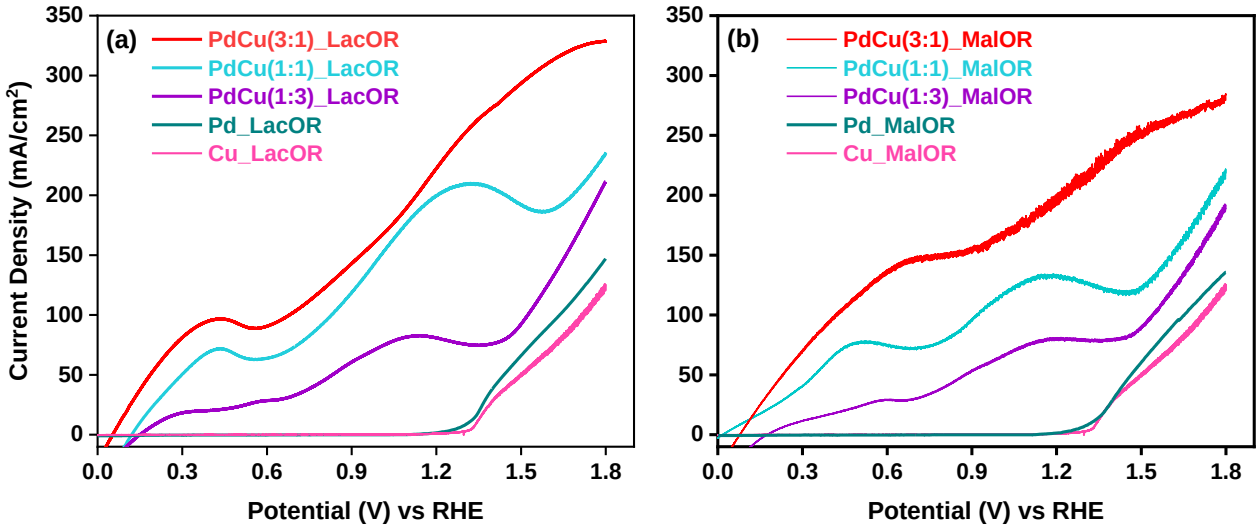

Figure 6.13 LSV results of various Pd:Cu ratios of Pd-Cu alloys for (a) LacOR, and (b) MalOR.

Figure 6.13b displays the LSV results for different PdCu alloy ratios for MalOR. All the PdCu alloys exhibited onset potentials below 0.2 V vs. RHE, whereas pure Pd and Cu showed onset potentials at 1.3 V vs. RHE. Among the PdCu alloys, both PdCu (3:1) and PdCu (1:1) exhibited the lowest onset potentials of 0.09 ± 0.01 V vs. RHE. The PdCu (3:1) catalyst exhibited catalytic current densities of 50 and 100 mA/cm^2 at applied potentials of 0.2 V and 0.4 V vs. RHE, respectively. Notably, the PdCu (3:1) alloy exhibited distinct LSV patterns for LacOR and MalOR, highlighting its exceptional catalytic performance.

To investigate the synergistic effects of Pd and Cu combinations, other metal alloys were also tested for LacOR and MalOR, with synthesis procedures kept consistent across all methods. The LSV results for various combinations of Pd-M (M = Cu, Co, Ag, Re) alloys for LacOR are shown in Figure 6.14a. Among the prepared alloys, PdAg and PdCu demonstrated comparable onset potentials of 0.06 V vs. RHE towards LacOR. While PdCu alloys achieved current densities of 50 and 100 mA/cm^2 at low applied potentials of 0.18 V and 0.6 V vs. RHE, respectively, PdAg required marginally higher voltages to achieve the same current densities. The PdCo and PdRe alloys exhibited higher onset potentials of 0.9 V vs. RHE. Figure 6.14b presents the LSV results for various ratios of PdM (1:1) (M = Cu, Co, Ag, Re) alloys for

MalOR. Among the prepared alloys, PdCu exhibited the lowest onset potential of approximately 0.1 V vs. RHE towards MalOR. PdCu achieved catalytic current densities of 50 and 100 mA/cm^2 at low applied potentials of 0.2 V and 0.4 V vs. RHE, respectively, while PdAg required slightly higher voltages to achieve the same current densities. All other PdM alloys showed a catalytic current density of 100 mA/cm^2 at a high applied potential of 1.5 V vs. RHE. Notably, PdAg exhibited entirely different LSV patterns for LacOR and MalOR. Another interesting observation is the exponential increase in current density from 1.4 V and above for PdRe, which showed significantly higher current densities (300 mA/cm^2) than PdCu at comparable voltages. This suggests the potential to exploit high potential regimes for faster kinetics by optimizing reaction parameters, such as the concentration of disaccharides and flow rate, while carefully avoiding or minimizing OER with PdRe.

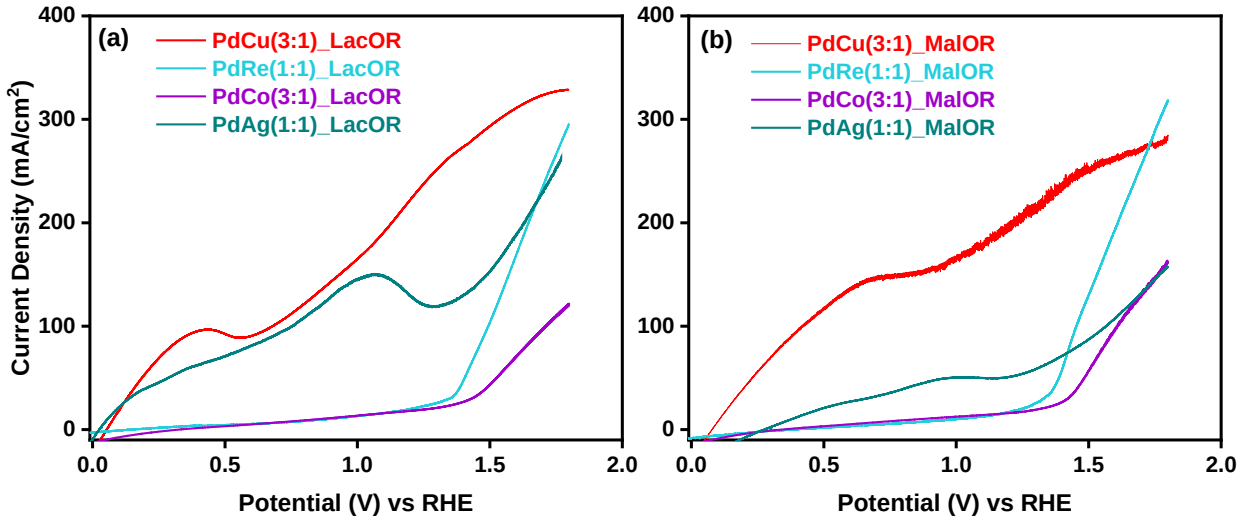

Figure 6.14 LSV results of various PdM (M= Cu, Co, Ag, Re) alloys for (a) LacOR and (b) MalOR.

The LacOR activity on PdCu (3:1) alloy was assessed using chronopotentiometry measurements as a function of applied current density in 1 M KOH and 0.05 M lactose, and the result are shown in Figure 6.15a. Measurements were conducted over 4 hours. At current densities of 10, 20, and 40 mA/cm^2, formic acid was observed to be the major product, with glycolic acid, lactic acid, acetic acid, and methanol as minor products. No significant potential change was observed at 10 and 20 mA/cm^2, whereas at 40 mA/cm^2, the potential increased from 0.77 V to 1.37 V vs. RHE after 3 hours. The observed potentials were 0.4 ± 0.1 V, 0.55 ± 0.1 V, and 1.34 ± 0.04 V vs. RHE for current densities of 10, 20, and 40 mA/cm^2, respectively. Additionally, a carbonate peak was detected in the ^{13}C NMR spectrum at 40 mA/cm^2. Similarly, MalOR activity on PdCu (3:1) alloy was evaluated under the same

conditions with 1 M KOH and 0.05 M maltose (Figure 6.15b). Formic acid was the major product across all current densities (10-40 mA/cm^2), with glycolic acid, lactic acid, and acetic acid as minor products. The potential remained stable at 10 and 20 mA/cm^2, measuring 0.53 ± 0.15 V and 0.65 ± 0.07 V vs. RHE, respectively. A carbonate peak was also observed in the ^{13}C NMR spectrum at 40 mA/cm^2.

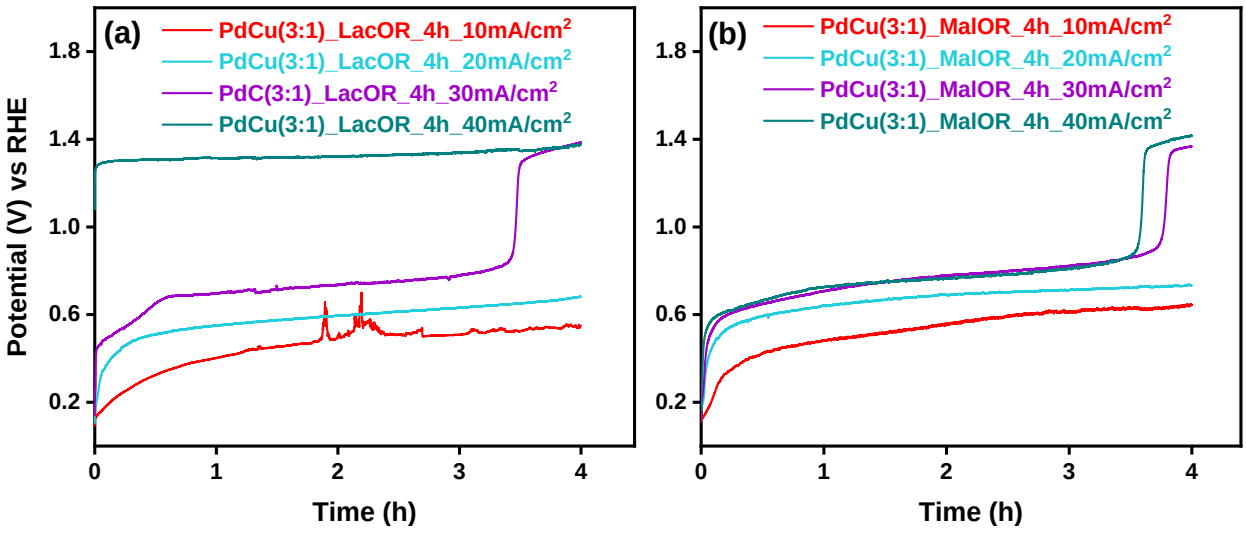

Figure 6.15 Chronopotentiometry measurement with PdCu (3:1) alloy electrocatalyst as a function of applied current density in 1 M KOH and (a) 0.05 M lactose, and (b) 0.05 M maltose.

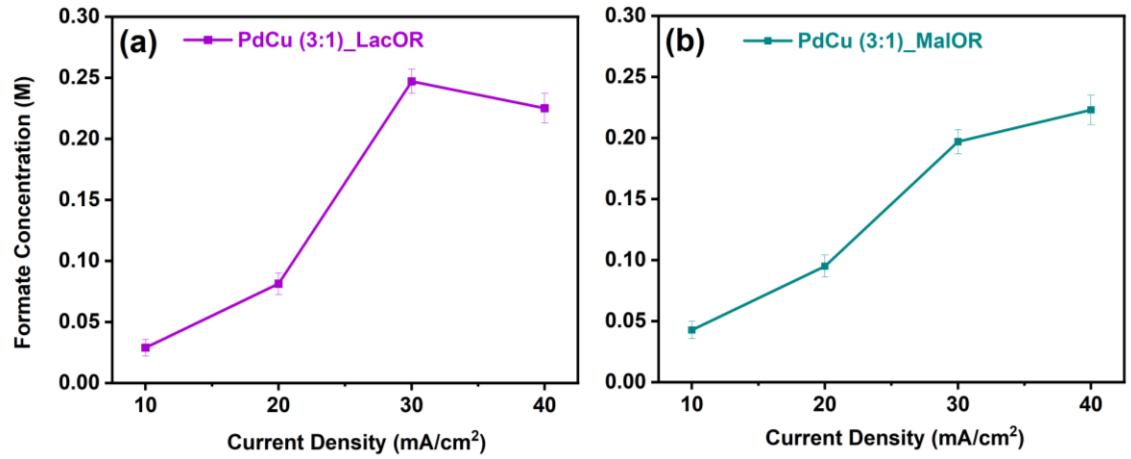

Figure 6.16 Formate production as a function of applied current density with PdCu (3:1) alloy electrocatalyst for (a) LacOR, and (b) MalOR.

Product analysis was carried out by NMR post-chronopotentiometry for LacOR, and the result is depicted in Figure 6.16a; results demonstrate that PdCu (3:1) alloy yield the highest formic acid (formate) production. At 10 mA/cm^2, formic acid concentration was 0.0290 M, increasing to 0.0813 M and 0.247 M at 20 and 30 mA/cm^2, respectively. A notable decrease in formic acid concentration at 40 mA/cm^2 was due to overoxidation of formate to CO_2. Similarly, for

MalOR, as the results shown in Figure 6.16b, the highest formic acid production was achieved with PdCu (3:1) alloy. Formic acid concentrations were 0.0428 M at 10 mA/cm^2, 0.095 M at 20 mA/cm^2, and 0.197 M at 30 mA/cm^2, with a significant increase to 0.223 M at 40 mA/cm^2.

The ^{1}H NMR spectra in Figures 6.17 and 6.18 display the products obtained from the oxidation of lactose and maltose, respectively, underscoring the efficient catalytic performance of the PdCu (3:1) alloy.

Chronopotentiometry experiments were conducted at different but constant current densities (10, 20, 30, and 40 mA/cm^2) for 4 hours, with subsequent product analyses as depicted in Figure 6.19 for LacOR and MalOR. Even at the lowest current density of 10 mA/cm^2, LacOR exhibited approximately 35% selectivity for glyceric acid and about 22% selectivity for formic acid (Figure 6.19a). At a higher current density of 40 mA/cm^2, the selectivity for formic acid peaked at around 75%, accompanied by a 95% conversion rate. For MalOR (Figure 6.19b), at a constant current density of 10 mA/cm^2, the selectivity for glyceric acid and formic acid was found to be 30and 42%, respectively. At 40 mA/cm^2, the selectivity for formic acid reached approximately 81% with 85% conversion rate.

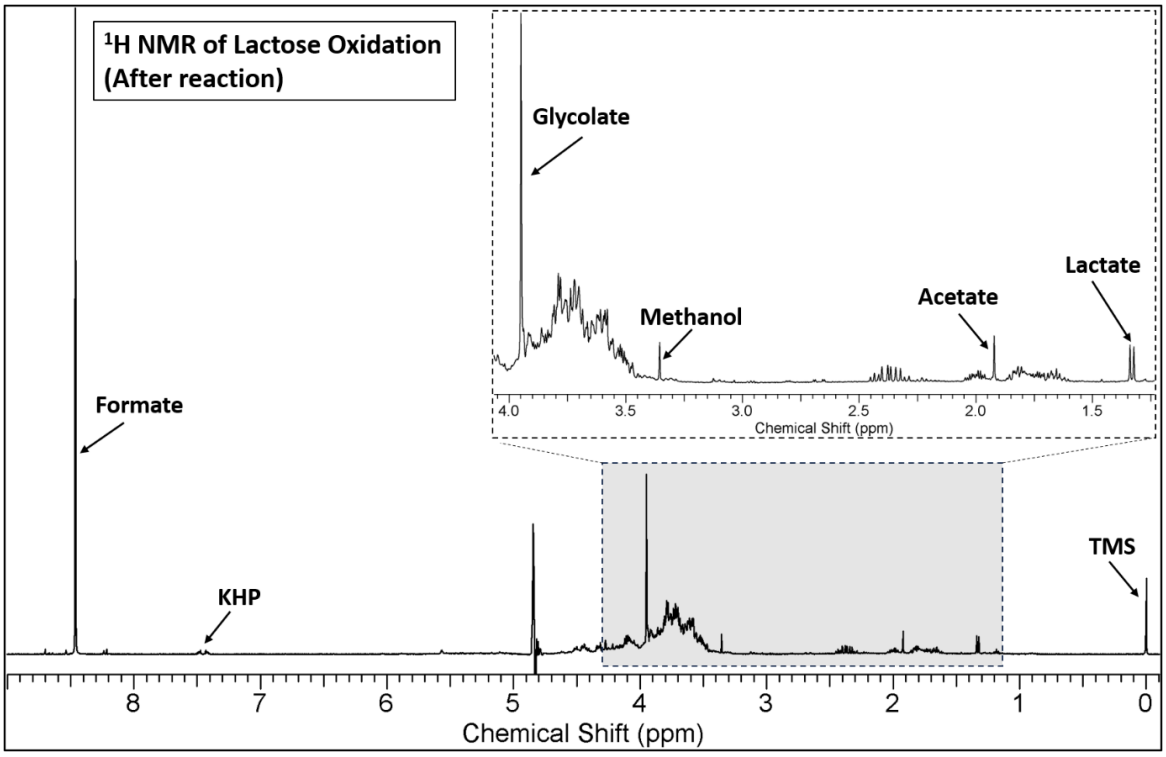

Figure 6.17 ^{1}H NMR spectral data of Lactose oxidation product at 30 mA/cm^2 constant current.

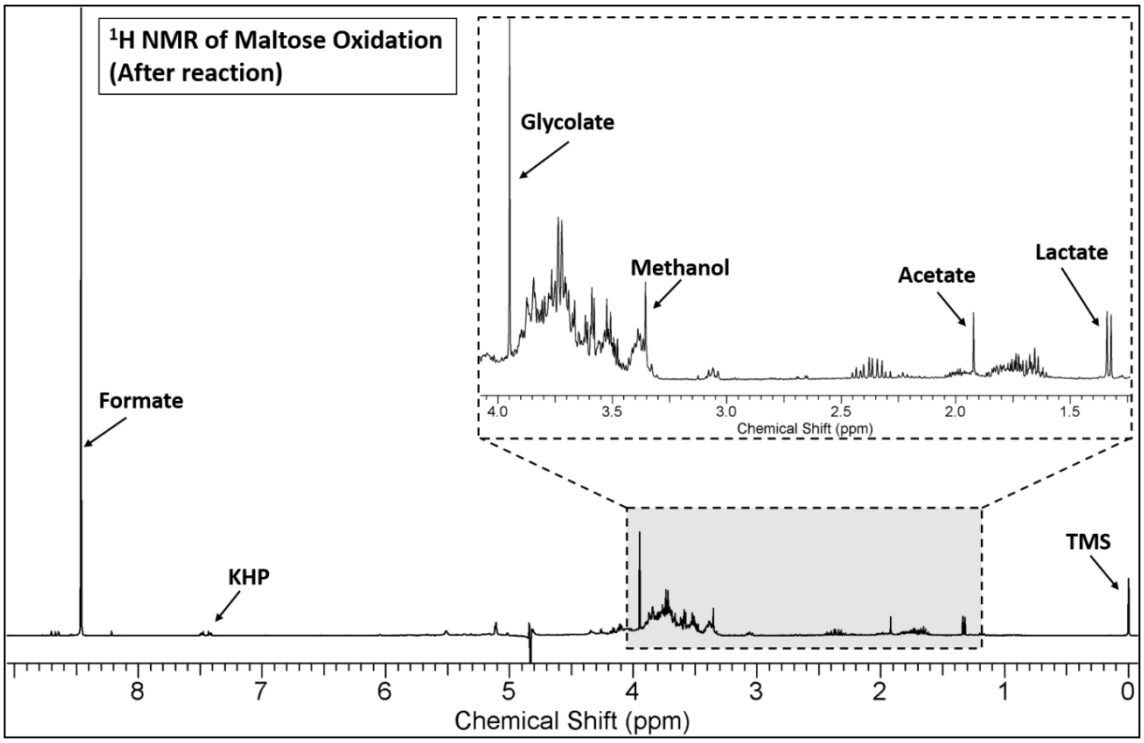

Figure 6.18 ^{1}H NMR spectral data of maltose oxidation product at 30 mA/cm^{2} constant current.

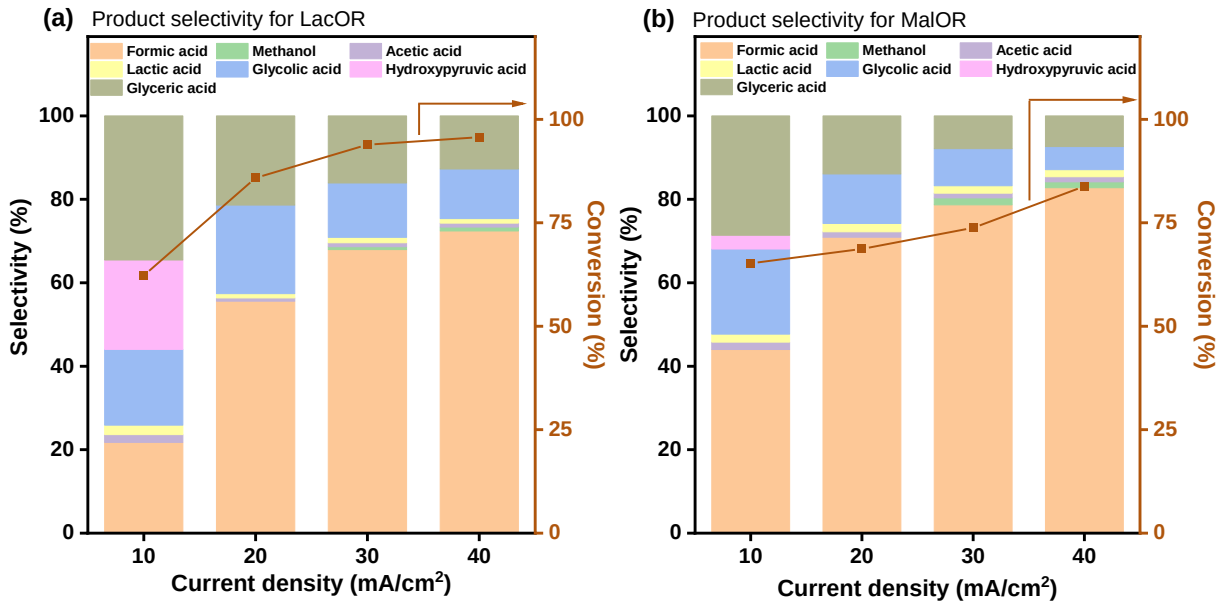

Figure 6.19 Percent selectivity and conversion plot of (a) LacOR, (b) MalOR.

As illustrated in Figures 6.17 and 6.18, the presence of some unreacted disaccharide and unidentified minor products complicates accurate carbon balance calculations. Nevertheless, based on a back calculation from the identified products and the initial concentration of disaccharide, it can be safely stated that more than 75-80% of the disaccharide is converted

into value-added products. These findings underscore the efficient catalytic performance of the PdCu (3:1) alloy for both LacOR and MalOR, demonstrating its potential for high selectivity and conversion rates in biomass oxidation reactions.

6.6.3 Electrolyzer performance for LacOR and MalOR

The two-electrode electrolyzer study was employed to assess the activity of the PdCu (3:1) alloy catalyst for LacOR and MalOR, alongside the concurrent HER performance. A sustainion membrane served as the separator between the two compartments of the electrolyzer. As illustrated in Figure 6.20a, the LSV curve for LacOR in the electrolyzer required a potential of 0.35 V to achieve 50 mA/cm^2 in the presence of lactose and 1.79 V in its absence. The system demonstrated a catalytic current density of 100 mA/cm^2 at a low applied potential of 0.84 V for LacOR. Similarly, Figure 6.20b shows the LSV curve for MalOR in the two-electrode system, where the PdCu (3:1) alloy achieved a catalytic current density of 50 mA/cm^2 at 0.45 V and 100 mA/cm^2 at 1.01 V. Notably, in both scenarios, no significant OER current was observed at 1.5 V when the experiments were conducted without lactose or maltose.

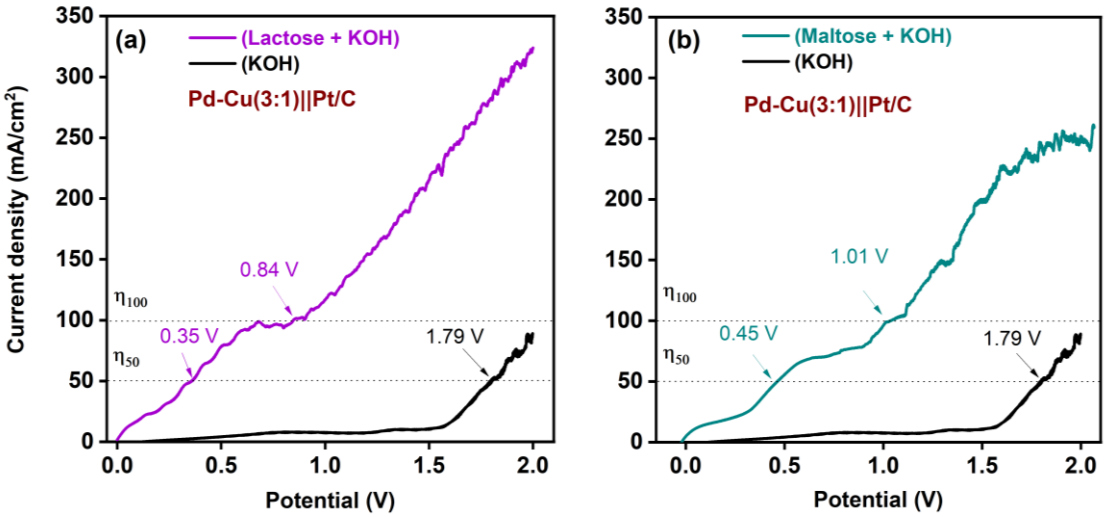

Figure 6.20 LSV of C12 molecules in 2 electrode alkaline electrolyzer with Pd-Cu(3:1) alloy as a anode and Pt/C as a cathode. (a) LSV for LacOR (b) LSV for MalOR.

A chronopotentiometry experiment was conducted for 100 hours at a current density of 400 mA over a 4 cm^2 electrode area (100 mA/cm^2) to evaluate the stability of the PdCu (3:1) alloy catalyst in the alkaline electrolyzer for LacOR and MalOR (Figure 6.21). For LacOR (Figure 6.21a), the system operated at an average potential of approximately 2.25 V throughout the 100-hour reaction, concurrently producing hydrogen at a rate of 160-170 mL/h. Similarly, for MalOR (Figure 6.21b), the average potential of the two-electrode system was around 2.2 V,

and the catalyst remained stable throughout the 100-hour operation, continuously producing hydrogen at a rate of 160-170 mL/h.

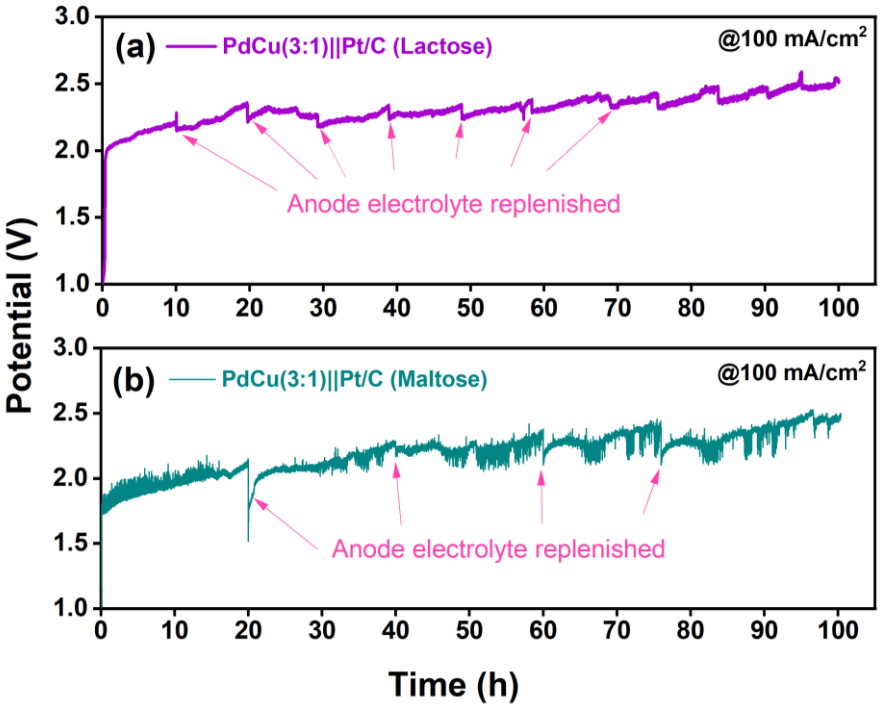

Figure 6.21 Sustainable operation of Lactose and Maltose electrooxidation process at 100 mA/cm^2 for 100 h.

These results highlight the robust performance of the PdCu (3:1) alloy catalyst in facilitating LacOR and MalOR, while maintaining high stability and efficiency in hydrogen production over extended periods. Nonetheless, further long-term studies (1000 and 10000 h) would be desired to demonstrate the sustainability for long periods under operating conditions.

6.7 Conclusion

This study explores PdCu alloys (and bimetal combinations) for electrocatalytic oxidation of lactose and maltose in alkaline conditions, coupled with HER. PdCu (3:1) demonstrates superior performance with low onset potentials and high current densities compared to pure Pd and Cu. It exhibits remarkable stability over 100 hours, maintaining consistent hydrogen production rates in chronopotentiometry tests. PdCu (3:1) shows significant formic acid selectivity in LacOR and high formic acid yield in MalOR, emphasizing its efficiency in converting sugars into value-added products. Extensive C-C cleavage occurs under operating conditions is evident from the selective formate production. Indeed, this is the observation is likely to help bigger biomass components like cellulose as well as microplastics. Electrochemical analyses reveal synergistic effects between Pd and Cu, enhancing catalytic

activity while mitigating overoxidation pathways. The two-electrode electrolyzer setup validates practical applicability, showing efficient coupling of LacOR/MalOR with concurrent HER. This underscores PdCu alloys as promising catalysts for biomass conversion, crucial for advancing sustainable energy technologies. PdAg (1:1) and PdRe (1:1) alloys demonstrate comparable activity, but at high potential. They may be explored further in detail.

6.8 References

1. T. Kåberger, Glob. Energy Interconnect. 2018, 1, 48.
2. D. Helm, Oxf. Rev. Econ. Policy 2016, 32, 191.
3. S. F. Lincoln, Ambio 2005, 34, 621.
4. T. Covert, M. Greenstone, C. R. Knittel, J. Econ. Perspect. 2016, 30, 117.
5. S. Shafiee, E. Topal, Energy Policy 2009, 37, 181.
6. M. Höök, X. Tang, Energy Policy 2013, 52, 797.
7. K. O. Yoro, M. O. Daramola, CO2 Emission Sources, Greenhouse Gases, and the Global Warming Effect, Elsevier Inc, Woodhead, Sawston 2020.
8. Y. S. H. Najjar, Innov. Energy Policies 2011, 1, 1.
9. H. Nazir, C. Louis, S. Jose, J. Prakash, N. Muthuswamy, M. E. M. Buan, C. Flox, S. Chavan, X. Shi, P. Kauranen, T. Kallio, G. Maia, K. Tammeveski, N. Lymperopoulos, E. Carcadea, E. Veziroglu, A. Iranzo, A. M. Kannan, Int. J. Hydrogen Energy 2020, 45, 13777.
10. R. Yukesh Kannah, S. Kavitha, Preethi, O. Parthiba Karthikeyan, G. Kumar, N. V. Dai-Viet, J. Rajesh Banu, Bioresour. Technol. 2021, 319, 124175.
11. H. Zhao, Z.-Y. Yuan, ChemSusChem 2021, 14, 130.
12. Y. Zhao, B. Jin, A. Vasileff, Y. Jiao, S.-Z. Qiao, J. Mater. Chem. A 2019, 7, 8117
13. (a)B. Rausch, M. D. Symes, G. Chisholm, L. Cronin, Science 2014, 345, 1326; (b) W. Li, N. Jiang, B. Hu, X. Liu, F. Song, G. Han, T. J. Jordan, T. B. Hanson, T. L. Liu, Y. Sun, Chem 2018, 4, 637;
14. a) B. You, Y. Sun, Acc. Chem. Res. 2018, 51, 1571; b) B. You, G. Han, Y. Sun, Chem. Commun. 2018, 54, 5943; c) Y. Xu, B. Zhang, ChemElectroChem 2019, 6, 3214.
15. a) H. Luo, J. Barrio, N. Sunny, A. Li, L. Steier, N. Shah, I. E. L. Stephens, M.-M. Titirici, Adv. Energy Mater. 2021, 11, 2101180; b) F. Arshad, T. u. Haq, I. Hussain, F. Sher, ACS Appl. Energy Mater. 2021, 4, 8685.
16. I. Chauhan, P. M. Vijay, R. Ranjan, K. K. Patra and C. S. Gopinath, *ACS Materials Au*, DOI:10.1021/acsmaterialsau.4c00024.
17. I. Chauhan, H. Bajpai, B. Ray, S. K. Kolekar, S. Datar, K. K. Patra and C. S. Gopinath, *ACS Applied Materials & Interfaces*, 2024, **16**, 26130–26141.
18. A. Saha, V. Murugiah, R. Ranjan, I. Chauhan, K. K. Patra, H. Bajpai, A. Saha and C. S. Gopinath, *Sustainable Energy & Fuels*, 2024, 8, 2954-2968.
19. J. Wang, B. Zhang, W. Guo, L. Wang, J. Chen, H. Pan and W. Sun, *Advanced Materials*, 2023, 35, 2211099.

20. C. Liang, R. Zhao, T. Chen, Y. Luo, J. Hu, P. Qi and W. Ding, *Advanced Science*, 2024, 11, 2308958.
21. L. Zhu, J. Huang, G. Meng, T. Wu, C. Chen, H. Tian, Y. Chen, F. Kong, Z. Chang, X. Cui and J. Shi, *Nature Communications*, 2023, 14, 1997.
22. H. Xu, P. Song, C. Fernandez, J. Wang, M. Zhu, Y. Shiraishi and Y. Du, *ACS Applied Materials & Interfaces*, 2018, **10**, 12659–12665.
23. X. Liu, B. Li, G. Han, X. Liu, Z. Cao, D.-E. Jiang and Y. Sun, *Nature Communications*, 2021, 12, 1868.
24. P. Hauke, T. Merzdorf, M. Klingenhof and P. Strasser, *Nature Communications*, 2023, 14, 4708.
25. H. Wang, M. Sun, J. Ren and Z. Yuan, *Advanced Energy Materials*, 2023, 13, 2203568.
26. F. H. Isikgor and C. R. Becer, *Polymer Chemistry*, 2015, **6**, 4497–4559.
27. C. Stylianopoulou, in *Elsevier eBooks*, 2023, pp. 114–125.
28. S. B. Aoun, G. S. Bang, T. Koga, Y. Nonaka, T. Sotomura and I. Taniguchi, *Electrochemistry Communications*, 2003, **5**, 317–320.
29. P. Parpot, V. P. Muiuane, V. Defontaine and A. P. Bettencourt, *Electrochimica Acta*, 2010, **55**, 3157–3163.
30. P. S. Roy and S. K. Bhattacharya, *Catalysis Science & Technology*, 2013, **3**, 1314.
31. M. Ma, W. Zhu, Q. Shao, H. Shi, F. Liao, C. Shao and M. Shao, *ACS Applied Nano Materials*, 2021, **4**, 1478–1484.
32. L. Yang, Z. Li, C. Chen, J. Wang, Q. Yin, Y. Zhang and P. Guo, *Inorganic Chemistry*, 2023, **62**, 15320–15328.
33. F. Xue, Q. Li, M. Lv, S. Weng, T. Li, Y. Ren, Y. Liu, D. Li, Y. He, Q. Li, X. Chen, Q. Zhang, L. Gu, J. Deng, J. Chen, L. He, X. Kuang, J. Miao, Y. Cao, K. Lin and X. Xing, *Nano Letters*, 2024, **24**, 6269–6277.
34. S. R. Chowdhury, P. Mukherjee and S. K. Bhattachrya, *International Journal of Hydrogen Energy*, 2016, **41**, 17072–17083.

Chapter 7

Conclusion and Future Plan

Drawing from the preceding discourse, the pursuit of energy-efficient hydrogen production from water emerges as a pivotal stride in shaping a sustainable energy landscape. Nevertheless, the sluggish kinetics inherent in water splitting reactions present a formidable obstacle to transitioning to a hydrogen-based economy from hydrocarbons. A range of catalysts, including precious and non-precious group-metal types, have been created to overcome this difficulty. This thesis advances the field of biomass oxidation and energy-efficient hydrogen generation from water. This entails optimising the physicochemical characteristics of electrocatalysts to create durable materials and investigating novel, low-energy approaches for affordable hydrogen production. *The third and sixth chapters provide a broad overview of the scope and objectives of this thesis, detailing our approach to the synthesis and property tuning of photo-electrocatalysts and electrocatalysts towards catalysing various electrochemical reactions, including CER, GLYOR, and GLUOR, which are involved in the production of hydrogen at a low cost.*

The **first and second chapters** of this thesis introduce the main areas of electro and photo-electrocatalysis and outline the experimental methods employed.

In **third Chapter** the development of a nanostructured Co-doped $BiVO_4$ (Co-BV) photoanode for efficient and sustainable photoelectrochemical chlorine evolution from simulated sea-water is discussed. This study highlights the challenges of sustainable hydrogen and chlorine production from sea-water splitting, emphasizing the importance of suitable photo-electrocatalysts. Successful Co-doping in the $BiVO_4$ crystal lattice was achieved, resulting in a photocurrent of 190 $\mu A/cm^2$ at 1.1 V vs. RHE and efficient chlorine evolution with 92% Faradaic efficiency. The Co-BV photoanode demonstrated decreased charge transfer resistance, enhanced charge carrier lifetime, and improved sustainability, making it a promising material for sea-water splitting. This work underscores the broader implications of using renewable resources for efficient fuel/energy production and the potential of solar energy in producing hydrogen through photoelectrochemical processes.

In **fourth Chapter** demonstrates the shape-controlled palladium nanocrystals, synthesized via colloidal chemistry, for electrochemical GLYOR at significantly low voltages. The study reveals that controlling the shape of electrocatalysts can modulate activity and selectivity, which is underexplored for many reactions, including GLYOR. Pd-NC anode exhibited the highest current density, reaching 100 mA/cm^2 at 0.85 V vs. RHE, the best reported for GLYOR, with an onset potential of 0.40 V. The Pd-NC electrocatalyst achieved the highest glycerol

conversion (85%) with 40% glyceric acid selectivity at a low applied potential of 0.6 V (vs. RHE). The assembled electrolyzer demonstrated sustainability at 10 and 50 mA/cm^2 up to 120 hours with GLYOR in water and simulated seawater, requiring only ~3.7 kWh/m^2 of H_2, in contrast to ≥5 kWh/m^3 with alkaline/PEM electrolyzers.

In **fifth Chapter** the synthesis of two-dimensional (2D) ultrathin nanosheet phosphates, including cobalt (CoP), copper (CuP), nickel (NiP), and a 3D snow-flake structure with iron (FeP) phosphates, is presented. The high density of surface-exposed active sites and substantial surface area of CoP allowed it to perform well as an electrocatalyst for GLYOR in an alkaline electrolyte. With an astoundingly low overpotential of 1.27 V (against RHE), CoP nanosheets demonstrated a low onset potential and excellent intrinsic stability. This work is the first to describe phosphate-based GLYOR electrocatalysts, demonstrating the extremely robust electrochemical stability of CoP under demanding alkaline conditions over a 200-hour continuous GLYOR operation.

In **sixth Chapter** subdivided into two parts. Chapter 4a focuses on demonstrating electrocatalytic glucose oxidation (GLUOR) with Pd NC, showing low onset potential (0.3-0.4 V vs. RHE) and efficient oxidation onset with glucose to glucaric acid. Additionally, a low-cost cathode NiP catalyst was synthesized as an alternative to graphite or Pt/C for the HER, with both catalysts employed in an alkaline electrolyzer for GLUOR. Chapter 4b explores a combined palladium-copper-based electrocatalyst for concurrent electrochemical oxidation of disaccharides (lactose/maltose) into formate and carbon-negative green hydrogen production, illustrating the process of formate production by electrochemical oxidation of disaccharides with said electrocatalyst.

Subsequent investigations will concentrate on the sophisticated development of catalysts for biomass oxidation and water splitting that exhibit increased stability and activity. Investigating novel dopants, support materials, and mechanistic research to comprehend kinetics and pinpoint active sites utilising sophisticated characterisation methods like in-situ IR or RAMAN are important fields. Integrating photo-electrocatalysis and electrocatalysis with renewable energy sources like solar energy will be prioritized to optimize large-scale hydrogen production. Efforts will also be made to scale up high-performance catalysts, design pilot-scale reactors, and investigate various biomass feedstocks, including agricultural and industrial waste.

By tweaking the catalysts' electrical structure, we hope to increase the selectivity of oxidised products. While this thesis work focused on C3 to C12 molecules, future research will target a broader range of biomass carbon molecules and microplastics. Advancing biomass oxidation on the anode side and implementing co-electrolysis on the cathode side, including CO_2, N_2, and nitrate reduction, will create a versatile and sustainable electrochemical platform. Life cycle assessments will be conducted to minimize the carbon footprint, contributing to a sustainable hydrogen-based energy economy.

ABSTRACT

Name of the Student: Inderjeet Chauhan **Registration No.:** 10CC18A26057

Faculty of Study: Chemical Sciences **Year of Submission:** 2024

AcSIR academic centre/CSIR Lab: CSIR-NCL, Pune

Name of the Supervisor(s): Dr. Chinnakonda S. Gopinath

Title of the thesis: "Energy Conversion through Photo-electrocatalysis and Electrocatalysis to Value-added Products from Simulated Seawater and Biomass Components"

A potential technique for producing renewable hydrogen, a clean fuel or energy carrier, which is projected to be the future fuel, to replace traditional carbon-based fossil fuel sources, is electrochemical (EC) water splitting. Although it is a mature technology, its overall cost-effectiveness is low and solar-to-hydrogen efficiency are still insufficient for widespread use. This is primarily due to the anodic oxygen evolution reaction's (OER) slow kinetics at high potential and the cogenerated O_2 production's low economic value. There have been significant efforts over the past few decades to investigate more kinetically advantageous oxidation processes; when they are combined with the hydrogen evolution reaction (HER), can simultaneously increase the yield of H_2 and provide more useful or valuable products in the place of O_2. Current thesis intends to highlight current developments about OER's alternate anodic options and the entire thesis explores few such options experimentally. Here, a brief overview of the fundamentals of EC water splitting and the essential elements needed for this system is given. Then, when combined with the concurrent HER, the advantages and disadvantages of other oxidation reactions, such as the oxidation of sea-water or organic-containing aqueous solution to chlorine, organic acids, various value-added compounds are examined and analyzed. The problems and prospects of these alternative HER-coupled oxidation processes for green energy production and environmental treatment are evaluated in this thesis.

List of publications emanating from the thesis

1. Nanostructured Co-doped BiVO4 for efficient and sustainable photoelectrochemical chlorine evolution from simulated sea-water. ***Inderjeet Chauhan*****,** Kshirodra Kumar Patra, Himanshu Bajpai, Nitin B. Mhamane, Kranti N. Salgaonkar and Chinnakonda S. Gopinath*. ***Dalton Trans.***, 2023,**52**, 2051-2061

2. Electrocatalytic Glycerol Conversion: A Low-Voltage Pathway to Efficient Carbon-Negative Green Hydrogen and Value-Added Chemical Production. ***Inderjeet Chauhan***, Himanshu Bajpai, Bishakha Ray, Sadhu K Kolekar, Suwarna Datar, Kshirodra Kumar Patra*, Chinnakonda S Gopinath*. ***ACS Appl. Mater. Interfaces,*** 2024, 16, 20, 26130–26141

3. Electrocatalytic and Selective Glycerol Oxidation to Formate on 2D 3d-Metal Phosphates Nanosheet and Carbon-Negative Hydrogen Generation. ***Inderjeet Chauhan,*** Pothoppurathu M. Vijay, Ravi Ranjan, Kshirodra Kumar Patra and Chinnakonda S. Gopinath* ***ACS Mater. Au***, 2024, Just Accepted Manuscript.

4. Electrocatalytic Glucose Oxidation: Insights from Palladium. ***Inderjeet Chauhan****,* Kshirodra Kumar Patra, Pothoppurathu M. Vijay, and Chinnakonda S. Gopinath* *(manuscript under preparation)*

5. Electrocatalytic Disaccharide Oxidation: Synergistic Activity of PdCu Alloy Catalysts. ***Inderjeet Chauhan,*** Kshirodra Kumar Patra, Pothoppurathu M. Vijay, and Chinnakonda S. Gopinath* *(manuscript under preparation)*

List of publications emerged from other related work

1. Design of Bi-functional Oxide Electrode for Selective Oxidative C-C Cleavage of Glycerol to Formate and Synchronized Green Hydrogen Production. Arindam Saha, Vasantharadevi Murugiah, Ravi Ranjan, ***Inderjeet Chauhan***, Kshirodra Patra, Himanshu Bajpai, Avishek Saha and Chinnakonda S. Gopinath* ***Sustainable Energy & Fuels***, 2024, Accepted Manuscript

2. Biomass components toward H2 and value-added products by sunlight-driven photocatalysis with electronically integrated Au δ−–TiO2: concurrent utilization of electrons and holes Himanshu Bajpai, ***Inderjeet Chauhan***, Kranti N Salgaonkar, Nitin B Mhamane, Chinnakonda S Gopinath* ***RSC Sustainability,*** 2023, 1, 481

3. A baby step in assembling and integrating the components of an artificial photosynthesis device with forced heterojunctions towards improved efficiency. Kranti N Salgaonkar, Himanshu Bajpai, Nitin B Mhamane, Naresh Nalajala, ***Inderjeet Chauhan***, Kavita Thakkar, Kavita Joshi, Chinnakonda S Gopinath*. ***J. Mater. Chem. A***, 2023, 11, 15168

4. Aqueous Methanol to Formaldehyde and Hydrogen on Pd/TiO_2 by Photocatalysis in Direct Sunlight: Structure Dependent Activity of Nano-Pd and Atomic Pt-Coated Counterparts. Naresh Nalajala, Kranti N Salgaonkar, ***Inderjeet Chauhan***, Siva Prasad

Mekala, Chinnakonda S Gopinath*. ***ACS Appl. Energy Mater.*** 2021, 4, 11, 13347–133603

5. Facet dependent bismuth series for the treatment of environmental pollutants. Abhaya Kumar Mishra, Subhashree Swagatika Kanungo, ***Inderjeet Chauhan***, TR Nivedhitha (Book Chapter)

List of invention disclosure filed emanating from the thesis

1. Electrocatalytic Conversion of Biomass components(s) into Value-added Chemicals and Concurrent Green Hydrogen Production (NCLI-INV-2023-0002) ***Inderjeet Chauhan***, K.K. Patra, & C. S. Gopinath

2. Electrocatalytic Conversion of Disaccharide into Value-added Chemicals and Concurrent Green Hydrogen Production (NCL-INV-2024-0002). ***Inderjeet Chauhan***, K.K. Patra, Vijay PM & C. S. Gopinath

List of conferences and seminars emanating from the thesis

1. **One day symposium on Catalysis and Renewable Energy Towards Meeting Sustainable Development Goals (SDG),** An invited talk on "Alternatives to Water Oxidation for Electrochemical Energy Conversion and Carbon- Negative Green Hydrogen Production" [27/06/2024] SSBLT, PAML Building, CSIR-NCL, Pune - 08, India

2. **Fifth HUMBOLDT KOLLEG on Global Impact of Pandemic on Healthcare, Economy and Environment,** Flash talk and poster presentation entitled “Electrocatalytic Glycerol Conversion: A Low-Voltage Pathway to Efficient Carbon-Negative Green Hydrogen and Value-Added Chemical Production”. [15/02/2024 – 17/02/2024] Bogmallo Beach Resort, Goa, India

3. **8th edition of the Hybrid International Conference on "Nanotechnology for Better Living"** Poster presentation entitled “Nanostructured Co-doped BiVO4 for efficient and sustainable photoelectrochemical chlorine evolution from simulated sea-water”. [25/05/2023 – 29/05/2023] National Institute of Technology (NIT), Srinagar, Jammu and Kashmir 190006

4. **International Materials Conclave (IMC-2023)** Oral presentation entitled “Nanostructured Co-doped BiVO4 for efficient and sustainable photoelectrochemical chlorine evolution from simulated sea-water”. [08/03/2023 – 10/03/2023] Centre for Materials for Electronics Technology (C-MET), Pune, Maharashtra, India

5. **Workshop on Electrochemical Science and Technology (Workshop-EST-2024).** [06/07/2024] Training School Hostel (TSH), Anushaktinagar, Mumbai 400094, India

6. **One Day Theme Meeting on Recent Trends in Solid State Chemistry.** [06/04/2024] DAE Convention Centre, BARC, Anushaktinagar, Mumbai-400094, India

Honours and Awards

1. **DST-INSPIRE Fellowship,** [2017] Ministry of Science and Technology, Government of India

2. **NCL RF - Agnimitra Memorial Poster Award 2021 and 2023** Awarded ***Best Poster Award*** in the area of Catalysis and Inorganic Chemistry as part of National Science Day Celebration 2021 and 2023, CSIR - NCL, Pune

3. **NCL RF Annual Students' Conference 2022** Secured ***Best working model presentation*** in the Annual Students' Conference 2022, CSIR - NCL, Pune

Dalton Transactions

ROYAL SOCIETY OF CHEMISTRY

PAPER

View Article Online
View Journal | View Issue

Cite this: *Dalton Trans.*, 2023, **52**, 2051

Nanostructured Co-doped $BiVO_4$ for efficient and sustainable photoelectrochemical chlorine evolution from simulated sea-water†

Inderjeet Chauhan,[a,b] Kshirodra Kumar Patra,[a] Himanshu Bajpai,[a,b] Nitin B. Mhamane,[a,b] Kranti N. Salgaonkar[a,b] and Chinnakonda S. Gopinath *[a,b]

Received 17th October 2022,
Accepted 9th January 2023

DOI: 10.1039/d2dt03369k

rsc.li/dalton

The co-production of hydrogen and chlorine from sea-water splitting could be a potential, sustainable and attractive route by any method. However, challenges to overcome are many, and critically, the sustainability and operating potential of the electrocatalyst are important. In this work, we report on Co-doping in the $BiVO_4$ (Co-BV) crystal lattice and employed the same as the photoanode; Co-BV exhibits a photocurrent of 190 μA cm^{-2} at 1.1 V *vs.* RHE (the reversible hydrogen electrode) in the acidic sodium chloride solution (pH 2.3) under one sun illumination. The best-performing photoanode, with 0.05 mol% of Co doping (0.05 Co-BV), selectively produced active chlorine with 92% faradaic efficiency at 1.1 V *vs.* RHE by successfully suppressing the kinetically sluggish oxygen evolution reaction (OER) and the stability of the catalyst was demonstrated for up to 20 h. This is the lowest operating potential reported for the chlorine evolution reaction (CER), thus far. The overpotential required for CER with 0.05 Co-BV is lower than that of OER, which leads to selective CER at 1.1 V (*vs.* RHE). Co-doping into the $BiVO_4$ lattice decreases the charge transfer resistance and enhances the CER kinetics due to its structural and electronic integration with the BV lattice. We demonstrate that Co-doping also improves the lifetime of the charge carrier and enhances the current density of CER and sustainability of the catalyst.

Introduction

To address the depletion of fossil fuels, rapid anthropogenic climate change, and severe environmental issues, there is an increasing push to use renewable resources, such as solar and wind energy, and carbon-free chemicals (such as hydrogen), for sustainable and efficient fuel/energy production. Solar energy is one of the most appealing methods and can be used to obtain hydrogen from water *via* photoelectrochemical (PEC) or photocatalytic water-splitting.[1a,b] In PEC water splitting, the semiconductor functions as a photoanode to oxidize water to oxygen on exposure to sunlight, and H_2 is produced on the cathodic side.[2] This could be an effective and environmentally sustainable way to generate pure hydrogen in a clean, cost-effective, and carbon-free approach. However, the key technicality and economically challenging aspect in PEC water splitting is the kinetically sluggish four-electron water oxidation process, which is the bottleneck for cost-effective green hydrogen production. Moreover, O_2 produced in this process has limited economic value (eqn (1)) but is produced at a high cost/energy, such as employing a high operating potential and noble metal catalyst.[3–6] Replacing water oxidation with any suitable electro-oxidant could potentially reduce the hydrogen production cost along with a value-added oxidized product and opens up a new pathway to produce two value-added chemicals concurrently.

$$2H_2O \rightarrow O_2 + 4H^+ + 4e^-, \quad E^\circ = 1.23\ V_{RHE} \qquad (1)$$

In contrast to the four-electron oxygen evolution reaction (OER), the chlorine evolution reaction (CER) is a two-electron process, and CER is also kinetically more favorable than OER. However, the theoretical potentials required for the OER and CER are 1.23 and 1.36 V, respectively. Considering the overpotentials required for both OER and CER, which predominantly depend on the material, a catalyst that works at a low (high) overpotential for CER (OER) is a key requirement to demonstrate the selective CER activity with sea/salt water, while fully avoiding OER. It is also well known that there are many advantages of operating at low overpotential, which is, in fact, a prerequisite for sustainability. It is also known that CER leads to acidic pH due to the solubilization of chlorine in water leading

[a]*Catalysis and Inorganic Chemistry Division, CSIR-National Chemical Laboratory, Dr. Homi Bhabha Road, Pune 411 008, India. E-mail: cs.gopinath@ncl.res.in*
[b]*Academy of Scientific and Innovative Research (AcSIR), Ghaziabad 201 002, India*

†Electronic supplementary information (ESI) available: SILAR schematics (Fig. S1), FESEM image (Fig. S2), surface profile (Fig. S3), photoluminescence (Fig. S4), chronoamperometry (Fig. S5), co-content by ICP (Table S1), lifetime decay (Table S2). See DOI: https://doi.org/10.1039/d2dt03369k

to the formation of hypochlorous acid (HClO), and hence the catalyst should withstand such conditions for sustainable activity.

Since sea water is an abundant source of aqueous NaCl (0.6 M or 3.5 wt%) as the electrolyte, few attempts have been made to use sea/salt water as feedstock in PEC devices to produce hydrogen and oxygen/chlorine. Moreover, the use of seawater potentially reduces the operational cost of PEC water-splitting devices, which otherwise use pure water and chemicals for the electrolyte solution. In addition to the above aspect, Cl_2 produced through CER is an industrially important chemical/intermediate for the production of several compounds, such as drugs, disinfectants, and polymers. Currently, about 53 million metric tons of chlorine are annually produced worldwide, mainly through the Chlor-alkali process.[7] Due to the sluggish four electron kinetics of OER, if CER can be carried out at low overpotential, there is a good possibility of increasing the H_2 production rate also through PEC means with non-precious metal group catalyst/metal.[8–10] (eqn (2))

$$H_2O + 2Cl^- \rightarrow H_2 + Cl_2, \quad E^\circ = 1.36\ V_{RHE} \qquad (2)$$

Very few reports are available to produce hydrogen and/or chlorine by PEC water splitting under visible light irradiation, and this fact highlights the complexity of sea-water splitting. An electrodeposited nanostructured WO_3 shows 70% faradaic efficiency and a photocurrent of 4.5 mA cm^{-2} at 1.3 V (*vs.* RHE) with predominant Cl_2 and significant oxygen generation, while hydrogen is stored in Pd-cathode.[11] A rutile TiO_2 has also been reported to be active under UV illumination for photoelectrochemical CER and exhibits 8 mA cm^{-2} at a relatively higher potential of 1.65 V (*vs.* RHE) in a neutral pH (pH = 7) solution.[12] An electrode consisting of nanostructured $BiVO_4/WO_3$ reached a photocurrent density of 2.5 ± 0.3 mA cm^{-2} at 1.42 V (*vs.* RHE) and showed 85% faradaic efficiency for Cl_2 production.[13] Although the above catalysts work with high photocurrent density, they either work at high overpotential, low faradaic efficiency, with UV light or exhibit poor stability. Hence the challenge is to produce a photoelectrocatalyst system that works for CER at low overpotential, which is also necessarily and significantly lower than that of OER, and possibly with high current density. In addition, the catalyst should absorb visible light and be stable under acidic pH conditions, as chlorine dissolution makes the solution acidic and corrodes the catalyst. Indeed, the real challenge is to bring all the above factors into one catalyst system to demonstrate a sustainable seawater-splitting photoelectrocatalyst, under favorable operating conditions. Since OER is favorable in neutral and alkaline solutions, most works reported for CER by the PEC process have been carried out under acidic pH (pH < 4). $BiVO_4$ (BV) is known to be a very good light-absorbing semiconductor (band gap 2.4 eV) and is used as a low-cost material for CER due to its favorable conduction and valence band edge positions. However, BV is unstable at pH ~ 1 and undergoes anodic dissolution due to the loss of V^{5+} ions. For the present studies, we have fabricated a Co-doped $BiVO_4$ (Co-BV) photoanode, which is stable at pH ~ 2.3 and above, and selectively produce active chlorine by suppressing OER in the PEC system using earth-abundant Co-BV. The doping of Co-ions into the $BiVO_4$ lattice decreases the charge transfer resistance, increases the lifetime of charge carriers, and enhances the CER kinetics. Moreover, the role of the Co is to provide a redox reaction site and acts as a co-catalyst to accelerate the CER. We observed a photocurrent of 67 μA cm^{-2} at 1.1 V *vs.* RHE with about 100 μg cm^{-2} of the photoanode material for CER under one sun illumination for virgin BV. In contrast, the 0.05 Co-BV photoanode exhibited a two-time higher photocurrent density of 190 μA cm^{-2} under similar reaction conditions.

Experimental methods and material preparation

Materials

Fluorine-doped tin oxide (FTO-735167) with a conductive surface resistance of 7 Ω cm^{-2} and thickness of 2.2 mm was purchased from Sigma Aldrich. Bismuth(III) nitrate pentahydrate ($Bi(NO_3)_3{\cdot}5H_2O$, cobalt(II) nitrate hexahydrate ($Co(NO_3)_2{\cdot}6H_2O$, glacial acetic acid (CH_3COOH) were supplied by Thomas Baker. Ammonium metavanadate (NH_4VO_3), isopropyl alcohol, DPD (*N*,*N*-diethyl-*p*-phenylenediamine) sulphate salt were purchased from TCI chemicals. Ultra-pure DI (de-ionized) water (18 MΩ) was used in all experiments.

Fabrication of BV and Co-BV photoelectrode

A simple SILAR (successive ionic layer adsorption and reaction) method was employed for the fabrication of the photoelectrode on the FTO substrate (refer to Fig. S1 in ESI†). The FTO substrate (area 1 × 2 cm^2) dimensions were pretreated by ultrasonically cleaning in soap and then in isopropyl alcohol, followed by drying in an oven at 333 K. Initially, two precursor solutions of Bi^{3+} and meta-vanadate (VO_3^-) were prepared for SILAR. The Bi^{3+} precursor solution was prepared by mixing Bi $(NO_3)_3{\cdot}5H_2O$ (25 mM) with glacial acetic acid and DI water in a ratio of 1 : 19 at 298 K. Similarly, the VO_3^- precursor solution was prepared by adding NH_4VO_3 (25 mM) to 40 ml DI water at 343 K. A single SILAR cycle consists of the immersion of the FTO plate into the Bi^{3+} precursor for 20 s, followed by the immersion into the VO_3^- precursor (at 343 K) for 20 s and then rinsing in the distilled water. For the BV electrode fabrication, 15 cycles of SILAR were repeatedly applied on the FTO plate to deposit material of 1 ± 0.05 μm thickness. After 15 SILAR cycles, the above electrode was dried at 333 K for 4 h and calcined at 723 K for 2 h in a muffle furnace under static air. For the Co-BV electrode fabrication, we modified the cation precursor solution by adding the required amount of Co $(NO_3)_2{\cdot}6H_2O$ (0.01, 0.05, 0.1, 0.5 mol%) to the Bi^{3+} ion precursor solution and the same SILAR process was used as that for BV; the resulting catalysts are designated as 0.01 Co-BV, 0.05 Co-BV, 0.1 Co-BV, and 0.5 Co-BV, respectively, throughout the manuscript, unless mentioned otherwise. The thickness of the photoanode layers was measured using a surface profilometer.

The typical photoanode (BV and Co-BV) thin film area prepared and utilized for all PEC and characterization measurements was 1 cm^2, and the amount of BV deposited was 100 ± 10 μg cm^{-2}.

Photoelectrochemical (PEC) measurements

All PEC studies were performed in one compartment cell made of quartz in a three-electrode configuration using the Gamry potentiostat (Model 3000). Ag/AgCl (saturated with 1 M KCl) and the graphite rod were used as the reference and counter electrode, respectively. The pH of the NaCl electrolyte was adjusted to 2.3 by adding 0.5 M H_2SO_4 and was purged by bubbling N_2 prior to any PEC measurement. All measurements were performed under one sun condition from Newport instruments 300 W Xe arc lamp equipped using an AM 1.5G filter. A NIST-certified lux-meter was used to confirm the light intensity to be 100 mW cm^{-2}. The electrode potential in the Ag/AgCl scale was converted to the RHE scale using the following eqn (3):

$$E_{RHE} = E_{Ag/AgCl} + 0.059pH + 0.197\ V \quad (3)$$

Photoelectrode characterization

The crystal structures and morphology of the pristine and doped BV catalysts were characterized by X-ray diffraction (XRD, Bruker Pan Analytic) equipped with Cu-Kα (1.5418 Å) radiation with a Ni filter. Field-emission scanning electron microscopy (FESEM) measurements were performed with an FEI NOVA NANOSEM 450 instrument. X-ray photoelectron spectral (XPS) measurements were recorded using a Thermo Fischer scientific instruments system equipped with a monochromatic Al Kα (1486.6 eV) X-ray source operating at 6 mA beam current and 12 kV. High-resolution transmission electron microscopy (HRTEM) measurements were performed using a JEOL JEM F-200 electron microscope operating at 200 kV. Raman spectra were recorded using an all-solid-state laser with an excitation laser source of 532 nm (Horiba Jobin Yvon HR800). The diffuse reflectance spectra were recorded using a UV-vis spectrometer (Shimadzu UV 2550) equipped with an integrating sphere in the wavelength range of 200–800 nm and $BaSO_4$ was used as a standard for the baseline correction. The Co content was measured using the ICP method and the results are shown in Table S1 (ESI†). Photoluminescence (PL) spectra and time-correlated single photon counting (TCSPC) decay study were performed using a Horiba FluoroMax spectrometer with an LED excitation source of 377 nm. The quality of the fit was judged by fitting parameters such as χ^2 (<1.2) as well as the visual inspection of the residual. A surface profilometer from Bruker was employed to measure the surface roughness and thickness.

Results and discussion

Fig. 1a shows the XRD patterns of the pristine BV and Co-BV thin films. The bare BV photoelectrode showed a pure monoclinic scheelite (m-s) phase structure (m-s BiVO4, JCPDs-00-014-0688) with a high-intensity parent peak appearing at 29.4° corresponding to the (121) facet.[14–16] No diffraction features corresponding to any cobalt oxide(s) were observed for any doping levels from 0.01 to 0.5 mol% of Co; as the doping level was less than 0.5 atom%, it may be difficult to detect. The diffraction peak intensities of $BiVO_4$ decreased significantly after Co-doping in BV and showed that Co-doping reduced the crystallinity of BV and possibly increased the defects in the lattice.[16] XRD measurements were made carefully with the

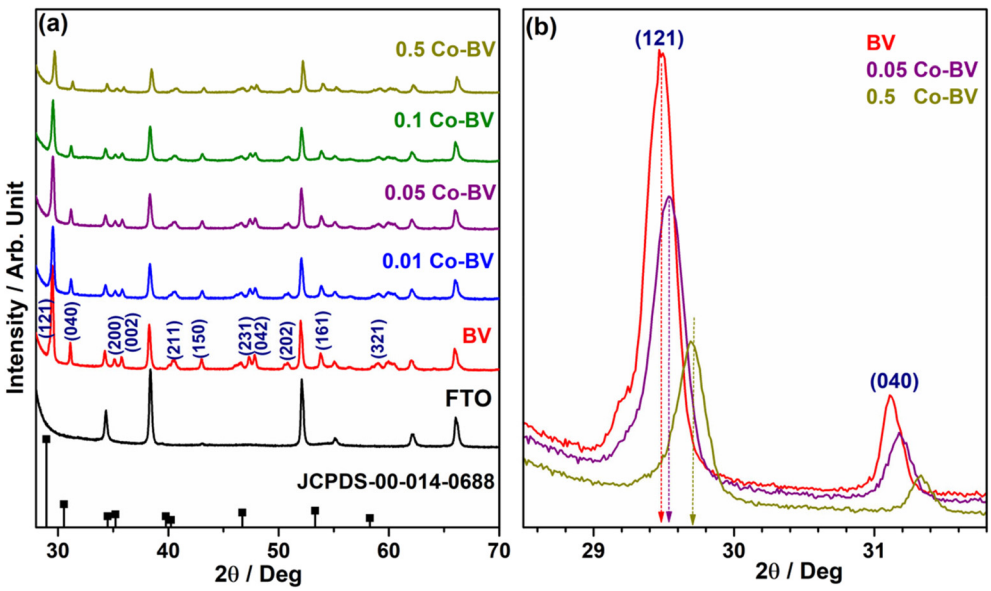

Fig. 1 (a) XRD patterns of the pristine BV and Co-doped BV catalysts. (b) Enlarged XRD pattern of BV, 0.05 Co-BV, and 0.5 Co-BV, to show the gradual shift in diffraction features to higher angle as well as line broadening.

same quantity of the catalyst in the thin-film form, and hence the results can be compared directly. Although close packing of the Co-BV particles increases, compared to BV (as shown in SEM, Fig. 2a and b), a decrease in diffraction feature intensity supports the Co-doping in the lattice of BV. The diffraction angle for all x Co-BV shifts to a higher angle compared to parent BV. Fig. 1b shows an observable shift for (121) and (040) features towards higher diffraction angle compared to that of pure BV. In addition, there is a significant line broadening occurring from 0.218 for BV to 0.260 for the 0.5 Co-BV for (121) feature. These two observations are typical for the introduction of smaller-size ions in place of the bigger ion. Final calculations involved in the synthesis step are expected to oxidize the cobalt to Co^{3+}. HR-TEM results also showed a reduction in the inter-layer d-spacing of (121) and the same is explained later (Fig. 2). This could be explained by the fact that the substitution of a larger cation (Bi^{3+}, ionic radii = 117 pm) by a smaller cation (Co^{2+}/Co^{3+} ionic radii = 79/68 pm) results

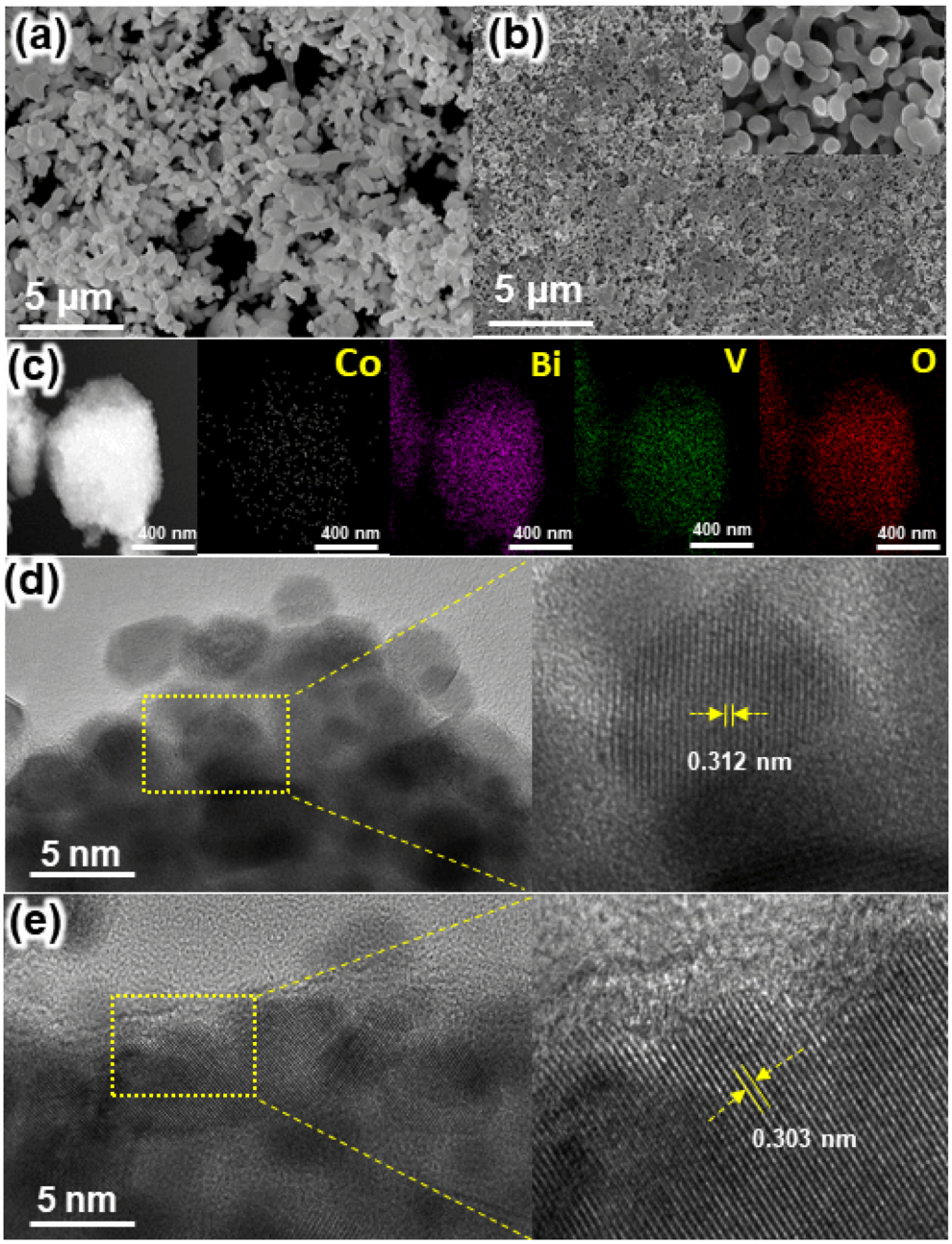

Fig. 2 Microstructural and elemental mapping characterization of BV and 0.05 Co-BV. FESEM images of (a) pristine $BiVO_4$ and (b) 0.05 Co-BV films are shown. Inset in panel b shows the enlarged view of 0.05 Co-BV and demonstrates the similarity of morphology to that of BV. (c) EDS for elemental mapping of 0.05 Co-BV, which demonstrates uniform doping of Co throughout the film. HRTEM images recorded are shown for (d) BV, and (e) 0.05 Co-BV. A significant decrease in the lattice parameter for the (121) facet was observed after Co-doping.

in a decrease in the lattice parameter or lattice contraction. It is to be noted that although ionic radii of V^{4+}/V^{5+} and Co^{2+}/Co^{3+} (72/68 pm) are comparable, a shift in diffraction features to a higher angle and lattice contraction rules out the doping of Co in the V-site. Irrespective of the oxidation state of Co, a very small size of Co^{3+} (compared to Bi^{3+}) is expected to generate structural stress in the BV lattice. Moreover, the iso-valent substitution of Bi by Co-ions into the BV lattice not only modulates the crystal structure, but also the electronic structure in the Co-BV system. It is to be noted that Bi has unoccupied 5f, and 6d orbitals, which are also very diffused; while Co has 4p and 4d unoccupied orbitals, and they are compact in nature. In addition, cobalt vanadate could be formed locally in the BV crystal lattice.

The freshly fabricated thin films were explored for surface morphology and elemental mapping by FESEM, TEM, and HRTEM, and the results are shown in Fig. 2. While the morphology of both the photoanodes (BV and 0.05 Co-BV) are similar, the particles were found to be more close-packed in the case of Co-BV than those in the parent BV. The pristine $BiVO_4$ showed relatively low-density (or sparsely-dispersed) nanoparticles, whereas Co-BV revealed a uniform and high-density coating of porous nanostructural units with a particle size range observed from 90 to 150 nm (refer to Fig. S2 in ESI†). It is also reiterated that except for adding the required Co-precursor to the Bi-precursor solution during the preparation by SILAR, no other changes in the preparation procedure were adopted for Co-BV. Indeed, it is interesting to observe that no morphological changes due to Co-doping were observed, but rather a density change. The average thickness of the film was found to be 1 ± 0.05 μm (see Fig. S3 in ESI†). The elemental mapping of Co, Bi, V, and O was explored by energy dispersive X-ray spectroscopy (EDS) for 0.05 Co-BV and the results are shown in Fig. 2c. While Bi, V, and O showed an equally dense distribution over the entire particle surface, a uniform and scarce distribution of Co-ions in the 0.05 Co-BV was observed. This also directly supports the uniform doping of Co-ions in the $BiVO_4$ lattice. TEM and HRTEM images recorded for BV and 0.05 Co-BV are shown in Fig. 2d and e, respectively. Fig. 2d shows a lattice spacing of 0.312 nm, and this corresponds to the (121) facet of $BiVO_4$, which is in good agreement with the reported values.[17,18] However we observed a decrease in the d_{121} lattice spacing of 0.303–0.306 nm for 0.05 Co-BV, which is attributed to the lattice contraction.[19] This is in good correspondence with the XRD results shown in Fig. 1. No isolated cobalt oxide was detected in the TEM images, supporting near-complete doping.

XPS studies of BV and 0.05 Co-BV catalysts were carried out to understand the electronic structure aspects, such as oxi-

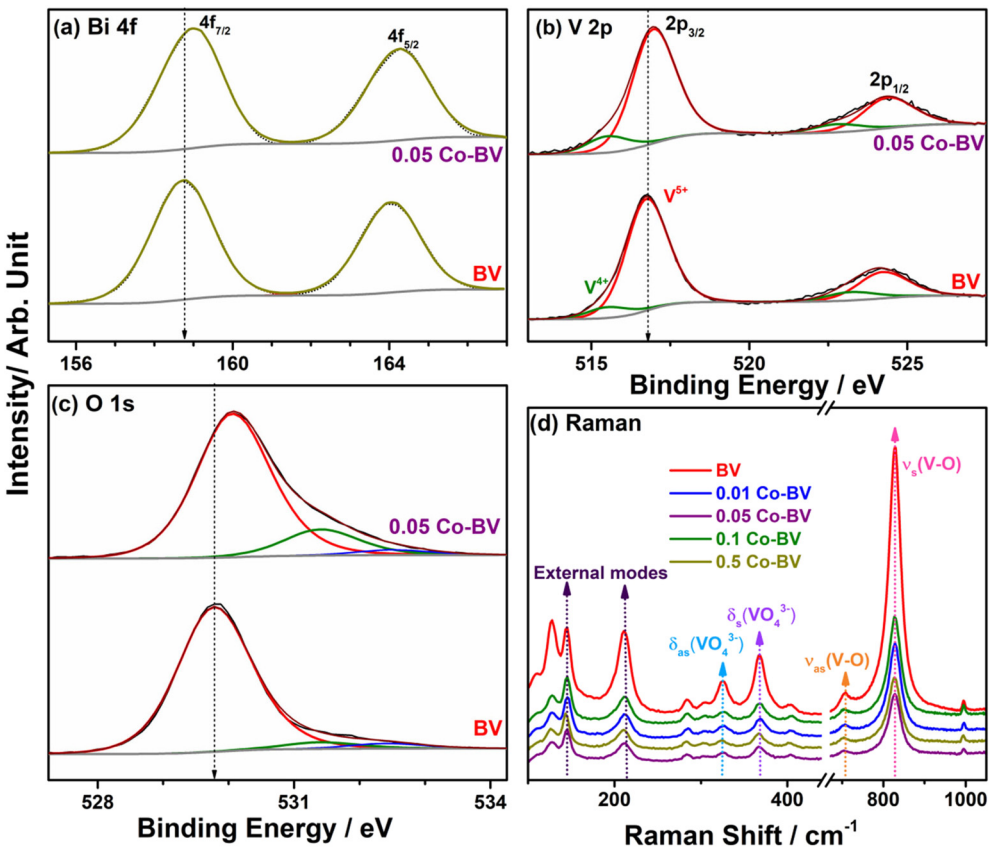

Fig. 3 (a) Bi 4f, (b) V 2p, and (c) O 1s core level spectra of BV and 0.05 Co-BV catalysts. (d) Raman spectra of the BV and *x* Co-BV catalysts.

dation states and the effect of Co-doping. Fig. 3a, b, and c show the XPS core-level spectra of Bi 4f, V 2p, and O 1s, respectively. XPS survey spectra showed the presence of Bi 4f, V 2p, O 1s, and C 1s peaks for both BV and 0.05 Co-BV. The absence of any Co features, especially Co 2p in the 775–810 eV BE range for 0.05 Co-BV was not surprising. This is attributed to the very small amount (0.05 atom%) of doped Co ions; further, as shown in Fig. 2c (EDS results), Co is distributed uniformly throughout the bulk, and hence the amount of Co present on the surface could be below the detection limit. Nonetheless, the Co content measured by the ICP method (Table S1 (ESI†)) is in accordance with the nominal input Co content. The Bi 4f spectrum of BV (Fig. 3a) showed a characteristic spin–orbit doublet of Bi $4f_{7/2}$ and $4f_{5/2}$ core levels at 158.8 and 164.1 eV, respectively (Δ = 5.35 eV), which corresponds to Bi^{3+} in BV. Similarly, 0.05 Co-BV showed Bi $4f_{7/2}$ and $4f_{5/2}$ core levels appearing at 159.1 and 164.35 eV, respectively. The shift in BE by 0.3 eV towards a higher BE side was observed for 0.05 Co-BV, compared to the un-doped BV, indicating the change in the surface electronic structure of 0.05 Co-BV after Co-doping.[20] The V 2p core level spectrum for BV and 0.05 Co-BV (Fig. 3b) broadens towards the lower BE side, suggesting the presence of more than one type of vanadium species. For BV, the V $2p_{3/2}$ core level shows an intense V^{5+} and a small shoulder peak, due to V^{4+}, at 516.8 and 515.4 eV, respectively.[21] However, for 0.05 Co-BV, V^{4+} shows a marginal shift in the core level towards the higher BE by 0.25 eV. Along with a shift in BE, an observable increase in intensity for V^{4+} was also observed.[21,22] Fig. 3c shows the O 1s spectra for BV and 0.05 Co-BV. O 1s for BV showed three peaks corresponding to the lattice oxygen, oxygen near defect sites (5%), and adsorbed species such as –OH, and H_2O, at a BE of 529.8, 531.5, and 532.5 eV, respectively. For 0.05 Co-BV, an increase in the oxygen defect sites (14%) and a shift in the lattice oxygen peak were observed. The V^{4+} species and the content of oxygen vacancies increased with Co-doping demonstrating a change in the electronic structure with Co-doping, which is expected to influence the catalytic activity/process.

Raman spectroscopy is sensitive towards finding any structural stress factors, such as doping, and oxygen vacancy in the crystalline materials, and it also complements the XRD results. In view of this, Raman spectra of all the catalysts were recorded and the results are shown in Fig. 3d. The peaks at 145 and 212 cm^{-1} correspond to the external vibration of BV. The peaks at 325 and 368 cm^{-1} are attributed to the V–O asymmetric vibration ($d_{as}(VO_4^{3-})$), and V–O bending vibration of the VO_4^{3-} tetrahedron unit ($d_s(VO_4^{3-})$), respectively.[23] Raman features observed at 708 cm^{-1} (the asymmetric V–O stretching mode n_{as}(V–O)), and 828 cm^{-1} (the symmetric V–O stretching mode n_s(V–O)), match very well with that of the m-s $BiVO_4$ phase. It was observed that the crystallinity of all Co-BV catalysts decreased significantly, with respect to BV; indeed, this is a clear indication that Co-doping occurs in the BV lattice and this possibly induces oxygen vacancies too. A significant increase in full-width at half maximum (FWHM) of BV (36.9 cm^{-1}) to 0.05 Co-BV (38.3 cm^{-1}) of 828 cm^{-1} (n_s(V–O)) feature supports the above conclusion. While the XRD data exhibited a shift in the diffraction features due to Co-doping in the BV lattice, the crystalline phase of BV remains intact. However, weak deformation of the VO_4 tetrahedron resulted in a decline in the intensity of the symmetric V–O stretching mode that was inversely correlated with the doped ion content. This weak deformation is attributed to the metal ion substitution at the Bi-site in the BV lattice. Earlier reports on the effect of Fe-doped $BiVO_4$ [24] and Ce-doped $BiVO_4$,[25] are in good agreement with the present findings.

The optical absorption of the photoelectrode materials was studied by UV-Vis absorption spectroscopy and the results are shown in Fig. 4a. The onset of light absorption was observed in the visible region from 530 nm, which is in good correspondence with the earlier reports.[18,19] Although structural changes were observed for Co-doping in BV in the earlier characterization studies, no significant change in the light absorption intensity was observed. Indeed, the bright yellow color remained the same for the bare and Co-BV photoelectrodes. The photoinduced electron–hole pair recombination of the

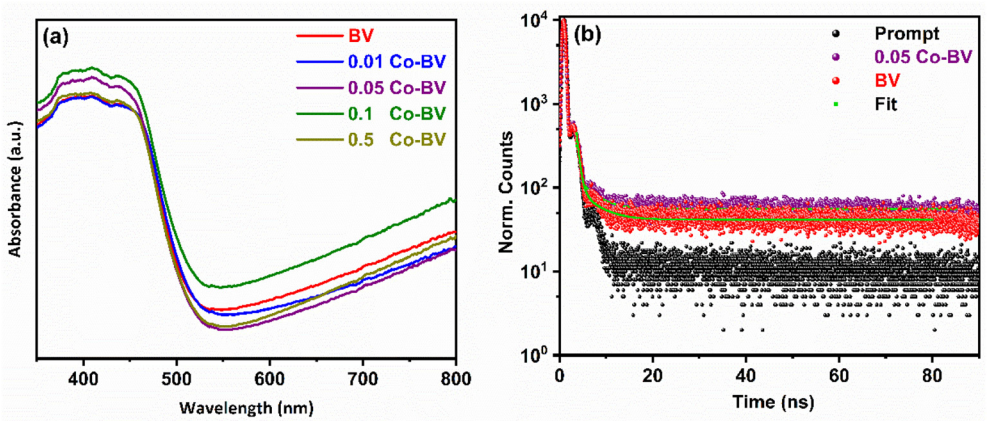

Fig. 4 (a) UV-visible absorption spectra of *x* Co-BV photoanodes. (b) Time correlated single photon counting (TCSPC) decay of the BV and 0.05 Co-BV. (λ_{ex} = 377 nm, λ_{mon} = 555 nm).

semiconductor could be explained from the photoluminescence spectra (see Fig. S4 in ESI†) recorded at the 510 nm excitation wavelength. The PL showed a broad emission peak between 530 and 650 nm for all the photoelectrodes. This indicated that there was no change in the bandgap of BV and 0.05 Co-BV due to doping and no states were created in the forbidden band-gap region. However, 0.05 Co-BV photoelectrode exhibited a lower emission peak intensity with respect to the BV photoelectrode, which suggested that the recombination of the electron and hole is likely minimized and a greater number of holes could be transferred to the photoelectrode surface to activate the chloride oxidation reaction. However, other dopant concentrations lead to an increment in the emission peak intensity, which corresponds to the lower and higher mol% of Co species acting as recombination sites and they are suppressing the CER reaction.

To confirm the Co doping in BV and consequent increase in the charge carrier lifetime, the time-correlated single photon counting (TCSPC) decay measurements were performed and the results are shown in Fig. 4b. The charge carrier lifetime decays for both samples were fitted using a second-order exponential function. The PL lifetime of the electron and hole pair recombination for the 0.05 Co-BV electrode was 4.05 ns, while the BV electrode was 3.61 ns (Table S2 in ESI†).[26,27] These results confirmed that the lifetime of the electron/hole pair of the doped Co-BV is significantly higher than that of the pure BV phase, suggesting that Co doping decreases the electron and hole recombination.

Photoelectrochemical characterization

CER performance in NaCl solution was evaluated, with pH adjusted to 2.3, in a single-compartment photo electrolysis cell (shown in Fig. 5a) for BV and *x* Co-BV, and the obtained results are shown in Fig. 5b and c. The PEC performance of all the photoelectrodes was characterized in a three-electrode system with BV or 0.05 Co-BV as the working electrode. The photoanode was illuminated from the backside through the FTO plate. The overall redox process occurring at both electrodes is shown in Fig. 5a. Under illumination, the photogenerated holes diffuse to the surface of BV and oxidize chloride

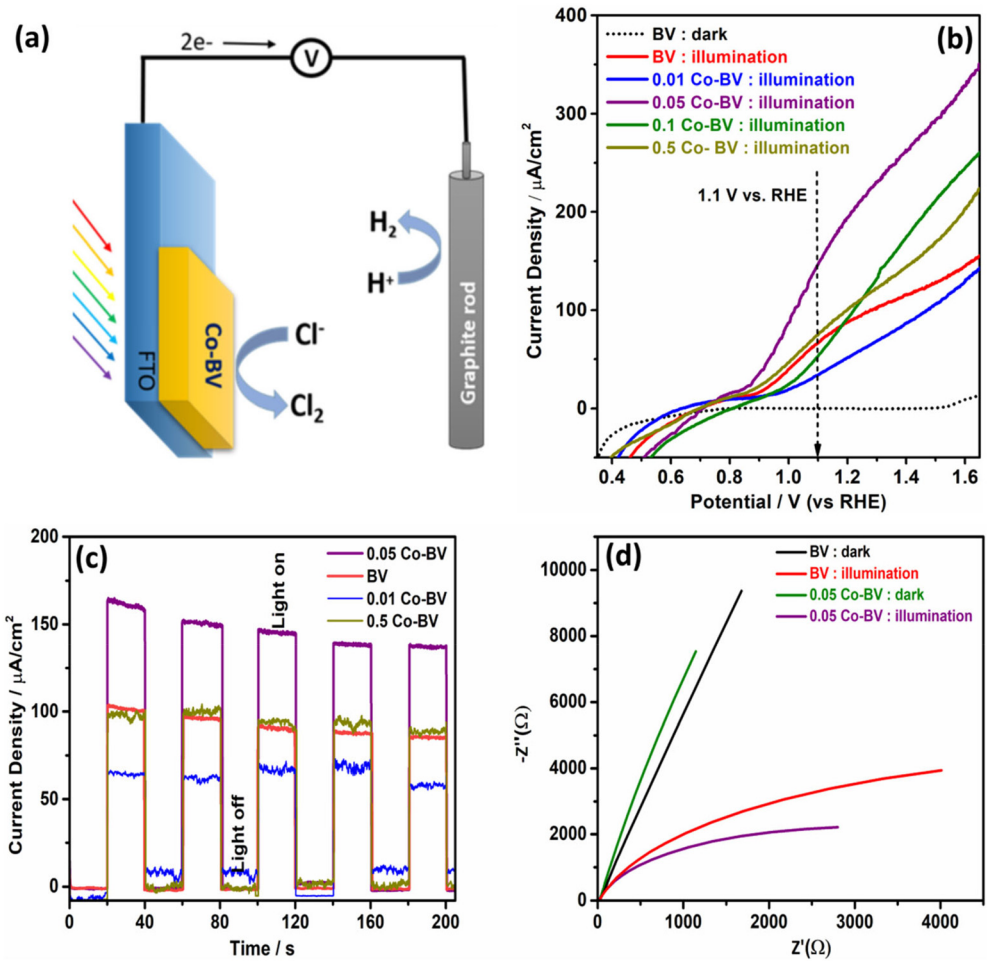

Fig. 5 Photoelectrochemical performance of pristine BV and *x* Co-BV. (a) Schematic to show the PEC set up and the overall reaction scheme of seawater splitting. (b) Linear sweep voltammetry in 1 M NaCl solution at pH = 2.3. (c) Transient photocurrent response at 1.2 V *vs.* RHE. (d) Nyquist plot (or EIS) recorded under dark and illumination conditions.

ions to chlorine over the catalyst surface. Electrons generated from the oxidation step are transferred through the external circuit and reduced H_2O to produce hydrogen on the graphite electrode. Although chlorine is sparingly soluble in water (up to 0.7 wt%), it reacts instantly with water and forms HClO.

A preliminary CER study was conducted using BV and all compositions of Co-BV (Fig. 5b). Fig. 5b shows the photocurrent density *vs.* potential (j–V) graph for BV and for all xCo-BV in 1 M NaCl under one sun irradiation conditions. Under the dark conditions, negligible anodic current density ($j \sim 1$ μA cm^{-2}) was observed with all the photoanodes. Upon one sun illumination, BV showed a photocurrent density of 67 μA cm^{-2} at 1.1 V *vs.* RHE. In contrast, the 0.05 Co-BV photoanode (1 μm thick film), under the same measurement conditions, showed a photocurrent density of 147 μA cm^{-2} at 1.1 V *vs.* RHE. More than two-fold enhancement in the photocurrent density after Co-doping is attributed to the enhanced charge separation induced by efficient diffusion of holes onto the catalyst surface as well as its utilization for chloride oxidation. A marginal shift in the CER onset potential was observed at around 0.9 V RHE for all anodes. While 0.05 Co-BV showed the lowest onset potential (0.88 V RHE), 0.1 and 0.01 Co-BV showed a marginally higher onset potential (0.96 V RHE). However, the CER current density increased significantly with 0.05 Co-BV, as compared to the BV photoanode with an increase in the applied potential. This result demonstrates that after Co-doping, Co-BV behaves as a multifunctional material; Co-BV absorbs visible light and is also an efficient co-catalyst that accelerates the CER activity. Furthermore, different amounts of Co were doped in BV and the resulting materials were evaluated for CER performance. The lowest amount of Co doping (0.01 mol%) showed 34 μA cm^{-2}, while the 0.05 mol% Co-doped system showed the highest current density of 147 μA cm^{-2} at 1.1 V *vs.* RHE. However, with further increase in the Co amount to 0.1 and 0.5 mol%, the photocurrent density decreased to 56 and 75 μA cm^{-2}, respectively, which underscores the importance of the optimum amount of Co-doping towards the best CER performance. 0.05 Co-BV was found to show the best performance; in view of this, 0.05 Co-BV was evaluated in detail and compared with parent BV. The results in Fig. 5b indicate that excess oxygen vacancies generated by Co-doping could behave as recombination sites for the electron–hole pairs and decrease the photocurrent density by hindering the CER performance.[28]

To study the instant photocurrent response of the photoanode, the chronoamperometry (j–t) analysis was performed at an applied potential of 1.2 V *vs.* RHE under chopped one sun illumination conditions, and the results are shown in Fig. 5c. The photocurrent increases instantly under illumination conditions and then drops to zero in the dark condition, underscoring that the current generation is exclusively due to light absorption. 0.05 Co-BV shows the highest photo response, as compared to BV and other x Co-BV, and it is in accordance with the LSV results (Fig. 5b). A high photocurrent response indicates the charge transfer resistance across the working electrode and the electrolyte should be lower for 0.05 Co-BV than that for BV. This was evaluated by electrochemical impedance spectroscopy (EIS) and the results are shown in Fig. 5d. In fact, it is evident from the Nyquist plot shown in Fig. 5d that Co doping in the $BiVO_4$ lattice decreases the charge transfer resistance and increases the charge mobility.[29] The relatively low charge transfer resistance in 0.05 Co-BV can be realized from the smaller radius of the arc.[30,31]

Furthermore, we studied the effect of the chloride ion concentration on the CER performance and the results are shown in Fig. 6a. We observed a gradual increase in the oxidation current on increasing the chloride concentration from 1 M to 4 M. A further increase in the chloride concentration to 5 M significantly decreased the CER current density, possibly due to a decrease in the ion mobility in the electrolyte solution. For the product quantification, the chronoamperometric (j–t) analysis was performed with the best active 0.05 Co-BV photoelectrode at different applied potentials (1.1 V, 1.3 V, and 1.5 V *vs.* RHE) under one sun illumination for 2 h and the results are shown

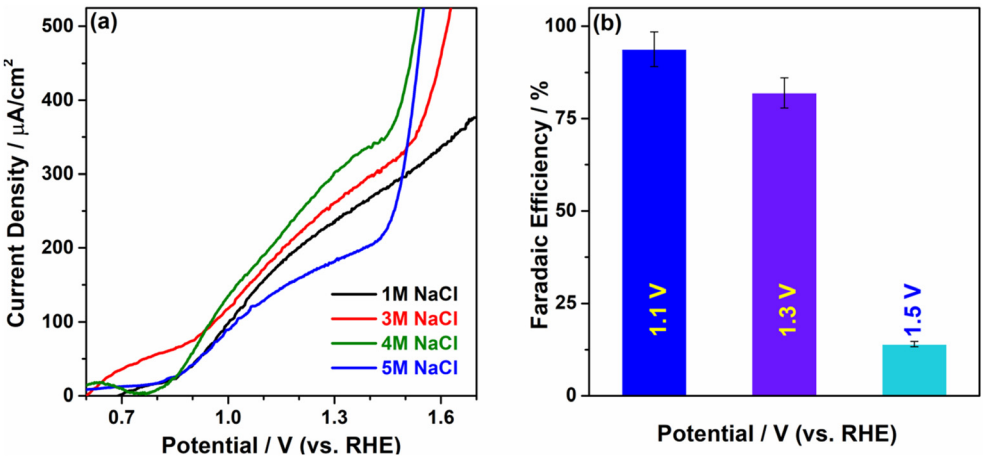

Fig. 6 (a) Linear sweep voltammetry in different molar NaCl concentrations with 0.05 Co-BV, pH 2.3 solution. (b) Faradaic efficiency at three different applied potentials for Cl_2 production. Error bars represent the standard deviation for three different measurements.

in (Fig. 6b). The amount of the dissolved active chlorine was measured by spectrophotometry using the *N*,*N*-diethyl-*p*-phenylenediamine sulfate (DPD) reagents.[32] Prior to the chronoamperometric evaluation, the electrolytic system was pre-purged with N_2 gas for 1 h. After 2 h of the constant photoelectrochemical run, the collected anodic products were analyzed to determine the faradaic efficiency of the process (Fig. 6b). For the 0.05 Co-BV electrode, the maximum faradaic efficiency of 92 ± 3% was observed at 1.1 V *vs.* RHE. However, the faradaic efficiency decreases to 82 ± 3% at 1.3 V *vs.* RHE. It is worth noting that at the lower potential, the CER current is quite stable in the *j*–*t* plot; however, the higher applied potential leads to a significant decrease in the CER activity due to increasing competition from the OER. As a result of low chlorine formation, faradaic efficiency of only 12 ± 5% was observed at 1.5 V *vs.* RHE. The increase in current density at higher applied potential is predominantly due to the contribution from OER (refer to Fig. S5 in ESI†). Indeed, this result demonstrates that the Co-BV system overcomes the aspect of lowering the overpotential of chlorine evolution and successfully avoids OER at a potential below 1.3 V *vs.* RHE. It is well-known that there are advantages of carrying out the reaction at low applied bias, which is of commercial interest.

A comparison of a few sea-water splitting PEC CER results reported in the literature is shown in Table 1. This comparison underscores the highest faradaic efficiency (95%) observed at the lowest applied potential, but at pH = 5.8 with the CoO_x-loaded $BiVO_4/WO_3$ catalyst reported by Okunaka *et al.*[33] and this result is comparable to the above for operating voltage and FE; however, the activity was demonstrated only for 1000 s. Other catalysts operate either at a high applied voltage (>1.1 V), high pH, or UV. However, it is also to be mentioned that the lowest current density was observed with the present catalyst. Nonetheless, it is to be noted that the amount of the catalyst employed in this work is a mere 100 μg cm^{-2}, and a fair comparison could not be made with other results, currently, as the catalyst content is not available. However, this work is superior in terms of operating at low pH and demonstrating longer sustainability (shown in the next section), which are necessarily required for the application aspects.

Sustainability aspects of 0.05 Co-BV catalyst

The stability test of the 0.05 Co-BV was performed in 4 M NaCl solution that was acidified to pH = 2.3, and at a constant applied potential of 1.1 V *vs.* RHE; the results are shown as a red trace in Fig. 7. We observed a nearly steady photocurrent

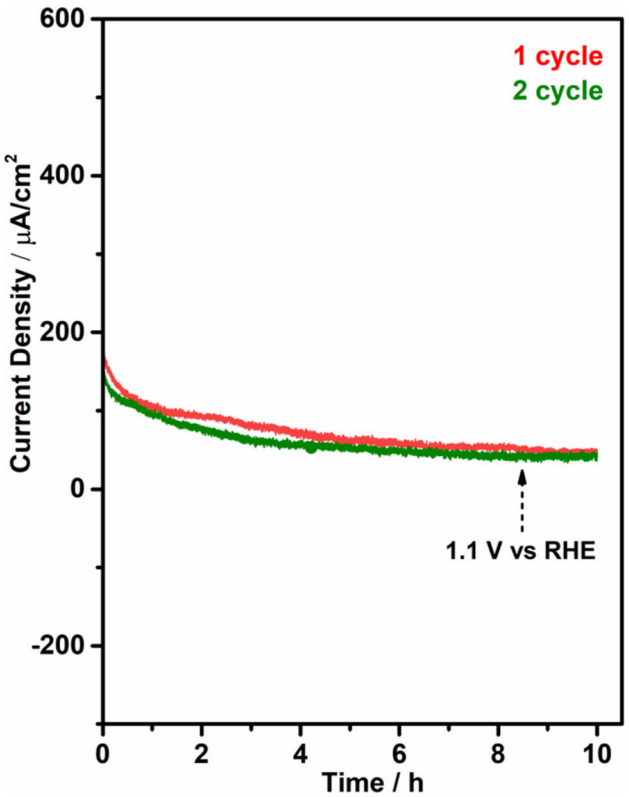

Fig. 7 Photoelectrochemical stability test for CER of 0.05 Co-BV at 1.1 V RHE under one sun illumination.

up to 10 h, indicating the high photostability of the catalyst. Although the applied potential employed was unfavorable (or not sufficient) for OER, still, some possibility of oxygen formation could hinder the rate of CER.[11] Therefore, we observed a A slight decrease in the photocurrent with respect to time. Furthermore, the photoanode used in the first experiment was used again for another 10 h, and the result was compared with the freshly prepared electrolyte (green line). The first and second 10 h experiments exhibited similar *j*–*t* behavior, and the observed difference is within the experimental error limit. In fact, the continuous formation of HOCl is expected to decrease the pH significantly, especially during the long duration of the reaction, and decrease the stability due to the dissolution of Bi^{3+} ions from the catalyst.[13] However, the doping of Co-ion in the $BiVO_4$ lattice seems to prevent photo corrosion in an acidic environment. A continuous flow from a larger

Table 1 Catalysts reported for chlorine and hydrogen evolution

Catalyst	Operating voltage (vs RHE)	FE (%)	j_{CER} mA cm^{-2}	Operating pH	Illumination conditions	Stability demo.	Ref.
$BiVO_4/WO_3$	1.42	85	2.5	1	1 sun	2 h	13
WO_3	1.3	70	4.5	6.5	1 sun	20 h	11
Rutile TiO_2	1.65	NA	8	7	UV; λ = 385 nm	NA	12
CoO_x-loaded $BiVO_4/WO_3$	1.0	95	1	5.8	1 sun with L-42 filter	0.27 h	33
Co-BV	1.1	92	0.19	2.3	1 sun	20 h	Present work

reservoir of NaCl solution to the electrochemical setup could be useful in preventing the corrosion caused by the decrease in pH during the long-duration electrolysis.

Conclusion

In summary, a simple and scalable SILAR process has been demonstrated to fabricate the earth-abundant-Co-doped BV photoanode to produce Cl_2 and H_2 concurrently. A high photocurrent to chlorine faradaic efficiency of 92% was observed for the best active 0.05 Co-BV composition of 190 μA cm^{-2} at 1.1 V *vs.* RHE. Co-doping in BV facilitated the efficient utilization of holes and enhanced the CER performance. This work demonstrated that molecules/ions having lower oxidation potential than water can reduce the overall cell potential and provide an efficient method for economical solar H_2 production. Simultaneously, the use of an HER catalyst in the counter electrode position could further improve the kinetics of the overall CER and HER reaction.

The sunlight-driven photoelectrochemical seawater splitting devices may be especially well suited to remote locations, where seawater and sunlight are abundant and relatively small amounts of chlorine or hypochlorite are needed for a variety of essential disinfecting purposes, such as the purification of drinking water. It is also worth evaluating Co-BV for real seawater splitting. The preparation method could be easily adapted for scale-up to large area panels and it is worth exploring the same.

Conflicts of interest

There are no conflicts to declare.

Acknowledgements

IC thanks DST, and INSPIRE for the research fellowship. HB and NBM acknowledge the research fellowship from UGC, New Delhi. KNS thank Sarthi fellowship from Maharashtra. CSG acknowledges the financial support through the NCP project (HCP-44) from the H2T program.

References

1 (*a*) C. S. Gopinath and N. Nalajala, A Scalable and Thin Film Approach for Solar Hydrogen Generation: A Review on Enhanced Photocatalytic Water Splitting, *J. Mater. Chem. A*, 2021, **9**, 1353–1371; (*b*) S. Rajaambal, K. Sivaranjani and C. S. Gopinath, Recent Developments in Solar H_2 Generation from Water Splitting, *J. Chem. Sci.*, 2015, **127**, 33–47.

2 S. He, Y. Meng, Q. Wu, J. Yang, S. Huang, X. Li, S. Tong, T. Asefa and M. Wu, Ta-Doped Porous TiO_2 Nanorod Arrays by Substrate-Assisted Synthesis: Efficient Photoelectro-catalysts for Water Oxidation, *Nanoscale*, 2018, **10**, 19367–19374.

3 M. R. Shaner, H. A. Atwater, N. S. Lewis and E. W. McFarland, A Comparative Technoeconomic Analysis of Renewable Hydrogen Production Using Solar Energy, *Energy Environ. Sci.*, 2016, **9**, 2354–2371.

4 (*a*) K. Sayama, Production of High-Value-Added Chemicals on Oxide Semiconductor Photoanodes under Visible Light for Solar Chemical-Conversion Processes, *ACS Energy Lett.*, 2018, **3**, 1093–1101; (*b*) A. Dubey, A. K. Mishra, S. Negi and C. S. Gopinath, Facile, sustainable and unassisted plain water oxidation on $Au/Ce_{0.9}Ti_{0.1}O_2$ nanorods in direct sunlight, *J. Chem. Sci.*, 2022, **134**, 61.

5 R. K. B. Karlsson and A. Cornell, Selectivity between Oxygen and Chlorine Evolution in the Chlor-Alkali and Chlorate Processes, *Chem. Rev.*, 2016, **116**, 2982–3028.

6 C. C. L. McCrory, S. Jung, J. C. Peters and T. F. Jaramillo, Benchmarking Heterogeneous Electrocatalysts for the Oxygen Evolution Reaction, *J. Am. Chem. Soc.*, 2013, **135**, 16977–16987.

7 K. Maeda and K. Domen, Photocatalytic Water Splitting: Recent Progress and Future Challenges, *J. Phys. Chem. Lett.*, 2010, **1**, 2655–2661.

8 N. Melián-Martel, J. J. Sadhwani and S. Ovidio Pérez Báez, Saline Waste Disposal Reuse for Desalination Plants for the Chlor-Alkali Industry. The Particular Case of Pozo Izquierdo SWRO Desalination Plant, *Desalination*, 2011, **281**, 35–41.

9 M. E. Porter and C. Van Der Linde, Toward a New Conception of the Environment-Competitiveness Relationship, *J. Econ. Perspect*, 1995, **9**, 97–118.

10 L. D. Schulte, J. R. Fitzpatrick, R. R. Salazar, B. S. Schake, B. T. Martinez, L. D. Schultr, J. R. Fitzpatrick, R. R. Salazarl, B. S. Schake and B. T. Martinezl, Cleanup of Hydrochloric acid Waste Streams from Actinide Processes Using Extraction Chromatography, *Sep. Sci. Technol.*, 2006, **30**, 1833–1847.

11 M. Jadwiszczak, K. Jakubow-Piotrowska, P. Kedzierzawski, K. Bienkowski and J. Augustynski, Highly Efficient Sunlight-Driven Seawater Splitting in a Photoelectrochemical Cell with Chlorine Evolved at Nanostructured WO_3 Photoanode and Hydrogen Stored as Hydride within Metallic Cathode, *Adv. Energy Mater.*, 2020, **10**, 1903213.

12 T. R. Harris-Lee, Y. Zhang, C. R. Bowen, P. J. Fletcher, Y. Zhao, Z. Guo, J. W. F. Innocent, S. A. L. Johnson and F. Marken, Photo-Chlorine Production with Hydrothermally Grown and Vacuum-Annealed Nanocry-stalline Rutile, *Electrocatalysis*, 2021, **12**, 65–77.

13 A. M. Rassoolkhani, W. Cheng, J. Lee, A. McKee, J. Koonce, J. Coffel, A. H. Ghanim, G. A. Aurand, C. Soo Kim, W. Ik Park, H. Jung and S. Mubeen, Nanostructured Bismuth Vanadate/Tungsten Oxide Photoanode for Chlorine Production with Hydrogen Generation at the Dark Cathode, *Commun. Chem.*, 2019, **2**(57), 1–7.

14 B. Zhang, H. Zhang, Z. Wang, X. Zhang, X. Qin, Y. Dai, Y. Liu, P. Wang, Y. Li and B. Huang, Doping Strategy to

Promote the Charge Separation in $BiVO_4$ Photoanodes, *Appl. Catal., B*, 2017, **211**, 258–265.

15 B. Zhou, X. Zhao, H. Liu, J. Qu and C. P. Huang, Visible-Light Sensitive Cobalt-Doped $BiVO_4$ (Co-$BiVO_4$) Photocatalytic Composites for the Degradation of Methylene Blue Dye in Dilute Aqueous Solutions, *Appl. Catal., B*, 2010, **99**, 214–221.

16 Y. Geng, P. Zhang, N. Li and Z. Sun, Synthesis of Co Doped $BiVO_4$ with Enhanced Visible-Light Photocatalytic Activities, *J. Alloys Compd.*, 2015, **651**, 744–748.

17 Z. Zhu, B. X. Jiang, R. J. Wu, C. L. Huang and Y. Chang, Photoreduction of CO_2 into CH_4 Using Novel Composite of Triangular Silver Nanoplates on Graphene-$BiVO_4$, *Catalysis*, 2022, **12**, 750.

18 S. S. Mali, G. R. Park, H. Kim, H. H. Kim, J. V. Patil and C. K. Hong, Synthesis of Nanoporous Mo:$BiVO_4$ Thin Film Photoanodes Using the Ultrasonic Spray Technique for Visible-Light Water Splitting, *Nanoscale Adv.*, 2019, **1**, 799–806.

19 W. Fang, L. Fu, A. Qin, Y. Lin and R. Xv, Highly Active and Self-Healing Co-Doped $BiVO_4$ Photoanode in Borate Buffer to Enhance Charge Separation and Water Oxidation Kinetics during Photoelectrochemical Water Splitting, *ACS Appl. Energy Mater.*, 2022, **5**, 6313–6326.

20 T. D. Nguyen, Q. T. P. Bui, T. B. Le, T. M. Altahtamouni, K. B. Vu, D. V. N. Vo, N. T. H. Le, T. D. Luu, S. S. Hong and K. T. Lim, Co^{2+} Substituted for Bi^{3+} in $BiVO_4$ and Its Enhanced Photocatalytic Activity under Visible LED Light Irradiation, *RSC Adv.*, 2019, **9**, 23526–23534.

21 (*a*) K. Sivaranjani, A. Verma and C. S. Gopinath, Molecular oxygen assisted oxidative dehydrogenation of ethyl benzene to styrene with nanocrystalline $Ti_{1-x}V_xO_2$, *Green Chem.*, 2012, **14**, 461–471; (*b*) P. Devaraji, N. K. Sathu and C. S. Gopinath, Ambient oxidation of benzene to phenol by photocatalysis on Au/$Ti_{0.98}V_{0.02}O_2$: Role of Holes, *ACS Catal.*, 2014, **4**, 2844–2853.

22 D. Kong, J. Qi, D. Liu, X. Zhang, L. Pan and J. Zou, Ni-Doped $BiVO_4$ with V^{4+} Species and Oxygen Vacancies for Efficient Photoelectrochemical Water Splitting, *Trans. Tianjin Univ.*, 2019, **25**, 340–347.

23 J. M. Wu, Y. Chen, L. Pan, P. Wang, Y. Cui, D. C. Kong, L. Wang, X. Zhang and J. J. Zou, Multi-Layer Monoclinic BiVO4 with Oxygen Vacancies and V^{4+} Species for Highly Efficient Visible-Light Photoelectrochemical Applications, *Appl. Catal., B*, 2018, **221**, 187–195.

24 C. Regmi, Y. K. Kshetri, T. H. Kim, R. P. Pandey and S. W. Lee, Visible-Light-Induced Fe-Doped $BiVO_4$ Photocatalyst for Contaminated Water Treatment, *Mol. Catal.*, 2017, **432**, 220–231.

25 S. Gu, W. Li, F. Wang, H. Li and H. Zhou, Substitution of Ce (III,IV) Ions for Bi in $BiVO_4$ and Its Enhanced Impact on Visible Light-Driven Photocatalytic Activities, *Catal. Sci. Technol.*, 2016, **6**, 1870–1881.

26 J. K. Kim, X. Shi, M. J. Jeong, J. Park, H. S. Han, S. H. Kim, Y. Guo, T. F. Heinz, S. Fan, C. L. Lee, J. H. Park and X. Zheng, Enhancing Mo:$BiVO_4$ Solar Water Splitting with Patterned Au Nanospheres by Plasmon-Induced Energy Transfer, *Adv. Energy Mater.*, 2018, **8**, 1701765.

27 O. F. Lopes, K. T. G. Carvalho, W. Avansi, D. M. B. Milori and C. Ribeiro, Insights into the Photocatalytic Performance of $Bi_2O_2CO_3$/$BiVO_4$ Heterostructures Prepared by One-Step Hydrothermal Method, *RSC Adv.*, 2018, **8**, 10889–10897.

28 W. Yao, H. Iwai and J. Ye, Effects of Molybdenum Substitution on the Photocatalytic Behavior of $BiVO_4$, *Dalton Trans.*, 2008, 1426–1430.

29 G. Liu, F. Li, Y. Zhu, J. Li and L. Sun, Cobalt Doped $BiVO_4$ with Rich Oxygen Vacancies for Efficient Photoelectrochemical Water Oxidation, *RSC Adv.*, 2020, **10**, 28523–28526.

30 K. K. Patra, P. A. Bharad, V. Jain and C. S. Gopinath, Direct Solar-to-Hydrogen Generation by Quasi Artificial Leaf Approach: Possibly Scalable and Economical Device, *J. Mater. Chem. A*, 2019, **7**, 3179–3189.

31 K. Sivaranjani, S. Agarkar, S. B. Ogale and C. S. Gopinath, Toward a quantitative correlation between microstructure and DSSC efficiency: A case study of $TiO_{2-x}N_x$ nanoparticles in a disordered mesoporous framework, *J. Phys. Chem. C*, 2012, **116**, 2581–2587.

32 Y. Huang, Y. Yu, Y. Xin, N. Meng, Y. Yu and B. Zhang, Promoting Charge Carrier Utilization by Integrating Layered Double Hydroxide Nanosheet Arrays with Porous $BiVO_4$ Photoanode for Efficient Photoelectrochemical Water Splitting, *Sci. China Mater.*, 2017, **60**, 193–207.

33 S. Okunaka, Y. Miseki and K. Sayama, Improvement of photoelectrochemical HClO production under visible light irradiation by loading cobalt oxide onto a $BiVO_4$ photoanode, *Catal. Sci. Technol.*, 2021, **11**, 5467–5471.

ACS APPLIED MATERIALS & INTERFACES

www.acsami.org

Research Article

Electrocatalytic Glycerol Conversion: A Low-Voltage Pathway to Efficient Carbon-Negative Green Hydrogen and Value-Added Chemical Production

Inderjeet Chauhan, Himanshu Bajpai, Bishakha Ray, Sadhu K. Kolekar, Suwarna Datar, Kshirodra Kumar Patra,* and Chinnakonda S. Gopinath*

Cite This: *ACS Appl. Mater. Interfaces* 2024, 16, 26130−26141

Read Online

ACCESS | Metrics & More | Article Recommendations | Supporting Information

ABSTRACT: Electrochemical glycerol oxidation reaction (GLYOR) could be a promising way to use the abundantly available glycerol for production of value-added chemicals and fuels. Completely avoiding the oxygen evolution reaction (OER) with GLYOR is an evolving strategy to reduce the overall cell potential and generate value-added chemicals and fuels on both the anode and cathode. We demonstrate the morphology-controlled palladium nanocrystals, afforded by colloidal chemistry, and their established morphology-dependent GLYOR performance. Although it is known that controlling the morphology of an electrocatalyst can modulate the activity and selectivity of the products, still it is a relatively underexplored area for many reactions, including GLYOR. Among nanocube (Pd-NC), truncated octahedron (Pd-TO), spherical and polycrystalline (Pd-PC) morphologies, the Pd-NC electrocatalyst deposited on a Ni foam exhibits the highest glycerol conversion (85%) along with 42% glyceric acid selectivity at a low applied potential of 0.6 V (vs reversible hydrogen electrode (RHE)) in 0.1 M glycerol and 1 M KOH at ambient temperature. Owing to the much favorable thermodynamics of GLYOR on the Pd-NC surface, the assembled electrolyzer requires an electricity input of only ∼3.7 kWh/m^3 of H_2 at a current density of 100 mA/cm^2, in contrast to the requirement of ≥5 kWh/m^3 of H_2 with an alkaline/PEM electrolyzer. Sustainability has been successfully demonstrated at 10 and 50 mA/cm^2 and up to 120 h with GLYOR in water and simulated seawater.

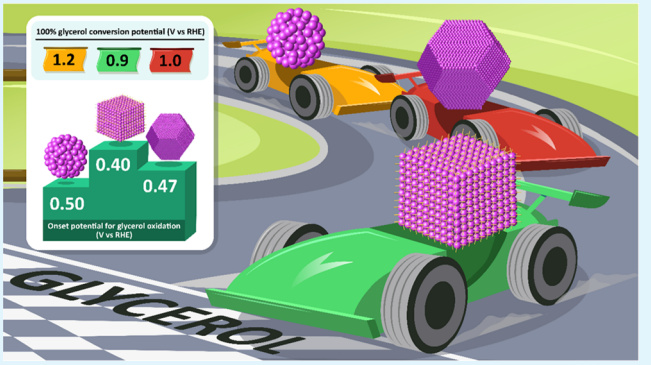

KEYWORDS: *palladium, electrocatalysis, glycerol, SDG, green hydrogen, nanocube*

1. INTRODUCTION

Biomass upgradation has the potential to produce sustainable biofuels and carbon-based chemicals.[1] Glycerol is an abundantly available byproduct of biodiesel and can be converted to value-added chemicals.[2−5] A large production of biodiesel generates surplus glycerol and subsequent reduction in price is unavoidable.[6] In fact, US DoE recommended glycerol as one of the top ten building blocks for the production of value-added chemicals.[7] A survey suggested that the global glycerol production could reach 4 billion liters per year by 2026.[8] Among various approaches, the glycerol oxidation reaction (GLYOR) with a suitable electrocatalyst provides a green route to synthesize value-added chemicals with the simultaneous evolution of hydrogen at the counter electrode.[1] Oxidation products such as glycolic and glyceric acids are important chemicals used in pharmaceuticals, cosmetics, and polymer industries.[9−11] Glyceric acid is also present in human body, is crucial for the glycolytic pathway, and acts as a reagent for variety of biological activities. Thus, electrochemical methods for up-scaling biomass could be an intriguing approach to convert low-cost glycerol to valuable chemicals.

Over the years, the electro-oxidation reaction of glycerol has been studied with various metal catalysts such as Au, Pd, and Pt.[12] In alkaline solution, Au catalyzed the partial oxidation of glycerol to glycolic acid efficiently, via C−C bond cleavage.[13,14] Significant progress has been made in nanostructuring the Au catalyst to increase the product selectivity and conversion rate. Oh et al. demonstrated the effect of nanostructuring of the Au catalyst and the local KOH concentration on GLYOR.[13] Many earth-abundant catalysts have been reported for GLYOR with

Received: February 10, 2024
Revised: April 24, 2024
Accepted: April 24, 2024
Published: May 8, 2024

high formic acid selectivity.[15,16] A cobalt oxide nanorod decorated on reduced graphene oxide (RGO) is effective for GLYOR with high formate selectivity; however, the high selectivity of formic acid production required a longer reaction time and a high potential.[17] Other strategies, such as defect creation on the electrocatalyst surface, are also suggested to boost the GLYOR performance.[18] Xia et al. reported a vacancy-rich NiCrO catalyst, which exhibits GLYOR performance with 99% conversion and 98% selectivity for formic acid production.[19] Furthermore, most of the GLYOR is favorable in alkaline solution, since the adsorbed OH^- ion is often a key intermediate for the electrocatalytic biomass oxidation reaction.[14] Interestingly, Li et al. have suggested a manganese oxide catalyst that exhibits high stability for hydrogen production coupled with GLYOR in an acidic electrolyte.[20] The use of acidic electrolyte could reduce the energy consumption. Moreover, engineering the microenvironment at the catalyst-electrolyte interface could steer the GLYOR performance. For example, the cation effect via an electric double-layer formation at the interface boosts the product selectivity by interacting with the glycerol oxidation intermediates.[21]

Wang et al. suggested that Au catalyzed the formation of glyceric acid and glycolic acid by suppressing the C−C bond cleavage.[14] Although Au catalyzed the conversion of glycerol to glycolic acid with high selectivity, the potential required to achieve 70% conversion is ∼1 V vs RHE.[13] However, achieving a high glycerol conversion and high selectivity of the desired product at low overpotential is paramount to evaluating the electrocatalyst efficiency, and essential to the feasibility as well as the scalability of the process. Moreover, a high applied potential may also lead to the production of CO_2, which should be avoided at all cost. Therefore, finding a new and suitable electrocatalyst with high intrinsic activity at low applied potential is a key parameter to improve the efficiency of the GLYOR process. Earlier observation suggested that the C−C bond dissociation energy is higher on the Pd surface as compared to Au and Pt; as a result, glyceric acid is more commonly produced on Pd.[12] Nonetheless, it is also shown that the selectivity and rate of reaction of the electrochemical process is strongly dependent on the nanocrystal morphology and local electrolyte environment.[22] Especially, Pd nanocubes (Pd-NC) with (100) facets exhibit a more favorable catalytic performance than truncated octahedra (Pd-TO), with (111) and (100) facets, and polycrystalline Pd.[23−25] Terekhina et al. investigated the effect of different crystallographic facets present on different morphologies (namely, octahedral (∼34 nm), rhombic dodecahedral (∼69 nm), and cubic (∼75 nm)) on the performance of GLYOR and observed that Pd-Octahedral exhibited the highest selectivity for C3 products, particularly glycerate. However, the glycerol conversion (≤21%) and selectivity are very low at room temperature.[26] Hence, a rational design of the Pd catalyst with high intrinsic activity is required to improve the GLYOR activity, possibly with smaller particle size.

Green H_2 is a vital and carbon-less clean energy feedstock and is often referred as future fuel. However, currently ∼95% of H_2 is produced from steam reforming of methane, which is unsustainable and noneco-friendly, due to the associated emission of 10−12 kg of CO_2 for every kg of H_2 produced.[27] Although water electrolysis is an efficient technology to produce clean and green H_2, the high voltage requirement in a commercial electrolyzer increases the cost of hydrogen (US$ 5−12/kg) and limits its large-scale applications.[28] The sluggish kinetics of the oxygen evolution reaction (OER) at high applied potential mainly consumes the input electricity and results in increased electrolyzer potential.[29] Various organic and inorganic oxidation strategies have been employed to decouple the OER.[30−32] A suitable coupling of organic oxidation with a different cathodic reaction can further maximize the energy efficiency of the overall electrochemical process. Although biomass components, such as furfural,[33] 5-hydroxymethyl furfural (HMF),[25,34,35] and glucose,[36] are employed to decouple OER, glycerol and glucose are particularly appealing because of their low cost and availability. Moreover, furfural and HMF are valuable platform chemicals, derived from glucose oxidation, and follow complex reaction pathways.[37,38] Therefore, replacing anodic water oxidation with GLYOR in an alkaline electrolyzer could be a more effective approach to improve the energy efficiency of H_2 production and generates value-added chemicals and fuels on both sides of the cell. If value-added products are also produced through nonfossil resources, green H_2 produced through GLYOR should be considered as carbon-negative.

Herein, we demonstrate that the selectivity and conversion of glycerol could be improved by controlling the facets of Pd nanocrystals. We synthesized various morphologies of Pd NPs (Pd-NC (nanocube), Pd-TO (truncated octahedron), and spherical and polycrystalline (Pd-PC)) and investigated the GLYOR activity and made an attempt to correlate them. The Pd-NC electrocatalyst deposited on a Ni foam achieved impressive 85% glycerol conversion with 42% glyceric acid selectivity at an exceptionally low applied potential (0.6 V vs RHE) in 0.1 M glycerol and 1 M KOH in 4 h. In contrast, Pd-TO and Pd-PC exhibited 70−75% glycerol conversion under similar conditions; this demonstrates the high intrinsic activity for GLYOR associated with Pd-NC than that of the Pd-TO and/or Pd-PC catalyst. At 1.2 V vs RHE, the Pd-NC catalyst exhibits near 100% conversion along with 40% glycolic and 34% formic acid selectivity. The morphology and active sites of the Pd-NC were controlled by the structure-directing chloride and bromide anions. Further, it has been demonstrated how the selection of capping agent (KCl and KBr) in Pd-NC synthesis is crucial for achieving better GLYOR performance. Moreover, when the Pd-NC electrocatalyst was assembled into a two-electrode alkaline electrolyzer, the input electricity consumed is only 3.7 kWh per m^3 of H_2, in contrast to the requirement of ≥5 kWh per m^3 of H_2 with commercial electrolyzers at a current density of 100 mA/cm^2. Finally, we also leveraged a facet-dependent concept to maximize GLYOR activity and concurrent carbon-negative H_2 production by designing different morphologies of Pd NPs with distinct structural characteristics.

2. EXPERIMENTAL AND CHARACTERIZATION

2.1. Materials and Chemical Reagents. Potassium tetrachloride palladate (K_2PdCl_4 − 98% Merck), potassium chloride (KCl − 99% Merck), potassium bromide (KBr − 99% TCI Chemicals), citric acid ($C_6H_8O_7$ − 98% Thomas Baker Chemicals), ascorbic acid ($C_6H_8O_6$ − 99% Merck), and poly(vinylpyrrolidone) (PVP) of M_W 40,000 were purchased from Sigma-Aldrich. Glycerol ($C_3H_8O_3$), potassium hydroxide (KOH-99% Thomas Baker Chemicals), hydrochloric acid (HCl), deuterium oxide (D_2O − 99.9% Merck), potassium hydrogen phthalate (KHP − 99.5% Merck), formic acid (HCOOH), glycolic acid ($C_2H_4O_3$), glyceric acid ($C_3H_6O_4$), lactic acid ($C_3H_6O_3$), acetic acid (CH_3COOH), oxalic acid ($C_2H_2O_4$), acetone (C_3H_6O), ethanol (C_2H_5OH), and *n*-hexane(C_6H_{14}) were purchased from TCI

https://doi.org/10.1021/acsami.4c02392
ACS Appl. Mater. Interfaces 2024, 16, 26130−26141

Chemicals with AR grade purity. The commercial 20% Pt/C was purchased from Merck Industry. Ni foam (thickness: 0.5 mm; porosity: ∼98%) was purchased from Global Nanotech, Mumbai. All precursors, solvents, and other compounds were used without any further purification.

2.2. Catalyst Preparation. *2.2.1. Synthesis of Pd-NC.* In 8 mL of water, 50 mg of PVP, 60 mg of ascorbic acid, and 300 mg of KCl were added in a 25 mL capacity 3-neck round-bottom flask (RBF). The flask was sonicated for 10 min to ensure that all of the ingredients were completely dissolved and kept at 80−85 °C under constant stirring in Ar atmosphere. 57−60 mg of K_2PdCl_4 dissolved in 3 mL of water was rapidly added to the aforementioned solution. The solution was kept at 85 °C for 3 h under constant stirring. After 3 h, the black-brown color nanoparticles-containing solution obtained was cooled to room temperature and collected in centrifuge bottles for cleaning. The nanoparticles were cleaned by centrifuging a solution containing an excess of acetone and a combination of ethanol and hexane (1:5) at 10,000 rpm for 5 min. The final black-brown colored material was dried in air oven at 60 °C to remove any solvent molecules. The above-mentioned procedure was adopted for Pd-NC with KBr as capping agent; however, 300 mg of KBr was employed at 85 °C, instead of KCl.

2.2.2. Synthesis of Pd-TO. The procedure was the same as that of Pd-NC, except that citric acid (60 mg) was used at 90 °C instead of KCl (300 mg) at 85 °C. The addition of the 3 mL Pd precursor solution was carried out slowly, requiring about 10 min.

2.2.3. Synthesis of Pd-PC. The procedure was the same as that of Pd-TO, but without the use of a capping agent (citric acid) at 90 °C.

2.2.4. Fabrication of Anode and Cathode Electrodes. 2.2.4.1. Pd Nanoparticle Anode. All of the electrodes were prepared by the drop-casting coating method. Initially, Ni foam was cleaned with 1 M HCl for a 30 min ultrasonication bath, and washed with deionized (DI) water and ethanol consecutively for 10 min in a sonication bath, followed by vacuum drying at 70 °C for 10 h. In a typical procedure, 3 mg of the Pd nanocatalyst was dispersed in 3 mL of iPA (isopropyl alcohol) and drop cast slowly over the 1 × 1 cm^2 Ni foam (NF) substrate and dried in a vacuum oven for 12 h. The spray coating method was also employed to prepare the Pd-coated NF anode and it showed the same activity as that of the drop-casting method within 5% error margin. Due to the large loss of anode material in spray coating in a small (1 cm^2) area, spray coating was restricted to bigger-size coating (4 cm^2).

2.2.4.2. Pt/C Cathode. A 20% Pt/C standard catalyst was used as the cathode part for the hydrogen evolution reaction (HER) by the spray coating method; the amount of catalyst was approximately 0.8 mg·cm^{-2}.

2.3. Materials Characterization. The morphology and compositional information on the Pd nanocrystals were obtained by field-emission scanning electron microscopy (FESEM; Nova Nano SEM 450). The high-resolution transmission electron microscopy (HRTEM), high-angle annular dark-field scanning transmission electron microscopy (HAADF-STEM), and energy dispersive spectroscopy (EDS) mapping were performed using a HRTEM (JEOL JEM F-200) operating at 200 kV. The samples for TEM and HRTEM were prepared by dropwise depositing a well-dispersed sample in iPA on a carbon-coated 200 mesh copper grid and dried overnight at 25 °C. The chemical oxidation state of the samples was determined using an electron spectroscopy for chemical analysis (ESCA) Thermo Scientific Kα spectrometer with a monochromatic X-ray source (Al Kα anode 1486.6 eV). ^{1}H NMR spectra were recorded using AV-NEO 400, Bruker BioSpin AG (400 MHz), and high-performance liquid chromatography (HPLC, Agilent Technologies, model 1250 infinity) was used to analyze and quantify the liquid sample products. The evolved gas was analyzed by gas chromatography (GC Agilent 7890A) equipped with a thermal conductivity detector (at 200 °C) and the generated gas was sampled with a 500 μL Hamilton syringe. The collected liquid sample was filtered through a 0.22 μm syringe filter and analyzed using HPLC equipped with an RID detector (Agilent Technologies, 1200 infinity series, 40 °C) and a H^+ column (Phenomenex, 7.8 mm × 300 mm, 30 °C). HPLC grade water and 5 mM H_2SO_4 was used as the eluent at a flow rate of 0.6 mL min^{-1}. The external standard method was used for the quantitative determination of each product.

2.4. KP-AFM Measurement. Atomic force microscopy (AFM) experiment was carried out using Dimension Icon (Bruker) at room temperature. A capacitor was formed between the sample surface and the tip, to which was applied DC and AC voltage. The contact potential difference (CPD) ($\Delta\phi$) is defined as $(\phi_{tip} - \phi_{film})/q$, where ϕ_{tip} and ϕ_{film} are the work functions of the tip and sample, respectively, and q is the magnitude of the charge. In the present experiment, a bias voltage $V_{tip} = V_{dc} + V_{ac}\sin(\omega t)$ was applied directly to the tip, holding the sample at ground potential, where ω is the cantilever resonant frequency. A feedback loop continuously adjusts V_{dc} to maintain a condition that minimizes the force component at a frequency between the cantilever tip and sample surface, and it is recorded as a function of the position, yielding a map of the sample surface potential. For the present set of experiments, an AC bias (5 V) was applied to the Ti−Ir-tip to produce an electric force. The surface potential images obtained by KPM were recorded for AC bias for the maximum potential of the Pd-NC, Pd-TO, and Pd-PC samples using a lift-off mode. In this method, a topographic line scan is recorded at a smaller distance, and the same line is rescanned in the lift mode with the cantilever tip raised to a lift height of 30 nm, where there is no effect of short-range forces. In this way, one gets both KPM and AFM information simultaneously from the same spot.

2.5. Electrochemical Measurements. All electrochemical experiments for GLYOR, OER, and HER were performed using the Gamry reference 3000 potentiostat in three- and two-electrode systems. The fabricated electrode on the NF was directly used as the working electrode. Graphite rod (5 mm in diameter) and Pt/C on NF were used as the counter electrode for HER in three- and two-electrode systems, respectively. Saturated calomel electrode (SCE) and Ag/AgCl electrode were used as the reference electrodes. All potentials in this work were given versus the reversible hydrogen electrode (RHE) according to the following equation

$$E_{RHE} = E_{SCE} + 0.05916\text{pH} + 0.241\ \text{V}$$

All polarization curves were recorded with 85% *iR* compensation, and all LSV data were collected with a sweep rate of 5 mV s^{-1}. The apparent current density was calculated using the electrode's geometric area. The double-layer capacitance (C_{dl}), which was derived from the cyclic voltammetry (CV) curves recorded in a potential range without any Faradaic current, served as the basis for calculating the electrochemical surface area (ECSA). 20, 40, 60, 80, and 100 mV/s were the scan rates employed. Plotting the measured cathodic charging currents against the different scan rates, such as 20, 40, 60, 80, and 100 mV/s, yielded the C_{dl} slope. The specific capacitance value (C_s) was kept in the range of 20−60 F cm^{-2} for the catalyst having a geometrical area of 1 cm^2 and we took C_s = 40 Fcm^{-2}. Finally, ECSA was obtained by dividing the C_{dl} by the C_s.[39,40]

The liquid and gaseous products were analyzed and quantified by ^{1}H NMR, HPLC, and GC analysis. The chronoamperometry testing in the three-electrode system was carried out at 0.6−1.2 V vs RHE for 4 h (0.1 M glycerol + 1 M KOH); chronopotentiometry testing with a two-electrode system was carried out at 10 and 50 mA cm^{-2} for 120 h. In the 4 h reaction, 450 μL of the electrolyte was added with 130 μL of D_2O and 20 μL of KHP (as an internal standard). KHP was employed as an internal standard for quantification of all of the products observed in ^{1}H NMR. The concentration of the liquid products formed after the electrocatalytic reaction was calculated using the following formula

$$\frac{n_x}{n_y} = \frac{I_x}{I_y} \times \frac{N_y}{N_x}$$

Here, n_x represents the molar concentration of KHP, I_x represents the integral area in ^{1}H NMR spectra for KHP, and N_x is the number of nuclei (4 equiv protons for KHP appearing at 7.25 ppm). Similarly, n_y is calculated from the above formula for the liquid product, I_y is the integral area of the product formed, and N_y is the number of nuclei

https://doi.org/10.1021/acsami.4c02392
ACS Appl. Mater. Interfaces 2024, 16, 26130−26141

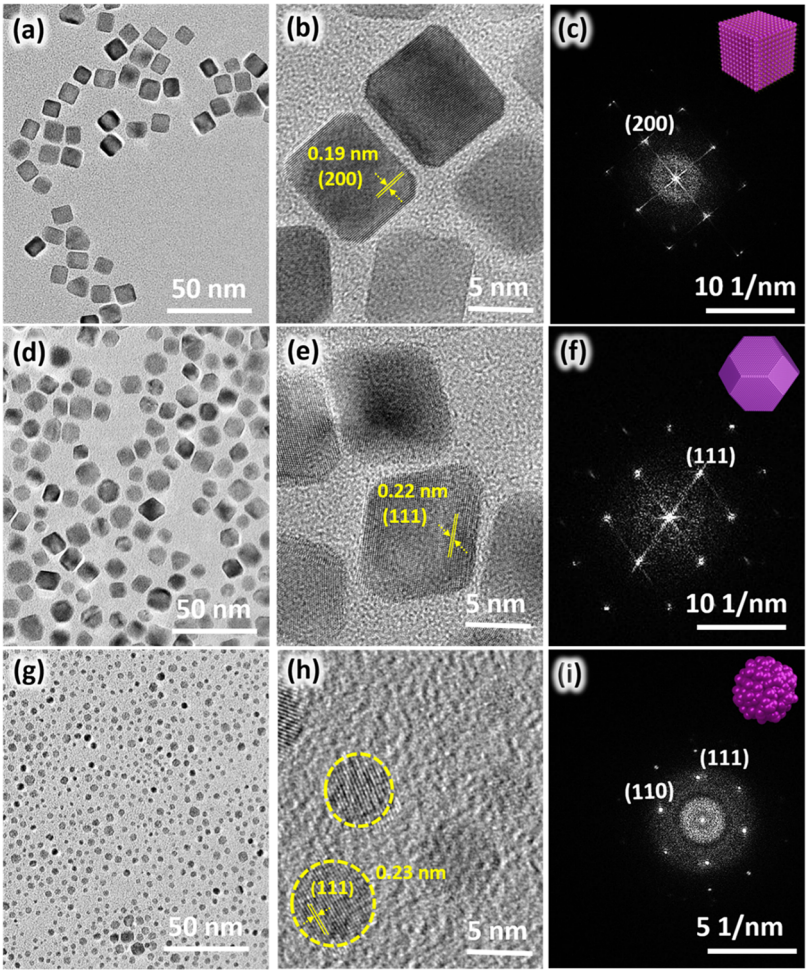

Figure 1. (a, d, g) TEM images of homogeneously dispersed as-prepared Pd-NC, Pd-TO, and Pd-PC; the corresponding high-resolution TEM images of the Pd nanoparticles are given in (b, e, h). (c, f, i) Selected-area electron diffraction (SAED) patterns of individual Pd-NC, Pd-TO, and Pd-PC.

associated with the peak. The concentration of the products obtained from the ^{1}H NMR was used to calculate the conversion, selectivity, and carbon balance.

$$\text{conversion}\ (\%) = \frac{n_{\text{glycerol,initial}} - n_{\text{glycerol,final}}}{n_{\text{glycerol,initial}}}$$

$$\text{carbonbalence}\ (\%) = \frac{n_{\text{sum of products}}}{3 \times n_{\text{glycerol,initial}}} \times 100$$

$$\text{selectivity}\ (\%) = \frac{n_{\text{product}} \times \text{carbon balance}}{n_{\text{sum of products}}} \times 100$$

where n is the number of moles.

2.5.1. Electrolyzer Setup. A flow electrolyzer with a 4 cm^2 geometrical area was used in a two-electrode system, and a sustainion membrane was used to exchange the anion and separate anode and cathode compartments for GLYOR and HER. A constant current of 10 mA·cm^{-2} (0.1 M glycerol + 1 M KOH) was used with 3 mL min^{-1} flow rate for longer hour stability, while a higher constant current of 50 mA cm^{-2} (0.1 M glycerol + 1 M KOH) was employed with 10 mL min^{-1} flow rate with a peristaltic pump. Due to excessive electrolyte consumption and H_2 generation, an additional electrolyte and a high flow rate were employed. Along with pure milliQ water, all stability reactions were carried out in saline water (3.5 wt % NaCl solution, comparable to seawater). The Faradaic efficiency (FE) of hydrogen production was evaluated by the following equation

$$\text{faradaic efficiency}\ (\%) = \frac{n_{\text{experimental}}}{n_{\text{theoritical}}} \times 100$$

where $n_{\text{experimental}}$ is the number of moles of H_2 collected experimentally. The theoretical amount of H_2 was calculated by the following equation, where Q is the transferred charge, n is the number of electrons transferred to form a H_2 molecule, and F is Faraday's constant (96,485 C mol^{-1}).

$$n_{\text{theoritical}} = \frac{Q}{n \times F}$$

The electricity consumption per m^3 of H_2 produced (W, kW per m^3 of H_2) was calculated as

$$W = \frac{n \times F \times V \times 1000}{3600 \times V_m}$$

where n is the number of electrons transferred to form each H_2 molecule, V is the applied voltage, and V_m is the molar volume of gas at normal temperature and pressure (22.4 L/mol).

3. RESULTS AND DISCUSSION

Different morphologies of Pd nanostructures were synthesized with a favorable reducing and structure-directing agent with K_2PdCl_4 as the Pd precursor (Figure S1).[41] The detailed synthesis procedure is described in the Experimental Section. It is to be noted that Pd-NC mentioned in the manuscript refers to Pd-NC synthesized using KCl as the capping agent, unless

https://doi.org/10.1021/acsami.4c02392
ACS Appl. Mater. Interfaces 2024, 16, 26130−26141

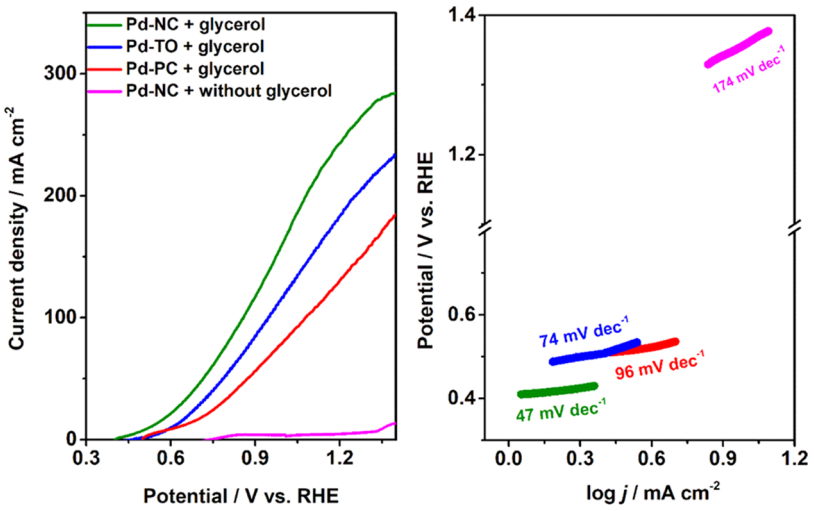

Figure 2. (a) Linear sweep voltammetry of various morphologies of Pd in 1 M KOH with and without 0.1 M glycerol (scan rate, 5 mV s^{-1}). (b) Tafel slope given for the measurements shown in panel (a).

noted otherwise. The structure and morphology of the Pd nanocrystals were first characterized using TEM, HRTEM, and SEM. Figure 1 shows the HRTEM images of the as-prepared Pd nanoparticles (NC, TO, and PC) with selected-area electron diffraction (SAED) pattern. Figure 1a shows the Pd-NC nanoparticles, which are in the size range of 8−10 nm. The HRTEM images of Pd-NC nanoparticles synthesized using KBr as the capping agent are included in Figure S2 for the comparison. The measured *d*-spacing is found to be 0.19 nm and it corresponds to the interplanar spacing of the (200) facet of a face-centered cubic (fcc) lattice (Figure 1b).[41] The corresponding SAED patterns of Figure 1b shown in Figure 1c show that the Pd-NC was a single nanocrystal with (200) facets. Figure 1d shows the TEM image of Pd-TO nanoparticles with a uniform TO morphology with 7−10 nm particle size range. The lattice *d*-spacing of Pd-TO is 0.22 nm and it corresponds to the (111) facets of Pd (Figure 1e).

The corresponding SAED pattern was recorded and shown in Figure 1f, which represents that the Pd-TO was a single nanocrystal. Pd-TO exhibits (111) as the dominant facet, along with (200) facet too. Figure 1g shows the TEM image of Pd-PC nanoparticles with uniform spherical particles of 3−5 nm size. HRTEM image of Pd-PC is shown in Figure 1h and the corresponding SAED pattern (Figure 1i) represent the polycrystalline nature of the NPs due to presence of various facets, including (110), (111), and (100). All the Pd nanostructures were drop cast on a NF and used for electrochemical measurements. SEM images shows a uniform coating of Pd on NF (Figure S3). Figure 2a shows the LSV plots of various morphologies of Pd nanostructure with different geometric current density. For water electrolysis (in the absence of glycerol), Pd-NC anode drive the OER and exhibited a significantly high onset potential at 1.5 V (vs RHE). In the presence of glycerol, the catalytic onset of GLYOR decreases dramatically to the low potential with all the three morphologies of Pd catalyst anode. Notably, Pd-NC shows the highest current density in the entire potential range, than the other two morphologies. The catalytic current density of 100 (250) mA/cm^2 was achieved at low potential of 0.85 (1.22) V vs RHE; to the best of our knowledge, this is the best GLYOR geometric current density reported for Pd-based and any electrocatalyst. In contrast, Pd-PC exhibit lower GLYOR current density among all three morphologies of Pd. Critically, Pd-NC shows the lowest onset potential at 0.40 V, while Pd-TO and Pd-PC exhibit an onset at 0.47 and 0.50 V vs RHE for GLYOR, respectively. Furthermore, the choice of the capping agent during Pd-NC synthesis also influences the GLYOR performance. A detailed discussion about the role of capping agent on GLYOR performance has been given in Supporting Information (Figures S4−S5).

Different morphologies of Pd exhibit almost similar Pd 3d core level spectra (Figures S5c−S6a,b). However, X-ray valence band spectra (XVB) in Figure S6c shows a characteristic change. Interestingly, Pd-NC shows a distinct onset of VB at Fermi level (E_F = 0 eV), compared to all other morphologies, truly representing metallic surface. Compared to Pd-NC, VB onset of Pd-TO is shifted by 0.3 eV to the higher BE. In general, VB feature appearing at low energy corresponds to higher activity. Pd-PC shows ultralow intensity below 2 eV, indicating a nonmetallic behavior, which is worth exploring further. This could be a reason for a relatively low activity observed with Pd-PC. These observations signify the enhanced catalytic activity associated with Pd-NC, and attributed to its unique electronic structure.

To study the effect of glycerol concentration on GLYOR, LSV analysis was performed on Pd-NC as a function of glycerol concentration (Figure S7). LSV measured in the potential ranging from 0.3 to 1.3 V vs RHE at a scan rate of 5 mV s^{-1}. LSV of GLYOR shows peak arise from the oxidation of chemisorbed glycerol on Pd surface. GLYOR current density increased when the glycerol concentration was increased from 0.05 to 0.2 M. However, no significant change in peak current density was observed when the glycerol concentration was between 0.5 and 1 M. Moreover, it is worth to mention that the onset potential of GLYOR was shifted to lower potential, when the glycerol concentration was kept at 0.05 to 0.2 M. However, the onset potential remains same at 0.5 and 1 M glycerol. This indicates that an optimum surface concentration of glycerol is required for oxidation. However, for the entire set of GLYOR experiments, 0.1 M glycerol concentration was chosen for a fair comparison with reported literature. The reaction kinetics was evaluated from the Tafel plot derived from the LSV data (Figure 2b). The Tafel slope of Pd-NC electrode was measured to be 47 mV/dec, which is the

https://doi.org/10.1021/acsami.4c02392
ACS Appl. Mater. Interfaces 2024, 16, 26130−26141

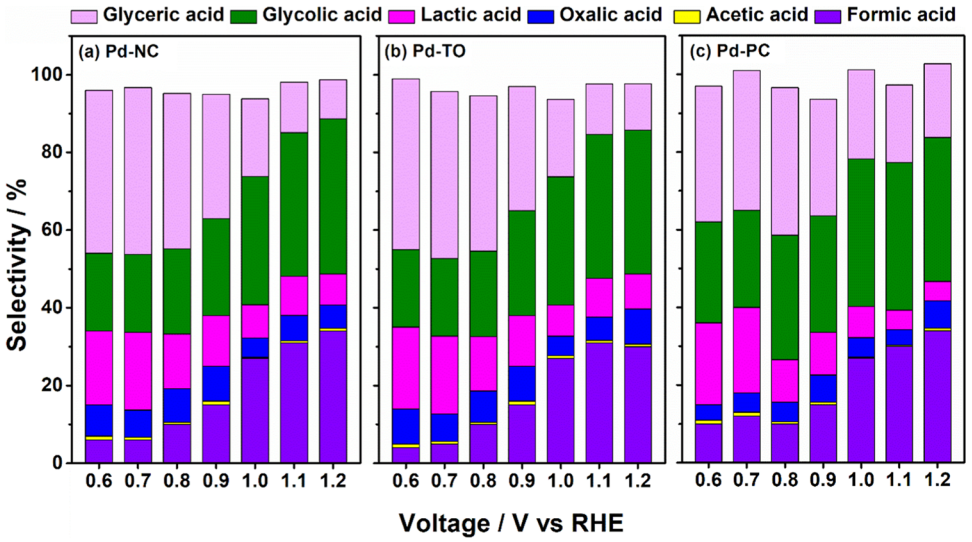

Figure 3. Product selectivity as a function of the applied potential observed for (a) Pd-NC, (b) Pd-TO, and (c) Pd-PC catalyst after 4 h of reaction.

lowest, than that of Pd-TO (74 mV/dec) and Pd-PC (96 mV/dec). Moreover, the calculated Tafel slope of 174 mV/dec for OER suggests that Pd-NC exhibited much slower kinetics at the anode in the absence of glycerol. The low Tafel slope value with Pd-NC electrode indicates that the GLYOR rate is high on all six (200) facets of the NC.

The GLYOR activity was evaluated with different morphologies of Pd NPs by chronoamperometry measurement as a function of applied potential in 1 M KOH and 0.1 M glycerol. All the chronoamperometry measurements were carried out for 4 h. The chronoamperometry results revealed that the current density of the GLYOR continuously declined as the reaction proceeds with time, and it reached to as low as 3−5 mA/cm^2 at the end of the reaction in 4 h (Figure S8). The rate of decrease of current density is significantly high in the case of Pd-NC, suggesting the high rate of GLYOR at low overpotential. The decrease in catalytic current density with all the three morphologies is mainly due to the depletion of the glycerol content and increase in value-added products content.

Figure 3 shows the products selectivity pattern from GLYOR at a potential range, from 0.6 to 1.2 V vs RHE, with three Pd nanocrystals. A similar selectivity pattern was observed with all three morphologies of Pd. At the lowest potential of 0.6 V vs RHE, glyceric acid was observed to be the major product, along with glycolic acid, lactic acid, oxalic acid and formic acid as the minor products. Notably, no appreciable change in products distribution was observed from GLYOR with various morphologies of Pd nanocrystals. At 0.6 V, the maximum selectivity of ∼65% was achieved for C3 products (glyceric and lactic acids) formation with Pd-TO (Figure 3b). When the potential increased to 1.2 V, the C2 products (glycolic, oxalic and acetic acid) reached the maximum selectivity of ∼50% with Pd-NC (Figure 3a), indicating that higher overpotential is required for the oxidative cleavage of C−C bond. The selectivity toward glycolic acid started to enhance at 1.0 V vs RHE with all three Pd morphologies. The formation of glycolic acid originated from the oxidative C−C bond cleavage of glyceric acid with simultaneous production of formic acid. Indeed, the total amount of glycolic and oxalic acids produced with all three Pd morphologies are almost equal to the amount of formic acid production, at high potentials (1.0−1.2 V). Critically, no carbonate feature was observed in ^{13}C NMR spectrum even at the highest applied potential.

This reiterates that no further oxidation of formic aid to CO_2 taking place during GLYOR process even at the highest potential (1.2 V vs RHE). A detailed carbon balance study was conducted at each applied potential of the GLYOR process and the results are given in Table S1 (Supporting Information). Our results are reproduced within an error margin of 5−10% in the carbon balance calculation. One millimolar KHP was used as an internal standard with each NMR sample for the quantitative determination of various products; hence, we attribute the relevant carbon balance error to sampling and measurement, rather than carbonate formation. In the GLYOR process, it is likely that some of the glycolic acid could get further oxidized to oxalic acid.[13] In fact, less than 5% of oxalic acid was observed throughout the potential range with any of the Pd nanocrystals supports the above conclusion. Electron withdrawing effect of the −COOH group with glycolic acid restricts the further oxidation of carbon atom containing hydroxyl group. It is likely that the partial reduction of glyceric acid to lactic acid was observed at lower applied potential, rather than from glycerol. The selectivity toward lactic acid was found to decrease at higher applied potential, due to further oxidation to formic acid and acetic acid. Therefore, a small amount of acetic acid was observed in the entire applied potential window. A schematic of the above-discussed points is shown as a possible mechanism in the Figure S9. Since the amount of lactic acid production is low (<10%) the contribution from the lactic acid pathway to the overall formic acid production is minimal. Finally, the GLYOR process could eventually stop at the stage of formic acid and oxalic acid, as higher potential is required to oxidize formic acid to CO_2.

To further gain insights into the mechanistic aspects, the products selectivity and glycerol conversion has been measured as a function of reaction time, and GLYOR performance was monitored periodically for every 1 h interval at 1.2 V vs RHE (Figure 4a). It was observed that the product distribution not only depends on the applied potential, but also on the reaction time. Pd-NC afforded outstanding conversion of 47% in just 1 h. However, Pd-TO and Pd-PC exhibited 30 and 28% glycerol conversion, respectively, under same experimental conditions.

https://doi.org/10.1021/acsami.4c02392
ACS Appl. Mater. Interfaces 2024, 16, 26130−26141

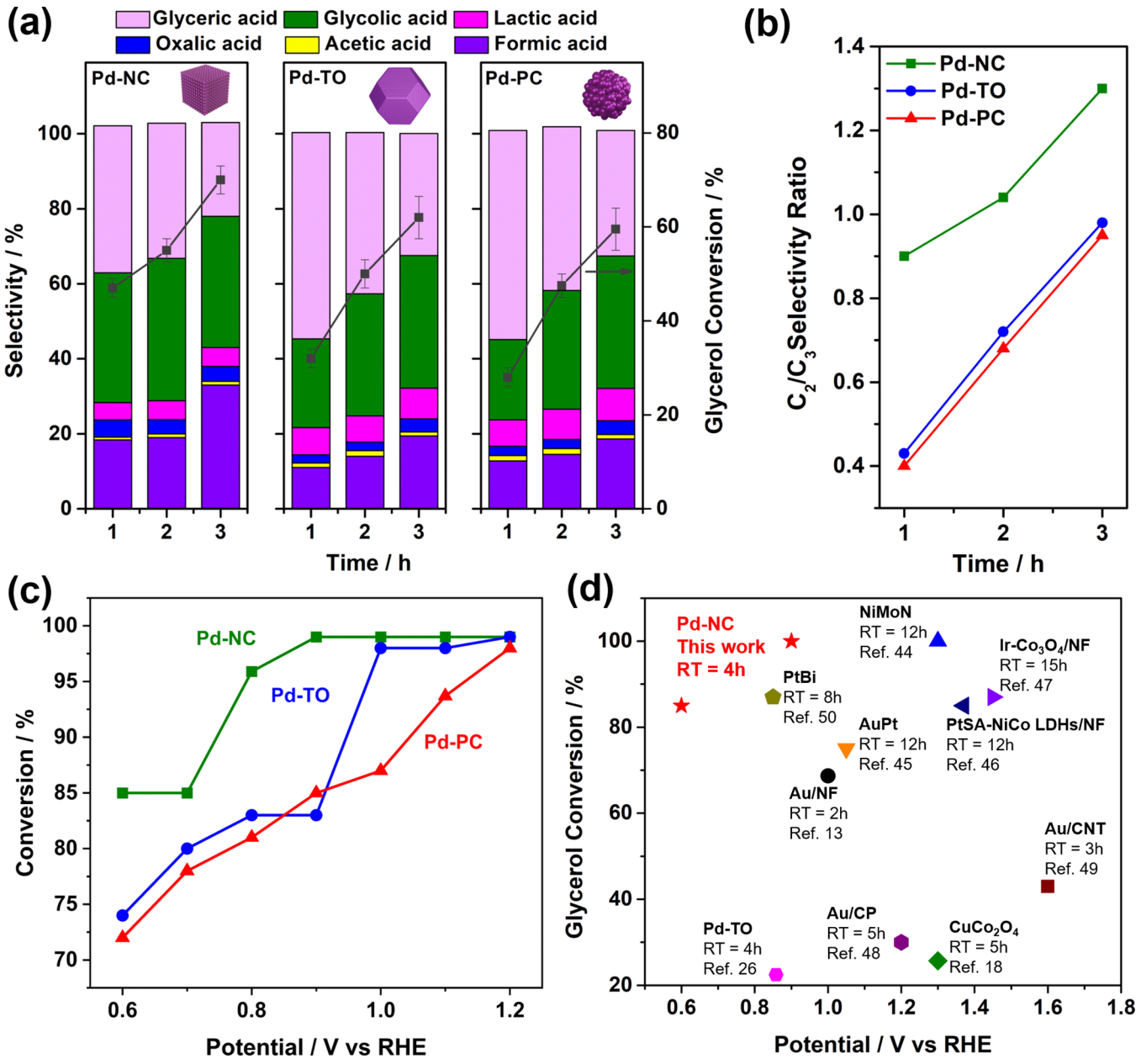

Figure 4. (a) Glycerol conversion and selectivity of different products as a function of the reaction time at 1.2 V vs RHE over different morphologies of Pd catalysts. (b) Change in ratio of C2/C3 products' selectivity as a function of GLYOR time at 1.2 V vs RHE. (c) Comparison of glycerol oxidation performance over different catalyst surfaces in alkaline solution, as a function of the applied potential. (d) A comparison of top-performing catalysts' results from the literature with the present results from Pd-NC under comparable conditions.

This result confirms that more rapid electron transfer occurs with the Pd-NC electrode, and it is in good agreement with Tafel plot analysis (Figure 2b). It is worth to note that the glyceric acid selectivity after the first hour of the rection is only 38% with Pd-NC, compared to 57 and 60% with Pd-TO and Pd-PC, respectively. The total C_2 oxidation products in Pd-NC were 42% after 1 h of the reaction. However, Pd-TO and Pd-PC exhibited 27 and 25% of C_2 selectivity, respectively (Figure 4a). Moreover, carbon balance studies were conducted after every hour of the GLYOR process and the results are given in Table S2 (Supporting Information). As the reaction proceeds, the ratio of C2 to C3 selectivity increases with all the three morphologies (Figure 4b), and attain almost similar product distribution after 3 h of reaction for Pd-TO and Pd-PC; while Pd-NC shows higher C2 products selectivity along with formic acid. This result confirms that the rate of oxidative cleavage of C−C bond is the highest with Pd-NC compared to other morphologies. Earlier studies proposed that the adsorption of OH^- ions on the catalyst surface is the rate-determining step for GLYOR.[13] This suggested the competitive oxidative pathway of adsorbed glycerol and glyceric acid with hydroxide ion on catalyst surface through a Langmuir−Hinshelwood mechanism.[42] Wang et al. observed that the cubic NPs with (100) facets were found to be more active for oxidative cleavage of C−C bonds and the oxidation of acetyl group (CH_3CO) to acetic acid is significantly inhibited on Pt (100) compared to Pt (111) surface and accelerate the formation of CO_2 due to more feasible breaking of C−C bond on (100) surface.[43]

https://doi.org/10.1021/acsami.4c02392
ACS Appl. Mater. Interfaces 2024, 16, 26130−26141

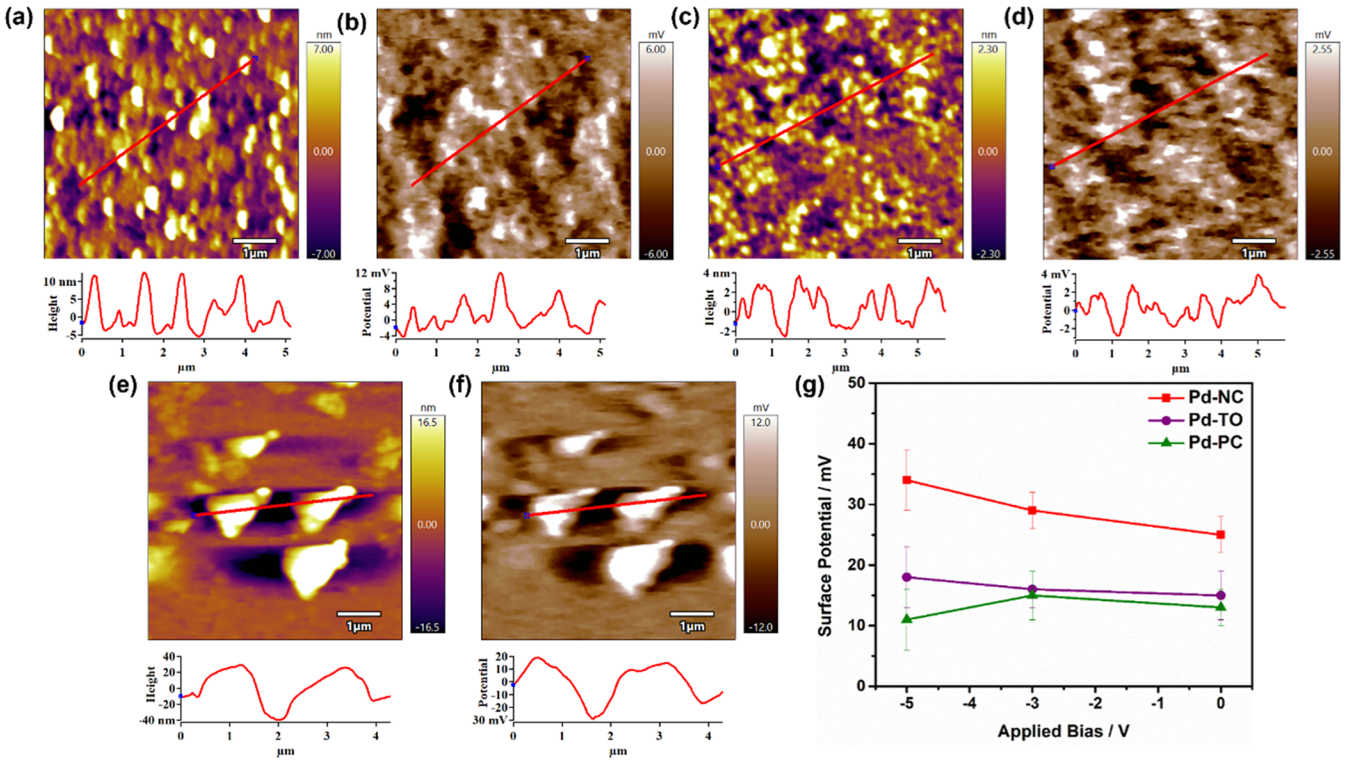

Figure 5. AFM topography and line profile analysis of (a, b) Pd-NC, (c, d) Pd-TO, and (e, f) Pd-PC. (g) KPM surface potential at different applied bias shows Pd-NC has higher surface potential then Pd-TO and Pd-PC.

Although the selectivity of different products are similar after 3 h of reaction, the glycerol conversion is significantly different with different morphology of Pd nanocrystals at a given applied potential (Figure 4c). For instance, Pd-NC exhibited 85% glycerol conversion after 4 h of reaction time at a low potential of 0.6 V compared to 72 and 74% conversion with Pd-PC and Pd-TO, respectively, under same experimental conditions. The GLYOR process catalyzed by Pd-NC shows near 100% conversion at 0.8 V; however, Pd-TO and Pd-PC exhibited near 100% conversion at 1 and 1.2 V, respectively. The complete conversion at this respective potential is fully supported by the disappearance of glycerol peak in the NMR spectrum (Figures S10−S12). Furthermore, the formation of different products was confirmed from HPLC by comparing with the standard samples (Figure S13). This reiterates that the rate of partial oxidation of glycerol is high on (100) facets of Pd-NC compared to additional (111) facets of Pd-TO and multiple crystalline facets of Pd-PC.

High GLYOR activity reported for different catalysts in alkaline solution are compared in Figure 4d and to the best of our knowledge Pd-NC shows the highest conversion at the lowest overpotential among all the catalysts. Han et al. demonstrated 29.7% electrocatalytic conversion of glycerol at 1.3 V vs RHE by integrating $CuCo_2O_4$ catalyst with carbon fiber electrode.[18] The NiMoN loaded on a carbon cloth exhibit 100% conversion at 1.3 V, but requires a long reaction time (12 h) for complete conversion.[44] AuPt[45] and Au[13] on NF shows comparable GLYOR activity of 70% conversion at an applied potential of 1 V (RHE); however, the latter (former) catalyst requires 2 h (12 h) reaction time. Furthermore, many precious metal catalysts exhibit near 100% conversion only at higher potential (≥1 V) and longer reaction time.[46−50] A similar report by Terekhina et al. observed the highest glycerol conversion to be 82% with Pd-octahedral morphology at 60 °C; while the same catalyst at 20 °C exhibits a mere 21% glycerol conversion to be noted.[26] It may be noted that KI capping agent was employed to synthesize Pd-cubic nanocatalyst, while the present work with highest GLYOR performance employed KCl; further KCl is also removed to the maximum level in the present work, as supported by LSV results shown in Figure S4. In addition, a large difference in particle size to be noted in the present work (Pd-NC ∼ 7−10 nm), while Pd-Octahedral[26] shows ∼34 nm.

To probe the morphology-dependent GLYOR activity, the ECSA of different catalysts was compared by deriving their C_{dl} values from CV. The CV profile was recorded in the nonfaradaic potential range of −0.7 to −0.9 V vs Ag/AgCl (Figure S14). The C_{dl} of the Pd-NC was calculated to be 9.3 mF/cm^2, which is higher than that of Pd-TO (5.5 mF/cm^2) and Pd-PC (0.9 mF/cm^2). Therefore, the ECSA of the different morphology of Pd NPs follows the order Pd-NC (232.5 cm^2) > Pd-TO (137.5 cm^2) > Pd-PC (22.5 cm^2). High ECSA of Pd-NC indeed enhances the glycerol conversion without changing the product selectivity.

4. KPFM STUDIES OF PD-NC, PD-TO, PD-PC

To further gain insight into understanding the structure−activity correlation, Kelvin probe force microscopy (KPFM) analysis of was carried out. KPFM is a powerful tool for visualizing the surface properties and correlate the electrocatalytic activity.[51] The surface charge on the active sites of catalyst regulates adsorption of reactant and used as a descriptor for correlating electrocatalytic activity.[52,53] In fact, the surface potential could be altered by the different arrangement of atoms on the surface. In KPFM, electrostatic force between the tip and the sample gives information about

https://doi.org/10.1021/acsami.4c02392
ACS Appl. Mater. Interfaces 2024, 16, 26130−26141

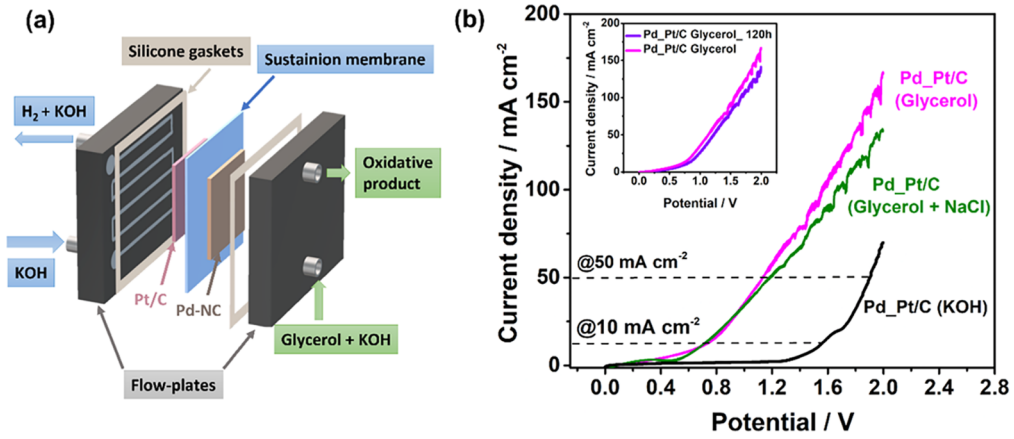

Figure 6. (a) Schematic of two-electrode alkaline electrolyzer performing GLYOR at the anode and HER at the cathode (b) LSV curve obtained for GLYOR in the electrolyzer using Pd-NC and Pt/C on Ni foam as anode and cathode, respectively.

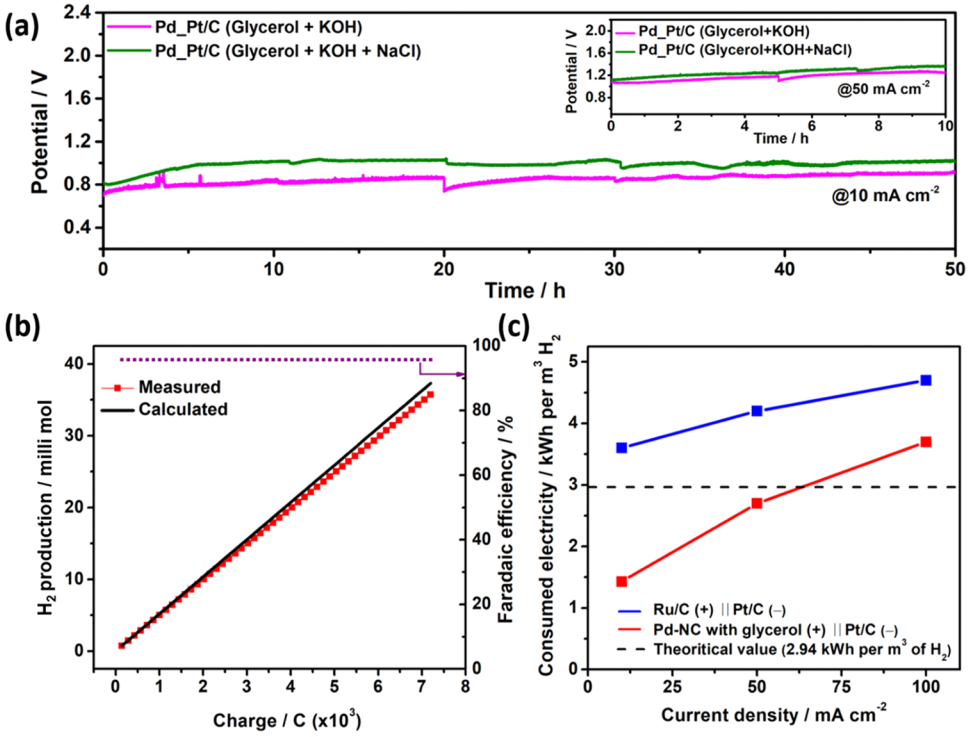

Figure 7. (a) Sustainability study of glycerol oxidation at 10 mA/cm^2 current density with two-electrode electrolyzer using Pd-NC as the anode, and Pt/C as the cathode. GLYOR and GLYOR with 3.5 wt % of NaCl solution was continuously performed one after another for 50 h each. (b) Amount of H_2 measured experimentally at the cathode and the corresponding theoretically calculated value. (c) Electricity consumed per m^3 H_2 production from GLYOR system and using conventional alkaline electrolyzer.

the contact potential difference (CPD) ($\Delta\phi$) between the conducting Ti−Ir-tip and the sample surface. The measured CPD is related to the surface potential. KPFM measurements were carried out to measure topographic surface aspects of Pd-NC, Pd-TO, Pd-PC on SiO_2 surface and its corresponding surface potential (Figure 5). Pd-NC and Pd-TO NPs shows typical AFM topography image and corresponding surface potential (Figure 5a−d). However, Pd-PC NPs shows triangular shape with nonuniform surface structure (Figure 5e,f). Significant agglomeration was likely due to the polycrystalline nature of the particles. Compared to Pd-TO and Pd-PC, the surface potential is higher with Pd-NC (Figure 5g). (100) facet is known to be unsaturated and exhibit open structure, then (111) or (110), and the same is attributed to high surface charge on Pd-NC. It is also ruled out for any artifacts that might arise due to line by line fitting by repeating the set of experiments for several cycles as well as on different batch materials, and reproducible surface potential values was observed. It is evident from the line profile analysis that edges of the NPs exhibited higher surface potential. Moreover, the diffusion of subsurface oxygen in (100) facets are relatively higher compared to (111) and (110) facets, as (100) facets are lower in Pd atomic density.[54]

Previous studies show a linear correlation between the surface potential and the oxygen storage capacity or the catalytic activity for CO oxidation. The atomic oxygen diffusion generates partial positive charges on the surface and enhances the catalytic activity for many applications.[53,55] By

https://doi.org/10.1021/acsami.4c02392
ACS Appl. Mater. Interfaces 2024, 16, 26130−26141

controlling the crystallographic facets of catalysts, activity modulation is possible, as it alters the surface potential, which in turn alters the charge transfer. Furthermore, we studied the surface potential of Pd-NC NPs synthesized with the KBr capping agent and a significant decrease in surface potential was observed as compared to Pd-NC synthesized with KCl (Figure S15). Since Br^- is a strong binding agent, the extent of poisoning of the catalyst surface is more, as indicated earlier. This result suggested that great care must be taken in choosing and removal of halide, given that these halide ions can inhibit the GLYOR performance.

5. ELECTROLYZER PERFORMANCE

One of the critical challenges in water electrolysis is the reduction of operating potential to bring down the electricity consumption. Due to the high overpotential associated with OER from water splitting, it will be nearly impossible to bring down the power consumption beyond a certain level. Nonetheless, the same was easily realized by coupling GLYOR and HER in a two-electrode electrolyzer (Figure 6a). The electrolyzer was assembled with Pt/C as the cathode and Pd-NC as the anode separated by an anion exchange membrane. A digital photograph of the electrolyzer setup is shown in Figure S16 and the details are mentioned in the Experimental Section. Figure 6b presents the LSV curve for GLYOR in the alkaline electrolyzer. It requires a voltage of 1.54 V to achieve 100 mA/cm^2. However, a significantly low OER current was observed at 1.54 V when the experiment was carried out without glycerol. Moreover, a current density of 10 and 50 mA/cm^2 was achieved with GLYOR at an applied potential of 0.62 and 1.13 V, respectively, which is less than the thermodynamic potential of 1.23 V for OER. A comparison of top-performing catalysts' results from the literature with the present electrolyzer result from Pd-NC is summarized in Table S3. It is apparent that Pd-NC is far superior in electrocatalytic performance to all other catalysts listed. Even with 3.5 wt % of NaCl solution (simulated seawater), the chloride oxidation is fully avoided; however, a marginal decrease in GLYOR current density was observed, which could be due to the adsorption of chloride ions on the Pd-NC surface. This observation enables further opportunity for, chlorine-free, seawater splitting coupled with GLYOR. Indeed, it is worth evaluating this reaction with real seawater, which contains many other ions.

A chronoamperometry experiment for 50 h was conducted at 10 mA/cm^2 current density to investigate the stability of the Pd-NC catalyst and the result is shown in Figure 7a. The voltage remains constant at ∼0.8 V throughout the 50 h operation and it shows the stability of the catalyst. We also evaluated the long-term operation of the electrolyzer with 3.5 wt % of NaCl solution at 10 mA/cm^2 current density and observed a marginal increase in operating potential. It is to be noted that the same catalyst was employed for both the above reactions continuously (GLYOR and GLYOR in simulated seawater), except the change in the NaCl-containing solution after 50 h. The electrolyzer continuously produced hydrogen at a rate of 0.71 mmol/h over 50 h and the faradaic efficiency (FE) of HER was observed to be ∼95% (Figure 7b). The FE of HER was calculated from the theoretical and experimental H_2 production and the detailed calculation is discussed in the Experimental Section. Moreover, we also carried out the stability test of the Pd-NC catalyst at 50 mA/cm^2 current density for 10 h (inset in Figure 7a). It can steadily work at 1.1 V and produced hydrogen at a rate of 1.1 mmol/h over 10 h. It is noteworthy to mention that the identical catalyst was utilized for a continuous duration of 120 h in all electrolyzer experiments.

From the above results it is evident that the GLYOR-based hydrogen production system requires an electricity input of ∼3.7 kWh per m^3 of H_2 at a current density of 100 mA/cm^2 (Figure 7c). However, a conventional electrolyzer requires 4.8 kWh per m^3 of H_2 under the same current density (Figure S17).[56] Furthermore, to achieve a current density of 50 mA/cm^2 it requires an input electricity of only 1.13 kWh per m^3 of H_2, which is even less than the theoretical value of 2.94 for the water splitting reaction at 1.23 V. This is possible by completely avoiding OER, and concurrently oxidizing glycerol to value-added products.

6. CONCLUSIONS

In summary, a unique morphology-dependent selectivity and conversion of GLYOR has been demonstrated with Pd NPs. Pd-NC selectively and efficiently upgrades glycerol to glyceric acid and glycolic acid at a high conversion rate; the global glycolic acid market was estimated at USD 281.2 million in 2022, with a 9.1% CAGR forecast from 2023 to 2030, and electrochemical routes can certainly play a major role.[49] The electrochemical oxidative cleavage of C−C bond is more favorable on Pd-NC compared to Pd-PC and Pd-TO morphology, suggesting the intrinsic activity of Pd (100) facets. Especially, when Pd-NC and Pt/C assemble as the anode and cathode, respectively, the electrolyzer requires an electricity input of only ∼3.7 kWh/m^3 H_2 at a current density of 100 mA/cm^2 in contrast to the 4.8 kWh/m^3 H_2 required for a conventional alkaline electrolyzer. Importantly, no run-away reaction occurs to CO_2 formation and a near 100% carbon balance was obtained. The reported electrocatalytic system provides a promising opportunity for the production of valuable chemicals from glycerol oxidation with concurrent high-purity hydrogen, and it can be considered as carbon-negative hydrogen.

■ ASSOCIATED CONTENT

Supporting Information

The Supporting Information is available free of charge at https://pubs.acs.org/doi/10.1021/acsami.4c02392.

Schematic representation (S1); HRTEM images (S2); FESEM image (S3); LSV (S4); XPS (S5) and XVB measurement (S6); LSV (S7); chronoamperometry (S8); reaction mechanism (S9); ^{1}H NMR result (S10−S12); HPLC data (S13); capacitance measurement (S14); AFM measurement (S15); photograph of electrolzer setup (S16); LSV obtained with electrolzyer (S17); activity comparison and carbon balance for products (Table S1) and reactant (Table S2); and activity data comparison from literature (Table S3) (PDF)

■ AUTHOR INFORMATION

Corresponding Authors

Kshirodra Kumar Patra − *Catalysis and Inorganic Chemistry Division, CSIR-National Chemical Laboratory, Pune 411 008, India;* orcid.org/0000-0002-1468-0946; Email: k.patra@ncl.res.in

Chinnakonda S. Gopinath − *Catalysis and Inorganic Chemistry Division, CSIR-National Chemical Laboratory,*

https://doi.org/10.1021/acsami.4c02392
ACS Appl. Mater. Interfaces 2024, 16, 26130−26141

Pune 411 008, India; Academy of Scientific and Innovative Research (AcSIR), Ghaziabad 201 002, India; orcid.org/0000-0002-4525-3912; Email: cs.gopinath@ncl.res.in

Authors

Inderjeet Chauhan − *Catalysis and Inorganic Chemistry Division, CSIR-National Chemical Laboratory, Pune 411 008, India; Academy of Scientific and Innovative Research (AcSIR), Ghaziabad 201 002, India*

Himanshu Bajpai − *Catalysis and Inorganic Chemistry Division, CSIR-National Chemical Laboratory, Pune 411 008, India; Academy of Scientific and Innovative Research (AcSIR), Ghaziabad 201 002, India*

Bishakha Ray − *Department of Applied Physics, Defence Institute of Advanced Technology (Deemed University), Pune 411 025, India;* orcid.org/0000-0002-1684-9960

Sadhu K. Kolekar − *Catalysis and Inorganic Chemistry Division, CSIR-National Chemical Laboratory, Pune 411 008, India;* orcid.org/0000-0001-8425-3328

Suwarna Datar − *Department of Applied Physics, Defence Institute of Advanced Technology (Deemed University), Pune 411 025, India*

Complete contact information is available at: https://pubs.acs.org/10.1021/acsami.4c02392

Notes

The authors declare the following competing financial interest(s): An invention disclosure was filed in 2023 based on the current work. CSIR-NCL is interested in commercializing the present findings.

■ ACKNOWLEDGMENTS

I.C. acknowledges the research scholarship from INSPIRE. H.B. thanks UGC. The authors thank Sibo Chetry for helping in XPS data plotting and acknowledge the financial support from CSIR for an NCP project (HCP-44) through the H2T program, and NCL for a translational project (MLP301226).

■ REFERENCES

(1) Lucas, F. W. S.; Grim, R. G.; Tacey, S. A.; Downes, C. A.; Hasse, J.; Roman, A. M.; Farberow, C. A.; Schaidle, J. A.; Holewinski, A. Electrochemical Routes for the Valorization of Biomass-Derived Feedstocks: From Chemistry to Application. *ACS Energy Lett.* **2021**, 1205−1270.

(2) Gallezot, P. Conversion of Biomass to Selected Chemical Products. *Chem. Soc. Rev.* **2012**, *41* (4), 1538−1558.

(3) Pagliaro, M.; Ciriminna, R.; Kimura, H.; Rossi, M.; Pina, C. D. From Glycerol to Value-Added Products. *Angew. Chem., Int. Ed.* **2007**, *46* (24), 4434−4440, DOI: 10.1002/anie.200604694.

(4) Quispe, C. A. G.; Coronado, C. J. R.; Carvalho, J. A., Jr. Glycerol: Production, Consumption, Prices, Characterization and New Trends in Combustion. *Renewable Sustainable Energy Rev.* **2013**, *27*, 475−493.

(5) Bajpai, H.; Chauhan, I.; Salgaonkar, K. N.; Mhamane, N. B.; Gopinath, C. S. Biomass Components toward H_2 and Value-Added Products by Sunlight-Driven Photocatalysis with Electronically Integrated $Au^{\delta-}$−TiO_2: Concurrent Utilization of Electrons and Holes. *RSC Sustainability* **2023**, *1* (3), 481−493.

(6) Monteiro, M. R.; Kugelmeier, C. L.; Pinheiro, R. S.; Batalha, M. O.; da Silva César, A. Glycerol from Biodiesel Production: Technological Paths for Sustainability. *Renewable Sustainable Energy Rev.* **2018**, *88*, 109−122.

(7) Werpy, T.; Petersen, G. *Top Value Added Chemicals from Biomass: Volume I -- Results of Screening for Potential Candidates from Sugars and Synthesis Gas*; U.S. Department of Energy Office of Scientific and Technical Information: Golden, CO (United States), 2004.

(8) Chong, C. C.; Aqsha, A.; Ayoub, M.; Sajid, M.; Abdullah, A. Z.; Yusup, S.; Abdullah, B. A Review over the Role of Catalysts for Selective Short-Chain Polyglycerol Production from Biodiesel Derived Waste Glycerol. *Environ. Technol. Innovation* **2020**, *19*, No. 100859.

(9) Sharad, J. Glycolic Acid Peel Therapy—a Current Review. *Clin., Cosmet. Invest. Dermatol.* **2013**, *6*, 281−288, DOI: 10.2147/CCID.S34029.

(10) Kim, K.-T.; Lee, J.-Y.; Kim, D.-D.; Yoon, I.-S.; Cho, H.-J. Recent Progress in the Development of Poly(Lactic-Co-Glycolic Acid)-Based Nanostructures for Cancer Imaging and Therapy. *Pharmaceutics* **2019**, *11* (6), No. 280, DOI: 10.3390/pharmaceutics11060280.

(11) Jem, K. J.; Tan, B. The Development and Challenges of Poly (Lactic Acid) and Poly (Glycolic Acid). *Adv. Ind. Eng. Polym. Res.* **2020**, *3* (2), 60−70.

(12) Li, T.; Harrington, D. A. An Overview of Glycerol Electrooxidation Mechanisms on Pt, Pd and Au. *ChemSusChem* **2021**, *14* (6), 1472−1495.

(13) Kim, D.; Oh, L. S.; Tan, Y. C.; Song, H.; Kim, H. J.; Oh, J. Enhancing Glycerol Conversion and Selectivity toward Glycolic Acid via Precise Nanostructuring of Electrocatalysts. *ACS Catal.* **2021**, *11* (24), 14926−14931.

(14) Wang, H.; Thia, L.; Li, N.; Ge, X.; Liu, Z.; Wang, X. Selective Electro-Oxidation of Glycerol over Au Supported on Extended Poly(4-Vinylpyridine) Functionalized Graphene. *Appl. Catal., B* **2015**, *166−167*, 25−31.

(15) Wu, G.; Dong, X.; Mao, J.; Li, G.; Zhu, C.; Li, S.; Chen, A.; Feng, G.; Song, Y.; Chen, W.; Wei, W. Anodic Glycerol Oxidation to Formate Facilitating Cathodic Hydrogen Evolution with Earth-Abundant Metal Oxide Catalysts. *Chem. Eng. J.* **2023**, *468*, No. 143640.

(16) Zhang, J.; Shen, Y.; Li, H. Electrolysis of Glycerol by Non-Noble Metal Hydroxides and Oxides. *ACS Appl. Energy Mater.* **2023**, *6* (10), 5508−5518.

(17) Sapner, V. S.; Tanwade, P. D.; Munde, A. V.; Sathe, B. R. Cobalt/Cobalt Oxide Nanorods-Decorated Reduced Graphene Oxide (Co/Co_3O_4 -RGO) for Enhanced Electrooxidation of Glycerol. *ACS Appl. Nano Mater.* **2023**, *6* (18), 16414−16423.

(18) Han, X.; Sheng, H.; Yu, C.; Walker, T. W.; Huber, G. W.; Qiu, J.; Jin, S. Electrocatalytic Oxidation of Glycerol to Formic Acid by $CuCo_2O_4$ Spinel Oxide Nanostructure Catalysts. *ACS Catal.* **2020**, *10* (12), 6741−6752.

(19) Xia, Z.; Ma, C.; Fan, Y.; Lu, Y.; Huang, Y.-C.; Pan, Y.; Wu, Y.; Luo, Q.; He, Y.; Dong, C.-L.; Wang, S.; Zou, Y. Vacancy Optimized Coordination on Nickel Oxide for Selective Electrocatalytic Oxidation of Glycerol. *ACS Catal.* **2024**, *14* (3), 1930−1938.

(20) Li, Y.; Wei, X.; Han, S.; Chen, L.; Shi, J. MnO_2 Electrocatalysts Coordinating Alcohol Oxidation for Ultra-Durable Hydrogen and Chemical Productions in Acidic Solutions. *Angew. Chem., Int. Ed.* **2021**, *60* (39), 21464−21472.

(21) Wu, J.; Li, J.; Li, Y.; Ma, X.; Zhang, W.; Hao, Y.; Cai, W.; Liu, Z.; Gong, M. Steering the Glycerol Electro-Reforming Selectivity via Cation−Intermediate Interactions. *Angew. Chem., Int. Ed.* **2022**, *61* (11), No. e202113362, DOI: 10.1002/anie.202113362.

(22) Patra, K. K.; Gopinath, C. S. CO_2 Electrolysis towards Large Scale Operation: Rational Catalyst and Electrolyte Design for Efficient Flow-Cell. *Chem. Commun.* **2023**, *59* (45), 6774−6795.

(23) Zhang, J.; Feng, C.; Deng, Y.; Liu, L.; Wu, Y.; Shen, B.; Zhong, C.; Hu, W. Shape-Controlled Synthesis of Palladium Single-Crystalline Nanoparticles: The Effect of HCl Oxidative Etching and Facet-Dependent Catalytic Properties. *Chem. Mater.* **2014**, *26* (2), 1213−1218.

(24) Zhang, H.; Jin, M.; Xiong, Y.; Lim, B.; Xia, Y. Shape-Controlled Synthesis of Pd Nanocrystals and Their Catalytic Applications. *Acc. Chem. Res.* **2013**, *46* (8), 1783−1794.

(25) Antolini, E. Palladium in Fuel Cell Catalysis. *Energy Environ. Sci.* **2009**, *2* (9), 915−931, DOI: 10.1039/b820837a.
(26) Terekhina, I.; White, J.; Cornell, A.; Johnsson, M. Electrocatalytic Oxidation of Glycerol to Value-Added Compounds on Pd Nanocrystals. *ACS Appl. Nano Mater.* **2023**, *6* (13), 11211−11220.
(27) Gopinath, C. S.; Nalajala, N. A Scalable and Thin Film Approach for Solar Hydrogen Generation: A Review on Enhanced Photocatalytic Water Splitting. *J. Mater. Chem. A* **2021**, *9* (3), 1353−1371.
(28) Nikolaidis, P.; Poullikkas, A. A Comparative Overview of Hydrogen Production Processes. *Renewable Sustainable Energy Rev.* **2017**, *67*, 597−611.
(29) Oener, S. Z.; Foster, M. J.; Boettcher, S. W. Accelerating Water Dissociation in Bipolar Membranes and for Electrocatalysis. *Science* **2020**, *369* (6507), 1099−1103.
(30) Chen, Y. X.; Lavacchi, A.; Miller, H. A.; Bevilacqua, M.; Filippi, J.; Innocenti, M.; Marchionni, A.; Oberhauser, W.; Wang, L.; Vizza, F. Nanotechnology Makes Biomass Electrolysis More Energy Efficient than Water Electrolysis. *Nat. Commun.* **2014**, *5* (1), No. 4036.
(31) Huang, H.; Yu, C.; Han, X.; Huang, H.; Wei, Q.; Guo, W.; Wang, Z.; Qiu, J. Ni, Co Hydroxide Triggers Electrocatalytic Production of High-Purity Benzoic Acid over 400 MA Cm^{-2}. *Energy Environ. Sci.* **2020**, *13* (12), 4990−4999.
(32) Sun, F.; Qin, J.; Wang, Z.; Yu, M.; Wu, X.; Sun, X.; Qiu, J. Energy-Saving Hydrogen Production by Chlorine-Free Hybrid Seawater Splitting Coupling Hydrazine Degradation. *Nat. Commun.* **2021**, *12* (1), No. 4182.
(33) Jiang, N.; Liu, X.; Dong, J.; You, B.; Liu, X.; Sun, Y. Electrocatalysis of Furfural Oxidation Coupled with H_2 Evolution via Nickel-Based Electrocatalysts in Water. *ChemNanoMat* **2017**, *3* (7), 491−495.
(34) Wang, T.; Tao, L.; Zhu, X.; Chen, C.; Chen, W.; Du, S.; Zhou, Y.; Zhou, B.; Wang, D.; Xie, C.; Long, P.; Li, W.; Wang, Y.; Chen, R.; Zou, Y.; Fu, X.-Z.; Li, Y.; Duan, X.; Wang, S. Combined Anodic and Cathodic Hydrogen Production from Aldehyde Oxidation and Hydrogen Evolution Reaction. *Nat. Catal* **2022**, *5* (1), 66−73.
(35) Jiang, N.; You, B.; Boonstra, R.; Rodriguez, I. M. T.; Sun, Y. Integrating Electrocatalytic 5-Hydroxymethylfurfural Oxidation and Hydrogen Production via Co−P-Derived Electrocatalysts. *ACS Energy Lett.* **2016**, *1* (2), 386−390, DOI: 10.1021/acsenergylett.6b00214.
(36) Liu, W.-J.; Xu, Z.; Zhao, D.; Pan, X.-Q.; Li, H.-C.; Hu, X.; Fan, Z.-Y.; Wang, W.-K.; Zhao, G.-H.; Jin, S.; Huber, G. W.; Yu, H.-Q. Efficient Electrochemical Production of Glucaric Acid and H2 via Glucose Electrolysis. *Nat. Commun.* **2020**, *11* (1), No. 265.
(37) Guo, W.; Heeres, H. J.; Yue, J. Continuous Synthesis of 5-Hydroxymethylfurfural from Glucose Using a Combination of AlCl3 and HCl as Catalyst in a Biphasic Slug Flow Capillary Microreactor. *Chem. Eng. J.* **2020**, *381*, No. 122754.
(38) He, O.; Zhang, Y.; Wang, P.; Liu, L.; Wang, Q.; Yang, N.; Li, W.; Champagne, P.; Yu, H. Experimental and Kinetic Study on the Production of Furfural and HMF from Glucose. *Catalysts* **2021**, *11* (1), No. 11, DOI: 10.3390/catal11010011.
(39) Xiong, T.; Zhu, Z.; He, Y.; Balogun, M.-S.; Huang, Y. Phase Evolution on the Hydrogen Adsorption Kinetics of NiFe-Based Heterogeneous Catalysts for Efficient Water Electrolysis. *Small Methods* **2023**, *7* (4), No. 2201472, DOI: 10.1002/smtd.202201472.
(40) Zhu, Z.; Luo, L.; He, Y.; Mushtaq, M.; Li, J.; Yang, H.; Khanam, Z.; Qu, J.; Wang, Z.; Balogun, M.-S. High-Performance Alkaline Freshwater and Seawater Hydrogen Catalysis by Sword-Head Structured Mo_2 N-Ni_3 Mo_3 N Tunable Interstitial Compound Electrocatalysts. *Adv. Funct Mater.* **2024**, *34* (8), No. 2306061, DOI: 10.1002/adfm.202306061.
(41) Nalajala, N.; Salgaonkar, K. N.; Chauhan, I.; Mekala, S. P.; Gopinath, C. S. Aqueous Methanol to Formaldehyde and Hydrogen on Pd/TiO_2 by Photocatalysis in Direct Sunlight: Structure Dependent Activity of Nano-Pd and Atomic Pt-Coated Counterparts. *ACS Appl. Energy Mater.* **2021**, *4* (11), 13347−13360.
(42) Busó-Rogero, C.; Grozovski, V.; Vidal-Iglesias, F. J.; Solla-Gullón, J.; Herrero, E.; Feliu, J. M. Surface Structure and Anion Effects in the Oxidation of Ethanol on Platinum Nanoparticles. *J. Mater. Chem. A* **2013**, *1* (24), 7068−7076, DOI: 10.1039/c3ta10996h.
(43) Wang, H.-F.; Liu, Z.-P. Comprehensive Mechanism and Structure-Sensitivity of Ethanol Oxidation on Platinum: New Transition-State Searching Method for Resolving the Complex Reaction Network. *J. Am. Chem. Soc.* **2008**, *130* (33), 10996−11004.
(44) Li, Y.; Wei, X.; Chen, L.; Shi, J.; He, M. Nickel-Molybdenum Nitride Nanoplate Electrocatalysts for Concurrent Electrolytic Hydrogen and Formate Productions. *Nat. Commun.* **2019**, *10* (1), No. 5335.
(45) Dai, C.; Sun, L.; Liao, H.; Khezri, B.; Webster, R. D.; Fisher, A. C.; Xu, Z. J. Electrochemical Production of Lactic Acid from Glycerol Oxidation Catalyzed by AuPt Nanoparticles. *J. Catal.* **2017**, *356*, 14−21.
(46) Yu, H.; Wang, W.; Mao, Q.; Deng, K.; Wang, Z.; Xu, Y.; Li, X.; Wang, H.; Wang, L. Pt Single Atom Captured by Oxygen Vacancy-Rich NiCo Layered Double Hydroxides for Coupling Hydrogen Evolution with Selective Oxidation of Glycerol to Formate. *Appl. Catal., B* **2023**, *330*, No. 122617.
(47) Xu, Y.; Liu, T.; Shi, K.; Yu, H.; Deng, K.; Wang, Z.; Li, X.; Wang, L.; Wang, H. Iridium-Incorporated Co_3O_4 with Lattice Expansion for Energy-Efficient Green Hydrogen Production Coupled with Glycerol Valorization. *Chem. Commun.* **2023**, *59* (13), 1817−1820.
(48) Xie, Y.; Sun, L.; Pan, X.; Zhou, Z.; Zheng, Y.; Yang, X.; Zhao, G. Carbon Paper Supported Gold Nanoflowers for Tunable Glycerol Electrooxidation Boosting Efficient Hydrogen Evolution. *Carbon* **2023**, *203*, 88−96.
(49) Zhang, Z.; Xin, L.; Qi, J.; Wang, Z.; Li, W. Selective Electro-Conversion of Glycerol to Glycolate on Carbon Nanotube Supported Gold Catalyst. *Green Chem.* **2012**, *14* (8), 2150−2152, DOI: 10.1039/c2gc35505a.
(50) Liu, L.; Liu, B.; Xu, X.; Jing, P.; Zhang, J. Heterogeneous Pt-Bi Hybrid Nanoparticle Decorated Self-Standing Hollow TiN Nanowire as an Efficient Catalyst for Glycerol Electrooxidation. *J. Power Sources* **2022**, *543*, No. 231836.
(51) Wang, Y.; Skaanvik, S. A.; Xiong, X.; Wang, S.; Dong, M. Scanning Probe Microscopy for Electrocatalysis. *Matter* **2021**, *4* (11), 3483−3514.
(52) Tao, L.; Qiao, M.; Jin, R.; Li, Y.; Xiao, Z.; Wang, Y.; Zhang, N.; Xie, C.; He, Q.; Jiang, D.; Yu, G.; Li, Y.; Wang, S. Bridging the Surface Charge and Catalytic Activity of a Defective Carbon Electrocatalyst. *Angew. Chem., Int. Ed.* **2019**, *58* (4), 1019−1024.
(53) Mhamane, N. B.; Panchal, S.; Kolekar, S. K.; Ranjan, R.; Salgaonkar, K. N.; Burange, A. S.; Nalajala, N.; Datar, S.; Gopinath, C. S. Possible Handle for Broadening the Catalysis Regime towards Low Temperatures: Proof of Concept and Mechanistic Studies with CO Oxidation on Surface Modified Pd−TiO_2. *Phys. Chem. Chem. Phys.* **2023**, *25* (33), 22040−22054.
(54) Kolekar, S. K.; Dubey, A.; Date, K. S.; Datar, S.; Gopinath, C. S. An Attempt to Correlate Surface Physics with Chemical Properties: Molecular Beam and Kelvin Probe Investigations of Ce_{1-x} Zr_x O_2 Thin Films. *Phys. Chem. Chem. Phys.* **2016**, *18* (39), 27594−27602.
(55) Cheon, J. Y.; Kim, J. H.; Kim, J. H.; Goddeti, K. C.; Park, J. Y.; Joo, S. H. Intrinsic Relationship between Enhanced Oxygen Reduction Reaction Activity and Nanoscale Work Function of Doped Carbons. *J. Am. Chem. Soc.* **2014**, *136* (25), 8875−8878.
(56) Ursua, A.; Gandia, L. M.; Sanchis, P. Hydrogen Production From Water Electrolysis: Current Status and Future Trends. *Proc. IEEE* **2012**, *100* (2), 410−426.

ACS MATERIALS Au
AN OPEN ACCESS JOURNAL OF THE AMERICAN CHEMICAL SOCIETY

pubs.acs.org/materialsau
Article

Electrocatalytic and Selective Oxidation of Glycerol to Formate on 2D 3d-Metal Phosphate Nanosheets and Carbon-Negative Hydrogen Generation

Published as part of ACS Materials Au virtual special issue "Celebrating the 25th Anniversary of the Chemical Research Society of India".

Inderjeet Chauhan, Pothoppurathu M. Vijay, Ravi Ranjan, Kshirodra Kumar Patra, and Chinnakonda S. Gopinath*

Cite This: https://doi.org/10.1021/acsmaterialsau.4c00024
Read Online

ABSTRACT: In the landscape of green hydrogen production, alkaline water electrolysis is a well-established, yet not-so-cost-effective, technique due to the high overpotential requirement for the oxygen evolution reaction (OER). A low-voltage approach is proposed to overcome not only the OER challenge by favorably oxidizing abundant feedstock molecules with an earth-abundant catalyst but also to reduce the energy input required for hydrogen production. This alternative process not only generates carbon-negative green H_2 but also yields concurrent value-added products (VAPs), thereby maximizing economic advantages and transforming waste into valuable resources. The essence of this study lies in a novel electrocatalyst material. In the present study, unique and two-dimensional (2D) ultrathin nanosheet phosphates featuring first-row transition metals are synthesized by a one-step solvothermal method, and evaluated for the electrocatalytic glycerol oxidation reaction (GLYOR) in an alkaline medium and simultaneous H_2 production. $Co_3(PO_4)_2$ (CoP), $Cu_3(PO_4)_2$ (CuP), and $Ni_3(PO_4)_2$ (NiP) exhibit 2D sheet morphologies, while $FePO_4$ (FeP) displays an entirely different snowflake-like morphology. The 2D nanosheet morphology provides a large surface area and a high density of active sites. As a GLYOR catalyst, CoP ultrathin (~5 nm) nanosheets exhibit remarkably low onset potential at 1.12 V (vs RHE), outperforming that of NiP, FeP, and CuP around 1.25 V (vs RHE). CoP displays 82% selective formate production, indicating a superior capacity for C−C cleavage and concurrent oxidation; this property could be utilized to valorize larger molecules. CoP also exhibits highly sustainable electrochemical stability for a continuous 200 h GLYOR operation, yielding 6.5 L of H_2 production with a 4 cm^2 electrode and 98 ± 0.5% Faradaic efficiency. The present study advances our understanding of efficient GLYOR catalysts and underscores the potential of sustainable and economically viable green hydrogen production methodologies.

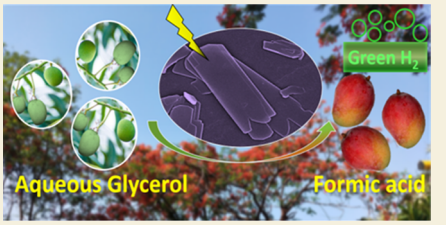

KEYWORDS: *2D material, electrolysis, earth-abundant material, sustainable development goals, Green H_2*

1. INTRODUCTION

The imperative quest for clean and renewable energy sources, driven by the increasing challenges of environmental damage and energy crises, has spurred intense research on viable alternatives. Solar, wind, and green hydrogen energy have emerged as pivotal contenders, garnering widespread attention for their potential to mitigate the adverse impacts of conventional energy production methods.[1−3] Among these, molecular hydrogen stands out as an attractive and carbon-neutral clean energy carrier, offering promise for a sustainable future.[4,5] Presently, the predominant method for hydrogen production, steam methane reforming, is marred by its unsustainability, as it relies heavily on fossil fuels and has a large amount of CO_2 emission.[6] Electrocatalytic water splitting is a compelling solution due to its capability of generating high-purity hydrogen, except for its cost. Nonetheless, this method is envisioned as a key player in the future hydrogen economy, providing an environmentally favorable alternative.[7−9] However, the current challenges in electrocatalytic water splitting are the high overpotentials required for the anodic oxygen evolution reaction (OER), leading to suboptimal energy conversion efficiency. Despite the theoretical voltage requirement of 1.23 V for OER, commercial electrolyzers typically operate at voltages around 2.0 V and higher.[10] Moreover, the coproduction of O_2 at the anode introduces the risk of

Received: April 2, 2024
Revised: April 27, 2024
Accepted: May 20, 2024

hazardous mixing with H_2 at the cathode, even in the presence of high-cost/sophisticated membranes due to crossover. Furthermore, the formation of reactive oxygen species in the presence of H_2, O_2, and catalysts poses a threat to the longevity of the electrolyzer, as it may degrade the membrane and reduce its operational lifespan.[11,12] These challenges underscore the need for innovative solutions that address the efficiency, safety, and longevity of electrocatalytic water splitting. Advancements in this field are crucial for realizing the full potential of hydrogen as a clean energy carrier and facilitating the transition toward a sustainable energy landscape.

The increasing global demand for sustainable energy resources has spurred intensive research into the development of efficient and environmentally benign catalysts for energy conversion processes. In this context, the selective electrocatalytic oxidation of glycerol is of particular significance due to its abundant availability as a byproduct in biodiesel production.[13] Glycerol, a trihydroxy sugar alcohol, presents a unique opportunity as a renewable feedstock for the synthesis of value-added products and as a potential energy carrier. It has been shown that various types of commercial products can be obtained by electrochemical conversion of glycerol oxidation, like glyceric acid, glycolic acid, lactic acid, and formic acid; indeed the industrial market value of formic acid (HCOOH) is the highest among these chemicals.[14] Methyl formate hydrolysis, which is one of the classic commercial processes for manufacturing formic acid, is often a difficult multistep process that operates at moderately high temperature (90−140 °C) and pressure (between 2 and 7 bar of methyl formate with steam) conditions.[15] Critically, the theoretical oxidation potential required to completely oxidize one molecule of glycerol into three molecules of formic acid is 0.69 V (vs RHE), which is much lower than the 1.23 V required for the OER under standard conditions.[16]

To date, the catalysts used for the glycerol oxidation reaction (GLYOR) have been primarily limited to noble metal-based catalysts, like Au,[17] AuPt,[18] Pt,[19] Pd,[20] PtSb,[21] and PtRuSn,[22] and non-noble metal-based catalysts, like NiOOH,[23−25] amorphous CoO_x,[26] $NiCo_2O_4$/NF,[27] Co-doped Ni−Fe,[28] $CuCo_2O_4$,[29] and $Ni_{0.33}Co_{0.67}(OH)_2$@HOS/NF.[30] However, the reaction pathways of GLYOR are intricate, resulting in the production of various C1−C3 intermediates due to the difficulties in efficient C−C bond cleavage. This complexity necessitates the development of nonprecious earth-abundant electrocatalysts for a highly efficient, low onset/overpotential, and selective GLYOR to possibly a single product. Therefore, it is crucial to explore alternatives to noble metals, considering their cost and availability constraints. The development of nonprecious metal catalysts could enhance the economic and environmental sustainability of the GLYOR process, addressing the challenges associated with the current noble metal-dominated catalyst landscape. Transition metal-based catalysts have emerged as promising candidates for catalyzing the GLYOR, offering a diverse range of active sites and redox capabilities. Among them, the synthesis of ultrathin two-dimensional (2D) nanosheets has garnered substantial attention for their intrinsic properties, including the high surface area, tunable composition, and enhanced catalytic activity.[31,32]

In this study, we present the synthesis of two-dimensional (2D) ultrathin nanosheet phosphates, specifically with Co, Cu, and Ni, and a three-dimensional (3D) snowflake-like structure with Fe. CoP serves as a high-performance electrocatalyst for the GLYOR in an alkaline electrolyte medium. The design rationale involves the use of a transition metal phosphate with a 2D nanosheet structure, with the aim of providing a large surface area and a high density of surface-exposed active sites. Among the phosphates, CoP demonstrates a low onset potential and superior intrinsic stability in an alkaline electrolyte. As a GLYOR catalyst, ultrathin CoP nanosheets with a thickness of ∼5 nm exhibit a remarkably lower onset at 1.12 V vs RHE than other phosphates. This value is significantly lower, and, to the best of our knowledge, this is the first phosphate-based study for glycerol oxidation. Furthermore, the optimal ultrathin CoP catalyst demonstrates highly durable electrochemical stability during 200 h of continuous GLYOR under alkaline conditions.

2. EXPERIMENTS AND CHARACTERIZATION

2.1. Materials and Chemical Reagents

Cobalt, copper, iron, and nickel phosphate catalysts were synthesized using a direct single-step solvothermal method. Cobalt chloride ($CoCl_2·6H_2O$), iron chloride ($FeCl_3$), nickel chloride ($NiCl_2·6H_2O$), copper chloride ($CuCl_2·2H_2O$), and monosodium phosphate (NaH_2PO_4) were used, as received (Merck). Glycerol ($C_3H_8O_3$), potassium hydroxide (KOH), hydrochloric acid (HCl), deuterium oxide (D_2O), potassium hydrogen phthalate (KHP), formic acid (HCOOH), glycolic acid ($C_2H_4O_3$), glyceric acid ($C_3H_6O_4$), lactic acid ($C_3H_6O_3$), acetic acid (CH_3COOH), acetone (C_3H_6O), ethanol (C_2H_5OH), and isopropyl alcohol (IPA) were purchased from TCI Chemicals. Commercial 20% Pt/C was purchased from the Merck Industry. All precursors and other chemicals were used as received. Ni foam (thickness: 0.5 mm; porosity: ∼98%) was purchased from Global Nanotech, Mumbai, and used after cleaning.

2.2. Material Characterization

The powder X-ray diffraction (XRD) patterns of the materials were evaluated to obtain the structure and phase purity using a Rigaku Miniflex-600 diffractometer with Cu Kα radiation (λ = 1.5418 Å). The morphology and compositional information of the phosphates were obtained using field-emission scanning electron microscopy (FESEM; Nova Nano SEM 450). High-resolution transmission electron microscopy (HRTEM), high-angle annular dark-field-scanning transmission electron microscopy (HAADF-STEM), and chemical mapping images were recorded using a JEOL JEM F-200 instrument operating at 200 kV. The TEM and HRTEM samples were prepared by depositing a very small amount of well-dispersed material in IPA on a carbon-coated 200 mesh copper grid and drying for 1 h. Atomic force microscopy (AFM) experiments were carried out using a CSI Nano-Observer instrument. The oxidation states of the constituent elements were determined using an X-ray photoelectron spectroscopy (XPS) (Thermo Scientific Kα) spectrometer operated with a monochromatic X-ray source (Al Kα anode: 1486.6 eV). Adventitious carbon appearing at 284.6 eV was used for any static charge correction. ^{1}H and ^{13}C NMR spectra were recorded on an AV-NEO 400 spectrometer, and a Bruker BioSpin AG system (400 MHz) was used to analyze and quantify the liquid products. The evolved gas was analyzed by gas chromatography (GC Agilent 7890A), equipped with a thermal conductivity detector (at 200 °C). Raman vibrational features were identified using a TechnoS IndiRAM CTR 500C Micro Raman Spectrometer with an excitation laser wavelength of 532 nm.

2.3. Electrochemical Measurements

2.3.1. Fabrication of the Working Electrode. The electrodes were prepared using a drop-casting technique, which involved cleaning of Ni foam (NF) with 1 M HCl ultrasonically for 30 min, followed by sequential rinsing in deionized water and ethanol, with each step lasting 10 min in a sonication bath. NF was then dried in a vacuum oven at 70 °C for 10 h. In a typical procedure, 3 mg of the M-PO_4 nanocatalyst was dispersed in a mixture of IPA and Milli-Q water

https://doi.org/10.1021/acsmaterialsau.4c00024
ACS Mater. Au XXXX, XXX, XXX−XXX

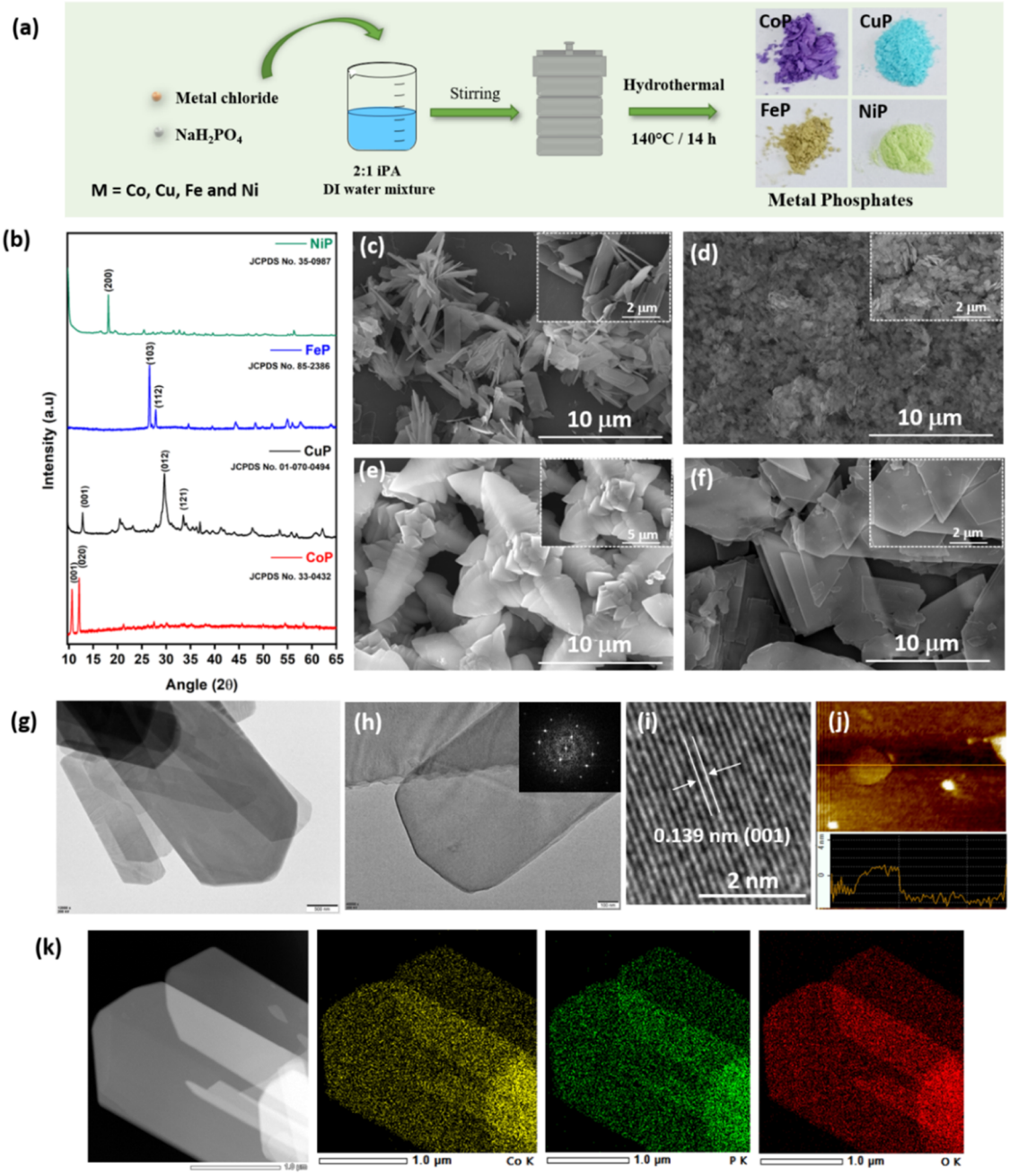

Figure 1. Synthesis and microscopy characterization of M-PO_4 (M = Co, Cu, Ni, and Fe) catalysts. (a) Schematic illustration of the M-PO_4 synthesis procedure. (b) XRD patterns of the as-prepared M-PO_4 samples. FESEM images of (c) CoP, (d) CuP, (e) FeP, and (f) NiP; insets in all these panels show FESEM images recorded at higher magnification. (g) TEM image of CoP, (h, i) HRTEM image of CoP, and SAED pattern (inset) obtained from (i) and (j) AFM images of single sheets of CoP to display the nanolevel (~3−4 nm) thickness. (k) HAADF−STEM−EDS elemental maps of the CoP nanosheets for Co, P, and O, and their uniform distribution observed all over the nanosheet.

(3:1), drop-cast onto an NF substrate (1 × 1 cm^2), and vacuum-dried for 12 h. For stability testing in the electrolyzer, a CoP electrode was prepared using a spray-coating method with a catalyst loading of 3 ± 0.1 mg/cm^2.

Electrochemical experiments for the GLYOR, OER, and hydrogen evolution reaction (HER) were conducted using a Gamry reference 3000 potentiostat in the three- and two-electrode systems. The fabricated NF electrode served as the working electrode, while a graphite rod (5 mm diameter) and Pt/C on NF were used as counter electrodes for the HER in three-electrode and two-electrode systems, respectively. A saturated calomel electrode (SCE) was used as the reference electrode. All potentials are reported versus the reversible hydrogen electrode (RHE) according to the following equation

$$E_{RHE} = E_{SCE} + 0.05916pH + 0.241V \quad (1)$$

Polarization curves were obtained with 85% *iR* compensation, and all linear sweep voltammetry (LSV) curves were recorded at a sweep rate of 5 mV/s. The apparent current density was calculated based on the geometric area of the electrodes. The double-layer capacitance (C_{dl}) was determined from cyclic voltammetry (CV) curves recorded within a potential range, where no Faradaic current was observed. Various scan rates (10, 20, 40, 60, and 80 mV/s) were utilized, and plotting the cathodic charging currents against these rates allowed the determination of the C_{dl} slope. The ECSA was determined using the following equation.[33]

$$ECSA = C_{dl}/C_{NF} \quad (2)$$

https://doi.org/10.1021/acsmaterialsau.4c00024
ACS Mater. Au XXXX, XXX, XXX−XXX

The C_{dl} value, representing the double-layer capacitance of the NF substrate in 1.0 M KOH,[34] is denoted C_{NF}. According to the formula, there is a direct correlation between the ECSA and C_{dl}. In simpler terms, when C_{dl} increases, ECSA also increases.[35]

The liquid and gaseous products were analyzed and quantified using ^{1}H and ^{13}C NMR spectroscopy, and gas chromatography (GC). Chronopotentiometry tests in a three-electrode system at 10 mA/cm^2 were conducted for 15 h (0.1 M glycerol and 1 M KOH). Chronopotentiometry tests in a two-electrode system were carried out at 20 mA/cm^2 for 200 h to identify the glycerol oxidation products and to determine the respective Faradaic efficiencies for hydrogen production. For this purpose, 450 μL of the electrolyte was mixed with 130 μL of D_2O and 20 μL of KHP (as an internal standard). KHP was employed as an internal standard for the quantification of all products observed by^{1}H NMR. The concentration of liquid products formed after the electrocatalytic reaction was calculated using the following formula

$$\frac{n_x}{n_y} = \frac{I_x}{I_y} \times \frac{N_y}{N_x} \tag{3}$$

Here, n_x represents the molar concentration of KHP, I_x represents the integral area in the ^{1}H NMR spectra for KHP, and N_x is the number of nuclei (4 equiv protons for KHP appearing at 7.25 ppm). Similarly, n_y is calculated from the above formula for the liquid product, I_y is the integral area of the product formed, and N_y is the number of nuclei associated with the peak. The concentration of the products obtained from the ^{1}H NMR spectroscopy was used to calculate the conversion, selectivity, and carbon balance.

$$\text{conversion (\%)} = \frac{n_{\text{glycerol,initial}} - n_{\text{glycerol,final}}}{n_{\text{glycerol,initial}}} \times 100 \tag{4}$$

$$\text{carbon balance (\%)} = \frac{n_{\text{sum of products}}}{3 \times n_{\text{glycerol,initial}}} \times 100 \tag{5}$$

$$\text{selectivity (\%)} = \frac{n_{\text{product}} \times \text{carbon balance}}{n_{\text{sum of products}}} \times 100 \tag{6}$$

where n is the number of moles.

2.3.2. Electrolyzer Setup. A flow electrolyzer with a geometrical area of 4 cm^2 was used in a two-electrode system, and a sustainion membrane was used to exchange the anion and separate the anode and cathode compartments for the GLYOR and HER. The flow plates were made of graphite. A constant current of 20 mA/cm^2 was used with a 3 mL/min flow rate of the solution (0.1 M glycerol + 1 M KOH) for longer stability with a peristatic pump.

$$\text{Faradaic efficiency (\%)} = \frac{n_{\text{experimental}}}{n_{\text{theoretical}}} \times 100 \tag{7}$$

where $n_{\text{experimental}}$ is the number of moles of H_2 collected experimentally. The theoretical amount of H_2 was calculated by the following equation

$$n_{\text{theoretical}} = \frac{Q}{n \times F} \tag{8}$$

where Q is the transferred charge, n is the number of electrons transferred to form one H_2 molecule, and F is the Faraday's constant (96,485 C/mol). The electricity consumption per m^3 of H_2 produced (W, kW per m^3 of H_2) is calculated as follows

$$W = \frac{n \times F \times V \times 1000}{3600 \times V_m} \tag{9}$$

where n represents the number of electrons transferred to produce each H_2 molecule, V denotes the applied voltage, and V_m is the molar volume of gas under standard temperature and pressure conditions (22.4 L/mol).

3. RESULTS AND DISCUSSION

In this study, metal (M = Co, Cu, Fe, and Ni) chloride precursors and monosodium phosphate were utilized for the synthesis of the corresponding metal phosphates using a single-step solvothermal process, as shown in Figure 1a. The synthesis process involved dissolving a 10 mM metal chloride and 20 mM phosphate precursor NaH_2PO_4 in a solvent mixture of isopropyl alcohol and ultrapure deionized water in a 2:1 ratio. This mixture resulted in a homogeneous solution, which was subsequently transferred into a 50 mL Teflon-lined stainless steel autoclave. The autoclave was then subjected to solvothermal treatment and maintained at 140 °C for 14 h in a hot air oven. Upon completion of the reaction, the autoclave was removed from the oven and allowed to cool naturally to the ambient temperature. Following the reaction, the products were filtered, subjected to multiple washes with deionized water, and finally washed with ethanol. The collected samples were then dried for 12 h in a vacuum oven, and then it was used to prepare the electrode for GLYOR. The color of the as-synthesized catalysts is shown in Figure 1a, and the catalysts are designated as CoP (violet), CuP (cyan), FeP (brown), and NiP (lime). The phase purity and crystallographic structures of the CoP, CuP, FeP, and NiP catalysts were determined using XRD. It should be noted that the environmentally benign hydrothermal synthesis of phosphate nanosheets is easy to scale up.

The narrow XRD patterns presented in Figure 1b demonstrate that the as-prepared metal phosphates exhibit a crystalline structure. CoP shows the formation of $Co_3(PO_4)_2 \cdot 8H_2O$ (JCPDS No.33-0432) with two major diffraction peaks at 10.57 and 12.09°, corresponding to the (001) and (020) crystallographic facets, respectively.[36] However, CuP (JCPDS No. 01-070-0494) displays major diffraction peaks at 12.71, 29.64, and 33.44°, which can be indexed to the (001), (012), and (121) facets, respectively.[37] FeP (JCPDS No. 85-2386) shows two major diffraction peaks at 26.62 and 27.8°, which can be indexed to (103) and (112) facets, respectively. NiP shows a major diffraction peak at 18.14° indexed to the (200) facet.[38] The layered 2D structure is evident from the XRD pattern, especially with high intensity for (00z) or (x00) with narrow features for all phosphates, except FeP. While NiP displays the (200) facet at 18.14°, CoP shows the (001) facet at 10.57°. The nanosheet morphology diminished in intensity for CuP, and a low-intensity (001) feature was observed. In contrast, $FePO_4$ does not display specific features for 2D morphology, which is supported by FESEM images (Figure 1e).

Morphological and microstructural analyses were conducted by using FESEM and HRTEM, respectively. A cursory look at the FESEM images reveals the influence of the cations on the morphology of the metal phosphates. Figure 1c,f shows bundles of sheet-like ultrathin 2D nanosheet structures for CoP and NiP, respectively; ultrathin nanosheets provide an almost transparent (for electron) appearance. The CoP appears to have a cactus−ovoid morphology with thin layers of CoP protruding from the center of the cacti. The square nanosheet and random morphology of CuP, depicted in Figure 1d, exhibit mixed morphological features. Nevertheless, a distinct morphological transformation is evident for FeP, as shown in Figure 1e, where a 3D snowflake morphology is observed. Figure 1g presents a TEM image providing detailed insight into the rectangular nanosheet structure of the CoP.

https://doi.org/10.1021/acsmaterialsau.4c00024
ACS Mater. Au XXXX, XXX, XXX−XXX

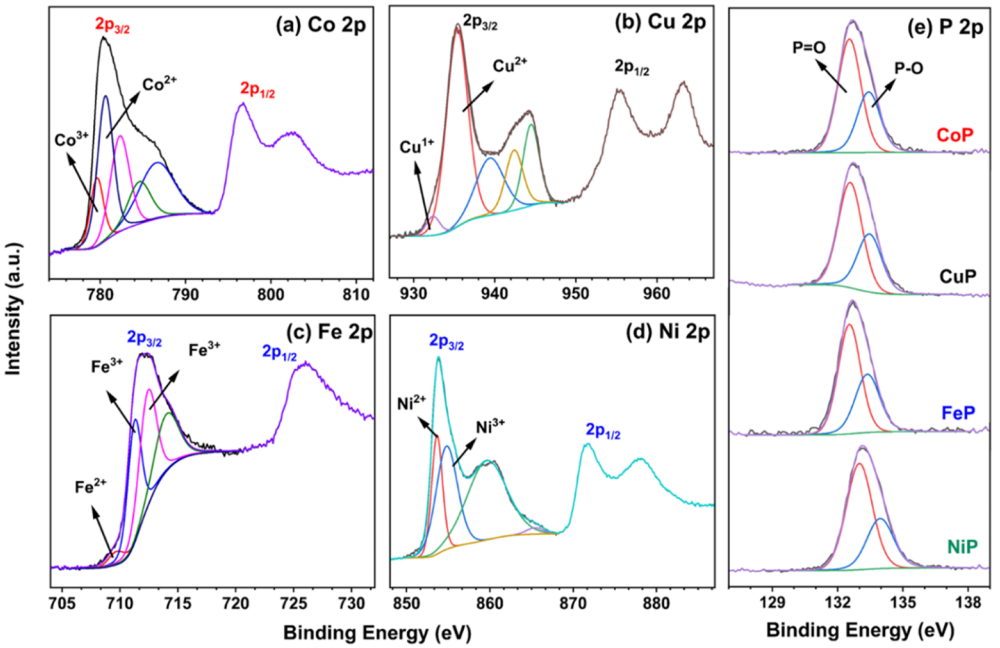

Figure 2. High-resolution XPS of (a) Co 2p, (b) Cu 2p, (c) Fe 2p, (d) Ni 2p, and (e) P 2p of the as-prepared metal phosphates.

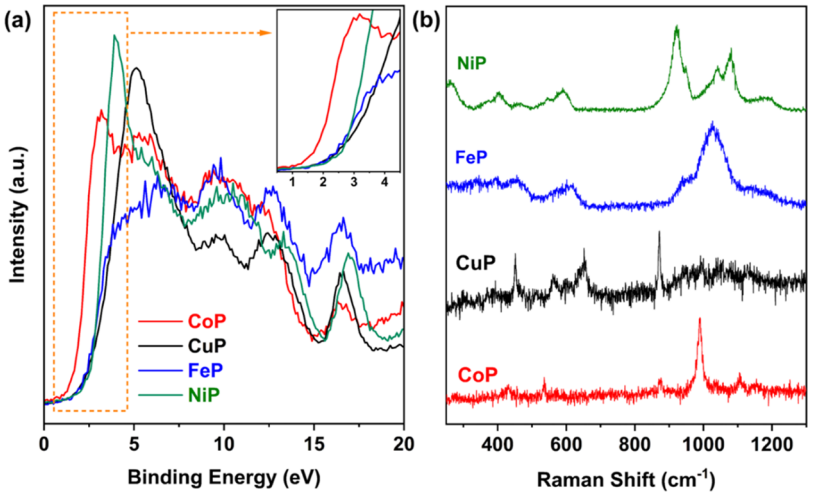

Figure 3. (a) X-ray valence band spectra of metal phosphates; the inset shows an enlarged view of VB onset. (b) Raman spectra of all metal phosphates.

Figure 1h,i shows the HRTEM images of the CoP. In Figure 1i, distinct lattice fringes are observed, revealing an interplanar spacing of 0.139 nm, which is attributed to the (001) facet of CoP, and matches the XRD data.[39] The selected area electron diffraction (SAED) pattern (inset) is shown in Figure 1i. To obtain more compositional information and understand the distribution of the constituent elements, additional investigations were conducted. Figure 1j shows the thickness of a single nanosheet of CoP, which is measured to be 3−4 nm; observation of such a thin nanosheet indicates the stacking of very few unit cells. Considering the unit-cell parameters of CoP ($a = b = 12.63$ Å, and $c = 5.017$ Å), 3−4-unit cells of CoP could be stacked into a single sheet. The hexagonal structure is evident from the nanosheet shown in TEM images (Figure 1g,h) and suggests a (001) facet. HAADF-STEM and elemental mapping in Figure 1k demonstrated the presence of cobalt (Co), phosphorus (P), and oxygen (O) as constituent elements in CoP. Moreover, a uniform distribution of all elements throughout the nanosheets was observed. Analogous patterns of the HRTEM images and elemental mappings were observed for other phosphates, as shown in the Supporting Information (Figures S1−S3 for CuP, FeP, and NiP, respectively).

3.1. Electronic Structure of Metal Phosphates

The surface chemical characteristics of all metal phosphates were investigated by XPS. The survey spectrum (Figure S4) reveals the presence of four elements (Co, Cu, Fe, and Ni) on the surfaces of CoP, CuP, FeP, and NiP, respectively, apart from P and O. High-resolution XPS spectra of (a) Co 2p, (b) Cu 2p, (c) Fe 2p, and (d) Ni 2p core levels for CoP, CuP, FeP, and NiP, respectively, and (e) P 2p are displayed in Figure 2. Deconvolution was carried out using Casa XPS software, and a Shirley background removal procedure was applied to all spectra. The Co 2p core-level spectra (Figure 2a) exhibit a spin−orbit doublet along with prominent satellite features.

https://doi.org/10.1021/acsmaterialsau.4c00024
ACS Mater. Au XXXX, XXX, XXX−XXX

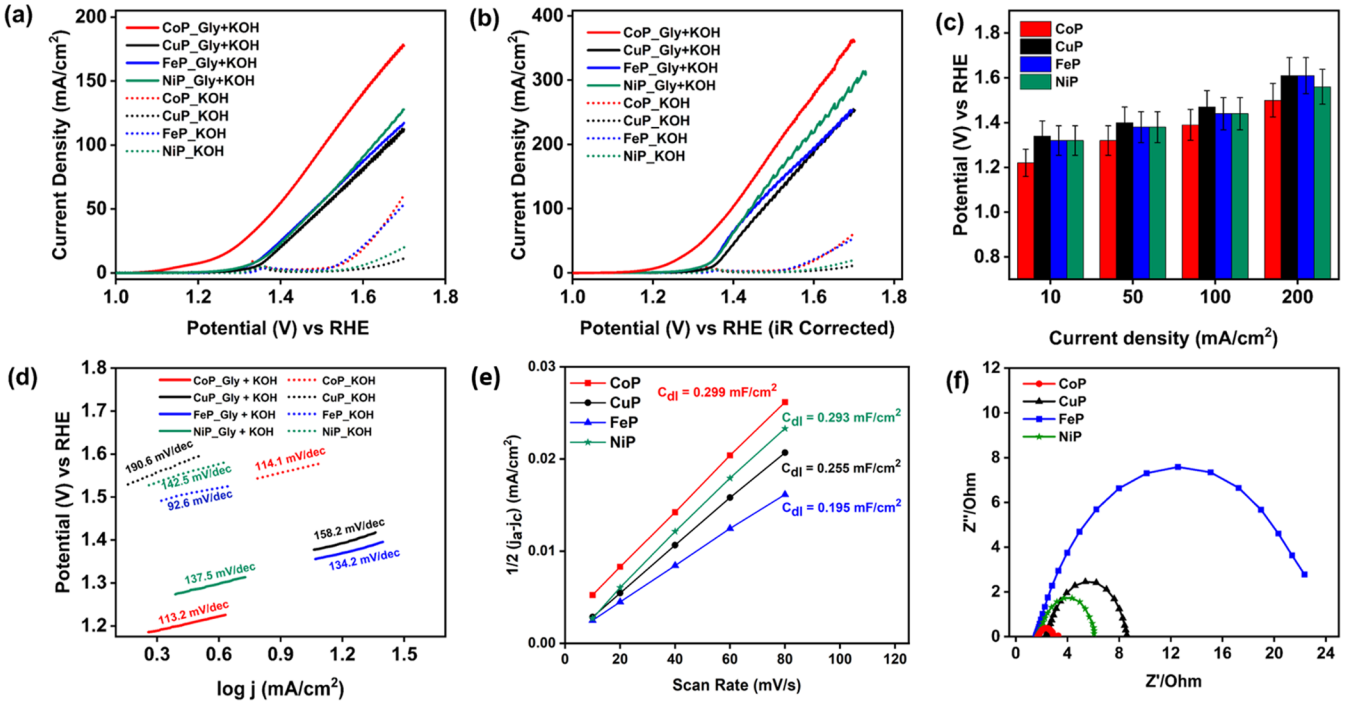

Figure 4. (a) Glycerol oxidation reaction (GLYOR) linear sweep voltammetry (LSV) curves (based on geometric current densities, mA/cm^2) for the series (Co, Cu, Fe, and Ni phosphate) on Ni foam at 5 mV/s in 0.1 M glycerol + 1 M KOH (solid line) with and without glycerol in 1 M KOH (dotted line). (b) 85% *i*R-corrected LSV curves. (c) Bar graph comparing the current densities for all phosphates. (d) Tafel plots of CoP, CuP, FeP, and NiP in 1 M KOH with and without 0.1 glycerol. (e) Capacitive current densities of different catalysts plotted against the scan rate of 10−80 mV/s and corresponding double-layer capacitance (C_{dl}) values estimated through linear fitting of the plots. (f) Nyquist plots of different catalysts recorded at a given potential of 0.35 V (vs SCE) with a frequency range of 0.1−100 kHz.

However, deconvolution indicates the presence of Co^{3+} ($2p_{3/2}$ at 779.6 eV) and Co^{2+} ($2p_{3/2}$ at 780.6 eV) oxidation states along with a subpeak at 782.3 eV and satellite features at a high binding energy (BE).[40] Similarly, a minor amount of Cu^{1+} ($2p_{3/2}$ at 932.2 ± 0.2 eV) and the majority of Cu^{2+} ($2p_{3/2}$ at 935.2 ± 0.2 eV) were observed with CuP (Figure 2b). The low-intensity feature observed at 932.2 eV is attributed to a possible reduction of Cu^{2+} to Cu^{1+} due to X-ray exposure.[41] The Fe $2p_{3/2}$ and $2p_{1/2}$ spin−orbit doublet exhibits multiple splitting and a very weak satellite, as depicted in Figure 2c for FeP. For FeP, Fe^{3+} (as in Fe_3O_4), Fe^{3+} (as in Fe-PO_4), and $Fe_3(PO_4)_2$ were observed at BEs of 711.2 ± 0.2, 712.4 ± 0.1 eV, and 714.2 ± 0.1 eV, respectively.[42] A minor peak observed at 709.6 ± 0.2 eV is attributed to the reduction of Fe^{3+} to Fe^{2+} due to X-ray exposure. In contrast, the XPS spectrum of Ni shows characteristic peaks for Ni^{2+} and Ni^{3+} at BEs of 853.5 ± 0.2 eV and 855.0 ± 0.2 eV, respectively, in Figure 2d, along with a broad satellite feature around 861 eV.[43]

Figure 2e shows the P 2p core-level spectra for all catalysts. The spectra show a broad peak, which upon deconvolution, reveals the $2p_{3/2}$ and $2p_{1/2}$ spin−orbit doublet centered at 133.0 and 133.9 eV, respectively, for all M-PO_4, except NiP. The O 1s for all phosphates recorded are shown in Figure S5; deconvolution shows three peaks at 530.5 ± 0.2, 531.5 ± 0.2, and 532.8 ± 0.2 eV. The first two features are attributed to O atoms predominantly associated with octahedral and tetrahedral coordination. The third feature at 532.8 eV is attributed to atmospheric contamination components, like water, CO_2.[44]

The X-ray valence band (XVB) spectra of all of the M-PO_4 catalysts are shown in Figure 3a. In the XVB spectra, the highest occupied VB appears between 1 and 5 eV for all catalysts. However, the presence of an intense main VB is attributed to the contributions of the M (Co, Cu, Fe, and Ni) 3d and O 2p orbitals. Interestingly, the CoP shows a distinct onset of VB at the lowest BE, compared to all other phosphates. Compared to the VB onset of NiP, the same for CoP is shifted by 0.7 eV to the lower BE. In general, the VB feature appearing at low energy corresponds to higher activity, while high BE features indicate reduced activity or greater stability of the material. Co metal oxidation to various oxide states by in situ XPS reveals the presence of Co^{3+} 3d features at lower BE in the VB, followed by the Co^{2+} 3d feature.[45] This asserts the predominant contribution of Co 3d orbitals to the electronic structure, while CuP and FeP exhibit a combination of metal 3d orbitals along with the O 2p orbitals. The NiP exhibits intermediate characteristics between the two sets. Further, the VB onset of NiP, FeP, and CuP are at the same BE, and the VB maximum appears at the lowest BE for NiP, followed by CuP and FeP. This indicates a trend in activity from high to low (CoP-NiP-CuP ∼ FeP), which is in conformity with the LSV results shown later.

3.2. Raman Spectral Studies

Raman spectra were recorded for M-PO_4, mainly to understand the structural aspects, and the Raman results are shown in Figure 3b. Distinct peaks corresponding to the vibrational modes of the free oxo-anion $(PO_4)^{3-}$ were observed in metal phosphates, encompassing a singlet (A_1) at approximately 971 cm^{-1}, a doublet (E) at around 465 cm^{-1}, and two triply degenerate (F_2) modes, namely υ_3 at 1027 and υ_4 at 567 cm^{-1}. The symmetric and asymmetric stretching modes of the P−O bonds were associated with υ_1 and υ_3, while υ_2 and υ_4 primarily involved O−P−O symmetric and asymmetric bending modes, with a minor contribution from P vibration.[46] In CoP, the

https://doi.org/10.1021/acsmaterialsau.4c00024
ACS Mater. Au XXXX, XXX, XXX−XXX

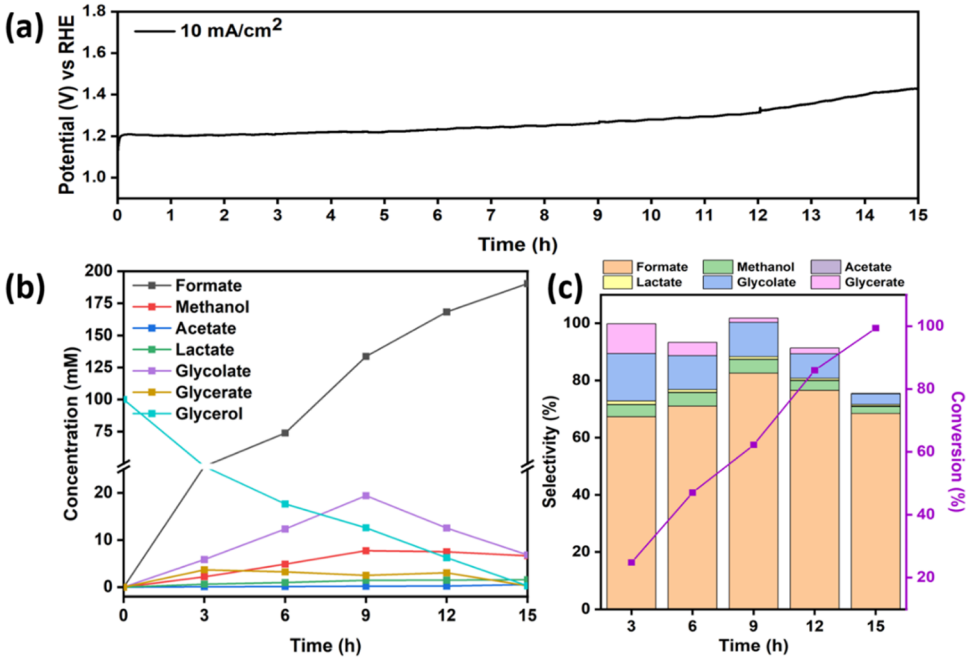

Figure 5. (a) Time-dependent chronopotentiometry (CP) reaction carried out at a constant current density of 10 mA/cm^2 for glycerol conversion using a CoP electrocatalyst. (b) Quantification of glycerol conversion and reaction products by ^{1}HNMR spectroscopy with CoP. (c) Glycerol conversion and product selectivity observed over a period of 15 h at a constant CP.

most prominent symmetric stretching peak was identified at 989 cm^{-1}, with corresponding antisymmetric and bending modes appearing weak at approximately 1100 and 420 cm^{-1}, respectively.[47] CuP exhibited only faint characteristic peaks related to the vibrations of $(PO_4)^{3-}$. FeP displayed a broad and intense symmetric stretching peak at 1025 cm^{-1}, indicating a nondistorted $(PO_4)^{3-}$ tetrahedral structure. Notably, FeP showed typical bulk characteristics in morphology and Raman spectra, whereas other phosphates demonstrated either shifts or low-intensity Raman features, suggesting their 2D nature.[48] On the other hand, NiP exhibited both features of antisymmetric modes between 1050 and 1100 cm^{-1}, with a red-shifted symmetric stretching peak at around 900 cm^{-1}. The split in the asymmetric stretching mode was attributed to the correlation effect induced by the coupling of Ni−O units in the structure.[46]

3.3. GLYOR Performance in an Alkaline Medium

Following a comprehensive analysis of the physical and chemical characteristics of the metal phosphates, electrochemical investigations of the GLYOR were conducted with electrocatalysts, as mentioned in Section 2. Given that the primary competing anodic reaction is the OER from water oxidation, an ideal GLYOR electrocatalyst should exhibit high activity toward glycerol oxidation and no (or limited) activity toward the OER. For comparison, water oxidation on these metal phosphate catalysts was also investigated under the same conditions in the absence of glycerol. The LSV polarization curves in Figure 4a depict the OER performance of metal phosphates, with and without 0.1 M glycerol. In the absence of glycerol, the metal phosphates demonstrated a notably high onset potential between the applied potential range of 1.55 to 1.68 V (vs RHE) required to achieve a current density of 10 mA/cm^2. In the presence of glycerol, the onset of GLYOR significantly decreased for all metal phosphates, indicating kinetically favorable glycerol oxidation over the OER. Specifically, CoP exhibited the lowest onset potential at 1.12 V vs RHE, followed by NiP, FeP, and CuP at 1.24, 1.24, and 1.27 V vs RHE, respectively. The *iR*-corrected polarization curves in Figure 4b reaffirm the trend observed for the catalytic activity of the electrocatalysts toward GLYOR. It is crucial to note that the catalytic performance of metal phosphates is intrinsic to the catalysts themselves, as bare Ni foam exhibits poor catalytic activity for GLYOR. Figure 4c presents a comparison of the voltage required by all metal phosphate catalysts to achieve current densities of 10, 50, 100, and 200 mA/cm^2. The disparity in the potential for GLYOR is shown in Figure 4c. In Figure S6, at current densities of 10, 20, and 50 mA/cm^2, CoP exhibits potential differences of 340, 350, and 350 mV between the GLYOR and OER, respectively. Additionally, an assessment of the electrocatalytic kinetics for both GLYOR and OER was conducted by Tafel plot analysis derived from the LSV data, as shown in Figure 4d. This result highlights a considerably reduced Tafel slope value of 113.2 mV/dec, specifically for GLYOR with CoP nanosheets among the metal phosphates. These findings underscore the superior electrocatalytic GLYOR performance of CoPs compared to metal phosphates. It may be noted that the Tafel slopes for GLYOR and OER are comparable, except for CuP, but at different potentials.

The C_{dl} measurements (Figure 4e) show that the C_{dl} for CoP is 0.299 mF/cm^2. However, the capacitance values observed for NiP (0.293 mF/cm^2), CuP (0.255 mF/cm^2), and FeP (0.195 mF/cm^2) are almost similar to those of CoP. The C_{dl} values are calculated from the CV graphs at different scan rates, as shown in Figure S7. The measured C_{dl} values and the corresponding ECSA values of CoP (7.475 cm^2), NiP (7.325 cm^2), CuP (6.375 cm^2), and FeP (4.875 cm^2) indicate that all of the electrocatalysts have almost the same number of active sites.[49,50] However, the intrinsic activity of the CoP is significantly higher as compared to other metal phosphate catalysts, which resonates in the XPS-VB spectra (Figure 3a);

https://doi.org/10.1021/acsmaterialsau.4c00024
ACS Mater. Au XXXX, XXX, XXX−XXX

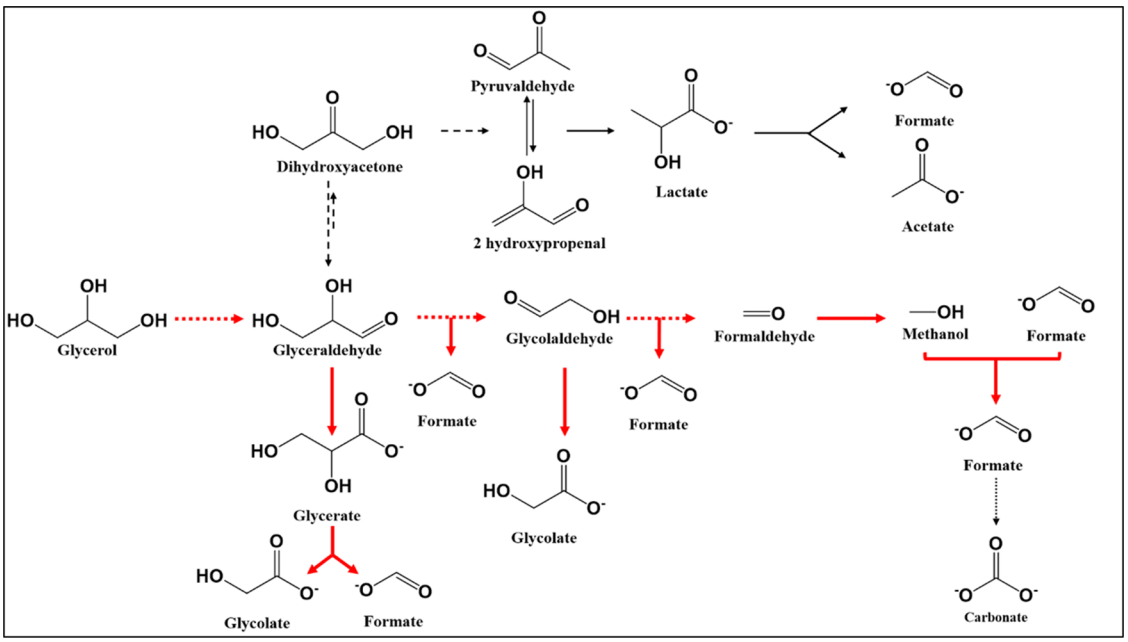

Figure 6. Proposed mechanistic pathway for the electrocatalytic oxidation of glycerol to formate on CoP in an alkaline medium, with emphasis on the suggested dominant pathways indicated by thick red arrows and dotted arrows showing unobserved intermediates. Solid and dashed black arrows indicate minor and alternate pathways for product formation.

CoP exhibits the lowest VB energy among phosphates, which leads to enhanced GLYOR activity.

To further investigate the interfacial reaction behavior of the catalyst, electrochemical impedance spectroscopy (EIS) was carried out. The EIS Nyquist plots presented in Figure 4f show a notable reduction in the charge transfer resistance (R_{ct}) of CoP compared to the other catalysts. Specifically, the R_{ct} of CoP (3 Ω) is significantly smaller than those of NiP (6.06 Ω), CuP (8.59 Ω), and FeP (24.62 Ω), indicating accelerated charge transfer kinetics between the CoP electrode and electrolyte. Despite the almost similar number of active sites in all electrocatalysts, CoP exhibited accelerated charge transfer behavior, which was mainly due to the high intrinsic activity of the active sites present, which enhanced GLYOR activity.

To assess the long-term performance of GLYOR and its anodic products, constant chronopotentiometry (CP) was conducted at 10 mA/cm^2 for 15 h. The stability of CoP was observed for the initial 12 h of CP, after which formate oxidation commenced (to carbonate) due to a decrease in the glycerol concentration and an increase in the OER. Consequently, achieving and maintaining a current density of 10 mA/cm^2 required an increase in the potential (Figure 5a). A significant potential increase during glycerol oxidation after about 12 h suggests the onset of formate oxidation to carbonate. Furthermore, the reaction mechanism was investigated by quantifying the 3 h interval samples using ^{1}H NMR analysis, as depicted in Figure 5b. A detailed carbon balance study was also conducted after each 3 h duration of the GLYOR process, and the results are listed in Table S1 in the Supporting Information. A decrease in glycerol content and a concurrent increase in formate concentration, as a function of reaction time along with near 100% carbon balance in 9 h suggest a 100% efficient conversion of glycerol to formate in 15 h (Figure 5b). The major intermediates detected in GLYOR included glycerate, glycolate, and methanol, while acetate and lactate were minor intermediates, as shown by ^{1}H NMR spectroscopy (Figure S8). As shown in Figure 5c, at 9 h, the formate selectivity reaches 82%, and glycerol conversion is at ∼62%. Over time, formate undergoes further oxidation to carbonate due to the decreasing reactant availability, leading to a conversion exceeding 80% and formate selectivity reaching 78% at 12 h. By the end of 15 h, 100% glycerol conversion was achieved, although the carbon balance is less than 100% due to the significant formation of carbonate through continued oxidation of formate, which is evident from the small carbonate peak observed in the ^{13}C NMR data (Figure S9). A similar kinetic study was conducted for CuP, FeP, and NiP, with quantification, and the glycerol conversion and product selectivity results are provided in Supporting Information (Figures S10−12 and Table S1). With NiP, under comparable conditions at a current density of 10 mA/cm^2, a noteworthy 93% glycerol conversion and 64% formate selectivity were observed after 12 h. However, the carbon balance diminished beyond this duration due to the continued oxidation of formate (Figure S12). Conversely, CuP and FeP exhibited lower conversion rates with approximately 50% selectivity for formate observed at a constant current density of 10 mA/cm^2 after 15 h. Notably, CuP and FeP necessitated an increase in the potential to achieve a desired current density of 10 mA/cm^2, leading to the oxidation of formate to CO_2 (Figure S13).

3.4. Proposed Mechanism Pathway for Glycerol Oxidation

The typical glycerol oxidation mechanism of a metal oxide or noble metal in an alkaline medium reported in the literature is as follows. First, a glycerol molecule is adsorbed on the catalyst surface, initiating dehydrogenation. This process leads to the formation of glycolaldehyde (GALD) or dihydroxyacetone (DHA), with subsequent reversible interconversion facilitated by base catalysis. Through a dehydration step, DHA can be transformed into pyruvaldehyde or 2-hydroxypropenal. These intermediates may undergo conversion into lactate via the Cannizzaro rearrangement, and subsequently, acetate and formate are produced through C−C cleavage (Figure 6).[51,52]

https://doi.org/10.1021/acsmaterialsau.4c00024
ACS Mater. Au XXXX, XXX, XXX−XXX

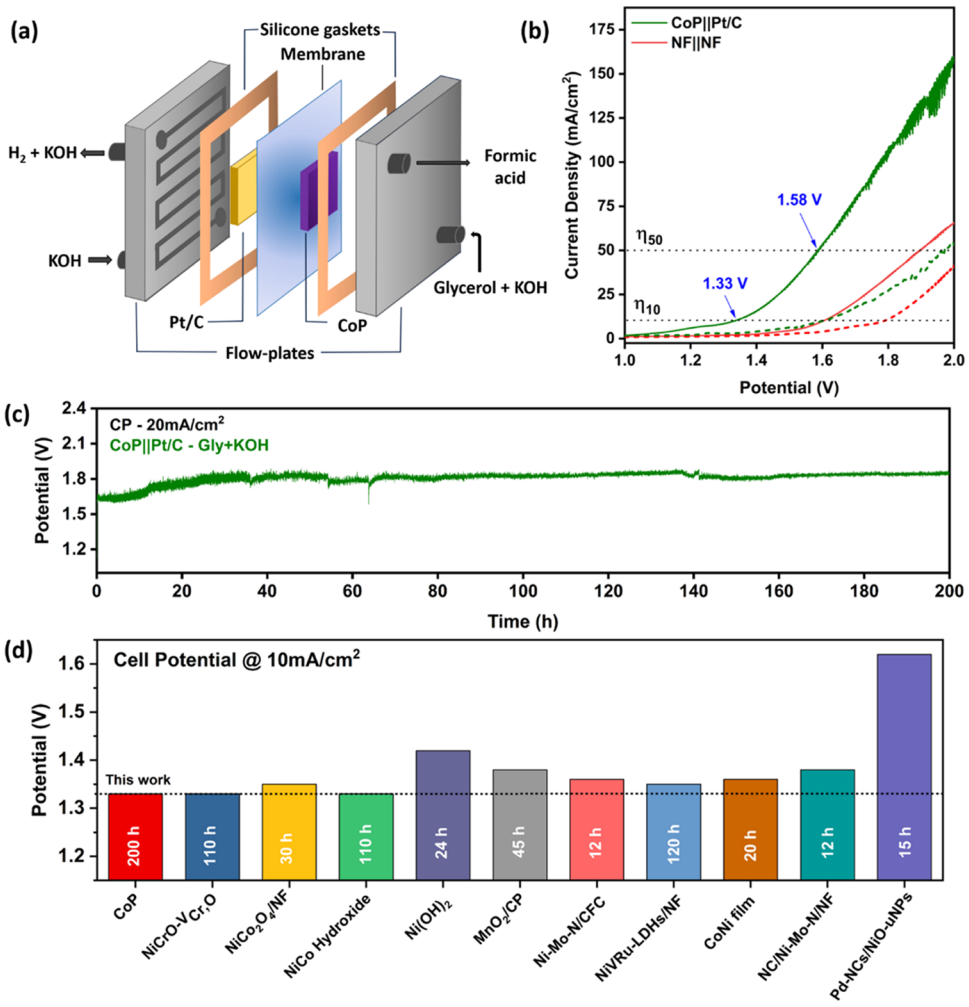

Figure 7. (a) Schematic of a two-electrode alkaline electrolyzer engaged in the GLYOR to formate at the anode and the HER at the cathode. (b) LSV plot observed for GLYOR in the electrolyzer, utilizing CoP/NF as the anode and Pt/C as the cathode (solid line, glycerol + KOH; dashed line, KOH). The same measurement was made on the NF also to rule out the GLYOR contribution. (c) Sustainability investigation of GLYOR at 20 mA/cm^2 was conducted using a two-electrode electrolyzer employing CoP||Pt/C. (d) Comparison of the electrolytic efficiency of GLYOR at 10 mA/cm^2 for CoP with alternate electrocatalysts reported in the literature.

In the current work, it is evident from Figure 5 that high formate selectivity with significant selectivity for glycolate and glycerate indicates that oxidation occurs at either end of the terminal carbon. Although no glyceraldehyde was observed in the present work, it is very likely to undergo fast oxidation to glycerate and subsequently to glycolate and formate. Minor amounts of lactate and acetate formed in the current reaction (Figure 5c) also indicate that a parallel mechanism, to a small extent, occurs through DHA and pyruvaldehyde. The major conclusion that could be derived is the efficient oxidative C−C cleavage of glycerol and all intermediates, such as glycerate and glycolate, followed by preferential/selective oxidation to formate, on the CoP catalyst under the current experimental conditions. It is also evident from Figure 5c that, irrespective of the nature of intermediates, all of them undergo oxidation to formate. This concept may be extended to larger molecules with suitable catalysts under relevant conditions and more effort in this direction is desired.

3.5. Sustainable Performance Study for the CoP Catalyst

In the realm of water electrolysis, a critical hurdle lies in the imperative reduction of the operational potential to curtail the input electricity consumption. The substantial overpotential inherent to the OER in water splitting renders it exceptionally challenging to achieve a noteworthy reduction in power consumption beyond a certain threshold. Nevertheless, this obstacle was effectively overcome by the synergistic coupling of GLYOR and HER in a two-electrode electrolyzer configuration, as shown in Figure 7a.

The electrolyzer architecture featured a Pt/C cathode and a CoP anode spatially segregated by an anion-exchange membrane, with specific details provided in Section 2. Figure 7b shows the LSV plot for GLYOR in an alkaline electrolyzer, which reveals the concurrent electrochemical generation of hydrogen and formate at room temperature. At higher temperatures, between 60 and 75 °C, a large enhancement in electrolyzer activity performance is expected; therefore, it is worth performing this experiment. With the electrolyzer setup at room temperature, a current density of 10 mA/cm^2 (50 mA/cm^2) was achieved at a notably low cell potential of 1.33 V (1.58 V), as shown in Figure 7b. Under these operational conditions, the system exhibited a simultaneous HER and glycerol oxidation performance. In contrast, a conventional water electrolysis experiment, employing a two-electrode setup with the same CoP||Pt/C cell but devoid of glycerol

https://doi.org/10.1021/acsmaterialsau.4c00024
ACS Mater. Au XXXX, XXX, XXX−XXX

supplementation required a higher cell potential of 1.60 V (1.89 V) to attain an identical current density of 10 (50) mA/cm^2. Due to the significantly more advantageous thermodynamics of GLYOR on the CoP surface, the constructed electrolyzer necessitates just ∼4.2 kWh/m^3 of H_2 at a current density of 100 mA/cm^2. This is in stark contrast to the ∼5.5 kWh/m^3 of H_2 required by conventional alkaline electrolyzers. The remarkable low cell voltage exhibited by the CoP||Pt/C system in the context of biomass component-assisted water splitting distinguishes it as an attractive feature relative to the majority of reported systems, as outlined in Table S2. Importantly, it is noteworthy that hydrogen constituted the exclusive gaseous product observed, with no oxygen- or carbon-containing byproducts, such as CO and CO_2. In addition, the sustainable performance of biomass component-based electrolysis was demonstrated via a chronoamperometry experiment for 200 h conducted at a current density of 20 mA/cm^2, and the results are shown in Figure 7c. It shows that the voltage remains constant at ∼1.63 V throughout the 10 h operation for glycerol oxidation, and further the ∼200 mV potential has been increased for secondary molecule oxidation, which is constant throughout the reaction and shows the stability of the catalyst. During the ongoing reaction within a 25 h time frame, the GLYOR sample was subjected to analysis via ^{1}H NMR. The results confirmed an increase in formate concentration, as depicted in Figure S14, along with glycerol conversion. Subsequently, after 75 h, the formate concentration decreased, which was attributed to its further oxidation to carbonates. To enhance the prolonged efficacy of the catalyst, the electrolyte was introduced into the solution after 75 h. Under a constant current density (CP) of 20 mA/cm^2, the hydrogen production rate remained constant at an average of 32.5 mL/h throughout the continuous operation of the overall reaction. The Faradaic efficiency of the HER was determined to be approximately 98%. The calculation of the FE for the HER involved a thorough analysis comparing the theoretical and experimental H_2 production, and detailed calculations are provided in Section 2. The catalytic performance of CoP is either comparable to or better than that of other electrocatalysts documented in the literature for overall electrolysis with GLYOR under the same conditions (Figure 7d). However, the current study shows sustainability for longer hours, along with a very high selectivity for formate production. This is depicted in Figure 7d, and many other catalysts are listed in Table S2. FESEM characterization (Figure S15) carried out after 200 h GLYOR (Figure 7c) exhibits intact nanosheet morphology, except for some agglomeration. The XRD pattern remains the same, as that observed in Figure 1b. These results indicate that the CoP catalyst remains stable and does not undergo any changes due to the prolonged reaction.

4. CONCLUSIONS

In conclusion, this study elucidates a distinctive morphology-dependent selectivity for formate and glycerol conversion on metal phosphates, showing simultaneous and highly efficient electrocatalytic hydrogen generation. Cobalt phosphate (CoP) has been identified as a novel and proficient catalyst, demonstrating both efficiency and stability in the selective production of formate through glycerol oxidation under alkaline conditions at ambient temperature. Particularly, ultrathin 2D-CoP nanosheets exhibit very high selectivity, achieving 82% formate yield compared to other phosphates. The electrochemical oxidative cleavage of the C−C bond is more favorable for CoP than for NiP, FeP, and CuP catalysts. The coupling of the anodic GLYOR and cathodic HER within the CoP||Pt/C two-electrode electrolyzer yields a current density of 10 mA/cm^2 with a minimal cell voltage of 1.33 V. Continuous operation of the GLYOR for over 8 days (24 × 7) indicates the enduring stability of the CoP catalyst under the present experimental conditions. Utilizing the earth-abundant transition metal phosphate for the electrocatalytic oxidation of glycerol paves the way for innovative designs and exploration of economical ways of addressing the GLYOR. These catalysts offer efficient and selective electrochemical glycerol oxidation, yielding formate and other value-added chemicals along with the production of environmentally friendly hydrogen resources.

The engineered CoP catalyst exhibits remarkable efficiency in catalyzing the conversion of glycerol to formate, thereby demonstrating promising prospects for its application in the conversion of diverse biomass feedstocks, including glucose, starch, and cellulose. The selective C−C cleavage strategy presented in this study is worth exploring with any of the larger molecules listed above and may be evaluated for depolymerization of low-molecular-weight polymers. Furthermore, carrying out electrocatalytic conversions at significantly higher temperatures (50 and 75 °C) is expected to substantially improve the performance. Another important aspect is the production of hydrogen under such conditions, which prudently employs waste/abundant carbon-containing molecules to produce value-added products; hence, the generated hydrogen becomes carbon-negative green hydrogen. This type of route may prove to be helpful in achieving net-zero targets sooner. Nonetheless, more work is required in this direction.

■ ASSOCIATED CONTENT

Supporting Information

The Supporting Information is available free of charge at https://pubs.acs.org/doi/10.1021/acsmaterialsau.4c00024.

HRETM images of CuP, FeP, and NiP (Figures S1−S3); XPS survey spectra of all M-PO_4 (Figure S4), O 1s XPS spectra (Figure S5); potential differences between GLYOR and OER in the CoP nanosheet (Figure S6); double-layer capacitance (C_{dl}) calculation (Figure S7); ^{1}H NMR spectra of the intermediate products (Figure S8); ^{13}C NMR spectra of GLYOR (Figure S9); GLYOR reaction, and selectivity conversion graph of CuP, FeP, and NiP (Figures S10−S12); chronopotentiometry reaction graph of all M-PO_4 (Figure S13); ^{1}H NMR spectra of GLYOR in an electrolyzer system with CoP||Pt/C (Figure S14); FESEM images (Figure S15); selectivity, conversion, and carbon balance of all M-PO_4 (Table S1); and comparison table of recently reported work in GLYOR and other low oxidizing molecules (Table S2) (PDF)

■ AUTHOR INFORMATION

Corresponding Author

Chinnakonda S. Gopinath − *Catalysis and Inorganic Chemistry Division, CSIR-National Chemical Laboratory, Pune 411 008, India; Academy of Scientific and Innovative Research (AcSIR), Ghaziabad 201 002, India;* orcid.org/0000-0002-4525-3912; Email: cs.gopinath@ncl.res.in

https://doi.org/10.1021/acsmaterialsau.4c00024
ACS Mater. Au XXXX, XXX, XXX−XXX

Authors

Inderjeet Chauhan − *Catalysis and Inorganic Chemistry Division, CSIR-National Chemical Laboratory, Pune 411 008, India; Academy of Scientific and Innovative Research (AcSIR), Ghaziabad 201 002, India*

Pothoppurathu M. Vijay − *Catalysis and Inorganic Chemistry Division, CSIR-National Chemical Laboratory, Pune 411 008, India*

Ravi Ranjan − *Catalysis and Inorganic Chemistry Division, CSIR-National Chemical Laboratory, Pune 411 008, India; Academy of Scientific and Innovative Research (AcSIR), Ghaziabad 201 002, India*

Kshirodra Kumar Patra − *Catalysis and Inorganic Chemistry Division, CSIR-National Chemical Laboratory, Pune 411 008, India;* orcid.org/0000-0002-1468-0946

Complete contact information is available at: https://pubs.acs.org/10.1021/acsmaterialsau.4c00024

Author Contributions

CRediT: **Inderjeet Chauhan** conceptualization, investigation, writing-original draft, writing-review & editing.

Notes

The authors declare no competing financial interest.

■ ACKNOWLEDGMENTS

I.C. acknowledges a research scholarship from DST-INSPIRE. We acknowledge financial support from the CSIR for an NCP project (HCP-44) through the H2T program.

■ REFERENCES

(1) Dresselhaus, M. S.; Thomas, I. L. Alternative Energy Technologies. *Nature* **2001**, *414* (6861), 332−337.

(2) Zhang, J.; Wang, H.; Tian, Y.; Yan, Y.; Xue, Q.; He, T.; Liu, H.; Wang, C.; Chen, Y.; Xia, B. Y. Anodic Hydrazine Oxidation Assists Energy-Efficient Hydrogen Evolution over a Bifunctional Cobalt Per selenide Nanosheet Electrode. *Angew. Chem., Int. Ed.* **2018**, *57* (26), 7649−7653.

(3) Gopinath, C. S.; Nalajala, N. A Scalable and Thin Film Approach for Solar Hydrogen Generation: A Review on Enhanced Photocatalytic Water Splitting. *J. Mater. Chem. A* **2021**, *9* (3), 1353−1371.

(4) Zhang, J.; Wang, T.; Liu, P.; Liao, Z.; Liu, S.; Zhuang, X.; Chen, M.; Zschech, E.; Feng, X. Efficient Hydrogen Production on $MoNi_4$ Electrocatalysts with Fast Water Dissociation Kinetics. *Nat. Commun.* **2017**, *8* (1), No. 15437.

(5) Rajaambal, S.; Sivaranjani, K.; Gopinath, C. S. Recent Developments in Solar H_2 Generation from Water Splitting. *J. Chem. Sci.* **2015**, *127* (1), 33−47.

(6) Navarro, R. M.; Peña, M. A.; Fierro, J. L. G. Hydrogen Production Reactions from Carbon Feedstocks: Fossil Fuels and Biomass. *Chem. Rev.* **2007**, *107* (10), 3952−3991.

(7) Holladay, J. D.; Hu, J.; King, D. L.; Wang, Y. An Overview of Hydrogen Production Technologies. *Catal. Today* **2009**, *139*, 244−260.

(8) Li, X.; Hao, X.; Abudula, A.; Guan, G. Nanostructured Catalysts for Electrochemical Water Splitting: Current State and Prospects. *J. Mater. Chem. A* **2016**, *4* (31), 11973−12000.

(9) Zheng, D.; Li, J.; Ci, S.; Cai, P.; Ding, Y.; Zhang, M.; Wen, Z. Three-Birds-with-One-Stone Electrolysis for Energy-Efficiency Production of Gluconate and Hydrogen. *Appl. Catal., B* **2020**, *277*, No. 119178.

(10) Qin, D.-D.; Tang, Y.; Ma, G.; Qin, L.; Tao, C.-L.; Zhang, X.; Tang, Z. Molecular Metal Nanoclusters for ORR, HER and OER: Achievements, Opportunities and Challenges. *Int. J. Hydrogen Energy* **2021**, *46* (51), 25771−25781.

(11) Rausch, B.; Symes, M. D.; Chisholm, G.; Cronin, L. Decoupled Catalytic Hydrogen Evolution from a Molecular Metal Oxide Redox Mediator in Water Splitting. *Science* **2014**, *345* (6202), 1326−1330.

(12) Wei, X.; Wang, S.; Hua, Z.; Chen, L.; Shi, J. Metal−Organic Framework Nanosheet Electrocatalysts for Efficient H_2 Production from Methanol Solution: Methanol-Assisted Water Splitting or Methanol Reforming? *ACS Appl. Mater. Interfaces* **2018**, *10* (30), 25422−25428.

(13) Kim, D.; Oh, L. S.; Tan, Y. C.; Song, H.; Kim, H. J.; Oh, J. Enhancing Glycerol Conversion and Selectivity toward Glycolic Acid via Precise Nanostructuring of Electrocatalysts. *ACS Catal.* **2021**, *11* (24), 14926−14931.

(14) Quispe, C. A. G.; Coronado, C. J. R.; Carvalho, J. A., Jr. Glycerol: Production, Consumption, Prices, Characterization and New Trends in Combustion. *Renewable Sustainable Energy Rev.* **2013**, *27*, 475−493.

(15) Bulushev, D. A.; Ross, J. R. H. Towards Sustainable Production of Formic Acid. *ChemSusChem* **2018**, *11* (5), 821−836.

(16) Rizk, M. R.; Abd El-Moghny, M. G. Controlled Galvanic Decoration Boosting Catalysis: Enhanced Glycerol Electro-Oxidation at Cu/Ni Modified Macroporous Films. *Int. J. Hydrogen Energy* **2021**, *46* (1), 645−655.

(17) Xie, Y.; Sun, L.; Pan, X.; Zhou, Z.; Zheng, Y.; Yang, X.; Zhao, G. Carbon Paper Supported Gold Nanoflowers for Tunable Glycerol Electrooxidation Boosting Efficient Hydrogen Evolution. *Carbon* **2023**, *203*, 88−96.

(18) Dai, C.; Sun, L.; Liao, H.; Khezri, B.; Webster, R. D.; Fisher, A. C.; Xu, Z. J. Electrochemical Production of Lactic Acid from Glycerol Oxidation Catalyzed by AuPt Nanoparticles. *J. Catal.* **2017**, *356*, 14−21.

(19) Zhang, Z.; Xin, L.; Li, W. Electrocatalytic Oxidation of Glycerol on Pt/C in Anion-Exchange Membrane Fuel Cell: Cogeneration of Electricity and Valuable Chemicals. *Appl. Catal., B* **2012**, *119*−*120*, 40−48.

(20) Chauhan, I.; Bajpai, H.; Ray, B.; Kolekar, S. K.; Datar, S.; Patra, K. K.; Gopinath, C. S. Electrocatalytic Glycerol Conversion: A Low Voltage Pathway to Efficient Carbon-Negative Green Hydrogen and Value Added Chemicals Production. *ACS Appl. Mater. Interfaces* **2024**, *16*, 26130−26141, DOI: 10.1021/acsami.4c02392.

(21) Lee, S.; Kim, H. J.; Lim, E. J.; Kim, Y.; Noh, Y.; Huber, G. W.; Kim, W. B. Highly Selective Transformation of Glycerol to Dihydroxyacetone without Using Oxidants by a PtSb/C-Catalyzed Electrooxidation Process. *Green Chem.* **2016**, *18* (9), 2877−2887.

(22) Kim, H. J.; Choi, S. M.; Green, S.; Tompsett, G. A.; Lee, S. H.; Huber, G. W.; Kim, W. B. Highly Active and Stable PtRuSn/C Catalyst for Electrooxidations of Ethylene Glycol and Glycerol. *Appl. Catal., B* **2011**, *101* (3−4), 366−375.

(23) Choi, S.; Balamurugan, M.; Lee, K.-G.; Cho, K. H.; Park, S.; Seo, H.; Nam, K. T. Mechanistic Investigation of Biomass Oxidation Using Nickel Oxide Nanoparticles in a CO_2 -Saturated Electrolyte for Paired Electrolysis. *J. Phys. Chem. Lett.* **2020**, *11* (8), 2941−2948.

(24) Taitt, B. J.; Nam, D.-H.; Choi, K.-S. A Comparative Study of Nickel, Cobalt, and Iron Oxyhydroxide Anodes for the Electrochemical Oxidation of 5-Hydroxymethylfurfural to 2,5-Furandicarboxylic Acid. *ACS Catal.* **2019**, *9* (1), 660−670.

(25) Li, J.; Wei, R.; Wang, X.; Zuo, Y.; Han, X.; Arbiol, J.; Llorca, J.; Yang, Y.; Cabot, A.; Cui, C. Selective Methanol-to-Formate Electrocatalytic Conversion on Branched Nickel Carbide. *Angew. Chem., Int. Ed.* **2020**, *59* (47), 20826−20830.

(26) Vo, T.-G.; Ho, P.-Y.; Chiang, C.-Y. Operando Mechanistic Studies of Selective Oxidation of Glycerol to Dihydroxyacetone over Amorphous Cobalt Oxide. *Appl. Catal., B* **2022**, *300*, No. 120723.

(27) Wu, G.; Dong, X.; Mao, J.; Li, G.; Zhu, C.; Li, S.; Chen, A.; Feng, G.; Song, Y.; Chen, W.; Wei, W. Anodic Glycerol Oxidation to Formate Facilitating Cathodic Hydrogen Evolution with Earth-Abundant Metal Oxide Catalysts. *Chem. Eng. J.* **2023**, *468*, No. 143640.

(28) Zhong, Z.; Li, M.; Wang, J.; Lin, J.; Pan, J.; Jiang, S.; Xie, A.; Luo, S. Co-Doped Ni−Fe Spinels for Electrocatalytic Oxidation over Glycerol. *Int. J. Hydrogen Energy* **2022**, *47* (29), 13933−13945.
(29) Han, X.; Sheng, H.; Yu, C.; Walker, T. W.; Huber, G. W.; Qiu, J.; Jin, S. Electrocatalytic Oxidation of Glycerol to Formic Acid by $CuCo_2O_4$ Spinel Oxide Nanostructure Catalysts. *ACS Catal.* **2020**, *10* (12), 6741−6752.
(30) Pei, Y.; Pi, Z.; Zhong, H.; Cheng, J.; Jin, F. Glycerol Oxidation-Assisted Electrochemical CO_2 Reduction for the Dual Production of Formate. *J. Mater. Chem. A* **2022**, *10* (3), 1309−1319.
(31) Wang, Y.; Zhang, M.; Liu, Y.; Zheng, Z.; Liu, B.; Chen, M.; Guan, G.; Yan, K. Recent Advances on Transition-Metal-Based Layered Double Hydroxides Nanosheets for Electrocatalytic Energy Conversion. *Adv. Sci.* **2023**, *10* (13), No. 2207519.
(32) Xie, H.; Li, Z.; Cheng, L.; Haidry, A. A.; Tao, J.; Xu, Y.; Xu, K.; Ou, J. Z. Recent Advances in the Fabrication of 2D Metal Oxides. *iScience* **2022**, *25* (1), No. 103598.
(33) Yang, J.; Xiao, Y.; Zhao, Q.; Zhang, G.; Wang, R.; Teng, G.; Chen, X.; Weng, M.; He, D.; Mu, S.; Lin, Y.; Pan, F. Synergistic Effect of Charge Transfer and Short H-Bonding on Nanocatalyst Surface for Efficient Oxygen Evolution Reaction. *Nano Energy* **2019**, *59*, 443−452.
(34) Li, N.; Ai, L.; Jiang, J.; Liu, S. Spinel-Type Oxygen-Incorporated Ni^{3+} Self-Doped Ni_3S_4 Ultrathin Nanosheets for Highly Efficient and Stable Oxygen Evolution Electrocatalysis. *J. Colloid Interface Sci.* **2020**, *564*, 418−427.
(35) Anantharaj, S.; Ede, S. R.; Sakthikumar, K.; Karthick, K.; Mishra, S.; Kundu, S. Recent Trends and Perspectives in Electrochemical Water Splitting with an Emphasis on Sulfide, Selenide, and Phosphide Catalysts of Fe, Co, and Ni: A Review. *ACS Catal.* **2016**, *6* (12), 8069−8097.
(36) Katkar, P. K.; Marje, S. J.; Kale, S. B.; Lokhande, A. C.; Lokhande, C. D.; Patil, U. M. Synthesis of Hydrous Cobalt Phosphate Electro-Catalysts by a Facile Hydrothermal Method for Enhanced Oxygen Evolution Reaction: Effect of Urea Variation. *CrystEngComm* **2019**, *21* (5), 884−893.
(37) Pujari, S. S.; Kadam, S. A.; Ma, Y.-R.; Jadhav, S. B.; Kumbhar, S. S.; Bhosale, S. B.; Gunjakar, J. L.; Lokhande, C. D.; Patil, U. M. Hydrothermally Synthesized Nickel Copper Phosphate Thin Film Cathodes for High-Performance Hybrid Supercapacitor Devices. *J. Energy Storage* **2022**, *52*, No. 105037.
(38) Sharma, P.; Radhakrishnan, S.; Khil, M.-S.; Kim, H.-Y.; Kim, B.-S. Simple Room Temperature Synthesis of Porous Nickel Phosphate Foams for Electrocatalytic Ethanol Oxidation. *J. Electroanal. Chem.* **2018**, *808*, 236−244.
(39) Bu, X.; Chiang, C.; Wei, R.; Li, Z.; Meng, Y.; Peng, C.; Lin, Y.; Li, Y.; Lin, Y.; Chan, K. S.; Ho, J. C. Two-Dimensional Cobalt Phosphate Hydroxide Nanosheets: A New Type of High-Performance Electrocatalysts with Intrinsic CoO_6 Lattice Distortion for Water Oxidation. *ACS Appl. Mater. Interfaces* **2019**, *11* (42), 38633−38640.
(40) Ranjan, R.; Tekawadia, J.; Jain, R.; Mhamane, N. B.; Raja, T.; Gopinath, C. S. Co_3O_4 for Sustainable CO_2 Reduction and Possible Fine-Tuning towards Selective CO Production. *Chem. Eng. J.* **2023**, *471*, No. 144459.
(41) Roy, K.; Gopinath, C. S. UV Photoelectron Spectroscopy at Near Ambient Pressures: Mapping Valence Band Electronic Structure Changes from Cu to CuO. *Anal. Chem.* **2014**, *86* (8), 3683−3687.
(42) Wang, Y.; Asunskis, D. J.; Sherwood, P. M. A. Iron (II) Phosphate $(Fe_3(PO_4)_2$ by XPS. *Surf. Sci. Spectra* **2002**, *9* (1), 91−98.
(43) Velu, S.; Suzuki, K.; Vijayaraj, M.; Barman, S.; Gopinath, C. S. In Situ XPS Investigations of $Cu_{1-x}Ni_xZnAl$-Mixed Metal Oxide Catalysts Used in the Oxidative Steam Reforming of Bio-Ethanol. *Appl. Catal., B* **2005**, *55* (4), 287−299.
(44) Jain, R.; Reddy, K. P.; Ghosalya, M. K.; Gopinath, C. S. Water Mediated Deactivation of Co_3O_4 Naonrods Catalyst for CO Oxidation and Resumption of Activity at and Above 373 K: Electronic Structural Aspects by NAPPES. *J. Phys. Chem. C* **2017**, *121* (37), 20296−20305.
(45) Reddy, K. P.; Jain, R.; Ghosalya, M. K.; Gopinath, C. S. Metallic Cobalt to Spinel Co_3O_4 —Electronic Structure Evolution by Near-Ambient Pressure Photoelectron Spectroscopy. *J. Phys. Chem. C* **2017**, *121* (39), 21472−21481.
(46) Ramana, C. V.; Ait-Salah, A.; Utsunomiya, S.; Becker, U.; Mauger, A.; Gendron, F.; Julien, C. M. Structural Characteristics of Lithium Nickel Phosphate Studied Using Analytical Electron Microscopy and Raman Spectroscopy. *Chem. Mater.* **2006**, *18* (16), 3788−3794.
(47) Mahmoud, B. A.; Mirghni, A. A.; Oyedotun, K. O.; Momodu, D.; Fasakin, O.; Manyala, N. Synthesis of Cobalt Phosphate-Graphene Foam Material via Co-Precipitation Approach for a Positive Electrode of an Asymmetric Supercapacitors Device. *J. Alloys Compd.* **2020**, *818*, No. 153332.
(48) Zhang, L.; Brow, R. K. A Raman Study of Iron−Phosphate Crystalline Compounds and Glasses. *J. Am. Ceram. Soc.* **2011**, *94* (9), 3123−3130.
(49) Jeon, S. S.; Kang, P. W.; Klingenhof, M.; Lee, H.; Dionigi, F.; Strasser, P. Active Surface Area and Intrinsic Catalytic Oxygen Evolution Reactivity of NiFe LDH at Reactive Electrode Potentials Using Capacitances. *ACS Catal.* **2023**, *13* (2), 1186−1196.
(50) Patra, K. K.; Gopinath, C. S. CO_2 Electrolysis towards Large Scale Operation: Rational Catalyst and Electrolyte Design for Efficient Flow-Cell. *Chem. Commun.* **2023**, *59* (45), 6774−6795.
(51) Terekhina, I.; White, J.; Cornell, A.; Johnsson, M. Electrocatalytic Oxidation of Glycerol to Value-Added Compounds on Pd Nanocrystals. *ACS Appl. Nano Mater.* **2023**, *6* (13), 11211−11220.
(52) Li, Y.; Wei, X.; Chen, L.; Shi, J.; He, M. Nickel-Molybdenum Nitride Nanoplate Electrocatalysts for Concurrent Electrolytic Hydrogen and Formate Productions. *Nat. Commun.* **2019**, *10* (1), No. 5335.

https://doi.org/10.1021/acsmaterialsau.4c00024
ACS Mater. Au XXXX, XXX, XXX−XXX